Ultrasound Imaging Innovations for Visualization and Quantification of Vascular Biomarkers

by

Yat Shun Yiu

A thesis
presented to the University of Waterloo
in fulfillment of the
thesis requirement for the degree of
Doctor of Philosophy
in
Electrical and Computer Engineering

Waterloo, Ontario, Canada, 2019

EXAMINING COMMITTEE MEMBERSHIP

The following served on the Examining Committee for this thesis. The decision of the Examining Committee is by majority vote.

External Examiner NAME: Dr. Michael L. Oelze

Title: Associate Head for Graduate Affairs, Department Head's Office, Graduate Advising

Professor, Department of Electrical and Computer Engineering, University of Illinois at Urbana-Champaign

Supervisor(s) NAME: Dr. Alfred C. H. Yu

Title: Professor, Department of Electrical and Computer Engineering, University of Waterloo

Internal Member NAME: Dr. George Freeman

Title: Associate Professor, Department of Electrical and Computer Engineering, University of Waterloo

Internal Member NAME: Dr. Derek Wright

Title: Lecturer and Graduate Attributes Lecturer, Department of Electrical and Computer Engineering, University of Waterloo

Internal-External Member:

NAME: Dr. Richard L Hughson

Title: Schlegel Research Chair in Vascular Aging and Brain Health,

Senior Director of Research, Research Institute for Aging

Professor, Department of Kinesiology, University of Waterloo

AUTHOR'S DECLARATION

This thesis consists of material all of which I authored or co-authored: see Statement of Contributions included in the thesis. This is a true copy of the thesis, including any required final revisions, as accepted by my examiners.

I understand that my thesis may be made electronically available to the public.

STATEMENT OF CONTRIBUTIONS

The author contributions for each Chapter are described below.

Chapters 1, 7: Billy Y. S. Yiu wrote the initial draft of the chapter.

Chapter 2 presents material from an article entitled "Live ultrasound color encoded speckle imaging platform for real-time complex flow visualization *in vivo*" which has been published in *IEEE Transactions on Ultrasonics, Ferroelectrics, and Frequency Control* © IEEE 2019. This article was co-authored by Billy Y. S. Yiu, Mateusz Walczak, Marcin Lewandowski, and Alfred C. H. Yu. M. Walczak and M. Lewandowski designed the ultrasound module. B. Y. S. Yiu designed the software console and imaging algorithm, performed all experiments, analyzed the data, and wrote the manuscript. A. C. H. Yu reviewed the results and manuscript prior to publication.

Chapter 3 presents material from an article entitled "High-frame-rate Doppler ultrasound bandwidth imaging for flow instability mapping" which has been published in *Medical Physics*. This article was co-authored by Billy Y. S. Yiu, Adrian J. Y. Chee, Guo Tang, Wenbo Luo, and Alfred C. H. Yu. G. Tang and W. Luo provided initial input to the concept. B. Y. S. Yiu designed the imaging algorithm, fabricated the phantoms, performed all the experiments, analyzed the data and wrote the manuscript. A. J. Y. Chee provided input in editing the manuscript. A. C. H. Yu reviewed the results and manuscript prior to publication.

Chapter 4 presents material from an article entitled "Spiral flow phantom for ultrasound flow imaging experimentation" which has been published in IEEE *Transactions on Ultrasonics, Ferroelectrics, and Frequency Control* © IEEE 2017. This article was co-authored by Billy Y. S. Yiu and Alfred C. H. Yu. B. Y. S. Yiu designed the phantom, performed the *in vitro* experiments, analyzed the data and wrote the manuscript. A. C. H. Yu reviewed the results and manuscript prior to publication.

A version of **Chapter 5**, titled "Visualization of Rat Choroid Vasculature Using Contrast-Enhanced Ultrasound Motion-Resistant Microvasculature Imaging" is being prepared for submission to the *IEEE*

Transactions of Ultrasonics, Ferroelectrics, and Frequency Control, co-authored by Billy Y. S. Yiu, Hanyue Shangguan, Raksha Urs, Jeffrey A. Ketterling, Ronald H. Silverman, and Alfred C. H. Yu. B. Y. S. Yiu designed the imaging algorithm and calibration phantom, performed the *in vitro* experiments, analyzed the data, and wrote the manuscript draft. H. Shangguan fabricated the ultrasound contrast. R. Urs, J. A. Ketterling and R. H. Silverman performed *in vivo* experiments. All authors will review the results and manuscript prior to submission.

A version of **Chapter 6**, titled "Instantaneous volumetric flow rate estimator for cerebral blood flow measurement" is being prepared for submission to the *IEEE Transactions of Ultrasonics, Ferroelectrics, and Frequency Control*, co-authored by Billy Y. S. Yiu, Jason Au, and Alfred C. H. Yu. B. Y. S. Yiu designed the imaging algorithm and calibration phantom, performed the *in vitro* experiments, analyzed the data, and wrote the manuscript draft. J. Au performed *in vivo* experiments. All authors will review the results and manuscript prior to submission.

Abstract

The existence of plaque in the carotid arteries, which provide circulation to the brain, is a known risk for stroke and dementia. Alas, this risk factor is present in 25% of the adult population. Proper assessment of carotid plaque may play a significant role in preventing and managing stroke and dementia. However, current plaque assessment routines have known limitations in assessing individual risk for future cardiovascular events. There is a practical need to derive new vascular biomarkers that are indicative of cardiovascular risk based on hemodynamic information. Nonetheless, the derivation of these biomarkers is not a trivial technical task because none of the existing clinical imaging modalities have adequate time resolution to track the spatiotemporal dynamics of arterial blood flow that is pulsatile in nature.

The goal of this dissertation is to devise a new ultrasound imaging framework to measure vascular biomarkers related to turbulent flow, intra-plaque microvasculature, and blood flow rate. Central to the proposed framework is the use of high frame rate ultrasound (HiFRUS) imaging principles to track hemodynamic events at fine temporal resolution (through using frame rates of greater than 1000 frames per second). The existence of turbulent flow and intra-plaque microvessels, as well as anomalous blood flow rate, are all closely related to the formation and progression of carotid plaque. Therefore, quantifying these biomarkers can improve the identification of individuals with carotid plaque who are at risk for future cardiovascular events. To facilitate the testing and the implementation of the proposed imaging algorithms, this dissertation has included the development of new experimental models (in the form of flow phantoms) and a new HiFRUS imaging platform with live scanning and on-demand playback functionalities. Pilot studies were also carried out on rats and human volunteers. Results generally demonstrated the real-time performance and the practical efficacy of the proposed algorithms.

The proposed ultrasound imaging framework is expected to improve carotid plaque risk classification and, in turn, facilitate timely identification of at-risk individuals. It may also be used to derive new insights on carotid plaque formation and progression to aid disease management and the development of personalized treatment strategies.

Acknowledgements

Flashing back to 2016 when my supervisor Prof. Alfred Yu asked if I want to pursue my PhD with him, I said yes without thinking twice. It is the second best decision in my life. I was his first Master student back in University of Hong Kong and now I am his first PhD student in University of Waterloo.

This PhD journey has been a great adventure for me and I have learnt a lot. Living alone in a new country is a whole new experience to me and I enjoy it a lot, especially when exploring new places and trying out new restaurants with my fellow labmates. The movie nights and board game nights we have in the lab are wonderful experiences.

I would like to thank Alfred for his supports and insightful advices. He has helped me overcome many challenges. Without his support, I will not be able to accomplish what I have done in this journey.

I would like to thank our lab manager Adrian Chee. It is delightful to work with him over the past several years. I still remember the night that we had to work on his first conference presentation in the hotel room, and the countless times that we had to work overnight to meet deadlines. He is the greatest companion that one can have. I am glad to have him alongside on this journey. Many thanks go to my fellow lab members Takuro Ishii, and Kit Ho; they have help me a lot over this journey.

I want to thank my parents for their unconditional love and support. They have provided positive encouragement throughout this journey and have done whatever they can to help me reach my life goals.

Thank you Julia Houston for editing my dissertation. She has proofread my thesis chapters 1, 5, 6, and 7 for spelling, grammar, punctuation, and capitalization errors. She has also edited the sentence structure, clarity and consistency of style and made helpful comments and suggestions.

Lastly, I would like to thank my lovely wife Selina for her love and support. Marrying her is the best decision I have ever made. It is not easy to maintain a long distance relationship but we have made it through. Her surprise parcels always cheer me up when I feel lost. Without her support, I will not be able to complete this journey.

This dissertation marks the end of one journey, and it is now time to start a new one.

Table of Contents

List of Figures

List of Tables

List of Symbols and Abbreviations

Symbols

ε	Random white noise
λ	Wavelength
μ_t	Local mean value of slow-time vector
ν	Fluid kinematic viscosity
φ_n	n^{th} Receive steering angle (Chapter 1)
φ_p	Updated AR model coefficient at p^{th} iteration
σ_t	Local standard deviation of slow-time vector
θ_n	n^{th} Transmit steering angle (Chapter 1)
θ	Revolution angle of a spiral (Chapter 3)
A	Cross-sectional area
$\mathbf{A}$	Angle matrix of multi-angle vector Doppler estimator
$\mathbf{A}^{\dagger}$	Pseudoinverse of angle matrix $\mathbf{A}$
$A_{x,y,t}$	Scattering strength of microbubble within the imaging view at time t
a	residual lumen size at stenosis
$a_{P,k}$	k^{th} complex AR parameter of a P^{th}-order complex AR model
B	Beam correlation width
B_x	Lateral beam correlation width
B_y	Azimuthal beam correlation width
B_z	Axial beam correlation width
C	Slow-time correlation coefficient
C_t	Microbubble correlation map (Chapter 5)
	Correlation-time curve (Chapter 6)
$\hat{C}_t$	Estimated correlation-time curve
$\overline{C_t}$	Averaged correlation-time curve

$C_t[l]$	l^{th} lag correlation coefficient at time t
c	Distal internal carotid artery diameter
c_0	Speed of sound
D	Nozzle diameter (Chapter 4)
	Mean correlation map (Chapter 6)
d	Displacement
d_x	Lateral displacement
d_z	Axial displacement
$e[n]$	n^{th} sample in the complex modeling error
e_p^f	Forward prediction error
e_p^b	Backward prediction error
F#	F-number
f_0	Transmit pulse center frequency
$f_{broad\text{-}view}$	Frame rate with HiFRUS imaging strategy
f_n	n^{th} mean slow-time frequency
$f_{scanline}$	Frame rate with scanline based imaging strategy
FV_{avg}	Mean flow velocity measured using TCD
FV_{peak}	Peak flow velocity measured using TCD
h	Height
K	Number of B-mode DAQ subsequence (Chapter 2)
	Persistence (Chapter 4)
	Number of estimates to be averaged (Chapter 6)
k	Pitch of the spiral phantom
L	Filter order for FIR filter (Chapter 2)
	Number of lag in autocorrelation (Chapter 6)

M	Number of sample per segment processed by a block of compute thread (Chapter 2)
	Sliding window step size in slow-time processing (Chapter 4)
	Decorrelation rate obtained from Gaussian curve fitting (Chapter 6)
M_{Tx}	Number of transmit steering angle
M_{Rx}	Number of receive steering angle
m_x	Simulated lateral tissue velocity
m_z	Simulated axial tissue velocity
$MVImage$	Microvascular image
N	Number of ensemble for slow-time processing
$N_{scanline}$	Number of scanline per image
P	Number of pulsing event (Chapter 2)
	Autoregressive model order (Chapter 4)
	Number of receive steering angles (Chapter 6)
$P_{x,y,t}$	Position of microbubbles in the imaging view at time t
$P'_{x,y,t}$	Estimated Position of microbubbles in the imaging view at time t
p	p^{th} iteration of AR modeling
PSF	Point spread function of the imaging system
Q	Number of executions of imaging sequence (Chapter 2)
	Volumetric flow rate (Chapter 4, Chapter 6)
	Accumulation frame (Chapter 5)
r	radius of the Archimedean spiral
Re	Reynolds number
s	Extracted speckle signal
$S_{AR}[f]$	Doppler power spectrum constructed from AR modeling
S_t	Extracted microbubble signal

t	Time
t_{PRI}	Pulse repetition interval
u	Average flow velocity
$\mathbf{u}$	Mean frequency mesurand vector
v	Velocity
$\mathbf{v}$	Velocity vector
v_x	Lateral velocity
v_y	Flow Flux
v_z	Axial Velocity
w	width
$x[n]$	Slow-time signal
x	Lateral position
z	Imaging depth (Chapter 1)
	Axial position (Chapter 5)

Abbreviations

2-D/3-D	Two-dimensional/Three-dimensional
ACR	Autocorrelation
API	Application programing interface
AR	Autoregressive
ASC	Analytic signal conversion
B-mode	Brightness-mode
BPM	Beat per minute
CAD	Computer-aided design
CBF	Cerebral blood flow
CCA	Common carotid artery
CESI	Color encoded speckle imaging

CEUS	Contrast-enhanced ultrasound
CFD	Computational fluid dynamics
CFI	Color flow imaging
CIMT	Carotid intima-media thickness
CE-MRA	Contrast-enhanced magnetic resonance angiography
CRA	Central retinal artery
CT/CTA	Computed tomography/Computed tomographic angiography
CUDA	Compute unified device architecture
DAS	Delay-and-sum
DAQ	Data acquisition
DDR3	Double data rate, version 3
DMA	Direct memory access
DSA	Digital subtraction angiography
DUBI	Doppler ultrasound bandwidth imaging
EC	Endothelial cell
ECA	External carotid artery
eNOS	Endothelial nitric oxide synthase
FDG	^{18}F-flurodeoxyglucose
FDM	Fused deposition modeling
FIR	Finite impulse response
FN	False negative
FOV	Field of view
FP	False positive
FPGA	Field-programmable gate array
FPS/fps	Frame per second
FWHM	Full-width at half maximum

GB	Gigabyte
GPU	Graphical processing unit
GSM	Gray scale median
HIF-1α	Hypoxia-inductible factor-1α
HiFRUS	High-frame-rate ultrasound
HRI	High resolution image
ICA	Internal carotid artery
ICAM-1	Intercellular adhesion molecule 1
IIR	Infinite impulse response
IVFRE	Instantaneous volumetric flow rate estimator
JSON	Javascript object notation
LDL	Low density lipoprotein
LRI	Low resolution image
MCA	Middle cerebral artery
MCI	Mild cognitive impairment
MRMVI	Motion-resistant microvascular imaging
MRA	Magnetic resonance angiography
MRI	Magnetic resonance imaging
MVI	Microvascular imaging
NASCET	North American symptomatic carotid endarterectomy trial
NO	Nitric oxide
OP	Open platform
PC	Personal computer
PCIe	Peripheral component interconnect express
PD	Pulsed Doppler
PDI	Power Doppler imaging

PET	Positron emission tomography
PRF	Pulse repetition frequency
PSF	Point spread function
PSV	Peak systolic velocity
PWV	Pulse wave velocity
PVA	Polyvinyl alcohol
RAM	Random access memory
RF	Radio frequency
ROC	Receiver operating characteristic
ROI	Region of interest
Rx	Receive
SMC	Smooth muscle cell
SNR	Signal-to-noise ratio
STL	Stereolithographic file format
TOF/TOF-MRA	Time-of-flight/Time-of-flight magnetic resonance imaging
T/R	Transmit/receive
TCD	Transcranial Doppler
TN	True negative
TP	True positive
Tx	Transmit
VA	Vertebral artery
VCAM-1	Vascular cell adhesion molecule 1
VEGF	Vascular endothelial growth factor
VPI	Vector projectile imaging
WHO	World health organization
WSS/WSR	Wall shear stress/Wall shear rate

Chapter 1
Introduction

1.1 Stroke, Dementia and Carotid Atherosclerosis

More than 25% of the global population age 18 or above has carotid atherosclerosis (Prati et al., 1992) that may lead to cerebrovascular diseases such as stroke and dementia (Eid et al., 2016; Gbinigie, Reckless, & Buchan, 2016; Kistler & Furie, 2000; Skagen, Skjelland, Zamani, & Russell, 2016; Wendell et al., 2012). In particular, thromboembolic events caused by carotid atherosclerosis account for at least 20% of ischemic stroke cases (Marulanda-Londono & Chaturvedi, 2016; Skagen et al., 2016). When carotid plaque ruptures, emboli are formed and cause thrombosis, leading to acute occlusion and subsequently ischemic stroke. In cases where the emboli are small, they may travel along the bloodstream to the brain and eventually block smaller cerebral arteries downstream, causing embolism and ischemic stroke or a transient ischemic attack that may result in dementia. However, carotid atherosclerosis can also lead to dementia under chronic exposure (Hofman et al., 1997; van Exel et al., 2002). The vascular hypothesis of Alzheimer's disease (de la Torre, 2018) suggests that carotid atherosclerosis compounded with aging may lead to substantial reduction in cerebral blood flow (CBF). Studies have shown that aging causes CBF to decline (Chen, Rosas, & Salat, 2011; Leenders et al., 1990), and atherosclerosis imposes an additional burden on the already declining CBF, leading to insufficient supply of oxygen and nutrients to meet the neurometabolic demand. This causes brain hypoxia/ischemia and consequently cognitive impairment. Cognitive impairment would eventually deteriorate to dementia under chronic exposure of CBF reduction.

Carotid atherosclerosis refers to the growth of fatty plaque along the arterial wall lining at the carotid that supplies oxygen and nutrients to the brain. *Atherosclerosis* is an inflammatory response of the intima to chronic injury (Davies & Woolf, 1993; Ross et al., 1986). At the lesion site, low density lipoproteins (LDLs) in the plasma enter the intima into the subendothelial space, and the LDLs are oxidized because of the increased oxidative stress. These oxidized LDLs trigger an inflammatory response, and monocytes (one type of leukocytes) are recruited to the lesion site to remove the oxidized LDLs through phagocytosis. These monocytes become rich in lipids and subsequently turn into foam cells, which turn into fatty dots or streaks, and later into plaque (Davies & Woolf, 1993; Falk, 2006; Steinberg & Witztum, 2002). At this early stage of atherosclerosis, the arterial wall lining has not been noticeably thickened and reduces the vessel lumen. As the atherosclerotic disease progresses, this immunoinflammatory response joins forces with a fibroproliferative response mediated by intima smooth muscle cells to repair the arterial injury. If the atherogenic stimuli persist over the course of

years, the reparative response may become and dominate; lumen is lost and blood flow reduced (Kragel, Reddy, Wittes, & Roberts, 1989). The reduced blood flow in the carotid could lead to vascular cognitive impairment and dementia with chronic exposure (de la Torre, 2000, 2016). In some cases, the foam cells and smooth muscle cells die by apoptosis or necrosis, leaving a destabilized lipid-rich core and a fragile and rupture-prone fibrous cap (Geng & Libby, 2002). When this fibrous cap ruptures, the lipid contents, or emboli, inside may leak, causing strokes.

Stroke occurs when blood stops being supplied to any part of the brain, causing hypoxia and eventually damaging brain cells. There are three types of stroke: ischemic, hemorrhagic, and transient ischemic attack. Among the three, ischemic accounts for 87% of all stroke cases in the United States (Kleindorfer et al., 2010; Mozaffarian et al., 2016). Stroke can be fatal if patients are not treated in time. Globally, stroke is the second leading cause of death (World Health Organization, 2018) and is fifth in the United States, where an estimated 7 million people over 20 years old self-reported having a stroke in 2010, giving the average prevalence of stroke in adults of 2.9% (2016 BRFSS Survey Data and Documentation, 2019). Every year, roughly 795,000 people experience stroke events, and 610,000 of them are first attacks (Benjamin et al., 2019) in the United States; among all these stroke incidences, 142,000 (18%) are fatal, and the rest result in various degrees of disabilities. This makes stroke the leading cause of serious long-term disability (Centers for Disease Control and Prevention, 2009); stroke survivors suffer from various complications including pain syndromes, cognitive impairment and dementia, gait instability, and falls and fractures. From 2014–2015, the direct cost of stroke was $28 billion in the United States (Agency for Healthcare Research and Quality, 2019), and the total direct medical stroke-related costs are projected to increase from $36.7–94.3 billion by 2035. This poses a huge financial burden on both patients and society.

The World Health Organization (WHO; 2019) defined *dementia* as “a syndrome in which there is deterioration in cognitive function beyond what might be expected from normal aging”. It is irreversible and progressive; a patient’s condition would only worsen over time. In the United States, dementia is the sixth leading cause of mortality, just after stroke. In 2010, Hebert, Weuve, Scherr, & Evans, (2013) estimated 4.7 million people had Alzheimer’s disease in the United States, the most common type of dementia. The estimated total monetary cost of dementia in 2010 was between $157 and $215 billion (Hurd, Martorell, Delavande, Mullen, & Langa, 2013), much higher than that of stroke. The cost of dementia is expected to dramatically increase as the projected number of people having dementia will be tripled in 2050 (Hebert et al., 2010).

To lower morbidity and mortality and lessen the financial burden of stroke and dementia, the prevention and management of carotid atherosclerosis may play a significant role (Baber et al., 2015;

Meschia et al., 2014; Napoli et al., 2006; van Exel et al., 2002). Current carotid atherosclerotic risk assessments rely on traditional cardiovascular risk factors (Assmann, Cullen, & Schulte, 2002; D'Agostino et al., 2008) and atherosclerotic-related arterial wall changes (Hathout, Fink, El-Sadern, & Grant, 2005; Stein et al., 2008). However, these risk factors have well-known limitations and cannot accurately assess individual risk (Weber et al., 2015). Atherosclerotic plaque with the similar arterial wall changes (e.g., degree of stenosis) could have substantial differences in their associated risk (Nighoghossian, Derex, & Douek, 2005; Rothwell, Gibson, & Warlow, 2000). Atherosclerotic risk assessment performance may be improved by incorporating vascular markers that are directly related to atherosclerosis (Ammirati, Moroni, Norata, Magnoni, & Camici, 2015; Palombo & Kozakova, 2016) to refine risk stratification over time (Stein et al., 2008). For example, disturbed flow has been shown to play a critical role in initiation and progression of atherosclerosis (Chiu & Chien, 2011), whereas plaque neovascularization is a predictor of future cerebrovascular events. These vascular biomarkers should therefore be routinely monitored to identify patients at risk (Mortimer, Nachiappan, & Howlett, 2018) and to evaluate intervention outcomes.

1.2 Outline of Study

1.2.1 Research Motivation and Hypothesis

Ultrasound imaging has been the primary imaging modality for screening and diagnostic evaluation of carotid arteries, helping the identification and grading of stenosis (Rafailidis, Charitanti, Tegos, Destanis, & Chryssogonidis, 2017). Ultrasound imaging can further contribute to the detection and risk stratification of atherosclerosis (Steinl & Kaufmann, 2015) by quantifying and visualizing vascular biomarkers. As will be discuss in Section 1.4, there are several biomarkers closely related to different stages of atherosclerosis such as disturbed flow, plaque neovascularisation, and volumetric flow rate that may be quantified by ultrasound. However, a frame rate of 1,000 frames per second (fps) or above is often required to quantify and visualize these vascular biomarkers consistently (Hoskins, 2010) because of their complex spatiotemporal dynamics. Current ultrasound scanners can only offer frame rates in the video range (<100 fps) and are thus incapable of quantifying these vascular biomarkers to facilitate timely identification of stroke and dementia risk.

Vascular biomarkers directly related to initiation, progression, and impact of atherosclerosis (e.g., complex flow, presence of unstable flow, plaque neovascularization, and volume flow rate) can potentially be visualized and quantified through the design of new high-frame-rate ultrasound (HiFRUS) functional mapping techniques. In recent years, HiFRUS imaging techniques (Jensen, Nikolov, Gammelmark, & Pedersen, 2006; Tanter & Fink, 2014) have been proposed to tackle the

limitations of existing imaging paradigms in assessing vascular functions. HiFRUS imaging techniques can be used to track the spatiotemporal dynamics of complex flow patterns at sub-millisecond resolution (Bercoff et al., 2011; Ekroll, Avdal, Swillens, Torp, & Lovstakken, 2016; Yiu, Lai, & Yu, 2014; Yiu & Yu, 2013).

1.2.2 Overall Goal and Specific Aims

Motivated by the hypothesis, the overall goal of this thesis is to devise a real-time imaging framework to quantify and visualize vascular biomarkers that can assess atherosclerotic risk and evaluate the impact of atherosclerosis, based on HiFRUS imaging techniques. The advantage of using a HiFRUS imaging approach is that an integrative framework can be developed to assess multiple parameters at the same time, thus allowing synchronous analysis of multiple parameters.

This goal can be achieved by meeting the following specific aims:

- Develop a live imaging platform capable of implementing and executing HiFRUS imaging algorithms in real time;
- Devise a flow phantom fabrication protocol that allows us to construct flow phantoms that facilitate the calibration of HiFRUS imaging algorithms;
- Formulate HiFRUS imaging methods to quantify and visualize vascular biomarkers that are related to carotid atherosclerosis; and
- Design a new HiFRUS-based volume flow measurement algorithm that can quantify blood flow rate.

Figure 1.1 shows a schematic overview of how these specific aims are connected to atherosclerosis and how each component of this dissertation is specifically designed to achieve the goal. The first aim (live imaging platform) plays a pivotal role in this thesis as it should enable the live imaging capacity of the imaging framework presented in this dissertation (see bottom row of Figure 1.1). The second aim provides calibration tools to evaluate the performance of the HiFRUS algorithms developed (green module in Figure 1.1). The third aim is to devise imaging algorithms to quantify disturbed flow related to the initiation and progression of plaque (purple module) and visualize plaque neovascularization that are linked to plaque vulnerability and future stroke risk (red module). The last objective is intended to enable the framework to measure cerebral blood flow that may be used to evaluate the impact of atherosclerosis on cerebral blood flow and monitor treatment outcome (dark gray module).

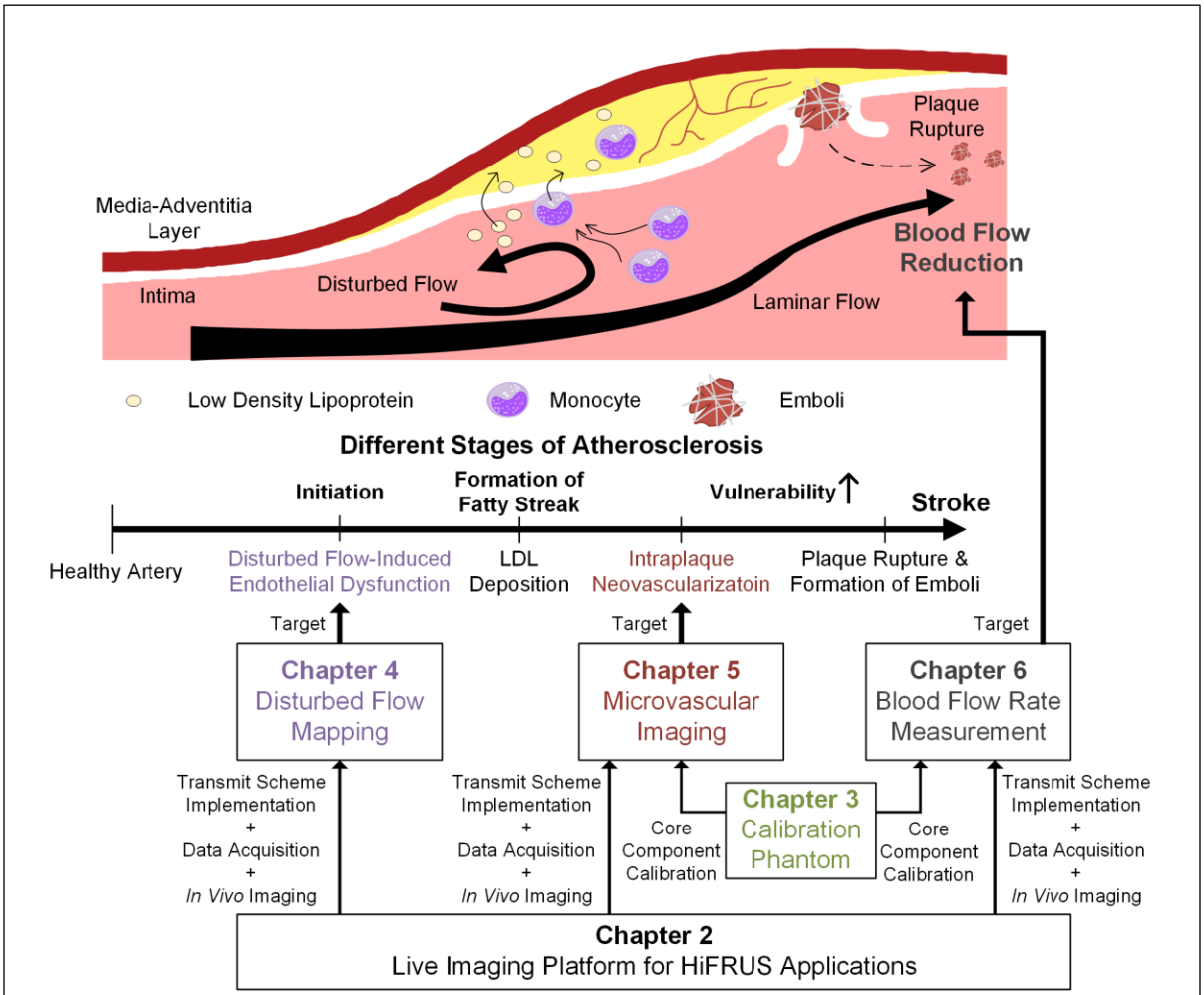

Figure 1.1. The illustration diagram shows the progression of atherosclerosis (top row), atherosclerosis stage timeline (mid-row), and schematic overview of each thesis chapter (bottom row) and to which target stage of atherosclerosis each chapter is connected.

1.2.3 Chapter Overview

The remainder of this introductory chapter is intended to provide an overview of the current strategies of assessing carotid atherosclerosis and its risk as well as to describe how vascular biomarkers play important roles in early atherosclerosis development and its progression and how imaging principles of HiFRUS imaging algorithms may be used to quantify and visualize vascular biomarkers. Thus, the next section provides a general overview on how current imaging modalities are used in assessing carotid atherosclerotic risk and their limitations. Then the chapter provides a summary of the roles of different vascular biomarkers in initiating and promoting atherosclerosis and how to evaluate the implication of atherosclerosis, followed by a description of the background principle of HiFRUS imaging techniques with two examples of how it can be used to facilitate the visualization and quantification of vascular

biomarkers. The sixth and final section summarizes the research problem and outlines the organization of the subsequent chapters in this thesis.

1.3 Current Risk Assessment Strategies of Carotid Atherosclerosis and Their Limitations

1.3.1 Digital Subtraction Angiography

Digital subtraction angiography (DSA) is an established imaging modality in assessing carotid artery disease in which an x-ray is used to investigate the vessel and plaque geometries. DSA is performed by selective catheterization of the carotid arteries via a transfemoral approach (Latchaw & Albers, 2017). During imaging, a plane of x-rays is transmitted through the field of view (FOV) to reach the image intensifier to reveal the internal tissue structures, while the common carotid artery is injected with iodinated contrast which blocks a portion of the x-ray beam to the image intensifier. This allows the moving blood containing contrast to be detected. The stationary soft tissue background around the carotid is then digitally subtracted by the computer program to visualize the vessel geometry. A series of image frames is acquired at 50-100 fps by repeatedly transmitting an x-ray beam through the FOV. Note that the image formed is a projection of the 3-D vessel geometry onto a 2-D plane. The actual 3-D geometry of the carotid can be acquired using 3-D DSA which rotates the x-ray beam and the intensifier to acquire multiple projections from different directions. The 3-D vascular geometry is reconstructed from these projections in a way similar to computed tomography (CT).

DSA provides accurate carotid stenosis anatomy with large FOV that allows the derivation of the *degree of stenosis* which is defined by the North American symptomatic carotid endarterectomy trial (NASCET: 1991) as

$$\%\, ICA\ Stenosis = (1 - {}^{a}/_{c}) \times 100\% \tag{1.1}$$

where a is the residual lumen size at stenosis and c is the distal internal carotid artery (ICA) diameter free of atherosclerosis. The high spatial (50 μm) and temporal (10 ms) resolution (Yuan et al., 2017) offered by DSA also enables the visualization of near-occlusion stenosis with string sign that magnetic resonance angiography cannot pick up (Latchaw & Albers, 2017). Various plaque characteristics such as surface irregularities and ulceration can easily be depicted by DSA as well. Furthermore, the time series acquired with DSA provides the direction of flow inside the vascular anatomy and the perfusion rate qualitatively. The contrast provided by DSA also highlights intraplaque hemorrhage associated with plaque rupture to determine plaque instability (Lovett, Gallagher, Hands, Walton, & Rothwell,

2004). These features collectively enable DSA to characterize plaque composition and morphology to evaluate plaque rupture risk.

However, there are several drawbacks to the extensive use of DSA, especially in carotid territory. First, DSA involves ionizing radiation with known side effects. Second, the invasive nature of this technique prevents the use of DSA as a screening tool. Third, DSA increases the risk of creating emboli and arterial dissections, resulting in subsequent cerebrovascular events (Barnett, Meldrum, & Elisaziw, 2002; Hessel, Adams, & Abrams, 1981). Barnett et al. used NASCET to show a 0.7% risk of persistent neurologic deficits or death associated with DSA. Fourth, the iodinated contrast used is nephrotoxic, which may cause acute kidney injury (Andreucci, Faga, Serra, De Sarro, & Michael, 2017).

1.3.2 Computed Tomographic Angiography

Computed tomographic angiography (CTA) and DSA both use x-rays to visualize the internal structures; the difference is that CTA uses a thin sheet of x-ray beams to generate a line projection of the internal structures, as opposed to a broad plane of x-ray beams in DSA to generate a projection image. This line projection is repeated by rotating the x-ray beam to acquire multiple realizations from different angles. The final CTA image is then reconstructed from these line projections accordingly. During CTA scan, iodinated contrast is injected intravenously to unveil the vascular anatomy at the FOV; this minimizes the adverse effect of catheterization, as mentioned above.

CTA images have a spatial resolution of half of DSA, but it is still sufficient to depict string sign rendered by near-occlusion stenosis (Latchaw & Albers, 2017). CTA can also be used to determine lipid volume (Homburg et al., 2011; Saba et al., 2012), degree of stenosis (Saba, Caddeo, Sanfilippo, Montisci, & Mallarini, 2007a), and plaque ulceration (Saba, Caddeo, Sanfilippo, Montisci, & Mallarini, 2007b), which is rupture prone. CTA can further be used to detect and visualize the plaque calcification (Link et al., 1996) because CTA does not use digital subtraction to suppress tissue background.

Similar to DSA, the drawbacks of CTA include the use of ionizing radiation and nephrotoxic contrast. The radiation dose of CTA is equivalent to or higher than DSA (Klingebiel et al., 2008; Manninen, Isokangas, Karttunen, Siniluoto, & Nieminen, 2012). These limitations prevent CTA from being used as a screening and routine monitoring tool for carotid diseases.

1.3.3 Magnetic Resonance Angiography

Time-of-Flight Magnetic Resonance Angiography

The most common method for magnetic resonance angiography (MRA) is time-of-flight (TOF), which is noncontrast-enhanced. TOF-MRA first repeatedly excites stationary tissues to a saturated state so

that the MR imaging signals from theses saturated stationary tissues are weak. In contrast, the excitation of blood never reaches a saturation state because it is constantly being washed away. This ensures high MR imaging signals coming from a blood flow region, creating strong vascular contrast to highlight the vessel lumen (Laub & Kaiser, 1988), which enables TOF-MRA to perform stenosis measurement.

TOF-MRA faces significant limitations when imaging carotid stenosis. First, MRA is susceptible to tissue motion; patient motion during the relatively long acquisition time could lead to motion artifact that significantly deteriorate image quality (Anderson et al., 1992). Second, MRA is not suitable to investigate arteries that have complex flow patterns such as flow retention and flow stagnation (Yucel et al., 1999). These flow patterns may cause excitation saturation in blood, which leads to a weak MR imaging signal, affecting the accuracy in stenosis measurement and ulceration detection (Etesami et al., 2013). Thus, TOF-MRA estimation performance depends on the wash-in efficiency of blood in the diseased area. Third, ulceration detection is influenced by ulceration orientation, location, shape, and size (Anderson et al., 1992; Etesami et al., 2013).

Contrast-Enhanced Magnetic Resonance Angiography

Similar to CTA, contrast enhanced (CE) MRA uses a contrast agent (paramagnetic substances such as chelate of gadolinium), which shortens the T1 relaxation time of the blood and in turn provides excellent contrast with surrounding tissues (Knopp, von Tengg-Kobligh, Floemer, & Schoenberg, 1999). The advantage is that the images no longer depend on the inflow blood; this significantly improves the accuracy of MRA in stenosis measurement and detection of ulceration (Etesami et al., 2013). As demonstrated by Koktzoglou, Walker, Meyer, Murphy, & Edelman (2016), CE-MRA was able to depict the luminal irregularity (e.g., stenosis) compared to TOF-MRA. The enhanced contrast also enables CE-MRA to detect intraplaque neovascularization and hemorrhages, as reported by Qiao et al. (2011); this is valuable in evaluating plaque rupture risk and associated stroke risk.

However, the use of gadolinium-based contrast poses a threat to patients with renal failure. Marckmann et al. (2006) have shown that gadolinium-based contrast would cause nephrogenic systemic fibrosis which severely disables patients and could be fatal. Therefore, the use of CE-MRA on patients with end-stage renal diseases is restricted. Aside from contrast, the limited availability and long waiting time of MRI scanners (Ariste & Fortin, 2007; Emery et al., 2009) hamper the use of MRA as a tool for routine monitoring of atherosclerosis progression.

1.3.4 Positron Emission Tomography

When assessing carotid atherosclerosis, positron emission tomography (PET) is mainly used to evaluate dynamic intraplaque activity such as inflammation, active plaque calcification, and other biologic

processes (Cocker et al., 2012; Papageorgiou, Briasoulis, Androulakis, & Tousoulis, 2017; Phelps, 2000). PET works by first injecting intravenously a radioactive tracer ^{18}F-flurodeoxyglucose (FDG) which has a short half-life. These FDGs are then taken up by active macrophages inside the plaque as glucose for glycolysis to generate energy. Unlike glucose, FDG cannot be metabolized further once phosphorylated by hexokinase and is effectively trapped within the cells (Joseph & Tawakol, 2016). The higher the rate of macrophage-related glycolysis, the higher the pro-inflammatory activation and FDG uptake (Tawakol et al., 2015). These radiotracers accumulate in the tissue, after which they release positrons that interact with electrons, leading to an annihilation event. Over this process, a pair of annihilation photons are created at a 180° angle, and they are finally detected by the PET scanner, which recognizes two photons that arrive simultaneously at 180° apart as having the same tissue origin, thus allowing localization and quantitation of intraplaque activity (Joseph & Tawakol, 2016; Tarkin, Joshi, & Rudd, 2014).

One limitation of PET is that the resolution is much less than that of CT or magnetic resonance imaging (MRI) because the released position randomly travels a minute distance before it is annihilated with another electron (Gogia, Kaiser, & Tawakol, 2016), resulting in ambiguity of exact origin. The combine use of PET/MRI or PET/CT offers the highest quality of images in terms of sensitivity and resolution.

1.3.5 Ultrasound Imaging

Ultrasound, including color Doppler and pulsed Doppler, is the primary imaging technique used for screening and diagnostic evaluation of carotid atherosclerosis (Rafailidis, Charitanti, et al., 2017). Ultrasound imaging uses noninvasive, cost-effective, safe, and fast-imaging technology with real-time feedback for atherosclerotic risk assessment (Liu, Hua, Feng, & Ovbiagele, 2016; Yuan et al., 2017). It is versatile and provides both anatomical and functional information at the same time for carotid disease diagnosis (von Reutern et al., 2012). In this subsection, various imaging modes are discussed as to how they can be applied to stratify atherosclerotic and stroke risk.

Anatomical B-mode Imaging

Brightness-mode (B-mode) imaging is the fundamental imaging mode of the ultrasound. Section 1.5.1 has a more detailed explanation on how a B-mode image is formed. In brief, a B-mode image is acquired by first transmitting a narrow ultrasound pulse into the FOV. The echoes reflected from tissues are then received, digitized, and dynamically focused to generate one scanline. This pulse-echo sensing procedure is then repeated across the transducer to scan the FOV, generating the B-mode image, which can readily be used to detect the presence of carotid plaque by direct observation of abnormal vessel

lumen narrowing (Latchaw & Albers, 2017). B-mode imaging can also be used to evaluate the carotid intima-media thickness (CIMT) measured as the gap between the double-line pattern identified in the vessel wall of common carotid arteries (CCAs). It is commonly recognized that CIMT thickening is the early sign of atherosclerosis (Ho, 2016; Liu et al., 2016; Nighoghossian et al., 2005).

The presence of carotid plaque and CIMT thickening can enhance the predictive power of traditional risk factors in future cerebrovascular events (Ho, 2016). One drawback of ultrasound imaging is that the image quality is operator dependent. To standardize the CIMT and plaque burden quantification, the American Society of Echocardiography has released a consensus statement which provides a recommended scanning protocol, instrumentation display, and other key requirements for operators (Stein et al., 2008).

Aside from measuring the luminal stenosis, plaque echogenicity from B-mode images provide useful information in characterizing plaque compositions and determining plaque instability. With a computer-assisted system, plaque echogenicity can be objectively measured as gray scale median (GSM) to improve reproducibility (Fosse et al., 2006) and intra-observer reliability (Iwamoto, Shinozaki, Kiuchi, Umahara, & Takasaki, 2003). The lower GSM, the more echolucent and the more vulnerable the plaque is. Patients with high GSM (> 30) have a lower annual rate of stroke (0.6%) than do patients with GSM of 15–30 (1.6%). The stroke rate is further increased to 3.6% for patients with plaque GSM less than 15 (Liu et al., 2016; Nicolaides et al., 2010). Moreover, intraplaque bright spots with shadowing indicate calcification. This could add information for a plaque instability evaluation.

Spectral Doppler Measurement

In cases where B-mode imaging does not give stenosis measurement with sufficient quality, spectral Doppler can be used instead to measure the peak systolic velocity (PSV), which is correlated to the degree of stenosis (Grant et al., 2003). The rationale is that when blood flow is forced to pass through a narrower lumen due to stenosis, the flow velocity increases; the narrower the vessel lumen, the faster the flow speed. Spectral Doppler provides velocity waveform measurement at one spatial location (Jensen, 2007) defined by the operators. To measure PSV using spectral Doppler, a range gate is first placed at the stenotic site and focused ultrasound beams are then transmitted at the range gate at a very high repetition frequency (5 to 20 kHz). The echo signal received from each transmission has a slight phase change because the blood cells within the range gate are moving. This phase shift translates into frequency shift in the derived Doppler spectrum, and can subsequently be determined using spectral analysis. This frequency shift is directly proportional to the velocity of the moving blood cells along the ultrasound beam direction (i.e., blood flow velocity), transmit pulse center frequency, pulse

repetition frequency, and ultrasound beam-flow angle correction. With this information, the PSV can then be calculated using the Doppler equation.

Jahromi, Cina, Liu, & Clase (2005) evaluated the sensitivity and specificity of PSV in determining degree of stenosis. They showed that PSV has a sensitivity of 98% and a specificity of 88% in identifying stenosis greater than 50% (NASCET 1991), and 90% and 94%, respectively, to detect stenosis greater than 70% narrowing. Aside from measuring PSV, spectral Doppler can also be used to detect turbulent flow. Turbulent flow is characterized by the fluctuations of flow velocities in space and time (Kajishioma & Taira, 2017), as compared to uniform flow and direction in the case of laminar flow. This fluctuation of flow velocities translates into wider Doppler spectral bandwidth since each flow velocity has a unique Doppler frequency shift. Thus, by analyzing the Doppler spectrum, one can detect turbulent flow (Garbini, Forster, & Jorgensen, 1982a, 1982b). This approach has demonstrated initial success in assessing plaque risk (Belcaro et al., 2001).

One drawback of spectral Doppler measurement is that the reliability of derived PSV is highly dependent on the beam-flow angle (McDicken & Hoskins, 2014). The spectral Doppler signal is significantly degraded at angles above 60° and are relatively null at an angle of 90° to the direction of blood flow. Another drawback is that spectral Doppler is limited to one spatial location. The placement of a Doppler range gate may also hinder the measured PSV value and hence risk classification. Other physiological factors may also have influences on PSV. For instance, a reduction in cardiac output, heart rate, or blood pressure can result in lower PSV (Latchaw & Albers, 2017). In contrast, contralateral occlusion may increase PSV. These influences may affect the degree of stenosis evaluation and in turn risk stratification.

Color Flow Imaging and Power Doppler Imaging

Color flow imaging (CFI) uses the same principle as spectral Doppler to detect and estimate blood flow velocities except CFI measures the mean Doppler frequency shift and repeats the estimation process over the entire FOV to derive a full flow velocity map, instead of the velocity waveform at a single range gate (Jensen, 2007, Evans, 2010). CFI can achieve roughly 10 – 20 fps in carotid imaging to visualize the blood flow velocity and directionality. The flow velocity map derived by CFI helps to identify ICA origin and course and is especially useful for tortuous arteries, high bifurcations. Areas of stenosis are seen as a reduced lumen with a red to blue shift due to Doppler aliasing.

The poststenotic mosaic color Doppler pattern also gives information on the flow instability at stenosis (Hallam, Reid, & Cooperberg, 1989; Middleton, Foley, & Lawson, 1988; Steinke, Kloetzsch, & Hennerici, 1990). Several techniques have been proposed to use Doppler variance to map flow

instability (Bascom, Cobbold, Routh, & Johnston, 1993; Poepping, Rankin, & Holdsworth, 2010; Thorne, Rankin, Steinman, & Holdsworth, 2010). The principle behind this is the same as that of spectral bandwidth estimation. The wide range of velocities causes an increase in the Doppler estimation variance in time. Thus, by tracking how the Doppler variance evolves over time, flow instability and location can be deduced. The advantage of CFI over spectral analysis is that a full-view mapping of velocity and Doppler variance can be derived at video frame rate. Similar to spectral Doppler, CFI also suffers from angle-dependence issues, including larger estimation variance and weak Doppler signal at a flow close to 90° beam-flow angle (McDicken & Hoskins, 2014). Furthermore, angle correction in spectral analysis cannot be applied in CFI as the vessel curvature (i.e., flow angles) vary spatially.

Power Doppler Imaging (PDI) is a variant of CFI in which the Doppler signal power is measured and rendered instead. PDI is effective in detecting small vessels with slow flow; this is particularly useful in detecting plaque ulceration as flow inside the ulcer is slow (Yuan et al., 2017). PDI is also useful in distinguishing nearly occluded lumen from occluded one. A narrow hairline pattern ("string sign") may be seen using PDI when spectral Doppler and CFI may miss.

Contrast-Enhanced Ultrasound

Like CTA and CE MRA, contrast-enhanced ultrasound imaging (CEUS) also uses contrast to enhance the flow signal quality for stenosis grading (Pianco & Paterni, 2015). Instead of using iodinated or gadolinium based contrast, CEUS uses tiny gas vesicles as contrast; these gas vesicles or microbubbles have an inert gas core that strongly reflect ultrasound pulses, creating high echo amplitude. These microbubbles only stay inside the vasculature due to their size (1–8 μm in diameter); this helps to map the vasculature, including stenosis. Given the high contrast between flow region and surrounding tissues, CEUS can readily delineate the plaque surface, highlighting the plaque surface irregularity (Rafailidis, Chryssogonidis, Tegos, Kouskouras, & Charitanti-Kouridou, 2017). CEUS also offers improved visualization of flow in the pre-, intra- and poststenotic part of the lumen, even in elongated plaques and high-grade stenosis (Clevert, Sommer, Zengel, Helck, & Reiser, 2011; Partovi et al., 2012; Piscaglia et al., 2012; ten Kate et al., 2010). This results in a higher accuracy in grading stenosis (Kono et al., 2004; Sirlin et al., 2001) and detecting plaque ulceration (ten Kate, van Dijk, et al., 2013a). In a comparison study, CEUS detected more ulcerations than CTA, especially small ulcerations (ten Kate, van Dijk, et al., 2013a), attributed to the higher spatial and temporal resolution achieved in CEUS.

Plaque neovascularization is a major feature of vulnerable plaque; plaques with neovascularization are prone to progression and rupture (Langheinrich, Kampschulte, Buch, & Bohle, 2007; Moreno,

Purushothaman, Sirol, Levy, & Fuster, 2006). These newly formed microvessels are small and cannot be imaged with CTA, MRA, or B-mode ultrasound because of the limited spatial resolution. In contrast, microbubbles inside these microvessels can easily be picked up by CEUS, making CEUS ideal to examine intraplaque neovascularization (Huang et al., 2016). Varetto et al. (2015) have compared the results obtained with CEUS and histopathology and concluded that there is a statistically significant correlation between plaque contrast enhancement and the extent of intraplaque vascularization. This demonstrates the potential of CEUS in assessing plaque vulnerability.

CEUS can also be used to perform molecular imaging like PET. The ultrasound contrast can be functionalized by incorporating ligands and antibodies to target specific cell surface proteins. For example, intercellular adhesion molecule 1 (ICAM-1), vascular cell adhesion molecule 1 (VCAM-1) and P-selectin have all been imaged with targeted ultrasound contrast (Alonso, Artemis, & Hennerici, 2014; Chen et al., 2002). In one study, VCAM-1 targeted microbubbles were used to monitor the therapeutic effects of statins on the ground that the use of statin was associated with a less endothelial expression of VCAM-1 (Khanicheh et al., 2013).

Although CEUS has the potential to improve the identification of stenosis, plaque ulceration, and neovascularization, there are still limitations including operator dependency, variability, and lack of standardized procedures (Johri, Herr, Li, & Nambi, 2017; Varetto et al., 2015). Semiautomated software for image analysis is required to increase reproducibility and homogeneity among operators. Furthermore, CEUS is relatively new and lacks the long-term epidemiologic data that would inform our understanding of how well the features associated with vulnerable plaque predict cerebrovascular events in the long-term.

1.4 Role of Different Vascular Biomarkers in Carotid Atherosclerosis

As discussed above, current ultrasound imaging strategies focus on plaque morphologies and degree of stenosis. However, these markers are surrogates (Ho, 2016), and they do not provide sufficient information for individual risk assessment. In contrast, there are several vascular biomarkers closely related to different stages of carotid atherosclerosis; these markers include oscillatory flow pattern, disturbed flow, plaque neovascularization, and cerebral blood flow rate. In this section, the relationship between atherosclerosis and these markers will be discussed one by one.

1.4.1 Endothelium, Oscillatory Flow Pattern and Disturbed Flow in Early Atherosclerosis

Normal Endothelial Function

The main function of endothelium is to regulate the vascular homeostasis. The endothelium (i.e., intima) together with the media and adventitia form the three-ply vessel. The endothelium is the innermost layer that is a single cell thick and is in direct contact with the flowing blood. It is constantly under wall shear stress, which is the component of frictional forces arising from blood flow and acting parallel to the vessel luminal surface (Davies, 1995; Fung, 1997; Li, Haga, & Chien, 2005). Under normal vascular tone, the magnitude of this shear stress ranges from 10–70 dyn/cm^2 in arteries (Chien, 1972; Malek, Alper, & Izumo, 1999; Nerem et al., 1998) and the endothelium is actively remodeling the vasculature in response to shear stress alternations to maintain the mean wall shear rate at 15-20 dyn/cm^2 (Giddens, Zarins, & Glagov, 1993; Girerd et al., 1996; Malek et al., 1999) and thus the vascular homeostasis (Cheng et al., 2006; Langille & O'Donnell, 1986; Pohl, de Wit, & Gloe, 2000). For example, in response to a chronic decrease in shear stress because of lowering of blood flow, an endothelium dependent intima-media hyperplasia or wall hypertrophy (Korshunov & Berk, 2003; Korshunov, Mohan, Georger, & Berk, 2006; Langille & O'Donnell, 1986; Melkumyants, Balashov, & Khayutin, 1989; Sullivan & Hoying, 2002;) takes place to reduces the lumen radius which increases the blood flow velocity and in turn the wall shear stress to restore it back to normal. This compensatory arterial response to changes in shear stress requires an intact, functional endothelium in response to shear stress alterations (Gibbons & Dzau, 1994; Langille & O'Donnell, 1986; Pohl et al., 2000).

Endothelial Dysfunction and Its Consequences

At lesion-prone sites, atherosclerosis begins with an impaired endothelium possibly caused by slow oscillatory flow or turbulent flow (Gambillara et al., 2006; Wang et al., 2016). These complex flow patterns coupled with chronic exposure of hypertension and hypercholesterolemia lead to endothelial dysfunction (Aboyans et al., 2006; Bonetti et al., 2003; Gimbrone, Topper, Nagel, Anderson, & Garcia-Cardena, 2000; Kohler & Jawien, 1992). Endothelial dysfunction is a critical pathophysiological factor in atherosclerosis, in that it leads to many pathophysiological consequences related to atherosclerosis (Bonetti et al., 2003; Gimbrone et al., 2000; Kohler & Jawien, 1992). In particular, it would

1) increase the permeability of endothelium to macromolecules such as lipoproteins;
2) reduce nitric oxide (NO) production by impairing endothelial NO synthase, increasing the oxidative stress in endothelium;
3) enhance the recruitment and accumulation of monocytes in the intima as foam cells, decrease endothelial cell (EC) regeneration and increase smooth muscle cell (SMC) proliferation and migration; and

4) disturb hemostatic balance of thrombotic and fibrinolytic states, enhance thrombin generation, platelet aggregation and adhesion, and fibrin deposition.

These consequences all play critical roles in promoting the formation of fatty streaks and atherosclerotic lesions (1 & 2) at the early stage of atherosclerosis, and sustaining plaque growth (3 & 4) in later stages (Steinberg, 2002).

Carotid as an Atherosclerotic Lesion-Prone Site

Disturbed flow naturally occurs in certain regions such as branching points and curvatures of conduit arteries, such as aorta and carotid. The vascular geometries at carotid bifurcations lead to slow oscillatory flow and a disturbed flow pattern (flow separation, recirculation, and reattachment; Lee, Antiga, Spence, & Steinman, 2008). These flow patterns subsequently lead to low and reciprocating shear stress and high spatial and temporal gradients of shear stress, resulting in modified local phenotype and function of vascular ECs (Huo, Wischgoll, & Kassab, 2007), making the carotid susceptible to atherosclerosis. The local differences in flow pattern and shear stress magnitude and gradient may explain the different rates of atherosclerosis progression among different vessels within the same individual, despite their exposure to the same systemic risk factors such as blood pressure and lipoprotein concentrations (Huo et al., 2007; Wissler, 1995).

Effects of Disturbed Flow on Endothelium – In Vitro Evidence

To study the effects of disturbed flow on endothelium, dozens of *in vitro* studies have been conducted (Chiu & Chien, 2011). *In vitro* models offer a well-controlled scenario that enables the investigation of the effects of disturbed flow on endothelial function one parameter at a time, providing valuable information on the mechanism that drives specific regions to atherosclerosis. Many studies have shown that there are significant differences in endothelial response between laminar flow and disturbed flow; these differences include morphology, proliferation, permeability, gene expression, and white blood cell responses. For example, Chiu, Wang, Chien, Skalak, & Usami (1998) showed that ECs exposed to a disturbed flow pattern have a rounded shape and a higher turnover rate as compared to those exposed to a laminar flow pattern. To be specific, the disturbed flow impaired the gap junction and intercellcular communication (DePaola et al., 1999), causing changes in morphology and consequently leading to a leaky intercellular junction. This leaky junction increased the permeability of macromolecules such as LDL (Phelps & DePaola, 2000). The endothelium exposed to disturbed flow also upregulated gene expressions that facilitate lipid accumulation (Chien et al., 2003), as well as gene expressions that recruit white blood cells such as monocytes (Barber, Pinero, & Truskey, 1999; Chien, 2003).

Furthermore, the local low shear rate facilitates the binding of white blood cells onto the endothelium (Skilbeck, Westwood, Walker, David, & Nash, 2001). These consequences collectively promote the formation of fatty streaks in the sub-endothelial space. These findings underscore the critical role of disturbed flow in an early stage and the progression of atherosclerosis.

Effects of Disturbed Flow on Endothelium – In Vivo Evidence

The pathophysiological insights gained *in vitro* need to be verified on *in vivo* models before translated to clinical practice. This verification is a daunting task due to the lack of appropriate *in vivo* models that can generate well-controlled flow patterns and the difficulty in determining the molecular and cellular responses *in vivo*. Despite of this, there are still several *in vivo* small animal models (rabbits and mice; Bassiouny et al., 1998; Godin, Ivan, Johnson, Magid, & Galias, 2000; Khatri et al., 2004; Korshunov & Berk, 2003; Meyerson et al., 2001; Sho, Singh, Xu, Zarins, & Masuda, 2001) and larger animal models (baboons, sheep and dogs; Clowes, Kirkman, & Clowes, 1986; Kohler & Kirkman, 1999; Kohler, Toleikis, Gravett, & Avelar, 2007; Kraiss et al., 1996). These models have demonstrated that the reduction in blood flow and shear rate and in turn shear stress would induce EC apoptosis and death and affecting the arterial remodeling (Cho et al., 1997; Sho et al., 2001). This reduction also leads to early neointimal hyperplasia (Clowes et al., 1986; Kohler & Kirkman, 1999; Korshunov & Berk, 2003; Kraiss et al., 1996), potentially due to increase in SMC migration and proliferation (Bassiouny et al., 1998; Godin et al., 2000; Kumar & Lindner, 1997; Meyerson et al., 2001), monocyte adhesion (Walpola, Gotlieb, Cybulsky, & Langille, 1995) and upregulation of genes (Godin et al., 2000), as well as an increase in oxidative stress (Khatri et al., 2004). Note that neointimal hyperplasia is a critical process leading to atherosclerosis and restenosis (Kohler & Kirkman, 1999).

In short, slow oscillatory flow and disturbed flow play critical roles in initiating and promoting atherosclerosis. These complex flow patterns are typically found at artery branches and curvatures; they induce low wall shear stress on the local endothelium, which increases permeability of LDL, enhances recruitment of monocytes, increases oxidative stress, increases apoptosis, and proliferation of ECs and SMCs. These consequences lead to formation of fatty streaks on the vessel, facilitate the progression of fatty streaks to plaque, and promote plaque growth. Therefore, routine monitoring of disturbed flow at lesion-prone sites such as carotid bifurcation should be incorporated into atherosclerosis screening procedures.

1.4.2 Plaque Neovascularization and Plaque Vulnerability in Mid-Late Stage of Atherosclerosis

Formation of Intraplaque Microvessels

Plaque neovascularization plays a major role in the transition of stable plaque to unstable and future lesion rupture (Michel, Virmani, Arbustini, & Pasterkamp, 2011). This neovascularization denotes the growth of new blood vessels into the atherosclerotic plaque; such growth can be induced by disturbed flow. As mentioned in previous subsection, disturbed flow exerts low shear stress on local endothelium which induces the protein expressions of vascular endothelial growth factor (VEGF) and hypoxia-inductible factor-1α (HIF-1 α: Cohklin, Zhong, Zhao, Lin, & Chen, 2002), critical factors in initiating and facilitating the angiogenesis. Aside from disturbed flow, oxidized LDL could induce expression of VEGF and HIF-1 α and promote angiogenesis as demonstrated in an *in vitro* monocyte-macrophage/endothelial cell co-culture model and a rabbit atherosclerosis model (Hutter et al., 2013). These findings suggest that disturbed flow and oxidized LDL have strong proangiogenic roles in inducing and supporting plaque neovascularization.

Intraplaque Vascularization, Intraplaque Haemorrphage and Plaque Vulnerability

These newly formed vessels are thin and have poor structural integrity because of the weak and incomplete gap junctions between ECs (Bobryshev, Cherian, Inder, & Lord, 1999; Sluimer et al., 2009). Sluimer et al. showed that more than 80% of this intraplaque microvessel network has a fragile structural integrity and is therefore susceptible to leakage of blood contents, including red blood cells, white blood cells, and plasma lipid into the intraplaque space (O'Brien, McDonald, Chait, Allen, & Alpers, 1996; van Lammeren et al., 2012; Virmani et al., 2005). This leaky microvessel network serves as an essential source of intraplaque hemorrhages (Di Stefano et al., 2009; Virmani et al., 2005) because platelets were found to enter the atherosclerotic lesion through this network (van Lammeren et al., 2012). These platelets further contribute to local inflammation, plaque instability and rupture, increasing lesion vulnerability (Moreno et al., 2004). These observations suggest that plaque neovascularization precedes intraplaque hemorrhages in atherosclerosis progression and potentially increases plaque vulnerability.

Plaque Neovascularization Provides Prognostic Information on Atherosclerosis

Because of their weak integrity, these immature microvessels are prone to bleed and rupture and consequently cause intraplaque hemorrhages. McCarthy et al. (1999) observed a significant correlation between the intensity of intraplaque hemorrhages and density of plaque microvessels in humans. This

is vital as it suggests that vascular density inside the plaque can be used to measure intraplaque hemorrhages and plaque rupture risk. Carotid intraplaque hemorrhage has been shown to carry prognostic value as a predictive marker of mortality in patients after carotid artery surgery (Falke et al., 1995). The value of using plaque vascular density to predict future cerebrovascular event was further demonstrated by Hellings et al. (2010) in a follow-up study of patients who underwent carotid endarterectomy. It was found that local plaque hemorrhage and increased intraplaque vascular density are independently correlated with future cardiovascular outcomes, and this relationship is independent from other clinical risk factors and medical drug usage (Hellings et al., 2010). Similar observation was made in an observational study where intraplaque hemorrhage is associated with previous cerebrovascular events (Qiao et al., 2012). This suggests plaque neovascularization and its density can provide prognostic information to evaluate atherosclerosis progression and vulnerability (Di Stefano et al., 2009; Sluimer et al., 2009). This is particularly important in the case of carotid atherosclerosis as carotid plaque rupture may lead to stroke (Qiao et al., 2012).

1.4.3 Impact of Carotid Atherosclerosis in Cerebral Blood Flow

Function of Normal Cerebral Blood Flow

Maintaining proper cerebral blood flow (CBF) is crucial in sustaining brain functions and viability by providing necessary nutrients such as oxygen and glucose to the brain, at the same time washing away metabolic wastes such as carbon dioxide and other harmful substances. The CBF is supplied by the internal carotid (ICA) and the vertebral arteries (VA), with carotid covering more than 80% of total CBF (Oktar et al., 2006). Typical global CBF for a healthy adult is roughly 50 ml/min per 100 g of brain tissue (Lassen, 1985) and is closely regulated by cerebral autoregulation (Panerai, 2008) within a narrow range. Cerebral autoregulation actively adjusts the cerebrovascular resistances (Panerai, 2008) to maintain cerebral perfusion pressure and flow rate. This flow rate, however, gradually decreases at a rate of 0.5% per year from age of 20 onwards (Leenders, 1990).

Atherosclerotic Burden on Cerebral Blood Flow

As carotid atherosclerotic plaque progresses, it starts to take up the vessel lumen, restricting blood supply to the brain. This flow reduction imposes an extra burden onto the already deteriorating CBF due to aging in the elderly (Chen et al., 2011; Leenders, 1990). As suggested by the vascular hypothesis of Alzheimer's disease (de la Torre, 2018), the CBF supply may no longer be able to meet the neurometabolic demands of the brain because of the imposed burden by atherosclerosis. This leads to hypoxia/ischemia to brain cells and later on brain atrophy with chronic exposure (de la Torre, 2000,

2016). This irreversible brain damage is eventually manifested as cognitive impairment and dementia (Liu & Zhang, 2012; Ruitenberg et al., 2005).

Evaluating Impact of Atherosclerosis Using Cerebral Blood Flow

Carotid atherosclerosis is a predictive factor in cognitive decline (Chao et al., 2010; Kitagawa et al., 2010; Xekardaki et al., 2014) and dementia (Encinas et al., 2003; Hirao et al., 2005; Schuff et al., 2009; Snyder et al., 2015). Many studies have shown that global CBF was lower in patients with cognitive impairment and dementia than in cognitive healthy individuals (Chao et al., 2010; Xedardaki et al., 2014). Using advanced neuroimaging techniques (Inui et al., 2017; Niwa et al., 2016; Xekardaki et al., 2014), regional CBFs of different parts of the brain have been quantified, and the CBF in patients with mild cognitive impairment (MCI) or dementia is 20% lower than those cognitive healthy individuals (Johnson et al., 2005). This CBF reduction was shown to precede cognitive deterioration in a 6.5 years follow-up study (Ruitenberg et al., 2005; Wolters et al., 2017). Thus, it is sensible to evaluate global CBF to assess the impact of atherosclerosis on cognitive function.

1.4.4 Summary

In this section, we have reviewed three vascular biomarkers closely related to different stages of atherosclerosis. First, low oscillatory flow and disturbed flow is shown to be atherogenic; they play significant roles in initiating fatty streak formation at the early stage of atherosclerosis through multiple pathways, as well as promoting plaque growth at the mid-late stage of atherosclerosis. Second, at the mid-stage of atherosclerosis, plaque neovascularization becomes an important indicator of plaque vulnerability; plaque with intraplaque microvessels is rupture-prone and has a higher chance of causing stroke and dementia. Lastly, carotid atherosclerosis is linked to CBF reduction, which harms cognitive function. Blood flow rate at carotid can therefore be used to evaluate the impact of atherosclerosis, providing prognostic information at different stages of atherosclerosis. Monitoring of these vascular biomarkers would provide prognostic information on atherosclerosis, facilitating treatment evaluation to avoid the progression of atherosclerosis which may lead to stroke and dementia.

1.5 High-Frame-Rate Ultrasound Imaging: A New Imaging Paradigm for Carotid Atherosclerosis Assessment

The vascular biomarkers discussed in the previous section are shown to carry valuable information in assessing atherosclerotic risk. However, the current scanline-based ultrasound imaging paradigm does not have sufficient spatial and temporal resolution to visualize and quantify these biomarkers. In this section, we present the general principle of a new imaging paradigm called high-frame-rate ultrasound

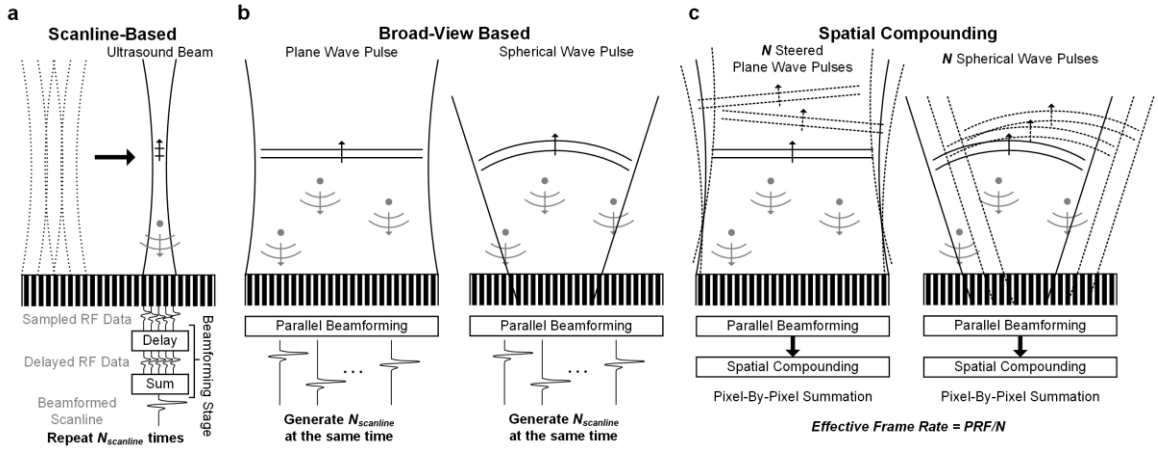

Figure 1.2. The image illustrates (a) scanline-based imaging, (b) broad-view imaging with single plane wave transmission and spherical wave transmission, and (c) broad-view imaging with multiple steered plane wave transmissions and spherical wave transmissions at shifted positions for spatial compounding.

imaging (HiFRUS). The feasibility of using HiFRUS to quantify these biomarkers will be demonstrated with two HiFRUS examples.

1.5.1 General Principle of High-Frame-Rate Ultrasound Imaging

In recent years, a new imaging paradigm, high-frame-rate ultrasound imaging (HiFRUS: Jensen et al., 2006; Tanter & Fink, 2014), has revolutionized how ultrasound image is acquired and formed. It offers a much higher frame rate (> 1000 fps) than the video frame rate (~24 fps) in a conventional ultrasound. Such a high-frame-rate enables us to capture fast-changing blood flow dynamics (Bercoff et al., 2011; Posada et al., 2016; Yiu et al., 2014; Yiu & Yu, 2013), arterial pulse wave propagation (Apostolakis, Nandlall, & Konofagou, 2016), and heart contraction dynamics (Cikes, Tong, Sutherland, & D'hooge, 2014; Poree et al., 2016). HiFRUS imaging also enables advanced imaging techniques such as the super resolution technique (Couture, Hingot, Heiles, Muleki-Seya, & Tanter, 2018) for microvascular imaging, ultrasound functional imaging (Errico et al., 2015), and slow-flow detection (Song, Manduca, Trzasko, & Chen, 2017; Tremblay-Darveau et al., 2018).

Figure 1.2(a) illustrates how an ultrasound image is formed in a conventional scanline-based paradigm. First, a focused ultrasound pulse (dark parallel lines) is transmitted into the region of interest (ROI). Reflected echoes (gray circular lines) from the scatterers (gray dot) on the ultrasound beam path (dark curvy lines) are then sampled and dynamically focused (also known as delay-and-sum; Jensen, 2007; see bottom part of Figure 1.2(a) to generate a scanline). This pulse-echo sensing process is repeated at different scanline positions (gray dotted lines) until the entire imaging region is scanned to form an image. The time needed to form one scanline is determined by time required for the echo from the desired imaging depth (z) to return and is equal to $2z/c_0$ where c_0 is the speed of sound of the medium

(typically 1540 cm/s for human tissue). This limits how fast one can repeat the pulse-echo sensing operation, and thus the frame rate $f_{scanline}$, which is defined as

$$f_{scanline} = \frac{c_0}{2zN_{scanline}} \tag{1.2}$$

where $N_{scanline}$ is the number of scanlines per image. From this equation, we can see that the spatial sampling ($N_{scanline}$) and time resolution (frame rate) are interdependent. To capture fast changing dynamics, we would have to sacrifice the spatial resolution or field-of-view (i.e., reducing $N_{scanline}$) to gain temporal resolution.

In the case of HiFRUS, the same pulse-echo sensing operation is conducted by transmitting a broad-view pulse, either plane wave (Tanter & Fink, 2014) or spherical wave (Jensen et al., 2006), to insonate the entire imaging view instead of a focused pulse, as illustrated in Figure 1.2(b). Echoes from the entire imaging view are sampled, and parallel beamforming (Yiu, Tsang, & Yu, 2011) is employed to generate an image frame for each pulse-echo sensing event. This significantly increases the frame rate by eliminating the $N_{scanline}$ term in (1.1) and now the frame rate $f_{broad\text{-}view}$ is expressed as

$$f_{broad-view} = \frac{c_0}{2z} \, . \tag{1.3}$$

One drawback of such framework is that the spatial resolution of the image formed is suboptimal because there is no transmit focusing. To overcome this issue, coherent compounding has been proposed by Jensen et al. (2006) and Tanter & Fink where multiple image frames acquired from different steering angles (for plane wave) or positions (for spherical wave) are coherently compounded pixel-by-pixel (see Figure 1.2(c)) to generate a high-resolution image. The overall image quality of coherent compounded image is better than those obtained using scanline-based method (Tiran et al., 2015). Even though additional transmissions are used for compounding which would lower the effective frame rate, a 1,000+ fps is still achievable, far beyond that of conventional methods.

1.5.2 Using HiFRUS to Resolve Complex Flow Dynamics

1.5.2.1 Color Encoded Speckle Imaging

The high-frame-rate achieved with HiFRUS has also alleviated the frame rate issue of color flow imaging. In color flow imaging, repeated transmissions (8-16 repetitions) at the same lateral position are typically needed to acquire the flow information (Evans, 2010; Jensen, 2007), further lowering the frame rate. In contrast, HiFRUS can capture flow information for the entire imaging view for each transmission (Bercoff et al., 2011; Yiu & Yu, 2013). This significantly improves the frame rate of color flow imaging, allowing one to capture the blood flow dynamics inside imaging view at a frame rate of

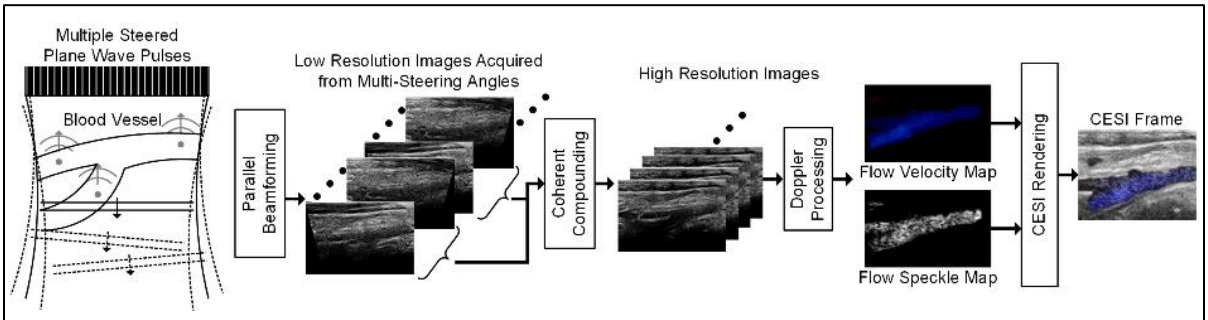

Figure 1.3. Illustration of CESI framework, from data acquisition to B-mode image formation, to full-view image formation to Doppler signal processing to extract flow velocity maps and flow speckle maps, and finally to CESI frame formation by overlaying the velocity map and speckle map on top of the high resolution image. Adopted from Yiu, Walczak, et al., 2019, with permission © IEEE 2019.

1,000+ fps, far beyond video display range. Such acquisition also retains the spatial coherency of flow pattern, which cannot be achieved with scanline-based imaging.

One particular example of such imaging technique is color-encoded speckle imaging (CESI: Yiu & Yu, 2013), where the moving blood speckles are extracted, color-coded, and rendered to show the blood flow directions and velocities inside blood vessels. Figure 1.3 illustrates the overall processing on how a color-encoded speckle image can be obtained from HiFRUS imaging. In brief, a broad-view ultrasound pulse, in this case a plane wave, is transmitted through the array transducer to insonate the imaging region. The received echoes from each transducer element are sampled, and parallel beamforming is then carried out to generate a full-view image as illustrated in the leftmost column of Figure 1.3. The low-resolution images generated from a group of transmit steering angles (usually 1−5) are then coherently compounded to generate high resolution images (HRIs). These HRIs are stacked together to form a 3-D data matrix, and pixel-based slow-time Doppler processing is subsequently executed. First, a finite impulse response (FIR) high-pass filter is applied along the slow-time direction to extract the fast-moving blood speckles (see second rightmost column in Figure 1.3). Next, from the extracted speckles, flow velocities are estimated using lag-one auto correlation (Kasai, Namekawa, Koyano, & Omoto, 1985) and flow detection is performed based on the post filtered Doppler power. At last, the color-coded flow velocity and flow speckles are overlaid on top of the B-mode images within the flow detected region to visualize the flow within the blood vessel (see rightmost column in Figure 1.3).

Movie 1.1 shows a CESI cineloop captured from a carotid bifurcation of a 28-year-old healthy volunteer, acquired at 1,500 fps and replayed at 50 fps, with a Doppler spectrogram acquired from CCA placed at the bottom. The moving speckles highlight the blood flow directions, and the color represents the axial flow velocities (moving toward or away from the transducer). As can be seen, blood from the common carotid artery (CCA) entered the internal carotid artery (ICA), and the blood speckle clearly

depicts the flow direction (left to right). During the peak systole, a circulatory flow pattern can be observed at the CCA/ICA branching point. This pattern was depicted by the change in color, as well as the change in flow speckle movement direction. From this, it can be appreciated that the HiFRUS imaging technique can be used to capture and visualize fast-changing blood flow dynamics inside the blood vessel in a coherent manner.

1.5.2.2 Multi-Angle Vector Doppler Imaging

As previously discussed, color flow imaging only estimates the blood flow velocity component along the transmit beam direction, and the resultant flow velocity estimate is thus angle dependent (McDicken & Hoskins, 2014). To address this issue, various cross-beam vector Doppler techniques are proposed (Capineri, Scabia, & Masotti, 2002; Kripfgans, Rubin, Hall, & Fowlkes, 2006; Pastorelli, Torricelli, Scabia, Biagi, & Masotti, 2008), where mean slow-time frequencies (i.e., flow velocities) are acquired from two different steering angles. The acquired mean frequencies are related to the axial (v_z) and lateral velocities (v_x) as follow:

$$v_z(cos\ \theta_1 + cos\ \varphi_1) + v_x(\sin\theta_1 + sin\ \varphi_1) = \frac{c_0}{f_0} f_1 \tag{1.4}$$

$$v_z(cos\ \theta_2 + cos\ \varphi_2) + v_x(\sin\theta_2 + sin\ \varphi_2) = \frac{c_0}{f_0} f_2 \tag{1.5}$$

where θ_1 and θ_2 are the transmit steering angles, and φ_1 and φ_2 are the corresponding receive steering angles, c_0 is the speed of sound, f_0 is the transmit pulse center frequency, and f_1 and f_2 are the corresponding mean slow-time frequencies from each steering angle, derived using lag-one auto correlation from the Doppler signals. The angle-independent flow velocity can then be solved as a two-equation, two-unknown problem. The limitation of this strategy is that additional transmissions are required to obtain the second mean frequency estimates; this further reduces the frame rate.

HiFRUS imaging offers the opportunity to derive flow vector maps at a very high-frame-rate. Yiu et al. (2014) and Ekroll et al. (2016) have demonstrated using HiFRUS to capture time-resolved complex flow patterns inside arteries. Figure 1.4 illustrates the overall process in deriving flow vectors using the HiFRUS technique. The principle behind this is similar to the cross-beam vector Doppler. Instead of

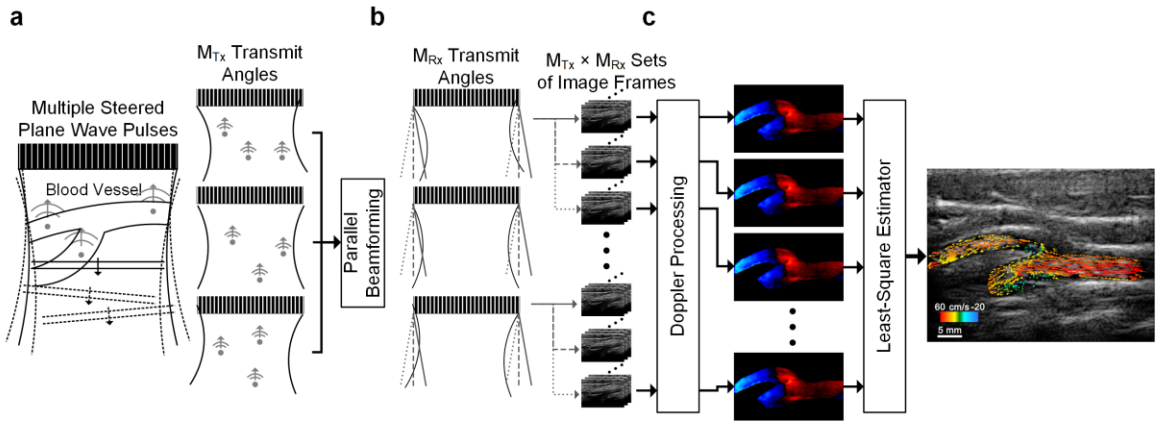

Figure 1.4. Illustration shows a diagram of a multi-angle vector Doppler imaging framework. (a) Multiple steered plane wave acquisition; (b) parallel beamforming with different receive steering angles; (c) pixel-based Doppler processing on each transmit-receive angle pairs to generate Doppler flow maps, followed by least-square estimator to derive the flow vector map.

transmitting two broad-view pulses just from two steering angles, multiple transmitting (Tx) steering angles ($M_{Tx} \geq 2$) are employed (see Figure 1.4(a)). A group of receive (Rx) steering angle ($M_{Rx} \geq 2$) is then used to beamform a set of image frames for each transmission, as shown in Figure 1.4(b: gray lines). This results in $M_{Tx} \times M_{Rx}$ sets of image frames, each of which has a unique Tx-Rx steering angle pair. As illustrated in Figure 1.4(c), for each of these image sets, pixel-based, slow-time processing is subsequently performed to derive the mean slow-time frequency, similar to CESI processing. These slow-time processing procedures include a FIR high-pass filter to suppress unwanted tissue clutter and lag-one auto-correlation to derive the mean slow-time frequencies. Each Tx-Rx angle pair generates a Doppler equation similar to (1.4) with corresponding θ and φ. These equations collectively form a system of equations with $M_{Tx} \times M_{Rx}$ equations and two unknowns (v_x and v_z) as described by Yiu and Yu (2016), which can be rewritten as:

$$\mathbf{Av} = \mathbf{u} \Rightarrow \begin{bmatrix} cos\ \theta_1 + cos\ \varphi_1 & \sin\theta_1 + sin\ \varphi_1 \\ \vdots & \vdots \\ cos\ \theta_{M_{Tx}} + cos\ \varphi_{M_{Rx}} & \sin\theta_{M_{Tx}} + sin\ \varphi_{M_{Rx}} \end{bmatrix} \begin{bmatrix} v_z \\ v_x \end{bmatrix} = \begin{bmatrix} u_1 \\ \vdots \\ u_{M_{Tx} \times M_{Rx}} \end{bmatrix} \quad (1.6)$$

where **A** is the angle matrix formed from the Tx-Rx angle pairs, **v** is the flow velocity vector, and **u** is the Doppler measurand vector formed from the right hand-side of (1.4). The flow velocity vector can finally be estimated by multiplying $A^{\dagger}$ (i.e., the pseudoinverse of A on both sides)

$$\mathbf{v} = \mathbf{A}^{\dagger}\mathbf{u} = (\mathbf{A}^{\mathrm{T}}\mathbf{A})^{-1}\mathbf{A}^{\mathrm{T}}\mathbf{u} \quad (1.7)$$

The derived flow vector **v** would have minimum mean-square error (Flynn, Daigle, Pflugrath, Linkhart, & Kaczkowski, 2011; Yiu et al., 2014), effectively reducing the effects of noise fluctuations in the estimates of mean slow-time frequency from different Tx-Rx angle pairs.

Movie 1.2 shows an *in vivo* example of vector flow imaging acquired from the carotid bifurcation of a healthy volunteer. The flow vectors are rendered as projectiles using the previously described technique called vector projectile imaging (VPI: Yiu et al., 2014) to dynamically visualize the complex flow patterns. Blood flow entering from CCA splits into internal and external carotid arteries (ICA and ECA) as it reached the bifurcation point. The flow acceleration during systole was depicted by the change in speed of the vector projectiles. Furthermore, flow recirculation was observed at the ICA entrance as highlighted by the circulatory motion of projectiles at the end of systole. This demonstrates that the HiFRUS imaging technique can be used to resolve complex flow dynamics and quantify and visualize vascular biomarkers such as disturbed flow, as shown in Movie 1.2.

1.6 Concluding Remarks

Ultrasound imaging is the primary imaging modality in carotid disease assessment; it is safe, fast, and cost-effective and can thus be used in routine monitoring. As discussed in Section 1.3, current imaging strategies in risk stratification focus on atherosclerotic-related geometrical changes such as CIMT thickening, presence of plaque, and degree of stenosis, which are surrogate markers only. However, ultrasound imaging may be used to visualize and quantify vascular biomarkers such as disturbed flow and plaque neovascularization to assess atherosclerotic risk at different stages with the HiFRUS imaging paradigm. Yet current ultrasound scanners are neither capable of resolving these vascular biomarkers because of limited spatial and temporal resolution nor supporting the development of relevant HiFRUS algorithms. The goal of this thesis is therefore to devise a new imaging framework to address these challenges, and the remaining chapters have been organized as follows:

- **Chapter 2** presents the framework and implementation details of a live CESI imaging platform, and two *in vivo* case examples are shown to demonstrate the platform's effectiveness in executing HiFRUS imaging algorithms and visualizing complex flow patterns;
- **Chapter 3** describes the design protocol of a spiral flow phantom that can be used to calibrate novel flow imaging algorithms and discuss how it is used to evaluate the performance of the HiFRUS multi-angle vector Doppler imaging method, a core component of HiFRUS imaging algorithms presented in later chapters;

- **Chapter 4** provides a theoretical framework of HiFRUS-based Doppler bandwidth imaging, specifically designed to map unstable flow that has been shown to initiate atherosclerosis, and compares the framework's performance with Doppler variance imaging (scanline based paradigm) in identifying unstable flow;
- **Chapter 5** describes a motion-resistant super resolution imaging framework targeted for visualizing intraplaque microvasculature (a biomarker of vulnerable plaque) and summarizes the *in vitro* and *in vivo* performances of the framework;
- **Chapter 6** presents a volumetric flow rate measurement algorithm that aims to quantify global cerebral blood flow, which can be used to evaluate the impact of atherosclerosis, and compares the performance of new estimator with existing tools under *in vivo* scenarios; and
- **Chapter 7** summarizes the contributions of this thesis and discusses the possible future directions in this research area.

Chapter 2
A Live Imaging Platform for High-Frame-Rate Ultrasound Imaging Algorithms

2.1 Introduction

Ultrasound imaging is in the midst of an innovation drive to extend its clinical functionality beyond what is available on current ultrasound scanners (Klibanov & Hossack, 2015). One noticeable trend is the development of high-frame-rate ultrasound (HiFRUS) imaging paradigms that make use of unfocused, broad-view insonation strategies like synthetic transmit aperture (Jensen et al., 2006; Poree et al., 2016) and plane wave excitation (Jensen, Stuart, & Jensen, 2016; Tanter & Fink, 2014). These newer imaging paradigms can readily obtain images at a much higher frame rate (>1000 frames per second (fps)) than conventional scanline-based imaging while maintaining comparable (or even better image quality (Jensen et al., 2006; Montaldo, Tanter, Bercoff, Benech, & Fink, 2009; Nikolov, Gammelmark, & Jensen, 1999). With a corresponding time resolution in the submillisecond range, HiFRUS has enabled the development of new flow imaging techniques to more coherently visualized flow patterns inside the cardiovasculature (Bercoeff et al., 2011; Posada et al., 2016). One example of HiFRUS-based flow imaging innovations is color-encoded speckle imaging (CESI) that can provide time-resolved visualization of complex flow dynamics via duplex rendering of blood speckles and axial velocity estimates (Yiu & Yu, 2013). We have previously shown that CESI can effectively highlight complex flow features such as jets and recirculation zones that are prevalent in the vasculature but cannot be visualized using conventional Doppler ultrasound imaging (Yiu & Yu, 2013). The formulation of CESI has already been extended further to perform flow vector estimation based on multi-angle Doppler measurement principles (Yiu & Yu, 2016), and the derived flow vectors, in turn, can be rendered dynamically as moving projectiles (Yiu et al., 2014) or pathlets (Angelelli et al., 2014).

Although a few HiFRUS-based flow imaging techniques have been successfully implemented on clinical scanners (Goddi et al., 2018; Hansen et al., 2017; Kim et al., 2017; Pedersen et al., 2012; Ricci, Ramalli, Bassi, Boni, & Tortoli, 2018), many of the flow imaging innovations have yet to be translated toward *in vivo* use. One major obstacle is the difficulty in developing, for every new imaging mode, a

suitable imaging platform that can be used easily for routine human scanning. It is well known that clinical ultrasound scanners are ill-suited for the realization of a new imaging mode (Tortoli & Jensen, 2006). Alternatively, it may be possible to make use of open-platform (OP) ultrasound scanners whose operations can be reconfigured to implement a new imaging mode (Boni, Yu, Freear, Jensen, & Tortoli, 2018). Nevertheless, not all ultrasound OPs are suitable for live human trials of new HiFRUS-based flow imaging methods. Some OPs simply do not allow reconfiguration of transmit operations of each array channel (critical to implement HiFRUS) (Ashfaq et al., 2006), while some do not grant access to the pre-beamformed data of each array channel (necessary to apply custom beamforming algorithms) (Wilson, Zagzebski, Varghese, Chen, & Rao, 2006). Even if channel domain operations are accessible, the OP's data streaming capacity might not be fast enough to facilitate live imaging (Cheung et al., 2012), or its physical size may be too large for it to be easily transportable to different places for multi-site human experimentation (Jensen et al., 2013). Moreover, the OP's user interface might lack the provision of real-time image view navigation and live rendering of image frames generated by the new imaging modes.

In this paper, we present the first successful live-mode implementation of CESI (Yiu & Yu, 2013) and its first *in vivo* application in visualizing flow dynamics in the human arteries. The development of this live CESI scanning platform is guided by our proposition that real-time image feedback is necessary to effectively perform *in vivo* CESI scans on humans, akin to the current use of ultrasound imaging in clinical practice. We have devised such a platform in the form of a software-oriented OP architecture (Boni et al., 2018), in which the entire signal processing chain (from beamforming to display rendering) is implemented through high-level programing. It makes use of a graphical processing unit (GPU) to perform both signal processing and display rendering, effectively leveraging the dual role that GPUs play as a many-core parallel processor and as a hardware-accelerated graphics renderer. Note that, from an ultrasound computing standpoint, GPU is known to be more energy-efficient than the central processing unit (So, Chen, Yiu, & Yu, 2011), and its programing is less labor-intensive than that for hardware oriented OPs that use field-programmable gate array (FPGA) as the primary computing device (Boni et al., 2016). These points of merit have motivated us to develop our live CESI scanning platform using a software-oriented approach. Subsequent sections of this paper will describe the hardware involved (Section 2.2) and the implementation methodology for live CESI (Section 2.3). Pilot application of live CESI in humans will also be presented. Its experimental protocol (Section 2.4) and representative results (Section 2.5) will both be shown.

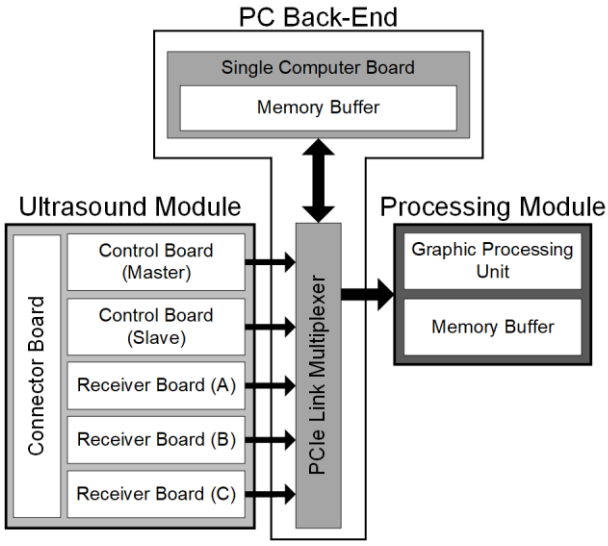

Figure 2.1. Block diagram showing the major modules inside the software-oriented OP for live CESI, including ultrasound module, PC back end, and processing module.

2.2 System Architecture

As described elsewhere (Yiu & Yu, 2013), the methodology of CESI involves three main stages. First, a set of plane wave pulses is sent at a high pulse repetition frequency (PRF), and a beamformed data frame is obtained from each firing. Second, the Doppler processing is performed individually at each pixel position in the beamformed data frame. At last, CESI frames are formed by simultaneously rendering flow speckles and color-coded axial flow velocity estimates. A pilot implementation of CESI has previously been realized based on offline processing of pre-beamformed data sets acquired over a few cardiac cycles (Yiu & Yu, 2013), but live CESI was not achieved in that proof-of-principle study due to bandwidth limitations in data streaming (Cheung et al., 2012). Seeking to overcome previous limitations, we have implemented CESI on a new OP with 4.8-GB/s data streaming capacity as required for live-mode implementation. A description of the system architecture is described in the following subsections.

2.2.1 Hardware Components

Our live CESI platform is built upon a software-oriented OP (USPlatform; us4us Ltd., Warsaw, Poland) that is equipped with a linear array (SL1543; Esaote, Genoa, Italy). As illustrated in Figure 2.1, this OP comprises three main modules: 1) ultrasound module, which is a 192-channel programmable ultrasound front-end module; 2) processing module, which is equipped with a GPU processor (GTX 1080Ti; NVidia Corporation, Santa Clara, CA, USA); and 3) personal computer (PC) back end (TSB7053; Trenton Systems, Lawrenceville, GA, USA). These three modules are interconnected through a

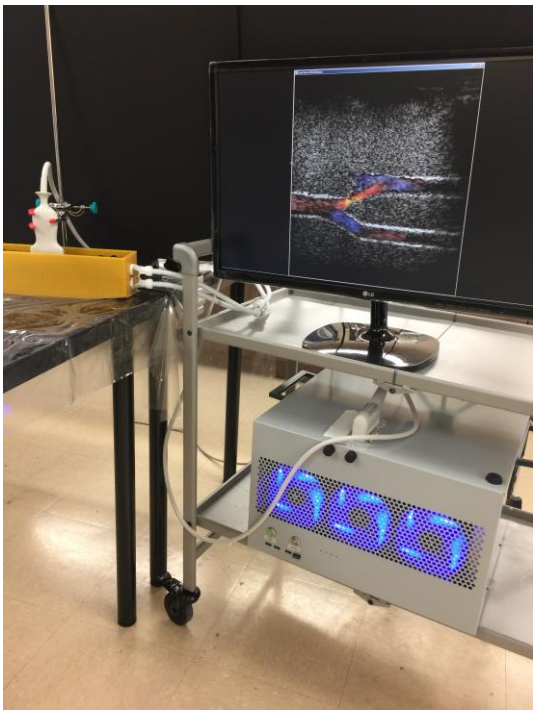

Figure 2.2. Photograph of the live CESI platform in operation. Shown in the system display is the real-time CESI output obtained from a carotid bifurcation phantom, whose fabrication details have been reported previously (Yiu & Yu, 2013).

Peripheral Component Interconnect Express (PCIe) backplane (BPG8032; Trenton Systems). The physical size of this platform is similar to a computer workstation, as shown in Figure 2.2. Thus, it can be deployed as a cart-based system that is transportable to facilitate multi-site human experimentation.

The ultrasound module and the processing module can essentially be regarded as PCIe devices that are connected to the PC back end, which can establish an active connection with one of these modules at a given time through a PCIe link switch as described earlier (Walczak, Lewandowski, & Zolek, 2013). During operation, the PC back end runs an imaging console to control the ultrasound module for ultrasound pulse transmission and pre-beamformed data acquisition (DAQ) over all array channels. The PC back end also buffers the acquired pre-beamformed data in the PC's random access memory (RAM) buffer and later transfers the data to the processing module for image formation and the Doppler signal processing.

The ultrasound module contains three component blocks: 1) connector board; 2) control boards; and 3) receiver boards. In terms of their function, the connector board serves as the interface between the ultrasound module and the array transducer, while the receiver boards acquire pre-beamformed data in parallel. The control boards are responsible for controlling pulse transmission sequence and synchronizing all operations.

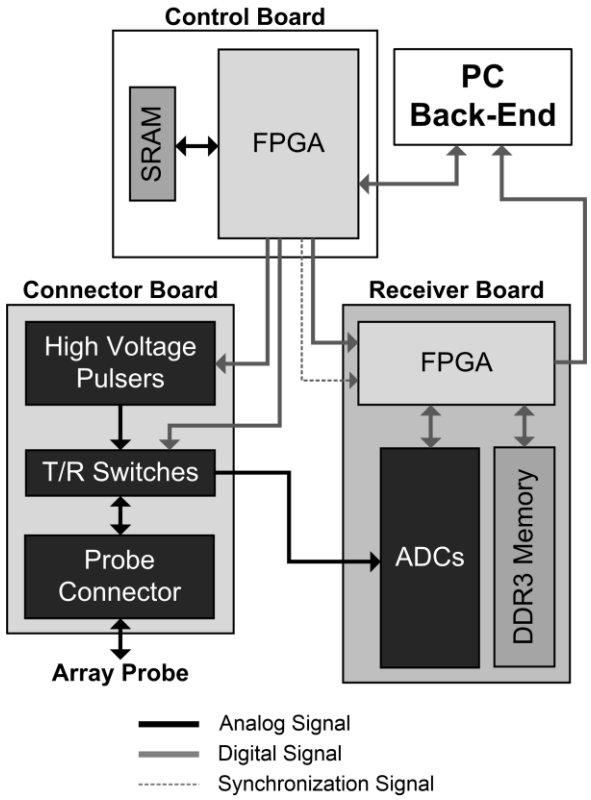

Figure 2.3. Data flow diagram showing the interactions within the ultrasound module between its three major components (connector board, control boards, and receiver boards). Interaction with the PC back end is also indicated as shown.

The processing module handles the pre-beamformed data received from the PC back end by performing various signal processing operations such as delay-and-sum (DAS) beamforming and the Doppler processing. This module contains a GPU with built-in internal memory to store pre-beamformed data. Its total processing power is enough to generate images in real time.

2.2.2 Data Flow Within System

The OP hardware for live CESI operates through a cascade of processes that are distributed among different hardware modules. During operation, each pulse-echo sensing event is handled by the ultrasound module. Figure 2.3 shows how the three components of the ultrasound module relay signals to each other to execute a pulse-echo sensing event. First, the transmit/receive (T/R) switches on the connector board are activated to open the high-voltage analog path between the transmit pulsers and 192 array elements that are linked through a series of high-voltage multiplexers. The control boards then instruct the pulsers to deliver high-voltage electrical signals to drive each element of the array transducer in order to transmit ultrasound pulses to the image view. After a microsecond-scale time delay, the control board instructs the T/R switches to change its state to instead activate its second

Table 2.1

ESTIMATION OF TRANSFER BANDWIDTH REQUIREMENTS FOR DIFFERENT IMAGING SCENARIO

Scenario (PRF)	Imaging Depth	Center Freq.	Sampling Freq.	Samples /Channel	Frame Data Size	Data/s
Superficial (10 kHz)	2 cm	15 MHz	50 MHz	1299	499 kB	4.6 GB/s*
Carotid (10 kHz)	4 cm	6 MHz	25 MHz	1299	499 kB	4.6 GB/s*
Kidney (5 kHz)	8 cm	10 MHz	25 MHz	2598	998 kB	4.6 GB/s*
Heart (4 kHz)	18 cm	3 MHz	25 MHz	5845	988 kB	4.3 GB/s#

*Assuming the use of a 192-element lineary array and 2 bytes per data sample

#Assuming the use of a 96-element phase array and 2 bytes per data sample

analog path that connects between the array transducer and the analog-to-digital converters on the three receiver boards. The radio frequency (RF) pulse echoes on each array element are then sampled. Note that each receiver board is responsible for performing 64 channels of time gain compensation, antialiasing filtering, amplification, digitization (RF sampling rate may be 25 or 50 MHz), and multi-channel data deserialization through an on-board FPGA codec. The deserialized pulse-echo data packet is then stored temporarily on each receiver board's DDR3 (double data rate, version 3) memory buffer (8 GB on each board; 24 GB in total).

During live-mode operations, after a pulse-echo imaging sequence (with P pulsing events) is executed Q times to acquire $P \times Q$ frames of pre-beamformed data, the entire batch of data packet stored on the receiver boards is streamed to the PC back end's 24-GB RAM buffer. This data transfer process is handled by a built-in PCIe direct memory access (DMA) transfer engine inside the FPGA on the receiver boards, each of which has its own PCIe DMA engine. The transfer link is a PCIe (version 2.0; × 16 lanes) bus that is capable of transferring data at a rate of 4.8 GB/s sustainably. Table 2.1 lists the transfer capacity for four common imaging scenarios with different combinations of view depth, PRF and RF sampling rate of our OP hardware. As summarized in Table 2.1, in practical imaging settings, the required data streaming rate is within the capacity of the PCIe bus.

Once the PC back end has received the incoming data packet from the receiver boards, it is first stored in the PC's RAM block together with frame batches from past time points. Note that, in the case when PC RAM is full, the earliest frame batch in RAM is erased in order to store the incoming frame batch. Afterward, data are fetched to the internal buffer of the processing module for beamforming and Doppler processing, whose implementation details will be discussed in Section 2.3.

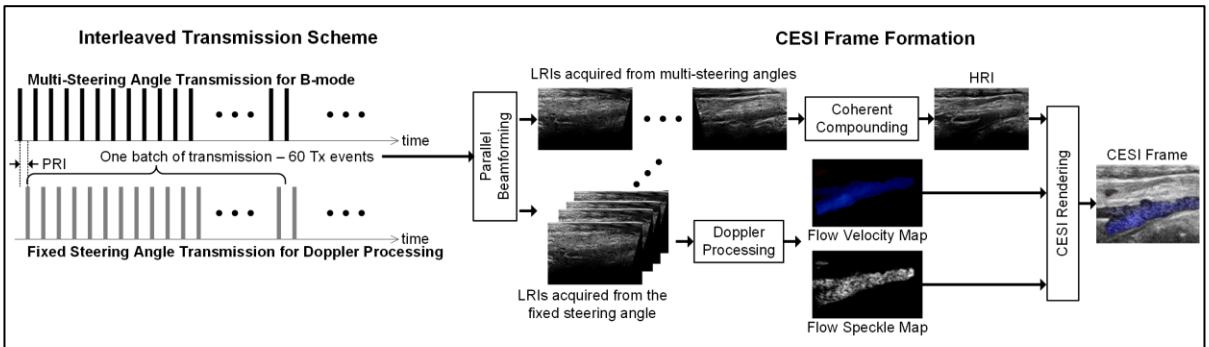

Figure 2.4. DAQ sequence and signal processing chain for live CESI. Each sequence comprises two interleaved subsequences. One of the subsequences is used to form a high-resolution B-mode image based on coherent compounding of LRIs formed from multi-angle plane wave excitation; the other subsequence is used to form a CESI frame via Doppler processing of LRIs formed from the same plane wave angle.

2.2.3 Software Interface

A live-mode implementation of CESI with slow-motion replay option is developed using a software-oriented design approach. The implementation is realized in the form of an imaging console with live feedback running in the PC back end. It is written in the C++ programming language with an US4US application programing interface (API) that enables communication between the PC back end and the ultrasound module. The console runs semi-automatically during operation, and it is responsible for handling a series of operations as described below.

1) Ultrasound Module Configuration

To realize live CESI, the ultrasound module's operations need to be configured to perform multi-angle plane wave pulse-echo sensing. This task is achieved through a text-based JavaScript Object Notation (JSON) configuration file. All the configuration parameters are specified in the JSON file, including array transducer, sampling frequency, number of active channels, and the maximum pulser voltage. The ultrasound module's pulse-echo imaging sequence is programed within the same JSON file by individually specifying the relevant parameters for each pulsing event (e.g., transmit steering angle, time interval between transmissions). When the codec is first run, the JSON file is used as initialization input to configure the ultrasound module, allocating internal buffers, and uploading imaging sequences to the on-board static RAM.

2) Image Sequence Programing

In the JSON file for ultrasound module configuration, an interleaved imaging sequence as shown in Figure 2.4 has been defined for live CESI to obtain both high-resolution B-mode image frames and time-resolved CESI frames. Each sequence of P pulsing events comprises two subsequences: 1) a B-

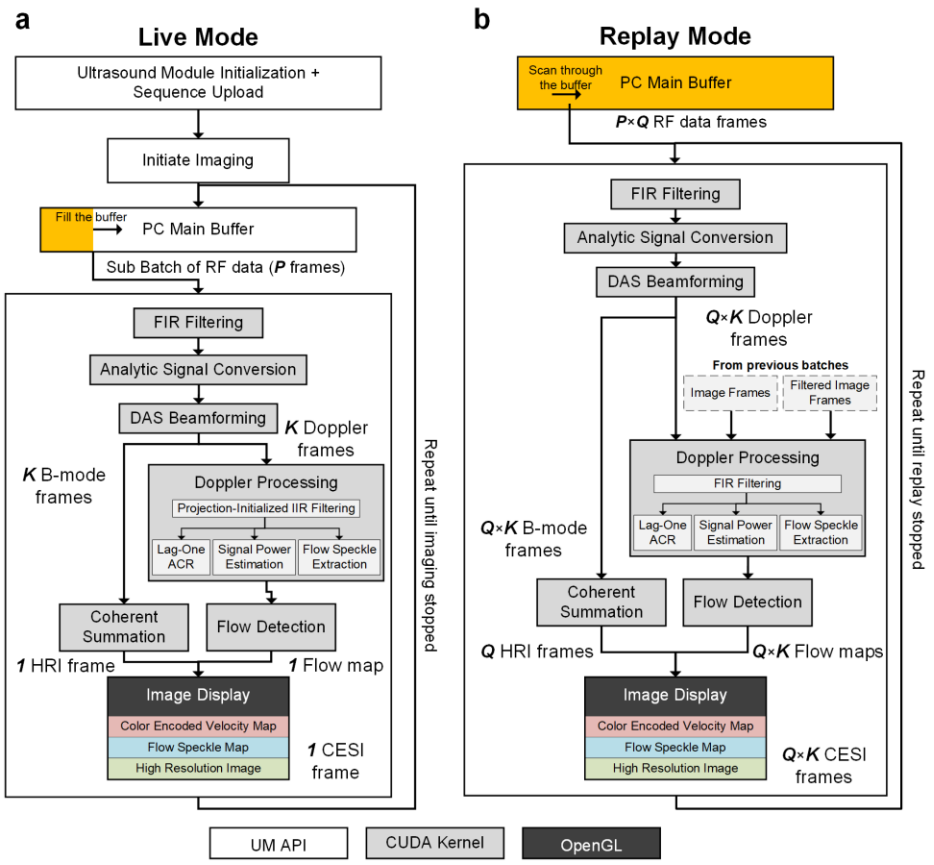

Figure 2.5. Operational flow of (a) live CESI mode and (b) slow-motion replay mode. Functions and kernels that are implemented with the US4US API, CUDA, and OpenGL are, respectively, colored in white, light gray, and dark gray.

mode DAQ subsequence with $K = P/2$ plane wave excitation pulses from different steering angles to facilitate coherent compounding (and thereby improve image quality) and 2) a CESI DAQ subsequence with $K = P/2$ plane wave excitation pulses from the same angle to realize time-resolved Doppler sampling. Pulse firings for these two subsequences are executed in tandem (i.e., a CESI DAQ event takes place in between two B-mode DAQ events, and vice versa). Therefore, for a given PRF, the effective DAQ rate for B-mode and CESI is equal to PRF/2.

3) Imaging Sequence Execution:

Within the C++ interface codec, a start function has been included to facilitate the commencement of the system's actual imaging operations. Once this function is called, the ultrasound module begins to transmit ultrasound pulses according to the imaging sequence specified in the JSON file. The codec then enters a waiting state, until a software interrupt is triggered either from the ultrasound module (see Section 2.2.3-4) or from the user to notify the console to pause, enter or exit the slow-motion replay mode, or terminate the program.

4) Live-Mode Data Handling

As described in Section 2.2.2, when ultrasound module completes the acquisition of $P \times Q$ frames, it immediately sends this pre-beamformed frame batch to the PC back end. In our interface codec, this operation is implemented through the use of software interrupts.When new data are ready to be streamed, the ultrasound module sends a software interrupt in the interface codec, after which the codec invokes a callback function to accept the incoming data and store them in the RAM. Within this callback function (see Figure 2.5(a)), the processing module is tasked to handle various signal processing operations for live CESI. First, data are transferred from PC RAM to the GPU global memory of the processing module. Note that, for live imaging, only a subbatch of P frames in the incoming frame batch (i.e., data for one of the Q iterations of DAQ sequence execution) is sent, since the limited refresh rate of the screen (typically 20–60 fps) implies that it is not necessary to process and render all raw data in real time. Image formation kernels are executed on each of the P raw data frames to derive beamformed data frames and a high-resolution B-mode image. Doppler processing kernels are also performed on beamformed data frames belonging to the CESI DAQ subsequence to form a CESI frame. Further remarks on these signal processing kernels are given in Section 2.3.

5) Replay-Mode Data Handling

When the slow-motion replay mode is enabled by the user, the console enters a subroutine (see Figure 2.5(b)) that performs time-resolved rendering of CESI frames. Here, the ultrasound module is first paused. Then, the entire PC RAM buffer containing all acquired pre-beamformed frame batches (since the earliest time point with data stored in the RAM) is stepwise transferred in batches of P frames (i.e., data for one complete DAQ sequence) to the processing module. For each batch, image formation and Doppler processing are performed (see Section 2.3), and the corresponding results are rendered at a video display frame rate (50 fps) to enable high-frame-rate CESI visualization of data acquired at the effective DAQ rate (i.e., PRF/2). The subroutine repeats until the replay mode is disabled by the user, after which the PC RAM is flushed and the ultrasound module is reactivated to perform live CESI scanning.

2.3 Real-Time Implementation of Color-Encoded Speckle Imaging

To facilitate high-speed execution of CESI processing operations, all image formation and Doppler processing tasks are executed on the GPU of the processing module via a single instruction, multi-thread strategy. The GPU computing kernels are programed using the C++ programming language and the compute unified device architecture (CUDA) API (version 7.5; Nvidia Corporation, Santa Clara, CA, USA). A general description on different GPU kernels is given in the following subsections.

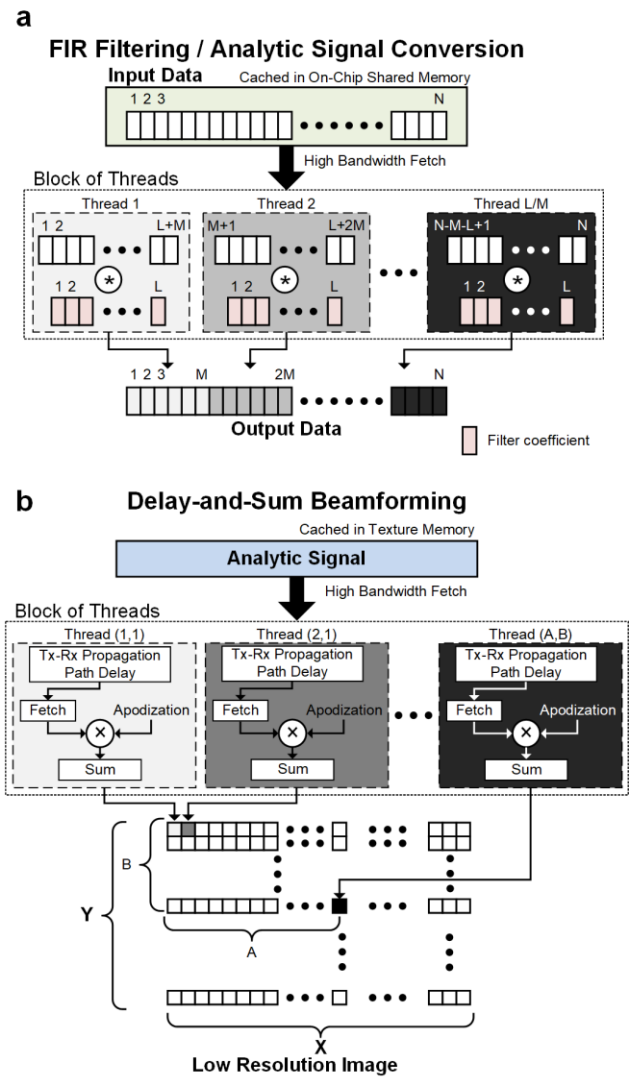

Figure 2.6. GPU kernel design for image formation tasks. (a) FIR filtering and analytic signal conversion are handled by dividing an N-sample channel data ensemble into M-sample segments (with an L-sample overlap) and assigning one thread to process each segment. (b) DAS beamforming is handled by assigning each thread to compute the beamformed data value for one pixel.

2.3.1 Image Formation With GPU

We have leveraged a set of GPU computing kernels that we have previously developed (Yiu et al., 2011) to perform parallel beamforming of raw data frames streamed into the processing module. Figure 2.6 conceptually illustrates the operation of various GPU kernels related to image formation from pre-beamformed data. These kernels are applied individually to each raw data frame (whether it is part of the DAQ subsequence for B-mode or CESI, and whether the console is running in live mode or replay mode). An additional GPU kernel on coherent compounding is also devised to obtain a high-resolution B-mode image from a B-mode DAQ subsequence. Further description on each kernel is given below.

1) Finite Impulse Response Filtering

A GPU kernel for bandpass filtering with a given bandwidth is first applied to suppress out-of-band noise in the pre-beamformed data samples of each array channel. As illustrated in Figure 2.6(a), this kernel is designed to apply an *L*-tap finite impulse response (FIR) filter individually on each channel's pulse-echo ensemble (with *N* samples), and the same process is repeated on other channels of the same frame and on other frames. It works by first copying the *N*-sample pulse-echo ensemble of a given channel to the GPU's shared memory (on-chip memory with short access time). Then, a block of compute threads is created, each of which is assigned to process an *M*-sample segment of the ensemble. Note that there is an *L*-sample overlap between two segments so that filter output transients can be safely discarded. Within each thread, the FIR filter operation is realized by convolving the filter coefficients (derived beforehand and stored in the GPU's shared memory) with the corresponding *M*-sample segment. The filter output from different threads is then concatenated and stored in the internal memory of the GPU.

2) Analytic Signal Conversion

In line with our previous work (Boni et al., 2016), this computing step is realized using an FIR filtering approach. The key difference between this FIR filter and the one described in the previous sub-subsection is that the filter coefficients are defined to yield a frequency response that corresponds to the definition of the Hilbert transform (instead of a bandpass frequency response). The bandpass filtered ensemble serves as the input to the FIR filter for Hilbert transform, in which the output yields the imaginary part of the analytic signal (while the bandpass filtered ensemble is the real part of the analytic signal). The computing result, which is a complex number, is stored in the GPU global memory for retrieval in subsequent beamforming operations.

3) DAS Beamforming

As illustrated in Figure 2.6(b), a pixel-based strategy is used to implement this kernel. Each thread is instructed to compute the beamformed value of one pixel in an image frame. Details of this process have already been published earlier (Yiu et al., 2011). In brief, three main steps are involved: 1) focusing delay calculation for all channels in the same frame; 2) retrieval of time-delayed analytic data values (with linear interpolation) from all channels from the GPU global memory; and 3) beamformed pixel value calculation based on weighted summation of the set of retrieved, interpolated analytic data values from all channels. This process is repeated for every pixel position in the image frame. The resulting beamformed data frame, which is derived from one pulse-echo sensing event, yields a low-resolution image (LRI).

4) Coherent Compounding

For LRIs formed from one complete B-mode DAQ subsequence (with K frames), a high resolution image (HRI) is derived by coherently summing the set of LRI frames as explained previously (Yiu et al., 2011). For this task, a GPU parallel processing kernel has been devised whereby each compute thread is assigned to derive one HRI pixel value based on the corresponding set of LRI pixel values at the same position. The resulting HRI frame is used for B-mode image rendering.

2.3.2 CESI Processing on the GPU

For LRIs that belong to a CESI DAQ subsequence, they are used as input for Doppler processing to derive CESI frames. Such processing can be considered as an enhanced version of conventional Doppler processing that is typically done with limited ensemble sizes (<10 samples) in color flow imaging (Evans, 2010). To realize this processing task in real time, the processing module has included a set of GPU-based Doppler processing kernels that are developed using the CUDA API. One particular advantage of using GPUs for CESI processing tasks is that the resulting image frames can be directly rendered on the screen through leveraging the GPU's conventional prowess in rendering hardware-accelerated graphics via the OpenGL API (version 4.6; Khronos Group, Beaverton, OR, USA) whose syntax is interoperable with CUDA within the same GPU kernel. Another advantage to be noted is that, as all CESI-related processing and rendering tasks are executed on the GPU, there is inherently limited data transfer between the pc back end and the processing module, and, in turn, the overall processing speed is further increased. A further description of the GPU kernels for CESI processing is presented as follows.

1) Live-Mode Doppler Processing

A pixel-based parallelization strategy is used here (see Figure 2.7(a)). We have first stacked the LRIs of the CESI DAQ subsequence (with K frames) to yield a set of slow-time data ensembles (one ensemble with K samples for each pixel position). Then, each block of GPU compute threads is assigned to handle one pixel's Doppler processing operations that include clutter filtering and flow estimation (including flow velocity, speckle, and power). For this task, each thread first loads into its shared memory, a slow-time ensemble of a particular pixel position. Clutter filtering is then performed by applying a $K \times K$ filter matrix to the slow-time ensemble, and the filter matrix is constructed as a L^{th}-order projection-initialized infinite impulse response filter (IIR) as described elsewhere (Bjaerum, Torp, & Kristoffersen, 2002). Then, flow estimation is performed by each thread in two forms. First, the mean flow velocity is estimated through calculating the lag-one autocorrelation (ACR) phase, similar to what is done to derive velocity estimates in color flow imaging (Evans, 2010). Second, the

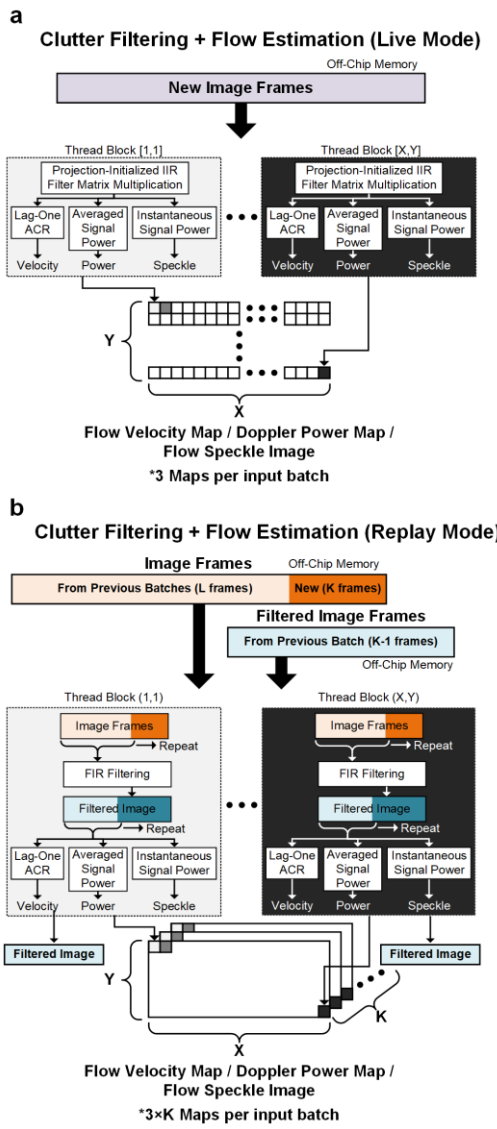

Figure 2.7. GPU kernel design for Doppler processing for (a) live CESI, which only works with slow-time samples in the current frame batch and (b) slow-motion replay mode, which makes use of past slow-time data samples.

mean flow power is computed by calculating the average squared magnitude of the post-filter data ensemble for each pixel. This quantity also represents the flow speckle strength at a pixel position. Results for all forms of flow estimation (velocity, power, and speckle) are then transferred to the GPU's global memory.

2) Replay-Mode Doppler Processing

A sliding window processing strategy is implemented to achieve time-resolved CESI rendering. In realizing this strategy, past CESI processing results are accumulated in the GPU global memory for

reuse in the processing of subsequent LRI batches formed from a CESI DAQ subsequence. Each GPU thread is assigned to perform the following tasks for one pixel position in the current CESI LRI batch with K frames. As shown in Figure 2.7(b), an augmented slow-time ensemble is first created from L past samples and K new samples at the same pixel position. Then, tissue clutter is suppressed by applying an L-tap FIR filter as similar to that described in Section 2.3.1-1 and discarding the filter output transients to obtain K filtered samples. Note that the merit of using an FIR filter here is that flow speckles remain coherent between adjacent CESI frames, whereas the projection-initialized IIR filter used in live-mode CESI may not achieve this (not a critical issue in the live mode because flow speckles are decorrelated anyway at a video-range frame rate of 50 fps). Next, the instantaneous flow speckle strength at each of the K slow-time sampling instants is calculated as the squared magnitude of each filtered data sample. On the other hand, the flow velocity and the mean flow power are derived by first forming an augmented, filtered slow-time ensemble from $K-1$ past filtered samples and K new filtered samples for the GPU thread's assigned pixel position. Subsequently, for each slow-time sampling instant, a K-sample sliding window (with the current sample and the past $K-1$ samples) is formed from the augmented ensemble, and the flow velocity is derived by computing its lag-one ACR phase (Evans, 2010), while the mean flow power is determined as the mean squared magnitude over this window. The corresponding $3 \times K$ flow estimates for each pixel position in a frame batch are then stored back to the GPU's global memory for subsequent processing.

3) Flow Mask Derivation

To determine whether a pixel position corresponds to the flow region, a GPU kernel is developed to derive a flow mask map from the obtained flow estimates. Here, each compute thread is assigned to derive the flow mask value for one pixel position, and it achieves so by determining whether that pixel's mean flow power is above a threshold (akin to the color gain threshold in color flow imaging (Evans, 2010)). The resulting flow mask map is stored to the GPU's global memory for use during CESI rendering.

4) Image Rendering and Display

In this final stage of CESI processing, image maps generated from previous stages, including B-mode HRIs, flow velocity maps, and flow speckle maps, are displayed to the screen console by invoking the relevant OpenGL syntax that directly renders pixel values stored in the GPU global memory to the respective screen positions. Specifically, for each CESI frame shown on the screen, it is rendered as three overlapping layers. First, the B-mode HRI is displayed at the bottom layer. Then, for pixel positions with an asserted flow mask value, their respective flow speckle value is rendered on top of

Table 2.2

PARAMETERS FOR IMAGING, BEAMFORMING, AND DOPPLER PROCESSING

Parameter	Value
Plane Wave Imaging	
View Depth (cm)	4.5
Sampling Frequency (MHz)	25
Pulse Repetition Frequency (kHz)	6
Center Frequency (MHz)	6
Pulse Duration (# cycles)	2
Transmit Aperture Size (# channels)	192
Steering Angles (B-mode DAQ)	[-15° to 15° (excluding 0°); spaced by 1]
Steering Angle (CESI DAQ)	-10°
Image Formation Processing	
Beamformer Aperture Size (# channels)	96
FIR Bandpass Filter Tap Count	64
FIR Filter Pass Band (MHz)	4 to 8
Hilbert Transform Filter Tap Count	51
Apodization	Hanning window
Image Size	256 × 256
Doppler Processing	
Live-Mode Ensemble Size	30
Clutter Filter Cutoff (Hz)	87.5
Live-Mode Clutter Filter Order	10
Replay-Mode Clutter Filter Tap Count	169
Sliding Step Size	1

the B-mode HRI. At these flow pixel positions, their respective axial flow velocity value is converted to a color code through mapping onto a hot-cold bicolor hue, and the resulting color code is transparently overlaid on top of the corresponding flow speckle through alpha compositing to yield the finalized CESI frame. In the live mode, the same process is repeated whenever a new frame batch is processed to provide real-time CESI rendering on the screen console. In the slow-motion replay mode, this rendering is performed at every slow-time sampling instant to realize time-resolved CESI visualization.

2.4 Experimental Methods

2.4.1 Data Acquisition Scenario

To demonstrate the use of our live CESI scanning platform *in vivo*, pilot trials have been conducted on a 31-year-old male volunteer's carotid arteries, brachial artery bifurcation, and the brachial vein. Note that the brachial artery bifurcation is known to have complex flow patterns like recirculation and

triphasic flow waveform. Thus, this imaging scenario serves as a good example to attest the ability of our platform to render complex flow in a time-resolved manner. In contrast, the flow dynamics of the brachial vein is known to change during maneuvers such as fist clenching. As such, imaging data were acquired during a clench-relax event, during which the volunteer first clenched his fist for 0.5 s before relaxing it. The venous flow dynamics of such maneuver event was analyzed to study how such maneuver affected the flow pattern. To help demonstrate the live use of CESI scanning platform, the imaging scene was concurrently recorded at 25 fps rate using an open-source screen recording software (CamStudio). Also, the processing time of the platform was determined using the CUDA profiler tool (Nvidia).

2.4.2 Parameters for Live CESI Platform

We have configured our software-oriented OP to operate with a 60-frame interleaved DAQ sequence with 30 pulsing events each for B-mode and CESI (i.e., $P = 60$, $K = 30$). In the live mode, a batch of 60 frames was streamed after five iterations of the interleaved DAQ sequence (i.e., $Q = 5$), thus yielding a live frame rate of 20 fps for a prescribed PRF of 6 kHz. Other processing parameters are listed in Table 2. One point worth noting about the choice of PRF for our interleaved DAQ sequence is that its value was rationally chosen to avoid reverberations in a B-mode DAQ event from emerging as crosstalk interference clutter in the next CESI DAQ event. Such issue is known to be significant if a high PRF is used (>10 kHz) or if a low ultrasound frequency is used to achieve better penetration (Avdal, Lovstakken, & Torp, 2015).

During the pilot trials, the 192-element linear array (SL1543) with 0.245-mm element pitch was connected to the live CESI scanning platform, and it was placed on the subject's left forearm (for imaging of the brachial artery bifurcation and vein). Image alignment was done with real-time image feedback provided by the system, and the key imaging parameters are listed in Table 2.2. These parameters generated a raw data traffic of 3.1 GB/s, and it was well within the real-time data transfer capacity of our live CESI scanning platform. Note that the sampling frequency (25 MHz) was more than four times the transmit center frequency (6 MHz), so the resulting pre-beamformed RF data were not affected by aliasing. In the PC back end, 10 GB of the total RAM block was allocated for raw data buffering, so our platform could store more than 3 s of raw data before the data buffer was filled.

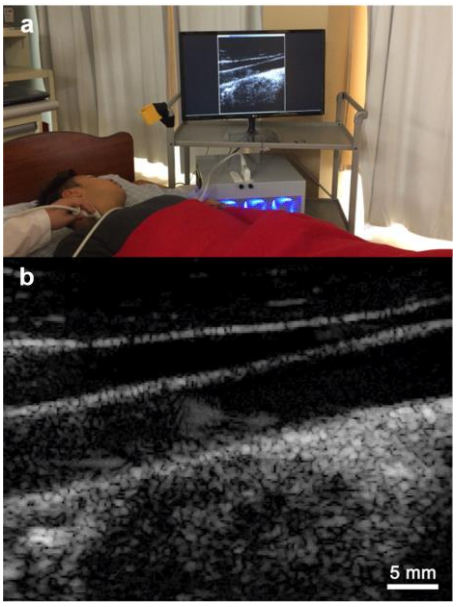

Figure 2.8. Demonstration of the live CESI platform being used in human studies. (a) Photograph of the imaging scene where the operator is navigating the linear array to locate the subject's common carotid artery. (b) Corresponding image window on the platform console.

2.5 Results

2.5.1 Real-Time Performance of Live CESI Platform

Our live CESI scanning platform was generally found to be effective in facilitating real-time image guidance and CESI visualization. As a visual demonstration, Figure 2.8 and Movie 2.1 show a synchronized rendering of the imaging scene (upper window) and the live CESI window on the platform's image console (lower window). As illustrated, while the operator tried to position the linear array to acquire a longitudinal view of the carotid arteries, the image view was rendered live on the screen. Accordingly, the operator was able to navigate and align the transducer properly against the long axis of the common carotid artery and then turn on live CESI visualization to observe vascular flow dynamics, as shown in Movie 2.1.

The live CESI rendering realized on our scanning platform matches well with the measured computational time for various processing steps as shown in Table 2.3. Specifically, it was found that 18.24 ms was required to handle one raw data frame batch (from 60 pulse-echo sensing events), corresponding to a real-time throughput of 55 fps that is within the live video display range. This overall time includes the entire processing sequence from raw data transfer (from the PC RAM block to the GPU global memory) to the derivation of CESI frame and its display to the screen through OpenGL. It should be noted that, in the replay mode, slow-motion rendering of CESI frames was also achieved in

Table 2.3
PROCESSING TIME FOR EACH RAW DATA FRAME BATCH

	Live Mode	Replay Mode
Data Transfer	7.09 ms	
Filtering & Analytic Signal Conversion	2.09 ms	
DAS Beamforming	8.03 ms	
Coherent Summation	0.06 ms	
Image Display	0.03 ms	
CESI Processing	0.94 ms	2.68 ms
Total	18.24 ms	19.98 ms

*Based on parameters in Table 2.2; Timed for forming 60 LRIs, 30 for B-mode and 30 for CESI processing (outputting 1 and 30 CESI frames for live-mode and replay mode respectively for the processing of each frame batch)

real time. The total processing time for each frame batch is 19.98 ms, corresponding to a 50-fps frame rate as required for real-time screen refreshing.

2.5.2 Time-Resolved CESI Rendering of Triphasic Flow in Brachial Artery Bifurcation

The slow-motion replay mode of our CESI platform was capable of temporally resolving triphasic flow at the brachial bifurcation. As presented in Movie 2.2, replay-mode CESI has enabled the visualization of flow dynamics throughout the entire cardiac cycle. The image view encompassed the main brachial artery and the two downstream branches (radial and ulner). For reference, two Doppler spectrograms obtained from the two downstream branches are rendered in the two right windows of Movie 2.2 (their respective range gate positions were marked by the yellow and red boxes in the cineloop). Also, a series of CESI frame snapshots at representative time points of the cineloop is shown in Figure 2.9. Note that the raw data for Movie 2.2 was captured at a nominal frame rate of 3000 fps (i.e., PRF/2), and processing was executed at 50 fps. The presented cineloop was temporally compressed offline to replay at an effective frame rate of 200 fps in order to more lucidly depict the temporal dynamics highlight temporal changes in the arterial flow pattern.

As shown in Movie 2.2, replay-mode CESI has consistently depicted how slow forward flow had occurred in the brachial bifurcation as the previous cardiac cycle approached its end diastole (see also Figure 2.9(b)). Then, the CESI cineloop showed that flow accelerated significantly as the next cardiac cycle commenced and approached peak systole. Also, flow was observed to transit from the main brachial artery into the radial and ulnar branches as indicated by the flow speckle trajectory, despite the presence of Doppler aliasing in the color-coded flow velocity estimates (Figure 2.9(c)). Following flow

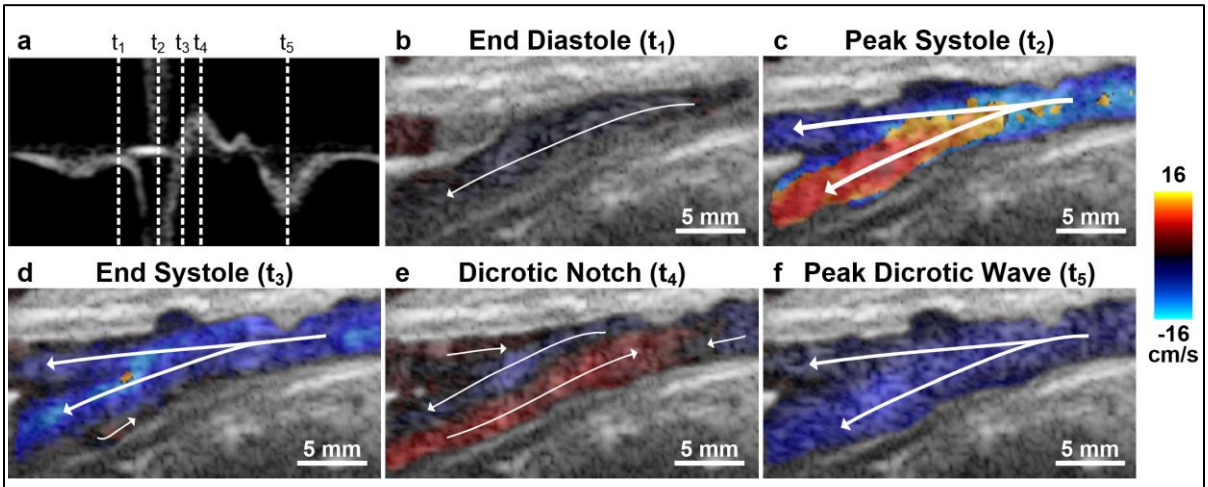

Figure 2.9. Time-resolved CESI visualization of brachial bifurcation flow dynamics. (a) Doppler spectrogram taken in the ulnar artery. It shows the relative time points of five CESI still-frame snapshots taken at (b) end diastole, (c) peak systole, (d) end of systole, (e) dicrotic notch, and (f) peak dicrotic wave. Flow directions in each CESI frame are illustrated by white arrows. See also Movie 2-2.

systole, flow was observed to decelerate rapidly (Figure 2.9(d)), and flow reversal had occurred in the ulnar branch as highlighted by the concurrent change in blood speckle movement direction and change in velocity color code (Figure 2.9(e)). Such flow reversal only lasted briefly, as forward flow resumed thereafter (Figure 2.9(f)) as the cardiac cycle entered the diastolic phase. These events are well aligned with the triphasic flow pattern rendered by the Doppler spectrogram obtained from the ulnar artery (Figure 2.9(a)).

2.5.3 CESI Visualization of Maneuver-Induced Change in Venous Flow

Time-resolved CESI visualization was found to be effective in revealing flow patterns in the brachial vein during a maneuver event. Movie 2.3 shows the corresponding results when the subject was tasked to perform a clench relax event of his left forearm. The upper window shows the brachial vein near the elbow region, with the radial veins (left) joining the brachial vein (right); the lower window shows the Doppler spectrogram obtained from the merging point of the venous branches. A corresponding still-frame time series of CESI snapshots for this imaging scenario is shown in Figure 2.10.

As shown in Movie 2.3 and Figure 2.10, when the subject's fist was initially relaxed, venous flow was characteristically slow (Figure 2.10(b)). As the subject clenched his fist, venous flow speed started to increase gradually and it attained first peak flow 70 ms later (Figure 2.10(c)) and it sustained for another 316 ms while the subject's fist remained clenched (Figure 2.10(d)). Venous flow began to decrease thereafter as the venous blood pool was depleted (Figure 2.10(e)), and it further dropped to a flowless state after the subject relaxed his fist (Figure 2.10(f)), as indicated by the flash artifact in Movie

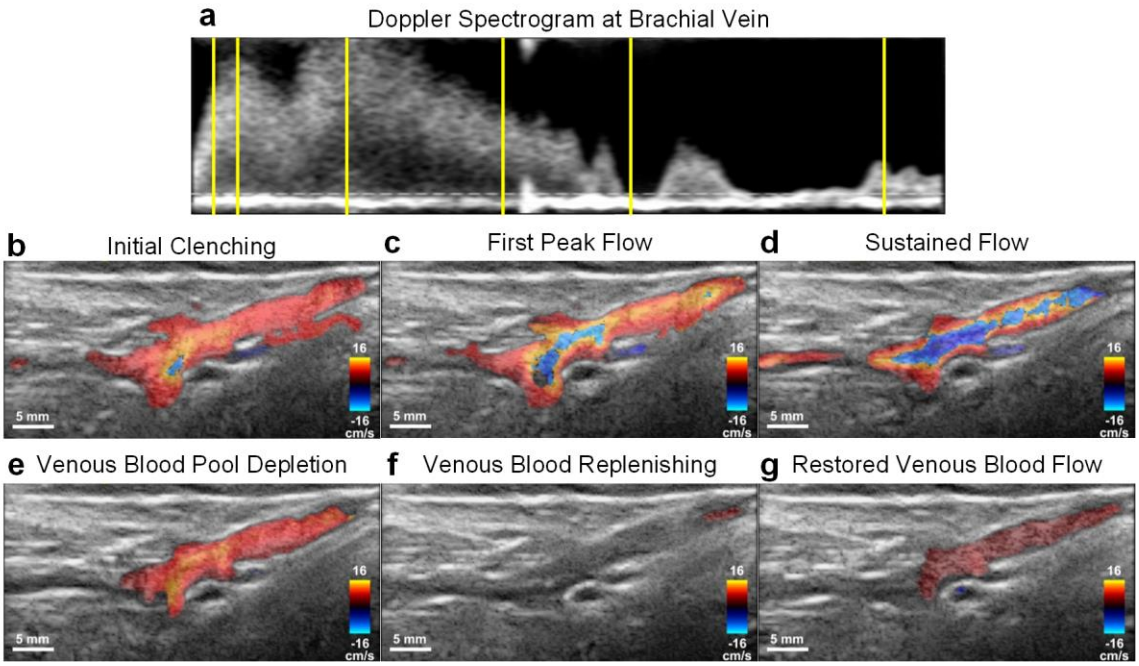

Figure 2.10. Time-resolved CESI visualization of flow dynamics in the brachial vein that is connected to radial veins. (a) Doppler spectrogram taken in the merging point between the venous branches. It shows the relative time points of five CESI still-frame snapshots taken at (b) start of fist clenching, (c) peak venous flow while fist was clenched, (d) sustained high venous flow while fist was clenched, (e) depleted venous flow while fist was clenched, (f) flowless phase while venous blood pool was replenishing, and (g) return of venous flow after subject fist was relaxed again. See also Movie 2-3.

2.3. It roughly took 694 ms to replenish the venous blood pool and venous flow returned to its baseline state (Figure 2.10(g)).

2.6 Discussion

2.6.1 Importance of Live CESI Scanning Platform for *In Vivo* Studies

As HiFRUS technology has matured in recent years, it has created new opportunities in developing new flow imaging techniques with fine temporal resolution. CESI is one particular example of a new time-resolved flow visualization technique that can outperform conventional Doppler ultrasound solutions (Yiu & Yu, 2013). However, without a live scanning platform that supports real-time realization of new imaging methods, it would be futile to foster CESI and other HiFRUS-based flow imaging techniques toward *in vivo* use, because ultrasound is widely expected to be a point-of-care imaging modality (Wells, 2006).

In this work, we have demonstrated how real-time CESI can be realized with both live rendering and slow-motion replay features. Our solution is based on the integrative use of: 1) a software-oriented OP

whose transmit-receive operations can be reconfigured via high-level programing (Section 2.2); 2) a high-performance GPU that can execute in real time the entire signal processing chain from beamforming to Doppler processing and display (Section 2.3); and 3) high-bandwidth communication between the software-oriented OP and the processing module, as facilitated through a PCI-e link and a PC back end (Figures. 2.1 and 2.3). Programing was carried out in JSON, C++, CUDA, and OpenGL (Figures. 2.5–2.7). The use of these compiled languages is essential to make the developed software more performance-efficient than those written in scripting languages like MATLAB and, in turn, favor real-time operability of the platform. This performance advantage is a key technical benefit our devised platform has over certain ultrasound research platforms that only allow researchers to execute processing and display operations through MATLAB. When comparing to other existing solutions implemented on real-time scanners such as color flow imaging (Evans, 2010; Kim et al., 2017), B-flow imaging (Lovstakken, Bjaerum, Martens, & Torps, 2006), and vector flow mapping (Goddi et al., 2018; Hansen et al., 2017; Pedersen et al., 2012; Ricci et al., 2018), our live CESI platform offers the unique advantage of providing on-demand, slow-motion playback of flow dynamics over the entire imaging view using HiFRUS data sets acquired at submillisecond temporal resolution. This HiFRUS-enabled technical feature is critical to the tracking of complex flow patterns with significant flow disturbance, for which frame rates of over 1000 fps are typically needed to enable proper visualization (Hoskins, 2010). In contrast, the conventional imaging paradigm falls short in providing the much needed frame rate to visualize complex flow patterns as the images are acquired on a line-by-line basis. Note that, with its fine temporal resolution, our CESI implementation can also derive flow speckle patterns that are more spatiotemporally coherent than those rendered in B-flow imaging, whose principles are based on conventional scanline-based imaging (Lovstakken et al., 2006). Although CESI does not provide flow vector information, it serves well to highlight flow trajectories via complementary rendering of flow speckles and velocity color codes, and such visualization is useful in identifying complex flow patterns with multiphase characteristics. Its algorithmic complexity is also lower than that for flow vector estimators (Ricci et al., 2018; Yiu & Yu, 2016).

The software-oriented OP leveraged in this work is commercially available to the larger ultrasound community. From an engineering standpoint, availability of the platform can potentially speed up the development of novel imaging algorithms by offering a suitable hardware for performance calibration and *in vivo* demonstration. From a clinical standpoint, this platform can facilitate the clinical translation of novel imaging algorithms to foster benchside to bedside adoption. Another advantage of this open platform is that all the imaging operations, from transmit sequencing to formation and display of images, are all software programmable. Hence, newly developed algorithms can be made available to

other research laboratories and clinical centers; researchers can download and execute shared software codec package on their platform to test new imaging modes. For this reason, multi-center clinical trial of novel imaging algorithms is possible.

2.6.2 *In Vivo* Applicability of Live CESI

The real-time efficacy of our live CESI scanning platform has been demonstrated through several *in vivo* pilot trials. It was found that our system was able to provide real-time image guidance for navigation and live CESI visualization (Figure 2.8, Movie 2.1, and Table 2.3), both of which are crucial to run routine *in vivo* studies. Also, the slow-motion replay mode of our platform has demonstrated strength in offering time-resolved visualization of complex flow dynamics in real time whenever the replay mode was activated. For example, triphasic flow pattern in the brachial bifurcation can be clearly observed (Figure 2.9 and Movie 2.2), while changes in brachial venous flow were visualized during a fist-clenching test (Figure 2.10 and Movie 2.3). These complex flow features are inherently difficult to visualize with conventional color flow imaging or B-flow imaging. Overall speaking, the initial results presented in this paper should pave way for further use of our live CESI scanning platform to conduct larger scale human studies. Of particular interest is the use of this platform to answer vascular physiology questions where conventional ultrasound cannot provide answers for, such as those that involve neurovascular control and complex blood flow (Au, Hughson, & Yu, 2018). The resulting experimental evidence to be gained would, in turn, substantiate the application merit of CESI, thereby garnering further interest from physiologists, clinicians, and the industry.

It should be emphasized that CESI's ability in resolving complex flow is a unique technical feature that bears clinical potential. For instance, it can be leveraged to noninvasively visualize the severity of local oscillatory flow that is known to be linked to atherosclerosis development and progression (Mohamied et al., 2015). Such visual insights may be further harnessed to derive indices of oscillatory flow, akin to those obtained using computational means (Gabriel, Ding, & Feng, 2017). With its complex flow visualization capability, CESI may also facilitate the identification of arterial segments with velocity profile skewing (i.e., wherein the maximum velocity emerges at a luminal location away from the centerline). From a hemodynamic analysis standpoint, such identification is important, because the derivation of wall shear stress (an important parameter linked to atherosclerosis (Mohamied et al., 2015)) from these flow segments is known to be prone to significant error for many existing algorithms that are based on the assumption of Poiseuille or Womersley flow profiles (Mynard, Wasserman, & Steinman, 2013). The use of CESI here would help to avoid making wall shear stress measurements in those arterial segments that are prone to yield inaccurate estimates.

2.6.3 Perspectives for Further Development

Without major modification, our live CESI scanning platform may be used as a customized OP that allows raw pre-beamformed data to be acquired for offline evaluation of the performance of other emerging HiFRUS-based motion analysis methods. For example, the same CESI DAQ subsequence can be used to capture wall motion and tissue strain, for which GPU computing kernels have already been developed (Idzenga, Gaburov, Vermin, Mensen, & De Korte, 2014). These pre-beamformed data sets may be used to analyze the GPU-computing performance of adaptive clutter filtering techniques like eigen filtering (Chee, Yiu, & Yu, 2017). On the other hand, the B-mode DAQ subsequence would provide raw data for the testing of emerging beamforming techniques such as Stolt's transform (Garcia et al., 2013) and minimum variance apodization for synthetic aperture imaging (Yiu & Yu, 2015). Also, with the use of a high-frequency array transducer and with our platform operating under the high sampling rate option (50 MHz), HiFRUS flow imaging may be achieved in smaller vessels, such as choroidal flow in the eye (Urs et al., 2018) and cardiovascular dynamics in mouse embryos (Ketterling et al., 2017).

One logical direction that can be pursued to expand the live scanning functionality of our platform is to implement flow vector estimation and visualization algorithms (Yiu et al., 2014; Yiu & Yu, 2016). Such work would enable the conversion of our platform into a research purpose and customizable version of the vector flow imaging mode available on some commercial scanners (Goddi et al., 2018; Hansen et al., 2017; Pedersen et al., 2012). To realize this goal, reprograming of the DAQ sequence would be required (although it should be trivial), and new GPU kernels for flow vector estimation and visualization need to be added to the processing module. Additional GPUs may be included as required to boost the platform's computing capacity for flow vector estimation tasks. Another direction of interest that can be pursued in the future is to reconfigure the platform's architecture for 3-D CESI investigations with 2-D arrays. Here, one obvious obstacle that needs to be overcome is to boost the total channel count of the platform to accommodate the significantly higher number of elements on a 2-D ultrasound array. One potential solution is to synchronize multiple copies of ultrasound front-end modules to form a composite platform, similar to what others have recently achieved using four units of a 256-channel, MATLAB-based software OP to drive a 1024-element 2-D array (Petrusca et al., 2017). Alternatively, it is possible to consider expanding the channel count of our current ultrasound front-end module to 256 channels and integrating it with newer spiral 2-D arrays with lower channel count and optimized element positioning (Roux et al., 2017).

Another direction that worths pursuing is to translate the CESI platform from a research-oriented scanner to a point-of-care scanner that can visualize complex flow dynamics to facilitate more informed

diagnoses. Critical to the success of such translational endeavour is to develop a user-friendly graphic user interface and to improve scanner's output image quality. The interface should be able to integrate into the workflow of clinicians and phyiologists; their input and feedback are therefore vital when designing such user interface. To improve the B-mode image quality, image filtering techniques such as despeckling (Tay, Garson, Acton, & Hossack, 2010) and sharpening (Anand, Shantha Selva Kumari, Thivya, & Jeeva, 2013) can be employed. Together, they provide better overall user experience to clinicans and phyiologists.

2.7 Conclusion

Practical realization of an emerging ultrasound imaging algorithm is critical to enable the algorithm's translation toward *in vivo* use. In this paper, we have substantiated such technical importance by presenting a live CESI scanning platform that can render complex flow dynamics in real time and can provide on-demand slow-motion playback of CESI frames on a time-resolved basis. With the new platform, CESI can be more efficiently applied to human experimentation. Such translational research effort would be essential to substantiate the role that new ultrasound imaging methods can potentially play in cardiovascular science and clinical diagnostics.

Chapter 3
Flow Phantom Design Protocol for Ultrasound Flow Imaging Experimentation

3.1 Introduction

In using ultrasound for flow estimation purposes, huge technological strides are being made to advance beyond the single-gate pulsed Doppler mode and color flow imaging (CFI) mode that are commonly found in clinical scanners (Evans, Jensen, & Nielsen, 2011). For instance, high-frame-rate CFI is nowadays achievable (Ekroll et al., 2013; Osmanski et al., 2012), and it can be rendered concurrently with flow speckles to enhance visualization quality (Yiu & Yu, 2013). Another technological trend of interest is the development of ultrasound vector flow imaging techniques (Jensen, Nikolov, Yu, & Garcia, 2016a), whose high-frame-rate extension can be realized using parallel data acquisition approaches that are based on broad-view excitation principles (Jensen, Nikolov, Yu, & Garcia, 2016b). The primary benefit offered by vector flow imaging is that the rendered flow information, consisting of both the flow angle and flow velocity magnitude, is in principle a more accurate representation of the actual hemodynamics within the vasculature being imaged. Alas, different formulations of vector flow imaging may be prone to various estimation errors (Hansen et al., 2009; Steel & Fish, 2002; Swillens, Segar, Torp, & Lovstakken, 2010). It is thus vital to systematically test and calibrate the performance of a novel flow imaging method before introducing it toward clinical use, as is the case with conventional Doppler ultrasound devices (Browne, 2014). In fact, the need for such performance calibration is becoming more pressing as high-frame-rate CFI and vector flow imaging are starting to be used clinically as new diagnostic options on commercial scanners (Goddi et al., 2017; Hansen et al., 2015; Hur et al., 2014; Tanaka et al., 2015).

On the topic of performance evaluation in ultrasound-based flow estimation, it is known that *in vivo* validation studies are challenging to carry out properly unless cross-referencing data are available from another imaging modality such as magnetic resonance imaging (Faurie et al., 2017; Hansen et al., 2009). As such, there is a practical need to devise methods and protocols that can enable quantitative examination of the efficacy of flow estimation methods under controlled flow conditions. Of particular interest is the development of *in vitro* flow phantoms, as they can serve well as investigative tools for

hardware implementation of flow estimation methods (Hoskins, 2008). Yet, it is not trivial to design suitable phantoms that can holistically assess the accuracy of the derived flow estimates. Existing models such as straight tubes (Wang, Herbst, Pye, Moran, & Hossack, 2017; Zhou, Kenwright, Wang, Hossack, & Hoskins, 2017) characteristically lack multi-directional flow behavior, while spinning disks (Kripfgans, Rubin, Hall, & Fowlkes, 2006; Walker, Henriksen, Ringqvist, & Ask, 2009) merely simulate tissue motion instead of flow dynamics. Anthropomorphic bifurcation models (Chee, Ho, Yiu & Yu, 2016; King, Ring, Moran, & Browne, 2010; Lai, Yiu, Poon, & Yu, 2013; Poepping, Nikolov, Rankin, Lee, & Holdsworth, 2002; Watts et al., 2007) are also not ideal from a performance calibration standpoint, because their geometries do not embody all possible curvature angles, and thus angle-specific estimation errors are prone to be overlooked. Indeed, since the flow dynamics in anthropomorphic phantoms can be rather complex (e.g., in cases with stenosis), derivation of their ground-truth flow profile is not a trivial task and typically requires the use of dedicated tools like particle image velocimetry (Kefayati & Poepping, 2013; Poepping et al., 2010).

Here, we present the design of a novel spiral flow phantom that is intended to serve as an accuracy evaluation tool for ultrasound-based flow estimation methods. In devising this new phantom, we have been working with the proposition that, in order to effectively identify angle-specific flow estimation errors, it is critical to formulate a vessel geometry that can comprehensively generate multi-directional flow (i.e., from 0° to 360°). Spiral vessel seemingly matches well with this proposition because: 1) its curvy geometry naturally gives rise to flow patterns that cover all possible flow angles; 2) its dimensions can be controllably defined to fit multiple spiral loops within the aperture width of a transducer (e.g., 4-cm width for linear arrays used in carotid scans). In line with this rationale, we have developed a systematic design protocol for spiral flow phantoms. Also, we have pursued the initial application of spiral flow phantoms in evaluating the flow rendering performance of CFI and vector flow imaging.

3.2 Phantom Design Protocol

3.2.1 Drafting of Casting Components

Our new spiral flow phantom was devised based on lost-core casting principles. To build this phantom, a set of casting components was first drafted using a computer-aided design (CAD) software (SolidWorks; Dassault Systemes, Waltham, MA, USA): 1) a multi-loop Archimedean spiral core; 2) an open-top phantom box; 3) two side plates. These components are intended to be assembled during phantom fabrication (described further in Section 3.2.2) such that upright, suspended mounting of the spiral core can be realized within the box cavity, as depicted in Figure 3.1(a). In order to achieve so,

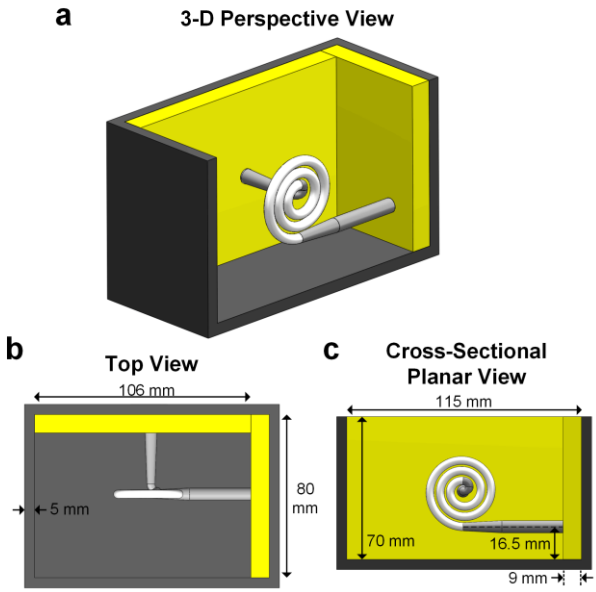

Figure 3.1. Conceptual illustration of the assembly of casting parts for spiral flow phantom construction. Three casting parts are involved: spiral core (white), phantom box (gray), and two side plates (yellow). Three different views of the assembly are shown (a) 3-D perspective view (proximal box side not shown), (b) top view, and (c) cross-sectional planar view. The spiral core was mounted in suspension within the phantom box cavity with the help of the two side plates. Dimensions of phantom box and side plates are labeled.

the two side plates would need to be placed adjacently against two of the phantom box's inner sides (Figure 3.1(b)), and they would provide structural support for the two ends of the spiral core (Figure 3.1(c)).

The dimensions of the spiral core geometry are illustrated in Figure 3.2. Note that, in a polar coordinate system, the radius of an Archimedean spiral is governed by the relation $r = k\theta$, where k and θ are the pitch and the revolution angle, respectively, and the spiral originates from the center at r = 0. In this work, our spiral core had three revolutions (i.e., $0 < \theta < 6\pi$) and a pitch of 5 mm (i.e., $k = 5/(2\pi)$ mm/rad), as well as a vessel diameter of 4 mm. Accordingly, the spiral core had a lateral span of 34 mm (see. Figure 3.2(a)), and its total segment length was 17.7 cm (from inlet to outlet). To facilitate connection to the flow circuit, a horizontal inlet connector (35-mm length and 6-mm diameter) was appended to the outer end of the spiral through a tapered adaptor (19-mm length and with 6- and 4-mm diameters, respectively, on its two ends). On the other hand, the last half turn of the inner spiral loop was directionally modified to make a tapered 90° turn out of plane (see Figure 3.2(b)) to link to an outlet flow connector perpendicular to the spiral plane (35-mm length and with 4- and 6-mm diameters at the two ends).

The open-top phantom box was drafted to be of 115×80×70 mm (length×width×height) in inner dimension. Each box side was of 5-mm thickness. On two of the sides, an 18-mm diameter circular

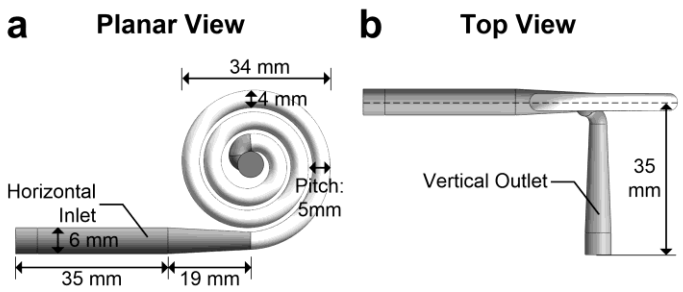

Figure 3.2. Vessel geometry for the spiral flow phantom. (a) Planar view of the three-loop spiral core with 4-mm diameter and 5-mm pitch. Horizontal inlet and tapered adaptor are also shown. (b) Top view of the spiral core, showing the inner spiral end's connection to an outlet perpendicular to spiral plane.

void was created at the respective location of the spiral core's inlet and outlet to facilitate the installation of quick-fit connectors toward the end of the phantom construction procedure.

The two side plates were drafted with different dimensions to support the mounting of the spiral vessel core within the void space of the phantom box. The inlet side plate was 80×70 mm^2 in plate area, while that for the outlet side plate was 106 × 70mm^2. Both plates were of 9 mm in thickness. Also, they each incorporated a cylindrical slot (6-mm diameter and 5-mm depth) at the position of the respective spiral core ends as mounting support during phantom fabrication.

3.2.2 Fabrication Procedure

With the CAD models of the casting components, the spiral flow phantom was built using a protocol that is modified from what we have reported earlier (Ho et al., 2017). Physical replicates of the casting components were first built using 3-D printing. This task involved importing the CAD models (saved in the STL stereolithography file format) into an open-source software (KISSlicer; versus 1.5) to derive 3-D printing instructions. The CAD models' 3-D printing codes were downloaded to a fused deposition modeling system (Model DX; CreatBot 3-D Printer, Zhengzhou, China) to create physical builds of the drafted models (0.1-mm layer thickness and 0.5-mm skin thickness). A photograph of the fabricated components is shown in Figure 3.3(a). Note that the 3-D printing material was in the form of polylactic acid (PLA) filaments. The key reason for using this type of 3-D printing material is that it is soluble in chlorinated solvents, thus making it possible to realize lost-core casting as required to form a spiral vessel lumen in the phantom. The physical build of the spiral vessel core (white) was formed with 12.5% infill, thereby creating a porous interior void to foster its dissolution during core removal. In contrast, the phantom box (off-white) and the side plates (yellow) were built with 100% infill to strengthen their mechanical rigidity.

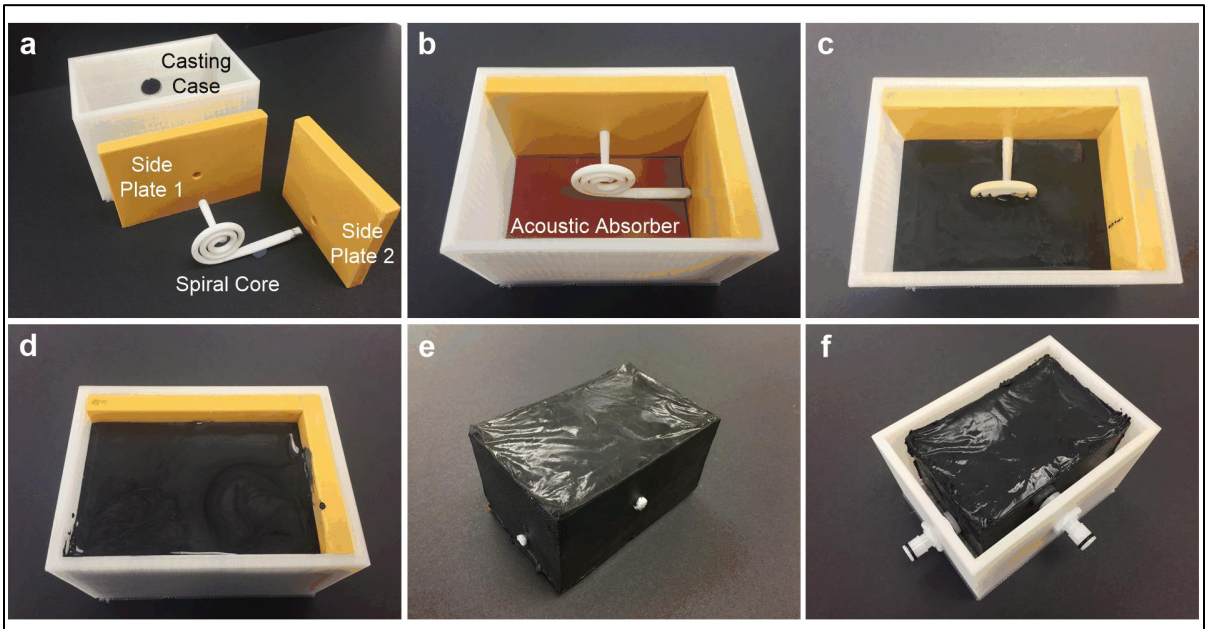

Figure 3.3. Stepwise illustration of the spiral flow phantom fabrication procedure. (a) Physical builds of the spiral core (white), phantom box (off-white), and side plates (yellow) were first generated using 3-D printing. (b) Spiral core was slotted into the side plates to form an L-shaped assembly, which was then inserted into the box cavity. Subsequently, PVA-based tissue mimicking mixture was poured into box cavity, which were photographed when it was (c) half-filled and (d) completely filled. (e) Following a freeze-thaw process, the spiral-core-containing tissue mimicking slab was taken out of the phantom box and was detached from the side plates. (f) After removing the spiral core, the completed phantom was remounted onto the phantom box with flow connectors installed.

After the 3-D printing process, the fabricated spiral vessel core was first polished with abrasive papers (400 grit size), and its surface was coated with a thin layer of petroleum to develop a smooth vessel core for use in lost-core casting. The core was then mounted onto the two side plates by inserting its inlet and outlet ends into the respective cylindrical slots on the side plates. In doing so, an L-shaped assembly was formed as the two side plates were perpendicularly angled to each other. The L-shaped assembly (with the spiral vessel core mounted in suspension) was then inserted into the void space of the phantom box at the respective sides that corresponded to the inlet and outlet (Figure 3.3(b)). An acoustic absorber sheet, in the form of silicone rubber (Norseal 9030; Saint-Gobain Performance Plastics, Chaineux, Belgium), was also placed at the inner bottom side of the box. Subsequently, tissue mimicking material was casted around the spiral vessel core by: 1) pouring a polyvinyl alcohol (PVA)-based mixture into the box cavity (Figures 3.3(c) and 3.3(d)); 2) subjecting the PVA-loaded phantom box to three 24-h freeze-thaw cycles. Note that, the PVA mixture was consisted of 10% PVA (341 584; Sigma-Aldrich, St. Louis, MO, USA), 3% graphite (282 863; Sigma-Aldrich), 0.3% potassium sorbate (85 520; Sigma-Aldrich), and 86.7% distilled water. As reported earlier (28), the acoustic speed and the attenuation coefficient of this tissue mimic were, respectively, 1535 m/s and 0.229 dB/(cm · MHz).

To remove the spiral vessel core that was embedded within the tissue mimic, first the slab was taken out of the phantom box, and then the two side plates were removed (Figure 3.3(e)). Next, the tissue mimicking slab was immersed within chloroform (372 978; Sigma-Aldrich) for 24 h to dissolve the PLA-based spiral vessel core and in turn vacate a luminal void of spiral shape. Also, quick-fit flow tube connectors (EW-06361-61; Cole-Parmer, Vernon Hills, IL, USA) were installed onto the two circular voids of the phantom box. Afterward, the coreless tissue mimicking slab was rinsed with distilled water, and it was reinserted into the phantom box by plugging the inlet and outlet ends into the respective flow connector on the box. A photograph of the completed phantom with the installed flow connectors is shown in Figure 3.3(f).

3.2.3 Connecting to Flow Pump

To complete the phantom construction process, flow tubing was appended to the external side of the two flow connectors on the phantom box. The tubing was then connected to a programmable gear pump whose implementation procedure was published in our earlier work (Ho et al., 2017). It should be emphasized that, during operation, flow entered the spiral lumen through the inlet at the outermost loop, transited through the three spiral loops, and exited through the perpendicular outlet at the spiral center. In this work, the pump was set to operate in the constant-flow mode with an inlet flow rate of 3 ml/s. The blood-mimicking fluid, whose properties were matched to those for human blood (4.1 mPa·s dynamic viscosity and 1037 kg/m3 density), was prepared based on a standardized formula (Ramnarine, Nassiri, Hoskins, & Lubbers, 1998) and a previously described laboratory procedure (Ho et al., 2017).

3.3 Experimental Methods

3.3.1 Computational Fluid Dynamics Simulations

To characterize the flow behavior within the spiral flow phantom, computational fluid dynamics (CFD) simulations were conducted on the CAD model using the SolidWorks Flow Simulation tool (Dassault Systems). For this task, we first encapsulated the spiral vessel lumen within a 70×45×35 mm^3 (length×width×height) simulation volume. Two-tiered meshing (fifth-level initial density followed by third-level refinement; defined in the CFD software) was then carried out on the volume to yield 109,000 simulation cells, of which 50,700 were fluid cells. Next, the inlet boundary condition was defined as a fully developed constant flow profile with 3 ml/s flow rate, while the outlet boundary condition was set to be a constant pressure outlet at atmospheric pressure (101,325 Pa). Also, the simulated fluid was set to match the properties of human blood.With these input parameters, the CFD solver derived the velocity profile and the flow trajectories within spiral vessel lumen using the Navier–

Stokes equation and the finite-volume method (Versteeg & Malalasekera, 2007). Convergence was achieved when the pressure difference between inlet and outlet became unchanged between computational iterations.

3.3.2 Clinical Ultrasound Scanning

As an initial application of the spiral flow phantom, CFI frames were acquired by using the clinical mode of a Sonix-Touch ultrasound scanner (Analogic Ultrasound, Peabody, MA, USA) and a 128-element linear array with 0.3048-mm pitch (L14-5; Analogic Ultrasound). 5 MHz, two-cycle ultrasound pulses were used for data acquisition, and the CFI field of view was aligned to the central plane of all three loops of the spiral lumen (96 CFI lines; ten firings per line; 50-mm imaging depth; and 5:1 beam interleaving). Also, data was acquired at two pulse repetition frequency (PRF) values (3.3 and 5.0 kHz) to obtain CFI frames with and without aliasing artifacts. With these two PRF values and the data acquisition parameters, the corresponding CFI frame rates were 10 and 7 fps. A wall filter cutoff of 25 Hz was applied, and persistence was set to three frames.

3.3.3 Vector Flow Imaging Experiments

As a further application demonstration of the spiral flow phantom, the flow pattern within the phantom was mapped using vector flow imaging. This work was performed using a research-purpose ultrasound system that consisted of the SonixTouch scanner's programmable transmit pulser and a pre-beamformed data acquisition system (Cheung et al., 2012). As described earlier (Yiu et al., 2014), plane wave excitation (5-MHz frequency and two-cycle pulse duration) was performed sequentially at 10-kHz PRF over three steering angles at −10°, 0°, and +10° (i.e., 3.3-kHz PRF for each angle), and pre-beamformed channel data were collected for each transmit event until the 16 GB on-board memory buffer was full (3-s duration for 50-mm imaging depth). The raw data were then streamed offline to a back-end computing platform, and receive beamforming was performed over three angles (−10°, 0°, and +10°) for each transmit event using a high-speed algorithm based on graphical processing unit technology (Yiu et al., 2011).

With the three-transmit, three-receive multi-angle configuration, a least-squares vector flow estimator (Yiu & Yu, 2016) was used to derive the axial and lateral velocity components at each pixel position. The parameters used for related signal processing operations, including clutter filtering (134th order finite impulse response filter with 166-Hz cutoff) and dealiasing via phase unwrapping, are the same as those reported earlier (Yiu et al., 2014). Note that, with the use of a slow-time sliding window strategy (window size: 128 and step size: 4), the downsampled frame rate was 833 fps. Dynamic rendering was subsequently applied to visualize the flow vector estimates in accordance with the vector

projectile imaging (VPI) framework (Yiu et al., 2014). B-mode image frames were also obtained via spatial compounding of the beamformed data frames from the nine transmit–receive angle pairs.

Secondary analysis of the acquired data was conducted by performing multi-gate Doppler spectrum analysis. In particular, we derived the Doppler spectral profile of different pixel positions along the spiral phantom's central horizontal axis at 25-mm depth. For this task, the slow-time ensemble of the unsteered angle pair (i.e., 0° transmit and 0° receive) was individually extracted for each pixel position along the central horizontal axis. After performing clutter filtering (same parameters as those used for vector flow estimation), fast Fourier transform was performed on each slow-time ensemble to obtain the corresponding Doppler spectrum for that pixel position, and it was converted into a velocity spectrum through the Doppler equation (for 0° beam-flow angle) (Evans et al., 2011). Phase unwrapping was also performed to extend the effective velocity spectral range (Lai, Torp, & Kristoffersen, 1997). For display, the entire set of velocity spectra along the central horizontal axis was stacked together, and they were collectively rendered as a grayscale map.

3.4 Results

3.4.1 Eccentric Flow Pattern Observed in Spiral Flow Phantom

From our CFD simulations, we found that the spiral flow phantom yielded cross-sectional flow profiles that followed an eccentric pattern with peak velocity deviating away from the center. This finding is illustrated in Figure 3.4(a) that shows the CFD-derived flow velocity magnitude over the entire spiral loop. As can be observed, at the inlet, flow velocity was fastest at the center of the vessel lumen. In contrast, as flow entered the spiral loop, the location where peak flow velocity appeared was skewed toward the outer wall of the loop. In other words, the spiral lumen geometry had exerted a centrifugal effect on the flow profile. This phenomenon is further illustrated in Figures 3.4(b) and 3.4(c) that depict the cross-sectional flow profile at different positions within the spiral loop. A key observation to be noted is that the peak flow velocity was always found within the right half of the cross section (i.e., in the outer wall half). Note that, the magnitude of the peak flow velocity had slightly decreased from the outer to the inner spiral loops. As shown in Figure 3.4(d), the CFD-derived peak flow velocity had dropped from 38.0 cm/s at the first segment position of the spiral vessel to 33.1 cm/s near the spiral center.

As an additional insight on the flow pattern within the spiral phantom, Figure 3.4(e) shows the velocity spectrum derived from multi-gate Doppler analysis at different pixel positions along the spiral phantom's central horizontal axis that corresponds to the horizontal line between positions 6 and 2 in Figure 3.4(a). This velocity spectrum plot shows the range of flow velocities observed in five spiral

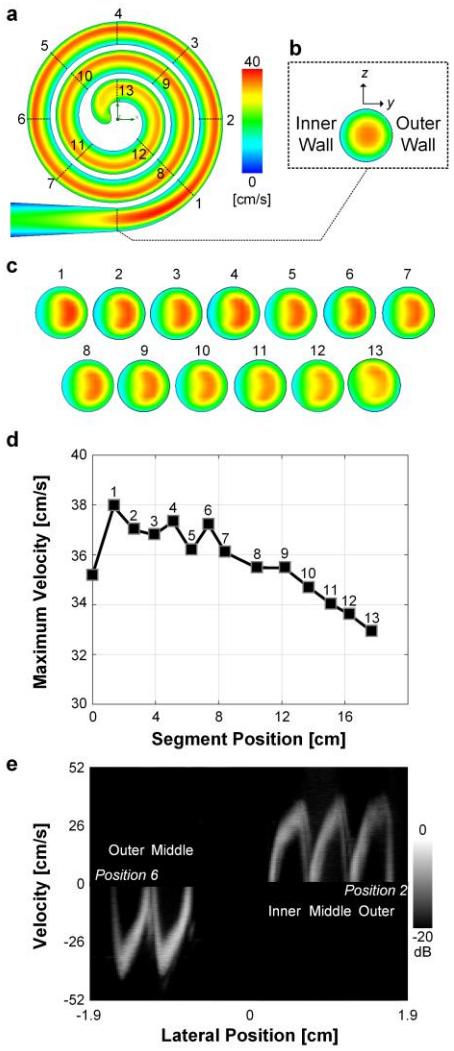

Figure 3.4. Flow velocity pattern within the spiral flow phantom. (a) CFD-derived velocity map along the central plane of the spiral vessel. (b) Cross-sectional velocity map at the inlet of the spiral vessel; left and right halves of the circular cross section, respectively, correspond to the inner and outer walls of the vessel. (c) CFD-derived cross-sectional velocity maps for 13 different segment positions within the spiral vessel (position as indicated in (a)]. (d) Plot of maximum cross-sectional flow velocity as a function of segment position, indicating decrease in maximum flow velocity toward the spiral center. (e) Velocity spectrum derived from multi-gate Doppler analysis for the central horizontal axis that cuts across from position 6 to position 2, covering five spiral lumen cross sections.

lumen cross sections encompassed by the horizontal axis: 1) to the left of spiral center, two cross sections (outer and middle) with downward flow; 2) to the right of spiral center, three cross sections (inner, middle, and outer) with upward flow. As can be observed, the velocity profile was eccentric in all of these five spiral lumen cross sections. Also, the detected maximum flow velocity magnitude was highest in the outermost spiral loop and was slightly decreased in the inner spiral loops. These results are synchronized with the CFD-derived findings.

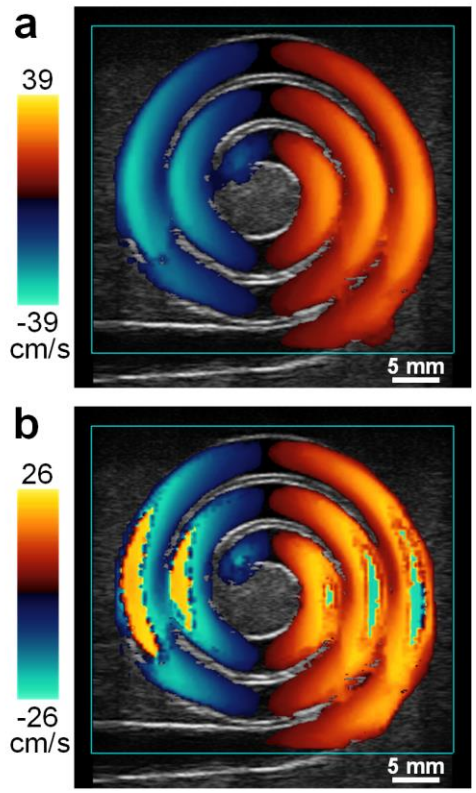

Figure 3.5. Spurious coloring artifacts in the CFI of the spiral flow phantom. CFI frames were obtained with two different PRF values (a) 5.0 and (b) 3.3 kHz. See Section III-B for other imaging parameters. The spiral vessel was rendered as a bicolored multi-loop. In (b), aliasing artifacts appeared when the flow direction was parallel to the depth axis.

3.4.2 Spiral Flow Phantom Reveals Spurious in CFI

Using the spiral flow phantom, we observed significant spurious coloring artifacts when performing CFI using the clinical mode of the SonixTouch scanner. For a case with steady flow (3 ml/s flow rate), Figure 3.5(a) shows a representative CFI frame obtained using a PRF of 5.0 kHz. In principle, flow should traverse through the three spiral loops with an eccentric cross-sectional profile, as illustrated in Figure 3.4. However, the corresponding CFI rendered the spiraling flow as a bicolored multi-loop, whereby flow toward the transducer was red-hued, while flow away from transducer was blue-hued. Also, the CFI color intensity varied depending on the revolution angle, with brightest hue and blackout observed when flow direction was, respectively, parallel to and perpendicular to the depth axis. More severe CFI coloring artifacts were observed when the PRF was lowered below the Doppler aliasing limit. Figure 3.5(b) shows a representative CFI frame obtained with a 3.3-kHz PRF for the same steady flow scenario. CFI aliasing artifacts in the form of sudden change in color hue (from red to blue, or vice versa) were observed when the flow direction was parallel to the depth axis. These artifacts serve well to illustrate the fundamental limitations of CFI technology in providing intuitive flow information.

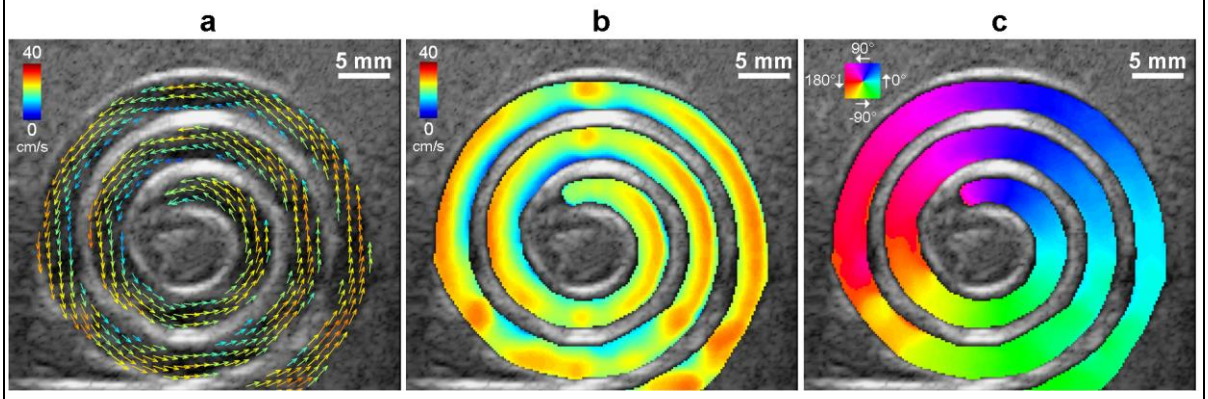

Figure 3.6. Vector flow imaging of the spiral flow phantom. (a) Representative vector flow image obtained using the procedure and parameters described in Section 3.3.3; vectors are shown at 0.2-mm spacing. Maps of estimated velocity (b) magnitude and (c) angle, generally showing consistency in flow vector estimation.

3.4.3 Consistent Rendering of Spiral Flow Pattern Obtained Using Vector Flow Imaging

In contrast to CFI, vector flow imaging was confirmed to yield a significantly more intuitive depiction of the flow field within the spiral phantom. This finding is evidenced by Figure 3.6(a) that shows, for the same steady flow scenario as that of Figure 3.4, a vector flow image frame (vectors shown at 0.2-mm pixel spacing; averaged over ten frames) that was obtained using the estimation framework described in Section 3.3.2. As can be observed, this vector flow image has by-and-large consistently depicted the flow speed and direction within the spiral lumen. As further analyses, Figure 3.6(b) and (c), respectively, show maps of the estimated velocity magnitude and angle (relative to the depth axis). Two observations of interest can be noted. First, Figure 3.6(b) has generally reconstructed the eccentric flow profile within the spiral lumen, whereby faster flow was found on the outer side of the spiral loop. Second, Figure 3.6(c) has correctly depicted the flow angle over the entire spiral loop.

As a quantitative insight into the vector flow estimation performance, Figures 3.7(a) and 3.7(b), respectively, plot the estimated lateral and axial velocities versus the corresponding CFD-derived values. One point worth noting is that at higher velocities, both the lateral and axial flow estimates showed an estimation bias. The greatest estimation bias was found at the maximum and minimum velocities (lateral flow: −12.9 and +12.8 cm/s bias, respectively, for maximum and minimum velocity; axial flow: −8.1 and +9.6 cm/s bias for these two velocities). The respective estimation bias for velocity vector magnitude is plotted in Figure 3.7(c) as a function of CFD flow angle. The average bias was found to range between −10 and 0 cm/s (i.e., underestimation was observed). Despite this glitch, the estimated flow angle was found to be highly correlated with the theoretical value for the entire angle range, as shown in Figure 3.7(d).

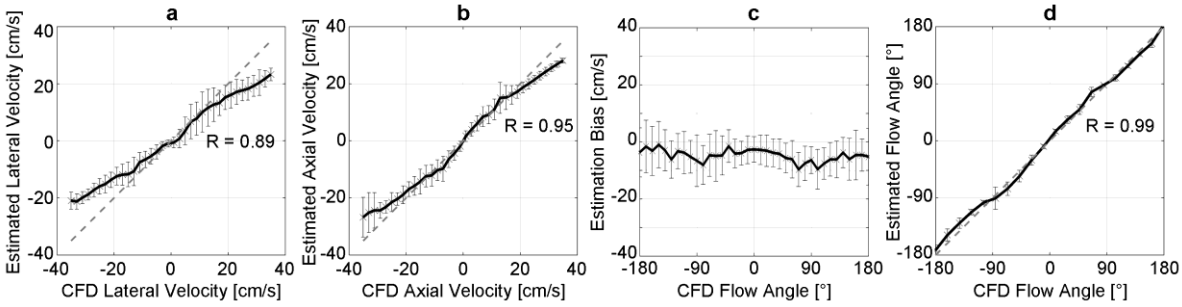

Figure 3.7. Accuracy analysis of flow vectors derived from the spiral flow phantom. Plots of estimated velocity versus CFD-derived velocity in (a) lateral and (b) axial directions, as extracted from the velocity values at different pixel positions within the spiral loop; error bars denote standard deviation over a minimum of 50 measurements. (c) Velocity vector magnitude estimation bias for the entire range of flow angles within the spiral lumen. (d) Estimated flow angle versus CFD-derived flow angle. Correlation coefficient (R) between the estimated and CFD-derived values are as indicated in (a), (b), and (d).

3.4.4 High-Frame-Rate VPI of Spiral Flow Pattern

The spiral flow phantom was found to be a useful tool in facilitating demonstration of high-frame-rate vector flow imaging, particularly the VPI framework that exemplifies dynamic flow visualization (Yiu et al., 2014). Movie 3.1 (right panel) shows a VPI cineloop of the steady flow pattern within the spiral flow phantom (833-fps imaging frame rate; 50 fps playback). This cineloop consistently depicted how flow traversed through the spiral loop from the inlet to the outlet at the spiral center (i.e., the expected flow trajectory). Such a visualization is distinctly more intuitive than displaying the flow vectors at fixed pixel positions (left panel of Movie 3.1), even though the latter is still more indicative of the spiral flow pattern than that rendered by clinical CFI as shown in Figure 3.5.

3.5 Discussion

3.5.1 Recap of Methodological Contributions

From a quality control standpoint, it is well recognized that diligent calibration of a new ultrasound-based flow estimation technique is necessary to hone the technique's readiness for clinical use. While computer simulations can be run as first-line tests to investigate the performance of flow estimation algorithms with respect to predefined flow profiles (Khoshniat et al., 2005; Steinman, Lui, Johnston, & Cobbold, 2004), it is equally important to design flow phantoms that can be used to test and refine the efficacy of a flow estimation algorithm's hardware implementation before applying it to *in vivo* studies (Hoskins, 2008). Here, we have devised a new spiral flow phantom design that is marked by a well-defined curvy vessel geometry based on the Archimedean spiral. This new phantom design framework is based on the integrative use of CAD drafting (Figures 3.1 and 3.2), 3-D printing, and lost-core casting

principles (Figure 3.3). When operating under steady flow conditions, flow traversal through the spiral loop naturally generated multi-directional flow that covered the entire angle range from 0° to 360°. Its corresponding cross-sectional flow pattern was in the form of an eccentric flow profile throughout the spiral loop (Figure 3.4), in line with earlier reports on the flow profile in curved vessels (Chang & Tarbell, 1988; Krams et al., 2005). Such flow characteristic is drastically distinguished from those observed in straight-tube phantoms (Wang et al., 2017; Zhou, Kenwright, et al., 2017). Also, its multi-directional flow behavior is more well defined than those from anthropomorphic flow phantoms (Chee et al., 2016; King et al., 2010; Lai et al., 2013; Poepping et al., 2002; Watts, 2007), thereby making it more effective in testing the efficacy of flow estimation algorithms under all possible beam-flow angles. It should be noted that the design protocol of the spiral phantom can be easily adapted to devise new imaging phantoms, such as a nozzle flow phantom for turbulent flow investigation. This involves CAD drafting of a flow nozzle and fabrication using 3-D printing, as will be detailed in Chapter 4. A similar protocol is also used to design the two-channel micro flow phantom (to be described in Chapter 5) for calibration of microvascular imaging.

3.5.2 Practical Value to Flow Imaging Experimentation

In this work, the spiral flow phantom has been initially used to examine the efficacy of CFI and vector flow imaging. Given the multi-directional nature of its flow pattern, our phantom effectively elicited various spurious coloring artifacts in CFI (Figure 3.5). The bicolored multi-loop (with angular variations in color intensity) observed in Figure 3.5(a) is seemingly an unintuitive rendering of the spiral flow pattern within the phantom. Such an unintuitive coloring is physically attributed to the beam-flow angle dependence of CFI: that is, CFI is only sensitive to axial flow as governed by the Doppler equation (Evans et al., 2011). The issue is aggravated by the presence of aliasing artifacts (Figure 3.5(b)).

Unlike CFI, vector flow imaging is potent in rendering the multi-directional flow pattern within the spiral vessel (Figure 3.6). In particular, our results have demonstrated that the least-squares multi-angle Doppler estimation framework (Yiu & Yu, 2016), when implemented using plane wave excitation, can produce flow vector estimates whose magnitude and angle are correlated with those derived using CFD (Figure 3.7). There were underestimation biases in the axial and lateral velocity estimates as well as the corresponding vector magnitude (below −10 cm/s on average for all beam-flow angles). As explained previously (Yiu & Yu, 2016), such an offset is typical of mean velocity estimation that was embedded within the least-squares multi-angle Doppler estimator. Note that these estimation biases did not significantly affect the flow visualization performance when the flow vector estimates were rendered dynamically by using the VPI algorithm (Yiu et al., 2014). Indeed, lucid visualization of flow traversal

through the spiral loop can be achieved (Movie 3.1). Such a visualization quality is essentially not achievable using CFI.

3.5.3 Limitation and Future Work

Since the primary focus of this paper is on reporting the engineering protocol for spiral flow phantom design, we have only conducted a proof-of-concept experimentation of our phantom at a single constant flow rate (3 ml/s). Our initial experimentation has nevertheless served well to develop foundational insight on the flow characteristics within a spiral vessel and to explore the feasibility of using a few different ultrasound flow estimation methods to accurately visualize such spiral flow behavior. In the future, different flow rates may be used in accordance with the specifications of the flow pump to realize a range of flow velocities. For our hardware, up to 30 ml/s flow rate can be readily achieved (Ho et al., 2017). It would be worthwhile to characterize the corresponding cross-sectional flow profile at different input flow rates, especially at high flow rates when the Reynolds number can be greater than the critical value of 2000 for turbulence to emerge (e.g., with a flow rate of 30 ml/s, the Reynolds number is calculated to be 2418 for our flow setup, according to textbook formula).

Another future development direction worth pursuing is to extend the operations of our spiral phantom to take into account pulsatile flow conditions. One possibility is to inject a flow pulse through the inlet into the spiral loop, and use high-frame-rate flow imaging to track the corresponding spatiotemporal flow dynamics within the spiral phantom. It would indeed be of practical interest to leverage this pulsatile flow experiment to comparatively assess the visualization quality of high-frame-rate CFI (Ekroll et al., 2013; Osmanski et al., 2012; Yiu & Yu, 2013) and high-frame-rate vector flow imaging (Jensen et al., 2016b). Such work would have significant clinical value if it is performed on commercial platforms that have already implemented these high-frame-rate flow mapping technologies (Goddi et al., 2017; Hansen et al., 2015; Hur et al., 2014; Tanaka et al., 2015). On a related note, it would be worthwhile to make use of a pulsatile spiral phantom to comparatively evaluate the robustness of different flow vector estimation formulations, such as multi-angle Doppler (Yiu & Yu, 2016), speckle tracking (van Cauwenberge et al., 2016), transverse oscillation and directional beamforming (Jensen et al., 2017). Likewise, our new phantom may be used to investigate the flow estimation impact of different clutter filters, including conventional filters (Bjaerum et al., 2002) and eigen-based adaptive filters (Yu & Lovstakken, 2010). This line of work will benefit the technical maturity of ultrasound flow imaging on the whole.

3.6 Conclusion

As new ultrasound flow estimation techniques are being developed, their performance needs to be systematically tested before applying them to human studies. The new spiral flow phantom presented in this paper is intended to model a vessel that is tortuous in nature. It can effectively allow researchers to characterize the accuracy of a flow estimation algorithm with respect to a well-defined multi-directional flow profile and, in turn, rectify algorithmic glitches at the signal processing level as well as calibrate performance at the hardware level. Overall, these engineering endeavors will help drive advances in vascular ultrasound technologies. They will correspondingly contribute to bolstering the clinical usefulness of ultrasound in vascular diagnostics.

Chapter 4
Mapping Disturbed Flow with High-Frame-Rate Doppler Bandwidth Imaging

4.1 Introduction

Risk stratification of carotid atherosclerotic stenosis is conventionally based on measurements of luminal narrowing (Hathout et al., 2005) and peak systolic velocity (Grant et al., 2003). However, atherosclerotic plaques with identical degree of stenosis could have substantial differences in their associated risk (Nighoghossian et al., 2005; Rothwell et al., 2000), thereby prompting for diagnostic considerations beyond the immediate stenotic site (von Reutern et al., 2012). From a hemodynamics standpoint, the presence of stenosis perturbs blood flow, and in turn it may lead to flow instability (Lee et al., 2008). This phenomenon forms the underlying basis for physical examinations of carotid atherosclerosis via the detection of carotid bruit using a stethoscope (Howard et al., 1989). Unstable blood flow (i.e., nonlaminar flow, including turbulence) has also been associated with atherogenesis and plaque progression (Chiu & Chien, 2011), as well as an increased risk for thrombosis and embolization (Bluestein, Niu, Schoephoerster, & Dewanjee, 1997; Wootton & Ku, 1999). Thus, monitoring blood flow instability could offer new clinical insights to understand the mechanism of atherosclerotic plaque development (Harry et al., 2008; Wang et al., 2016).

From a fluid dynamic standpoint, arterial flow is considered to be unstable when a small flow disturbance grows in strength as it traverses downstream. Correspondingly, an *unstable flow region* refers to a zone where the net strength of disturbances is sufficiently large to break the laminar layers of flow. This unstable flow is characterized by the fluctuations of flow velocities in space and time (Kajishima & Taira, 2017). Medical imaging modalities have been leveraged to derive the flow turbulence index (Dyverfeldt et al., 2008; Kefayati, Holdsworth, & Poepping, 2014; Wong et al., 2009), a parameter describing the variance in flow velocities at specific cardiac instances between multiple consecutive cardiac cycles. For example, phase-contrast magnetic resonance imaging has demonstrated feasibility in mapping turbulent flow regions from measurements of intra-voxel mean velocity variations (Dyverfeldt et al., 2008; Ha et al., 2016). Similarly, Doppler ultrasound was used to calculate the turbulence index by measuring the standard deviation of flow velocities over successive cardiac

cycles (Poepping et al., 2010; Thorne et al., 2010). However, fluctuations in heart rate and stroke volume (Holdsworth, Norley, Frayne, Steinman, & Rutt, 1999) pose a significant drawback for the turbulence index approach due to its susceptibility to inter-cardiac-cycle variations.

Instead of relying on measurements over multiple cardiac cycles, it is possible to detect unstable flow by identifying high-frequency velocity fluctuations at specific instants in a cardiac cycle (Sabbah, Blick, & Stein, 1977). Instantaneous blood velocity fluctuation can be measured using an intravascular catheter (Sallam et al., 1983), but this approach is highly invasive and is thus not ideal. As an alternative, Doppler ultrasound has been used to noninvasively detect flow instability in the form of Doppler spectral broadening (as an effect of flow velocity fluctuations) based on the characterization of Doppler spectral bandwidth (Garbini et al., 1982a, 1982b; Bascom et al., 1993). This approach has demonstrated initial success in assessing plaque risk (Belcaro et al., 2001). Yet, Doppler ultrasound, which only operates on a single range gate (Rubens, Bhatt, Nedelka, & Cullinan, 2006), is far from ideal in mapping flow instability because it lacks the ability to track fluctuations in flow velocities in multiple spatial positions.

Perhaps one workaround of Doppler ultrasound's single-gate data acquisition paradigm is to perform Doppler-based color flow imaging (CFI) that can provide color-coded rendering of mean axial velocity estimates or velocity variance estimates (Evans, 2010). With CFI, which is essentially a full-view version of single-gate Doppler ultrasound, unstable flow regions may be visually identified as puff-like color patches (Tamura, Cobbold, & Johnston, 1991) or mosaic color patterns (Hoit, Jones, Eidbo, Elias, & Sahn, 1989; Sahn, 1988) in the CFI frame. Nevertheless, there are multiple caveats in using CFI for flow instability analysis. First, although CFI can yield real-time frame rates within the video display range (~20 fps), its time resolution is inadequate to follow the fast-changing nature of unstable flow (Hoskins, 2010). Second, its data acquisition conventionally involves multiple firings over each of the scanlines in the image view (Evans, 2010), so each CFI frame is not able to capture a coherent spatial snapshot of unstable flow. Third, CFI's derivation of flow estimate at a pixel position is inherently prone to significant fluctuations and inaccuracies because each slow-time ensemble used for Doppler processing is limited in size (8–16 samples) as constrained by real-time requirements. Given all these issues, it is well possible that puff-like or mosaic coloring patterns in a CFI frame are simply spurious artifacts rather than true indications of unstable flow, especially if CFI parameters are not tuned properly.

In this work, we present a new ultrasound framework called Doppler ultrasound bandwidth imaging (DUBI) that can map flow instability at all pixel positions within the image view based on local Doppler bandwidth analysis. In formulating DUBI, we hypothesized that broad-field insonification methods,

which are used for high-frame-rate ultrasound imaging (Tanter & Fink, 2014), can be leveraged to: (a) facilitate simultaneous mapping of flow instability at all pixel positions, and (b) acquire slow-time data with larger ensemble sizes than that obtainable in CFI and without lengthening the observation period, as required for consistent Doppler bandwidth analysis. We further hypothesized that to achieve consistent characterization of Doppler bandwidth at each pixel position, model-based signal processing tools such as autoregressive (AR) modeling (Burg, 1972) may be applied as they are known to yield consistent Doppler spectra estimates. Note that the merit of AR modeling in conventional Doppler ultrasound has previously been established (Cloutier, Allard, & Durand, 1996; Cloutier, Chen, & Durand, 2001; Guo et al., 1993). This technique can effectively reduce random fluctuations in the Doppler spectra and is less sensitive to intrinsic spectral broadening caused by the use of small Doppler window sizes (Cloutier et al., 1996; Mo & Cobbold, 1986).

This paper shall present the theoretical (Section 4.2.1) and implementation (Section 4.2.2) details of DUBI. Also, based on a nozzle-flow model (Section 4.2.3), a receiver operating characteristic (ROC) analysis of DUBI's efficacy will be presented (Section 4.3.1) with reference to benchmark images derived from contrast-enhanced ultrasound (CEUS) (ten Kate, van den Oord, et al., 2013). Further characterization of DUBI's performance will be presented in terms of its ability to identify flow instability in anthropomorphic carotid bifurcation phantoms with different degrees of stenosis (Section 4.3.2).

4.2 Materials and Methods

4.2.1 Theoretical Principles of DUBI

4.2.1.1 Background description

Doppler ultrasound bandwidth imaging is founded upon the general principle that unstable flow can be characterized by the presence of a wide range of velocities (due to velocity fluctuation) at a given pixel position (or sample volume) (Antiga & Steinman, 2009). Such extended range of velocities represents an extrinsic factor for Doppler spectral broadening (Bascom et al., 1993; Garbini et al., 1982a, 1982b) and would result in a wider bandwidth. To track changes in Doppler bandwidths over all pixel positions, we have exploited the following principles:

1. Broad-view insonation as enabled by unfocused plane wave transmission strategy (Tanter & Fink, 2014);
2. Coherent broad-view image formation by parallel beamforming of channel-domain pulse-echo data received from each unfocused transmission (Cheung et al., 2012);

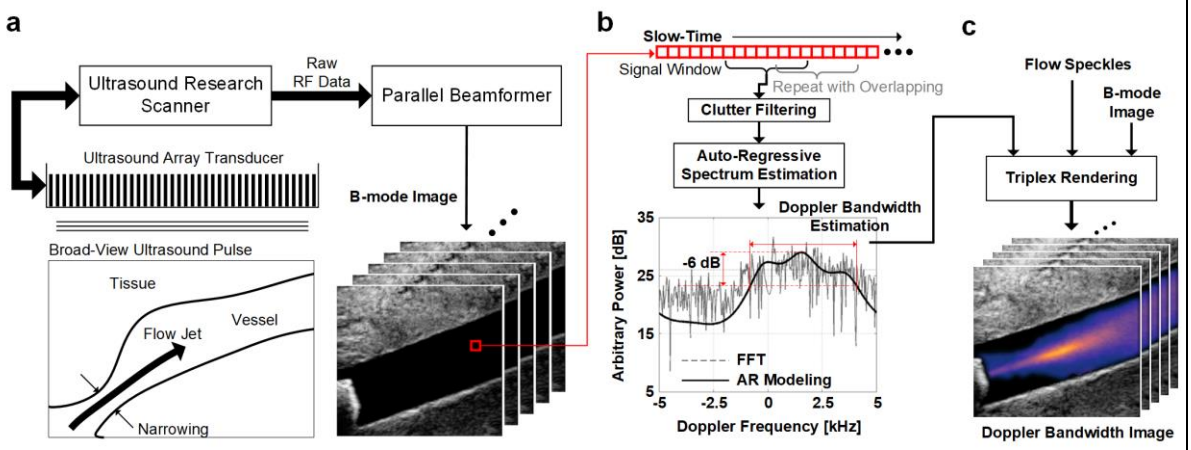

Figure 4.1. Conceptual illustration of DUBI. (a) Plane wave data acquisition at a region of interest using a research-purpose ultrasound scanner that generates highframe- rate ultrasound images; (b) Overview of the Doppler bandwidth estimator for a slow-time ensemble extracted from the B-mode images (indicated by the red box in (a)), with the estimated Doppler power spectrum (dashed line) and the AR estimated spectrum (solid line) shown for illustration; (c) Doppler bandwidth images (DUBI frames) generated by overlaying color-coded Doppler bandwidth estimates on top of flow speckles and the B-mode image.

3. Simultaneous slow-time sampling for all pixels within the image view (Bercoff et al., 2011; Hasegawa & Kanai, 2008);

4. AR modeling to derive instantaneous Doppler bandwidth at each pixel position.

In the following, further details will be presented on how each principle was incorporated into DUBI.

Note that, aside from velocity fluctuations due to unstable flow, two other factors may lead to extrinsic Doppler spectral broadening, including: (a) the existence of a spatial flow velocity gradient within the sample volume (Garbini et al., 1982a, 1982b); (b) temporal variations in flow velocity (i.e., acceleration or deceleration) (Cloutier et al., 1996). DUBI has sought to reduce the impact of these two alternative sources of extrinsic spectral broadening by limiting the effective axial range, lateral width, and observation period (to be discussed further in Section 4.2.2). Doppler spectral broadening may also arise intrinsically (sometimes referred to as Doppler ambiguity(Garbini et al., 1982a)) due to the finite transit time of blood scatterers (Yu, Steinman, & Cobbold, 2006) and, to a lesser extent, flow instability (Garbini et al., 1982a). DUBI was developed on the assumption that transit-time broadening was not as significant as extrinsic Doppler spectral broadening due to unstable flow. The intrinsic spectral broadening effects of flow instability were assumed to be insignificant too since it was confirmed to be even less prominent than transit-time broadening (Garbini et al., 1982b).

4.2.1.2 Coherent slow-time sampling of blood flow using broad-view ultrasound imaging

As illustrated in Figure 4.1(a), a plane wave excitation scheme was used to acquire slow-time signals simultaneously over the entire image view. In line with our previously published work (Yiu et al., 2014; Yiu & Yu, 2013), for each acquisition, an unfocused pulse was first transmitted through the array transducer to insonate the entire image view. On reception, raw radiofrequency (RF) data were acquired from each array channel and were beamformed in parallel to generate a full-view image. This pulsing sequence was repeated to capture temporal information over different phases of a cardiac cycle. In turn, a 3-D data matrix (Figure 4.1(a) lower right corner) was formed by stacking the generated image frames. Clutter filtering was then applied to the data matrix along the slow-time axis to suppress tissue echoes for every pixel (see Figure 4.1(b)). After that, Doppler bandwidth was estimated from each filtered blood flow signal ensemble as described in the next subsection.

4.2.1.3 Doppler bandwidth estimation through autoregressive modeling of slow-time signal

For a given pixel position, its Doppler bandwidth over a short period was estimated by first deriving an AR model of the slow-time ensemble and then estimating the signal model's spectral power. In the DUBI framework, the Doppler bandwidth was determined as the full-width at half maximum (FWHM) of the power spectrum. This process was repeated for every image pixel to generate a DUBI frame as a depiction of flow instability over the image view. To track the evolution of Doppler bandwidth over time, the entire estimation procedure was repeated at subsequent time points (*M* slow-time samples apart) to generate a time series of DUBI frames over the image view, as illustrated in Figure 4.1(b).

Derivation of AR model parameters: In the DUBI framework, the nth sample in a slow-time ensemble with *N* samples was modeled by the following equation for a P^{th}-order complex AR model representation (Cloutier et al., 1996; Guo et al., 1993):

$$x[n] = -\sum_{k=1}^{p} a_{p,k}\, x[n-k] + e[n] \tag{4.1}$$

where $a_{P,k}$ is the k^{th} complex AR parameter of the model, and $e[n]$ is the n^{th} sample in the complex modeling error. The set of AR parameters $\{a_{P,k}\}$ was iteratively estimated using Burg's method (Burg, 1972; Ubeyli & Guler, 2004) that yields better spectral estimation reliability than Yule-Walker method (de Hoon, van der Hagen, Schoonewelle, & van Dam, 1996). Burg's method works by iteratively minimizing the mean of forward and backward prediction errors.

Doppler bandwidth estimation approach: With the AR parameters, the modeled power spectrum of the slow-time signal was next computed. For this task, Doppler power spectrum $S_{\text{AR}}[f]$ for the ensemble

$x[n]$ was constructed from the AR model through parametric spectral fitting as defined by the following equation:

$$S_{AR}[f] = \frac{\sigma_p^2 \Delta t}{\left|1 + \sum_{k=1}^{p} a_{pk} e^{-j2\pi f k \Delta t}\right|^2} \tag{4.2}$$

where f is the bin frequency, Δt is the pulse repetition interval and σ_p^2 is the average of mean powers of forward and backward prediction errors. After normalizing $S_{AR}[f]$ to its maximum power, the Doppler bandwidth of the slow-time ensemble was determined as the FWHM of $S_{AR}[f]$, as illustrated in the spectrum shown in Figure 4.1(b).

Advantages of AR-based Doppler bandwidth estimation: Through the use of AR modeling, DUBI's Doppler bandwidth estimation process became a task of finding the FWHM over a smoothened Doppler power spectrum. In turn, it was not susceptible to random spectral spikes that might arise in Doppler power spectra derived from the classical periodogram approach (see the dotted line of the Doppler spectrum in Figure 4.1(b)) as discussed by Mo & Cobbold (1986), thereby improving the consistency of Doppler bandwidth estimates. Such improvement in estimation performance has been confirmed by past investigations that used AR modeling in Doppler signal analysis (Cloutier et al., 2001). Another advantage of deriving the Doppler power spectrum using an AR modeling approach was that the spectrum could be reconstructed with a finer spectral resolution and not be bounded by the number of samples in the slow-time signal. In doing so, the resulting Doppler bandwidth estimates were more accurate as they were less prone to discretization noise.

4.2.1.4 DUBI as a triplex display mode

With the derived Doppler bandwidth estimates at every pixel position over different time instants, DUBI frames were formed as a new triplex display scheme to facilitate visualization of flow instability in an image view over time. As shown in Figure 1(c), DUBI would synchronously display: (a) the Doppler bandwidth map annotating the flow instability of each pixel location; (b) flow speckle pattern revealing the flow trajectory; (c) B-mode image showing the anatomical structure. Note that DUBI's flow speckle co-visualization was adopted from our group's previous work on color-encoded speckle imaging, in which flow speckle values were derived at different pixel positions by calculating the power of the corresponding slow-time ensemble after clutter filtering (Yiu & Yu, 2013). To form DUBI's triplex display, the flow speckle map was first overlaid on top of the B-mode image at flow regions and was displayed as the base layer. Then, the Doppler bandwidth estimates were mapped to a thermal hue with brighter colors corresponding to higher Doppler bandwidths. This color map was subsequently

overlaid using alpha compositing principles. For non-flow region, its transparency was set to 100% to reveal the anatomical structure. For flow regions, the transparency was set to 70% to reveal the flow speckle pattern and the color-coded Doppler bandwidth estimates. This rendering strategy was repeated over different time points, and the image frames were stacked together to form a cineloop.

4.2.2 Implementation Methods of DUBI

4.2.2.1 Imaging hardware and data acquisition

DUBI was implemented on a programmable research platform that was built upon our group's prior work in ultrasound flow imaging innovations. (Yiu et al., 2014; Yiu & Yu, 2013). The platform consisted of a 128-channel programmable transmit frontend (SonixTouch; Analogic Ultrasound, Peabody, MA, USA), a pre-beamformed DAQ tool with 40 MHz sampling rate and 12-bit resolution (Cheung et al., 2012), and a high-speed processing platform based on graphical processing unit (GPU) technology (GTX 1080; NVidia Corporation, Santa Clara, CA, USA) for beamforming and signal processing. Our research platform was programmed to perform high-frame-rate data acquisition as required. Broad-view acquisition at 10 kHz was achieved with unsteered plane wave excitation (0° transmission; 5 MHz center frequency, 5-cycle pulse) using an L14-5 linear array (0.3048 mm pitch; Analogic Ultrasound). Accordingly, raw data frames were acquired at a rate of 10,000 fps. Also, the transmit pulse shape yielded an effective axial range of 0.77 mm according to established formulas (Jensen, 2007). In each acquisition, the raw channel-domain data were stored on the DAQ tool until the internal 16 GB memory buffer was filled (3 s duration at 5 cm imaging depth). The data were then streamed offline to the GPU platform for processing.

4.2.2.2 Plane wave image formation

For each frame of the acquired dataset, parallel beamforming was performed on the GPU computing platform using a codec programmed in Matlab (R2016a; Mathworks Inc., Natick, MA, USA) in which the GPU-accelerated parallel beamforming library (Yiu et al., 2011) was invoked. The codec first applied a 3–7 MHz bandpass filter to the received RF data on a per-channel basis to suppress out-of-band white noise. The filter was implemented as a finite-impulse-response (FIR) filter in Matlab, with minimum filter order (30 taps) formulated using the Parks-McClellan equiripple design algorithm (McClellan & Parks, 2005). The analytic form of the acquired data was subsequently obtained using a FIR-based Hilbert transformer (50th order) as described earlier (Yiu et al., 2011). With the analytic RF data, image frames (with 0.2 mm pixel spacing) were finally parallel beamformed using our GPU-based delay-and-sum algorithm (64 array channels were used with Hanning apodization). This three-stage process was repeated for the data of different slow-time sampling instants, thereby generating a stack

of image frames over slow-time for Doppler signal processing and bandwidth estimation. Note that, for our 64-channel receive aperture configuration, the effective lateral width was estimated to range between 0.31 and 0.77 mm for a 2–5 cm imaging depth range, as determined based on well-known formulas (Jensen, 2007). Also, with its apodization profile, our receive beamformer's maximum sidelobe magnitude (occurred at 2 cm depth) was found to be 27.6 dB lower than that for the main lobe, according to in-house point target simulations.

4.2.2.3 Signal processing for Doppler bandwidth estimation

Doppler bandwidth estimation was performed at various slow-time instants on a per pixel basis. First, a Doppler clutter filter was applied to suppress tissue echoes; this filter was implemented as a FIR high-pass filter with 0.05 normalized cutoff frequency (i.e., 250 Hz for 10 kHz slow-time sampling rate), and its filter order was optimized to be 135 taps using the equiripple filter design algorithm. For flow regions, Doppler bandwidth estimation was performed over each slowtime ensemble with N = 100 samples, equivalent to windows of 10 ms observation period. This relatively short duration was chosen to limit spectral broadening induced by rapid acceleration (and deceleration) of blood flow. The corresponding AR-based Doppler spectrum was subsequently derived as described in Section 4.2.2. For our implementation, an 8^{th}-order AR model was chosen as its performance has been shown to be similar to higher order models (up to 16^{th} order) in earlier work (Cloutier et al., 2001). Also, the AR-modeled power spectrum was formed with a 10 Hz spectral resolution (i.e., 0.001 normalized frequency relative to slow-time sampling rate) to avoid spectral discretization noise.

To accelerate the derivation of each DUBI frame, Doppler bandwidth estimation for multiple pixels was executed concurrently by devising a GPU-based parallel computing kernel for AR modeling. This GPU kernel was implemented using the C++ programming language and the compute unified device architecture application programming interface (ver. 7.5; NVidia Corporation). Its formulation, as explained in the next sub-subsection, was based on a public-domain computing algorithm for Burg's method (Vos, 2013). After completing the Doppler bandwidth estimation process for each DUBI frame, it was repeated at other slow-time sampling instants to generate a time series of Doppler bandwidth maps. In particular, a repetition was performed after shifting the observation window by 25 samples along slow-time (i.e., M = 25; with 75% overlap for N = 100). The effective frame rate of the Doppler bandwidth maps was 400 fps (10,000 fps raw data frame rate divided by 25). The resultant Doppler bandwidth maps were finally rendered as described in Section 4.2.1.4.

4.2.2.4 GPU-Based Implementation of Burg's Method

For our GPU computing kernel for Doppler bandwidth estimation, a thread block was allocated to handle the estimation of Doppler bandwidth for the slow-time ensemble of one pixel in the DUBI frame. Note that the corresponding slow-time ensemble $x[n]$ was first transferred to the shared memory of the GPU for fast data access. The thread block, containing N threads (i.e., same as the slow-time ensemble size), then proceeded to derive the set of P^{th}-order AR parameter values for that slow-time ensemble by executing a fast implementation of Burg's method (Vos 2013) that involved P iterations from $p = 1$ to $p = P$. Within each iteration, two computational steps were carried out. First, the compute threads were tasked to calculate the forward and backward prediction error ensembles, respectively denoted as e_p^f and e_p^b. Specifically, for the p^{th} iteration, the n^{th} thread was tasked to compute the n^{th} sample in the following error ensemble (each with N samples):

$$e_p^f[n] = x[n] + \sum_{k=1}^{p} a_{p,k} x[n-k] \tag{4.3}$$

$$e_p^b[n] = x[n] + \sum_{k=1}^{p} a_{p,k} x[n-p+k] \tag{4.4}$$

Note that the mean of (4.3) and (4.4) corresponded to the error term $e[n]$ in the AR model stated in (4.1) for the p^{th} iteration.

In the second computational step of the same iteration, a sub group of threads were tasked to compute the intermediate AR parameters $a_{p,k}$. It achieved so by updating the intermediate AR parameters using the following equations:

$$a_{p,i} = a_{p-1,i} + \varphi_p a_{p-1,p-i}^* \tag{4.5}$$

where $i = 1, 2, \ldots, p-1$, $a_{0,0} = 1$, * denotes complex conjugate, and

$$a_{p,p} = \varphi_p \tag{4.6}$$

$$\varphi_p = \frac{-2\sum_{n=p}^{N-1} e_{p-1}^f[n] e_{p-1}^{b*}[n-1]}{\sum_{n=p}^{N-1} \left(\left| e_{p-1}^f[n-1] \right|^2 + \left| e_{p-1}^b[n-1] \right|^2 \right)} \tag{4.7}$$

The set of AR model coefficients was finalized after repeating the above computational steps for P iterations.

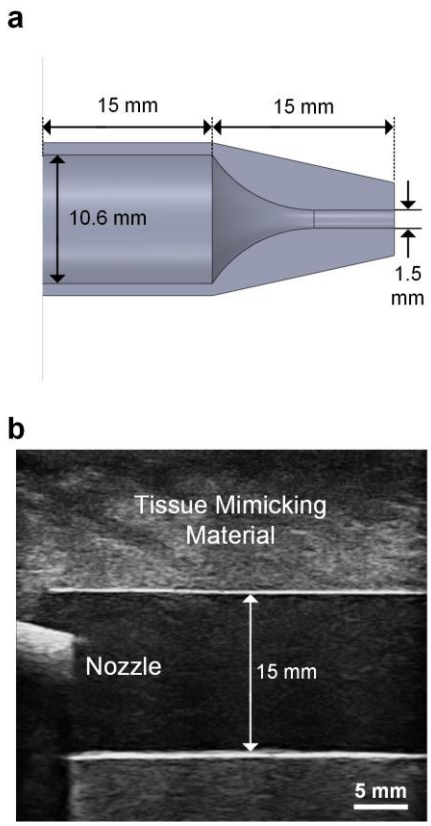

Figure 4.2. Overview of nozzle-flow phantom. (a) Cross-sectional view of the discharge nozzle showing the narrowing flow channel; (b) B-mode image of the discharge nozzle inserted into a 15 mm diameter wall-less PVA flow phantom (the interior of the discharge nozzle cannot be visualized due to acoustic shadowing of the fabrication material).

4.2.3 Experimental Testing Methods

4.2.3.1 Nozzle-based unstable flow model

To evaluate the performance of DUBI in identifying unstable flow zones, a nozzle-flow setup was devised to generate flow conditions ranging from laminar to turbulent flow. The flow conditions were characterized by their Reynolds number Re, defined as $Re = \underline{u}D/v$, where u is the average flow velocity, D is the nozzle diameter and v is the fluid kinematic viscosity. Since the average velocity term u is known to be equal to flow rate Q divided by cross-sectional area A (i.e., $u = Q/A$), the Reynolds number could be readily rewritten as $Re = 4Q/\pi Dv$. Based on this relation, we realized different values of Re by changing the flow rate. In turn, a series of flow conditions with progressing degree of flow disturbance was generated by increasing the flow rate. For each of these flow conditions, the stable and unstable flow regions were identified with the aid of CEUS (to be discussed in Section 4.2.3.3).

Table 4.1

FLOW RATE AND ROI SIZE FOR EACH FLOW CONDITION

Flow conditions in Reynolds number *Re*	Flow rate (ml/s)	ROI length (mm)	
		Stable	Unstable
375	1.8	34.1	–
750	3.5	18.2	8.4
1125	5.2	6.2	19.2

In terms of the nozzle design, it was shaped as a curved funnel to progressively narrow the flow channel's diameter from 10.6 to 1.5 mm over a 15 mm passage (see Figure 4.2(a)) which gradually increased the flow velocity (Hussain et al., 1976). The model's base was elongated by 15 mm so that a flow connector (EW-06361-61; Cole-Parmer, Vernon Hills, IL, USA) could be securely affixed to the base end. The nozzle was then inserted into a phantom made of poly-vinyl alcohol (PVA) (fabrication details discussed in Section 4.2.3.2) for flow to be discharged into a 15 mm diameter straight tube flow channel. The phantom provided an acoustic window to image the discharged flow from the nozzle. Note that this nozzle-flow geometry serves as an idealized model of stenosis (with 90% reduction in diameter in this case).

4.2.3.2 Fabrication of nozzle-flow model and flow circuit setup

3-D printing was leveraged to physically construct the nozzle. First, its physical dimensions were drafted on computer-aided design (CAD) software (SolidWorks; Dassault Systems, Waltham, MA, USA). To compile 3-D printing instructions, the CAD model (saved in STL stereolithographic file format) was imported into a slicer software (KISSlicer; ver 1.5). The instructions were then downloaded to a fused deposition modeling (FDM) system (Model DX; CreatBot 3D Printer, ZhengZhou, China) with a nozzle size of 0.25 mm to create the physical models. Layer and skin thicknesses of 0.1 and 0.5 mm were used, respectively.

The flow phantom was fabricated based on investment casting principles according to the protocol reported in our previous work (Ho et al., 2017). In this study, a PVA-based wall-less flow phantom with a 15 mm diameter flow channel across a tissue mimicking slab was fabricated. The flow channel was formed by first embedding a straight rod in PVA solution and then removing the rod after the solution has congealed. The straight rod was 15 mm in diameter with a length of 280 mm, and it functioned as the negative replica of the flow channel. For the phantom to grip onto the inlet nozzle and outlet flow connector, 30 mm on both ends of the rod were narrowed to 9 mm diameter (effective

length of the flow channel became 220 mm). Similar to the nozzle, the inner core was drafted on SolidWorks and was physically constructed using the FDM system with the same settings. Next, the rod was gently polished using an abrasive paper (400 grit size) and was suspended in the phantom case ($80 \times 295 \times 70$ mm^3, w × l × h) by mounting it onto two side plates. Tissue mimicking material was casted around the straight rod by: (a) pouring PVA solution into the phantom case, (b) administering three freeze–thaw cycles (freeze in −20°C for 24 h followed by thawing at 4°C for 24 h). Note that the PVA mixture consisted of 10% PVA (341584; Sigma-Aldrich, St Louis, MO, USA), 3% graphite (282863; Sigma- Aldrich), 0.3% potassium sorbate (85520; Sigma-Aldrich), and 86.7% distilled water. The acoustic attenuation and speed of this tissue mimicking material were respectively 0.229 dB/(cm·MHz) and 1535 m/s as reported earlier (Ho et al., 2017). Upon completing the thermal cycling process, the flow channel was instated by simply sliding the straight rod out from one end of the phantom.

After the flow phantom was fabricated, the nozzle was affixed into the inlet flow connector. The setup was then connected to a programmable flow pump (details described elsewhere (Vos, 2013)) that fed blood mimicking fluid at constant flow rates according to the parameters listed in Table 4.1 to generate a range of flow conditions as discussed earlier. Note that the blood mimicking fluid was fabricated using an Orgasol-based standardized formula (Ramnarine et al., 1998) and a laboratory procedure that we have described previously (Ho et al., 2017). Its dynamic viscosity (4.1 mPa·s) and density (1037 kg/m^3) were matched to that for human blood. Figure 4.2(b) shows a B-mode image of the inlet segment of the assembled flow phantom captured using a clinical scanner (SonixTouch; Analogic Ultrasound).

4.2.3.3 Identification of unstable flow region with CEUS

To facilitate the identification of regions with the presence of unstable flow, microbubble contrast agents were administered to trace its flow trajectories (Zhang et al., 2011). The rationale behind was that laminar flow occurs when fluid flows in parallel layers with no disruption between the layers. As such, microbubbles in stable regions would move in a straight path. On the contrary, unstable flow would correspond to cases where trajectories of the microbubbles were observed to have crossed each other's path. In accordance with this notion, a bolus of microbubble contrast agents (USphere Prime; Trust BioSonics, Hsinchu, Taiwan) were slowly injected manually to the inlet of the flow phantom for CEUS imaging.

Plane wave data acquisitions were repeated for all flow rates using the same data acquisition scheme described in Section 4.2.2.1, but with a 5 MHz, 2-cycle pulse at 50% of the original transmit power

Table 4.2

FLOW RATE AND ROI SIZE FOR EACH FLOW CONDITION

Flow conditions in Reynolds number *Re*	Persistence *K* (Frames)	Overlapping (Frames)	Effective frame rate (fps)
375	240	224	625
750	120	112	1250
1125	80	74	1667

instead to excite the microbubbles in the stable cavitation regime. High-frame-rate CEUS images were then generated through the same image formation method described in Section 4.2.2.2. To highlight flow trajectories, high-persistence B-mode images were rendered by averaging the beamformed RF signal magnitude over multiple frames before log compression. This allowed the hyperechogenic microbubbles to create streaks along their trajectory, representing the flow path lines. This process was repeated every *K* frames with overlapping to generate a cineloop of flow path lines for analysis.

The image persistence and overlapping (i.e., effective frame rate) were adjusted according to the flow rate to normalize the microbubbles' retention time (in terms of frame numbers) and in turn generate a consistent trace. Table 4.2 summarizes the CEUS-rendering parameters for three representative flow conditions. For each flow condition, the flow trace of microbubbles were carefully examined frame by frame to identify crossing trajectories of microbubbles that were proximally closest to the nozzle. This crossing point was identified as the intermediate boundary where flow transitioned from laminar to turbulent; regions before and after the intermediate boundary were categorized as stable and unstable flow regions respectively. Regions of interest (ROIs) were then selected manually using a Matlab built-in function; the height of the ROI was set to 1.5 mm to match the nozzle diameter. The length of ROIs varied depending on the position of the intermediate boundary; an extra 2.5 mm margin was reserved for both stable and unstable zones from the intermediate boundary as a conservative stance in avoiding ambiguity when selecting ROIs for performance analysis. This process was repeated for all flow conditions and the ROI sizes of each zone for the different flow rates are summarized in the two rightmost columns of Table 4.1.

4.2.3.4 ROC analysis of Doppler bandwidth measurements

To assess DUBI's sensitivity and specificity in determining flow instability, an ROC analysis was conducted. The procedure involved the following key steps. First, the measured Doppler bandwidth estimates within the ROIs for all image frames were classified as either belonging to the stable flow (negative) or unstable flow (positive) groups based on the CEUS reference data. Next, a bandwidth

threshold was set to categorize the measured bandwidths to their predicted conditions (stable or unstable); Doppler bandwidth above the threshold was categorized as positive (i.e., unstable) and vice versa. True negative (TN) and false positive (FP) were computed from the stable group, while true positive (TP) and false negative (FN) were counted from the unstable group. This process was repeated at different bandwidth thresholds ranging from 0.1 to 10 kHz with 0.1 kHz increment, and each corresponding set of TN, FN, TP, and FP values was computed. Using these data, the sensitivity (TP/(TP+FN)) and specificity (TN/(TN+FP)) of the test were derived to plot the ROC curve. The area under curve was calculated as a summative measure of the ROC. Also, Youden index (Sensitivity+Specificity–1) was computed for all points on the ROC curve to identify the optimal cutoff that maximizes both sensitivity and specificity with equal weight (Fluss, Faraggi, & Reiser, 2005).

4.2.3.5 Comparative analysis with CFI

The performance of DUBI was contrasted against that for conventional CFI. To facilitate such comparison, CFI frames were computed by applying CFI's scanline-based imaging paradigm to re-process the raw channel-domain datasets that were acquired as described in Section 4.2.2.1. Specifically, our platform's GPU beamformer was reconfigured to perform quad-line parallel receive beamforming on each frame of channel-domain data. The full image view was divided into 48 zones, each of which comprised four beams in adjacent lateral positions. Quad-line beamforming was performed over each zone for 10 consecutive pulsing events before advancing to the next zone. Accordingly, at each pixel position in a CFI scanline, the slow-time ensemble was 10 samples in size with 10 kHz sampling rate, yielding an observation period of 10 ms (i.e., same as that for DUBI). The effective CFI frame rate was 20.8 fps. For each slow-time ensemble, tissue clutter was suppressed using a first-order infinite impulse response high-pass filter (0.05 normalized cutoff; with projection initialization) (Bjaerum et al., 2002), and then mean flow velocity and velocity variance were estimated via Kasai's autocorrelation algorithm (Kasai et al., 1985). The flow estimates of different pixels in the CFI frame were mapped to a hot-cold hue to render mean flow velocity information. They were also mapped to a tricolor hue to render both mean velocity and variance information, in line with previously published work (Hoit et al., 1989; Sahn, 1988; Tamura et al., 1991).

4.2.3.6 Case demonstration using anthropomorphic phantoms

To further demonstrate the efficacy of DUBI to detect flow instability in a physiologically relevant condition, a series of imaging experiments was conducted on a healthy carotid bifurcation model, a moderately stenosed bifurcation (50% eccentric stenosis relative to the internal carotid artery diameter, as defined based on the NASCET criterion (Gasecki, Eliasziw, Furguson, Hachinski, & Barnet, 1995)),

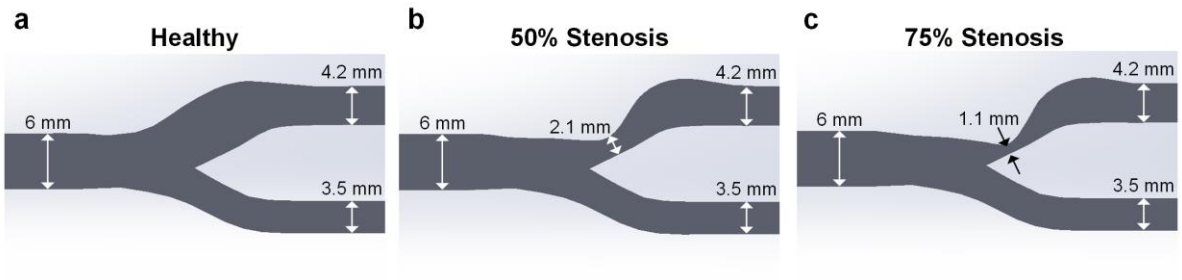

Figure 4.3. Overview of carotid bifurcation phantom. Cross-sectional view of the (a) healthy carotid; (b) 50% eccentric stenosis; and (c) 75% eccentric stenosis at the internal branch. The diameter of the common, internal and external branches were 6 mm, 4.2 mm and 3.5 mm respectively. The vessel diameters at the narrowing were 2.1 mm and 1.1 mm for 50% and 75% stenosis respectively.

and a severely stenosed bifurcation (75% eccentric stenosis). These geometries have well-studied flow characteristics as obtained from Doppler ultrasound (Wong et al., 2008) and particle image velocimetry (Kefayati et al., 2014).

The bifurcation phantoms were fabricated using the same investment casting procedures as described in Section 4.4.2. The vessel cores (healthy, 50% and 75% eccentric stenosis) were identical to the core geometries previously reported (Chee et al., 2016), for which the unstenosed diameters of the common, internal, and external carotid artery branches were 6.0, 4.2, and 3.5 mm, respectively (see Figure 4.3(a)). For moderately and severely stenosed model, the diameter of the internal branches after constriction were respectively 2.1 mm and 1.1 mm as shown in Figures 4.3(b) and 4.3(c). The vessel cores were first drafted using CAD software (SolidWorks) and were physically fabricated using the FDM system mentioned earlier. The physical builds of the vessel cores were subsequently embedded in PVA solution inside a phantom box ($80 \times 295 \times 70$ mm^3, $w \times l \times h$) and three freeze–thaw cycles were administered to solidify the PVA solution. Lastly, the vessel geometries were instated by removing the core (through snapping the core at the bifurcation site and sliding out the snapped parts from both ends).

During experiments, the bifurcation phantoms were connected to the programmable flow pump that was driving a pulsatile flow profile (20 ml/s systolic flow rate; 60 bpm). Plane wave imaging was performed with the transducer surface angled at 20° against the phantom surface using a custom-made PVA coupling wedge. Note that our use of the angled coupling wedge was inspired by another study that used slanted gel pads to generate more favorable beam-flow angles when performing clinical Doppler ultrasound (Park, Jung, Choi, & Byun, 2016). With this experimental configuration, DUBI cineloops were obtained using the same protocol as described in previous subsections.

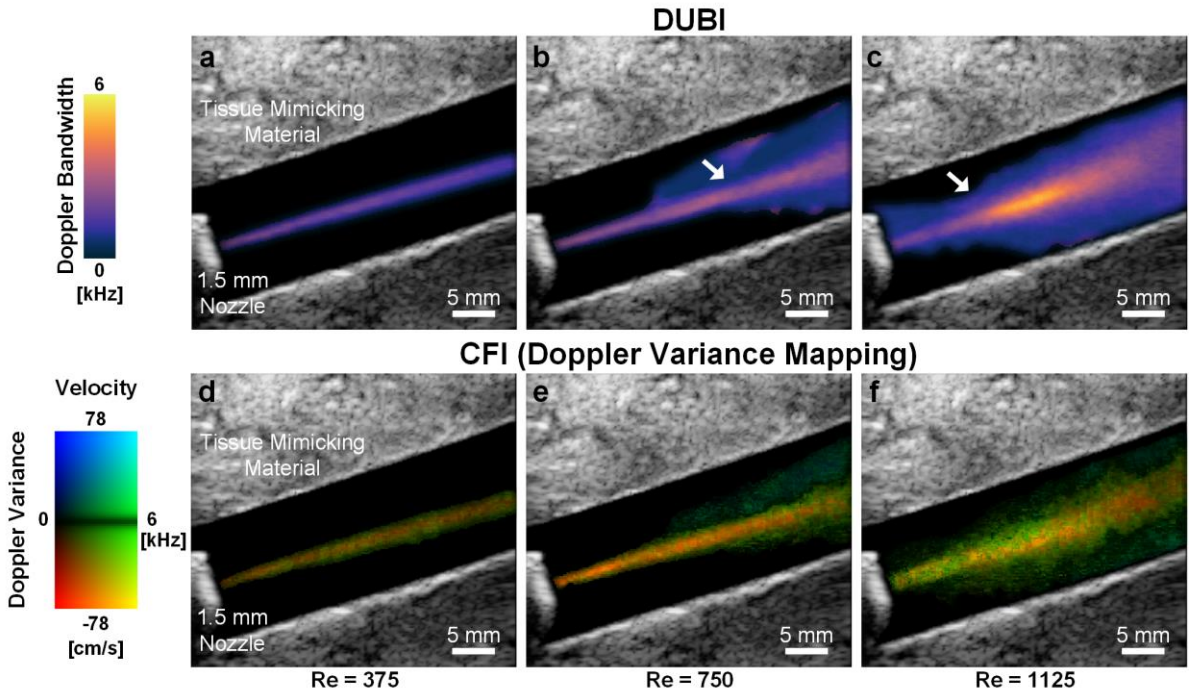

Figure 4.4. Maps of mean Doppler bandwidth (top row; derived from DUBI) and mean Doppler variance (bottom row; derived from CFI variance mapping) acquired over a 0.5-s period in a nozzle-flow phantom. Results for three Re values are shown: 375 (left column), 750 (middle column), and 1125 (right column). The white arrows indicate the intermediate boundaries between stable flow (narrow flow stream) and unstable flow (diverging pattern).

4.3 Results

4.3.1 Findings from Nozzle-Flow Phantom

4.3.1.1 DUBI revealed spatial temporal dynamics of unstable flow patterns

Doppler ultrasound bandwidth imaging was found to be effective in visualizing the spatiotemporal dynamics of unstable flow patterns (in both magnitude and spatial distribution) that cannot be perceived with conventional Doppler ultrasound. Movie 4.1 shows DUBI cineloops of three flow conditions with Re of 375 (left column), 750 (center column), and 1125 (right column). Note that the beam-vessel angle was 70° in all three cases. Cineloops on the top row of Movie 4.1 shows high-frame-rate DUBI (400 fps effective frame rate) being played back in slow motion at 50 fps. CFI cineloops are shown in the middle row for mean flow velocity mapping at a frame rate of 20.8 fps, and in the bottom row for co-rendering of mean velocity and velocity variance (referred to as Doppler variance maps in prior work (Hoit et al., 1989; Sahn, 1988; Tamura et al., 1991)).

As shown in Movie 4.1, for both DUBI and CFI (velocity maps and Doppler variance maps), stable laminar flow stream at low Re can be visualized, and transitional flow from laminar to unstable disturbance at higher Re can be observed. However, CFI velocity maps were not able to visualize the initiation of flow instability developed at higher *Re* values; this could be due to the lack of sensitivity of mean flow velocity rendered by CFI to flow instability. CFI variance maps were also not effective in highlighting the starting point of flow instability in the nozzle-flow phantom. On the other hand, for DUBI, its measured Doppler bandwidths were observed to be commensurate with the increase in *Re*. One particular observation is that the high Doppler bandwidth pattern (bright orange color) started to diverge after passing through the mid-section of the imaging view. This trend enabled us to use DUBI to more effectively identify the development of flow instability.

4.3.1.2 DUBI was effective in depicting unstable flow regions

To further analyze the trends observed in Movie 4.1, still frames of mean Doppler bandwidth were obtained by averaging over 0.5 s for the three flow conditions. Results are shown in Figure 4.4 (top row) with the intermediate boundary between stable and unstable flow indicated by white arrows (as determined from CEUS). Comparative findings derived from CFI variance mapping (i.e., mean Doppler variance) are also shown on the bottom row of Figure 4.4. One general observation to be noted is that, as Re increased from 375 to 750 and 1125, the maximum value in DUBI's mean Doppler bandwidth maps had increased from 2.1 to 3.1 and 5.2 kHz. More importantly, for the *Re* = 1125 case, the development of unstable flow corresponded to a spatial peak zone in the mean Doppler bandwidth maps derived from DUBI. The 5.2 kHz spatial peak value in the unstable flow zone was significantly higher than the spatial maximum of 2.4 kHz in the upstream flow jet near the nozzle. Such visualization was not clearly highlighted in the mean Doppler variance maps, because the upstream flow jet was found to yield similar mean Doppler variance values (spatial maximum: 6.7 kHz) as those in the unstable flow region (spatial maximum: 7.1 kHz).

4.3.1.3 DUBI yielded similar findings as CEUS

To confirm that pixel positions with high Doppler bandwidth estimates in DUBI correspond to unstable flow, CEUS cineloops acquired from the three identical flow conditions are rendered as Movie 4.2 for comparison with Movie 4.1. As illustrated in Movie 4.2, trailing path lines of contrast agents were highlighted by high-persistence rendering of Movie 4.2. As shown in this movie, microbubbles moved in straight path lines when the flow rate (and *Re*) was low (as highlighted in the left cineloop); correspondingly a low Doppler bandwidth was recorded in Movie 4.1.

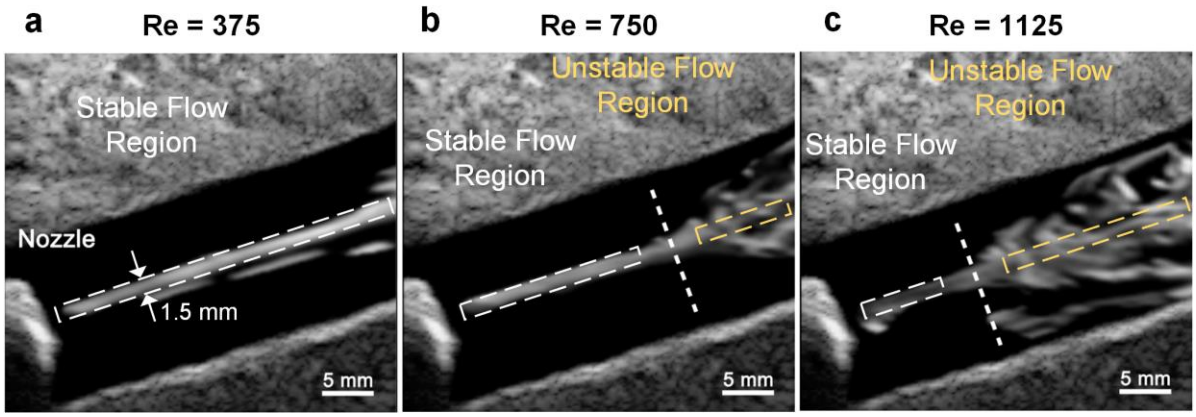

Figure 4.5. Representative CEUS image frames obtained from (a) Re = 375 with persistence = 240 frames, (b) Re = 750 with persistence = 120 frames, and (c) Re = 1125 with persistence = 80 frames. Thick dash lines identify the intermediate boundaries; flow traces were straight before the dash line but began to diverge afterwards. The white and yellow boxes (1.5 mm in height) respectively indicate the stable and unstable flow region used for ROC analysis.

In contrast, as *Re* increased (*Re* = 750 and 1125), streak traces of contrast agents crossing paths were evident (center and right cineloops of Movie 4.2). They signify flow perturbations in the form of the mixing of flow layers. These flow perturbations became more significant as they propagated and eventually transitioned to unstable flow. Positions where flow path lines deviated from the straight trajectory were also reflected by the high Doppler bandwidth observed in Movie 4.1, as well as Figures 4.4(b) and 4.4(c).

As a further analysis, Figure 4.5 shows selected CEUS frames of Movie 4.2 with dashed lines drawn on the figure to indicate the intermediate boundary between stable and unstable flow. The location of these boundaries in the high *Re* cases (middle and right frames) was found to be in close proximity with the location where a rise in Doppler bandwidth estimate started to appear in Figure 4.4, thereby indicating that Doppler bandwidth can be a reliable indicator to discern flow instability.

4.3.1.4 DUBI showed strong ROC performance in mapping flow instability

Figure 4.6(a) plots the ROC curve (dark line) of DUBI with samples collected from all the ROIs at the three flow rates. As can be observed, the ROC curve (with an area under curve of 0.85) was positioned above the diagonal line (gray dashed line), thereby indicating that DUBI has positive predictive power in determining flow instability. The Youden index is also plotted in Figure 4.6(a) (gray line) as a global indicator of sensitivity and specificity. The optimal Youden index was found to be 0.54 when sensitivity and specificity were respectively 0.72 and 0.83. This optimal point corresponded to a bandwidth threshold of 2.4 kHz, as indicated in the bi-population histogram shown in Figure 4.6(b). These ROC findings represent significant improvements over the ones obtained from Doppler variance mapping.

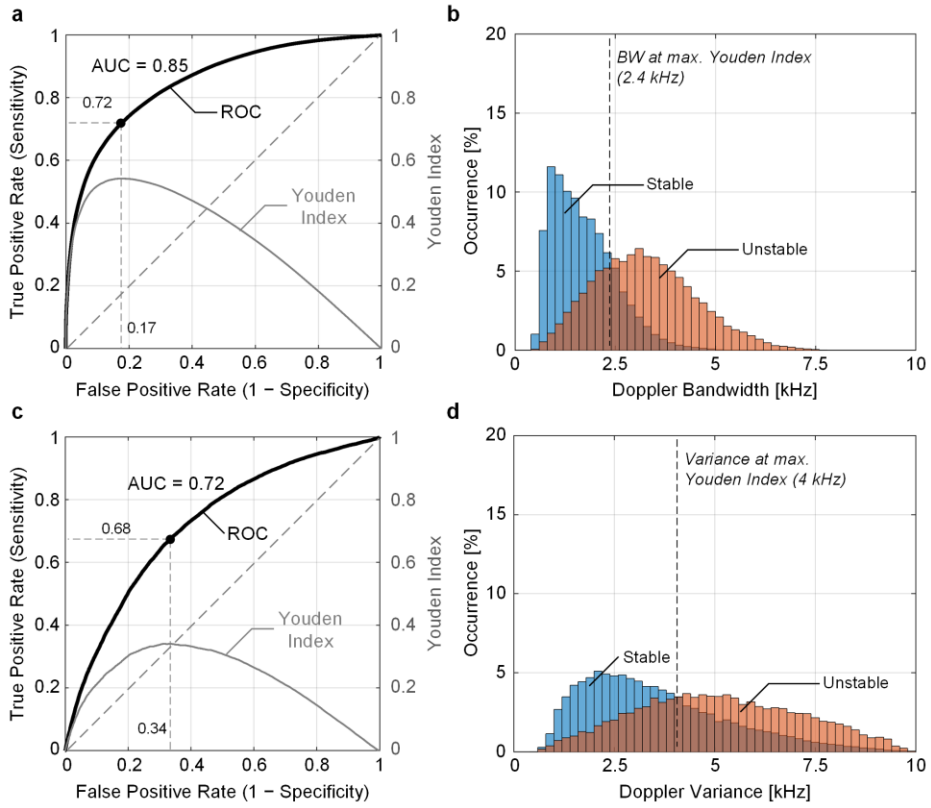

Figure 4.6. Sensitivity and specificity analysis of DUBI. (a) ROC curve (dark line) for unstable flow classification (with an area under curve of 0.85) and the corresponding Youden index (gray line) at different false positive rates; the black dot indicates the optimal classification performance when Youden index attained its maximum. The diagonal dash line represents the theoretical ROC curve for random guessing. (b) Doppler bandwidth distributions from stable (in blue) and unstable flow (in orange) regions, with the optimal bandwidth threshold marked by the black dash line. The deeper color depicts the overlapping area between the two distributions. Corresponding result for Doppler variance mapping are shown in (c) and (d) for comparison. The area under ROC curve for Doppler variance mapping was 0.72.

As shown in Figures 4.6(c) and 4.6(d), the optimal sensitivity and specificity of Doppler variance mapping were 0.68 and 0.66, and they were achieved with a maximum Youden index of 0.34 and a bandwidth threshold of 4.0 kHz. The area under ROC curve for Doppler variance mapping (0.72) was also lower than that for DUBI.

4.3.2 Findings from Carotid Bifurcation Experiments

4.3.2.1 DUBI highlighted unstable flow emerging from stenosis stie

When DUBI was applied to pulsatile carotid bifurcation phantoms, it was observed to be capable of highlighting flow instability that arises downstream from the stenosis site in diseased bifurcations. The top row of Movie 4.3 shows a series of DUBI cineloops for different bifurcation geometries: healthy

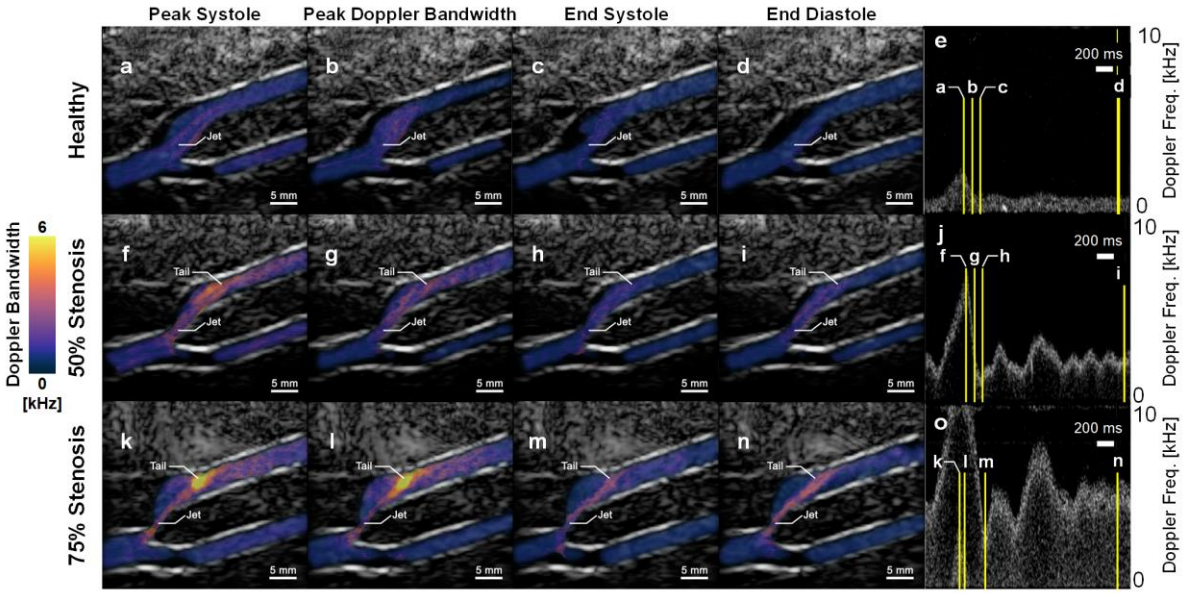

Figure 4.7. DUBI frames at different phases of the cardiac cycle. Top, middle, and bottom rows respectively show Doppler bandwidth maps measured from (a–d) healthy, (f–i) 50% eccentric stenosis and (k–n) 75% eccentric stenosis bifurcation phantoms with their corresponding Doppler spectrogram shown on the rightmost column (e, j, o). First to fourth columns show frames captured at (a, f, k) peak systole, (b, g, l) peak flow disturbance, (c, h, m) end systole and (d, i, n) end diastole respectively with their relative time points indicated on the spectrograms.

(left) and diseased (center: moderate 50% eccentric stenosis; right: severe 75% eccentric stenosis). For reference, the bottom row of Movie 4.3 shows the corresponding Doppler spectrograms taken from a 1 × 1 mm^2 sample volume placed at the flow jet, as indicated in the cineloop. The primary observation to be noted is that the range of Doppler bandwidths increased in the stenosed vessel (upper branch) because of the lumen narrowing at the stenosis site. This observation was consistent with our findings from the flow nozzle model, whereby an increasing Re would result in greater Doppler bandwidth (in the bifurcation experiments, the flow profile remained unchanged but the "nozzles" were narrower as stenosis increased). Doppler bandwidths in the healthy model were low (<1.4 kHz) throughout the entire cardiac cycle. In contrast, high Doppler bandwidths (>2.4 kHz) were observed in both diseased models, especially at the flow jet region during flow systole and the dicrotic wave phase of the cardiac cycle.

Selected frames of DUBI are shown in Figure 4.7 to facilitate further interpretation of the information provided by DUBI at specific time points of interest. This figure depicts frames from peak systole (column 1), at the instant with peak Doppler bandwidth measured in a cardiac cycle (column 2), end systole (column 3), end diastole (column 4), and the corresponding Doppler spectrogram at the stenosis site (column 5). Three main observations can be made. First, the maximum Doppler bandwidth

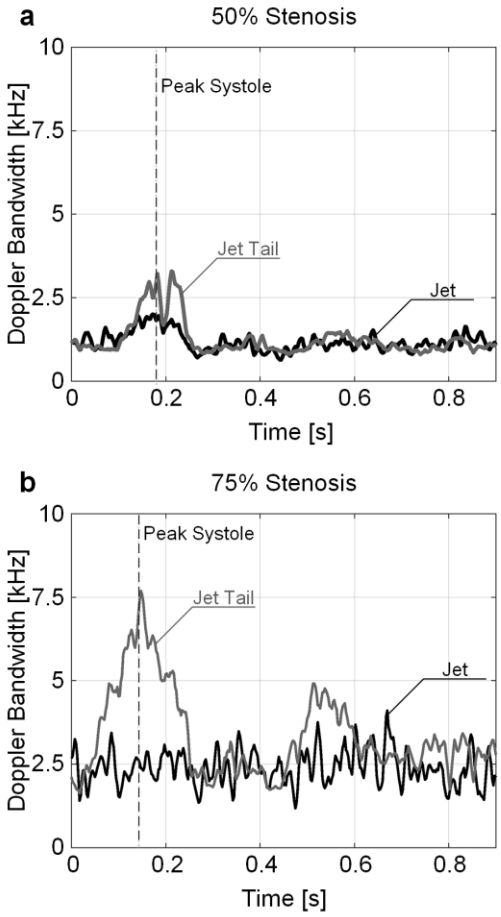

Figure 4.8. Time traces of Doppler bandwidth acquired at the jet (dark line) and the jet tail (gray line) as marked in Movie 4.3 for (a) 50% and (b) 75% stenosed bifurcation. The gray dotted line marks the time point at peak systole.

increased as the degree of stenosis increased, as reflected by the brighter thermal hue in DUBI frames. Second, the peak Doppler bandwidth was found at the jet tails (Figures 4.7(k) and 4.7(l)) where flow perturbations were strongest. Third, for the 50% stenosis model (Figure 4.7 middle row), significant increase in Doppler bandwidth was only found during flow systole, whereas for the 75% stenosis model, its high-range Doppler bandwidth sustained throughout the entire cardiac cycle (Figure 4.7 bottom row). The timing and positions of peak Doppler bandwidth were in general consistent with those measured using turbulence intensity under similar flow conditions as previously reported (Kefayati et al., 2014; Wong et al., 2008).

4.3.2.2 Maximum Doppler bandwidth is correlated with degree of stenosis

As a further analysis of DUBI, Figure 4.8 shows time traces of the measured Doppler bandwidths at the stenotic jet area (dark line) and its tail (gray line) for the two diseased bifurcation phantoms. A dash

line to indicate peak systole is also included in this figure, and the sample volume positions are labeled in Movie 4.3. For the 75% stenosis model, the maximum Doppler bandwidth at the jet tail was significantly higher (7.7 kHz) compared to that for the 50% stenosis model (3.3 kHz). Also, the Doppler bandwidth at the jet tail in the 75% stenosis model showed greater temporal fluctuation over the cardiac cycle, and it expectedly showed a decreasing trend during end systole (100 ms after peak systole) since flow deceleration naturally favored reestablishment of stable flow conditions. Another point worth noting is that in both diseased models, the Doppler bandwidth at the flow jet was lower than that at the jet tail. This finding expectedly indicates that flow instability mainly emerged not at the flow jet, but downstream from the jet. For the 75% stenosis model, at the stenotic flow jet, Doppler bandwidth was found to show a greater extent of fluctuation. This trend is likely because the higher temporal variation in jet speed for the 75% stenosis model naturally favors transitioning between stable and unstable flow regimes.

4.4 Discussion

4.4.1 DUBI as a new framework for mapping flow instability

Visualizing unstable flow noninvasively is not a trivial task. In particular, two practical flow characteristics must be addressed when devising a new flow instability mapping framework: (a) at a given time instant, unstable flow pattern may vary spatially because of its dissipative nature; (b) over a cardiac cycle, flow conditions may vary temporally due to the pulsatile nature of blood flow. DUBI has been specifically designed to visualize and track these spatiotemporal dynamics. It is equipped with three key features that have collectively enabled visualization of unstable flow. First, it can track spatial variations in flow instability (via local Doppler bandwidth measurements) over the entire image view at high-frame-rates beyond the video display range (Figure 4.1(a)). Second, it uses an AR modeling approach to consistently derive Doppler bandwidth estimates (Figure 4.1(b)). Third, its triplex display approach enables simultaneous visualization of flow instability information (Doppler bandwidth), flow trajectory (flow speckles), and the anatomical background (Figure 4.1(c)).

We have demonstrated DUBI's efficacy in identifying unstable flow for a series of flow conditions ranging from laminar to turbulent flow. The performance of DUBI was first evaluated on a nozzle-flow setup (Figure 4.2) with CEUS images acquired as benchmarking references (Movie 4.2 and Figure 4.5). Unstable flow regions were found to correspond to high Doppler bandwidth regions in DUBI (Movie 4.1 and Figure 4.4). Such correspondence was broadly found to be sensitive and specific in comparison to conventional CFI mapping of Doppler variance (Figure 4.6). The practical merit of DUBI was also

established through a series of carotid bifurcation experiments (Movie 4.3 and Figure 4.7). It was found to be effective in identifying unstable flow at the jet tail downstream from a stenosis site (Figure 4.8).

DUBI represents the first image-based, noninvasive flow instability mapping framework with fine temporal resolution. From a clinical diagnosis standpoint, this framework unlocks new potentials in improving atherosclerotic disease management. For example, emergence of unstable flow can indicate the onset of plaque formation, so DUBI may help facilitate early diagnosis of atherosclerosis. In addition, new insights on plaque progression may be obtained in correlation with the intensity and size of flow instability zones, since unstable flow has been shown to contribute to the progression of an atherosclerotic plaque (Chiu & Chien, 2011). Moreover, given that our nozzle-flow setup has demonstrated initial potential in detecting flow instability emerging from a stenosed flow outlet, DUBI may be further developed as a new tool in valvular stenosis diagnostics to complement other emerging ultrasound techniques (Hansen et al., 2017).

4.4.2 Limitations and Future Work

In the future, DUBI can be further refined to address a few technical shortcomings. First, since the Doppler equation is well known to be dependent on the beam-flow angle, the Doppler bandwidth estimates are also inherently dependent on this parameter. It would be beneficial to derive angle-independent Doppler bandwidth estimates by developing a data regularization scheme based on the local beam-flow angle at each pixel position, which can be estimated using a flow vector estimator (Ekroll et al., 2016; Yiu & Yu, 2016). Note that the regularization scheme should also take into account the issue of intrinsic spectral broadening due to the finite transit time of blood scatterers through the sample volume (the extent of intrinsic spectral broadening is known to be angle-dependent as well) (Yu et al., 2006). In doing so, the sensitivity and specificity of DUBI can likely be further improved.

From a signal processing standpoint, three enhancements can be made to improve the performance of DUBI. First, adaptive clutter filtering techniques like eigen-filtering can be introduced to improve the quality of flow detection in the presence of tissue motion (Mauldin, Lin, & Hossack, 2011; Yu et al., 2008). The real-time feasibility of this technique has already been established (Chee et al., 2017), and its statistical performance has been confirmed to be superior to conventional clutter filters (Chee & Yu, 2018). Second, in making Doppler bandwidth measurements, it may be worthwhile to introduce the use of more robust model-based estimators like the Matrix Pencil technique (Yu & Cobbold, 2008b) that derives coefficients via total-least-squares error minimization instead of AR modeling's least-squares error minimization. Such improvement will increase the consistency of the resulting Doppler bandwidth estimates. Third, non-parameteric method such as multitaper spectral analysis can also be

considered to derive Doppler bandwidth, instead of using model-based approach. Multitaper spectral analysis has been shown to derive spectrograms with reduced biases and variances than that of classical periodogram (Thomson, 1982; Babadi & Brown, 2014), thereby providing more consistent Doppler bandwidth estimates. However, the spectral resolution is limited by the available ensemble length used for spectral analysis, and may compromise the accuracy in identifying unstable flow. Further investigations are thereby required to study the tradeoff between estimation bias, variance and Doppler spectral resolution in identifying unstable flow region when using multitaper techniques.

4.5 Conclusion

Flow instability is undisputedly a significant biomechanical factor that influences the pathophysiology of atherosclerosis. In this paper, we presented a new high-frame-rate ultrasound framework called DUBI to noninvasively map flow instability over an image view at fine temporal resolution by tracking the local Doppler bandwidth over time. With this technique, new functional indices for unstable flow quantification may be derived in the future. In turn, this framework can potentially help facilitate risk stratification of atherosclerotic plaques with better efficacy than existing routines used in clinical practice.

Chapter 5
A Motion-Resistant Microvascular Imaging Framework for *In Vivo* Application

5.1 Introduction

Plaque neovascularization plays an important role in the transition of stable plaque to unstable and future lesion rupture (Michel et al., 2011); it denotes the growth of new blood vessels into the atherosclerotic plaque. These newly formed vessels are thin and have poor structural integrity because of the weak and incomplete gap junctions between endothelial cells in the intima layer (Bobryshev et al., 1999; Sluimer et al., 2009). Slumier et al. showed that more than 80% of this intraplaque microvessel network has a fragile structural integrity and is therefore susceptible to leakage of blood contents including red blood cells, white blood cells, and plasma lipid into the intraplaque space (O'Brien et al., 1996; van Lammeren et al., 2012; Virmani et al., 2005). The low-density lipoproteins entering the intraplaque space are oxidized because of the local oxidative stress and consequently induce expression of vascular endothelial growth factor (VEGF) and hypoxia-inductible factor-1α. These induced protein expressions further promote angiogenesis, as demonstrated in a rabbit atherosclerosis model (Hutter et al., 2013), and more immature microvessels are formed. This leaky microvessel network servers as an essential source of intraplaque hemorrhages (Di Stenfano, Felice, & Balbarini, 2009; Virmani et al., 2005) because platelets were found to enter the atherosclerotic lesion through this network (van Lammeren et al., 2012). These entered platelets contributes to local inflammation, plaque instability and rupture, increasing lesion vulnerability (Moreno et al., 2004). These observations suggest that plaque neovascularization precedes intraplaque hemorrhages in atherosclerosis progression and subsequently increases plaque vulnerability.

Several studies have suggested that plaque neovascularization can be used to assess future stroke risk. For example, McCarthy et al. (1999) observed a significant correlation between the intensity of intraplaque hemorrhages and density of plaque microvessels in human. This suggests that vascular density inside the plaque can be used to measure intraplaque hemorrhages and evaluate plaque rupture risk. Carotid intraplaque hemorrhage is a predictive marker of mortality in patients after carotid artery surgery (Falke, Matzsch, Sternby, Bergqvist, & Stavenow, 1995). The value of using plaque vascular density to predict future cerebrovascular event was further demonstrated by Hellings et al. (2010) in a follow-up study of patients who underwent carotid endarterectomy. The authors found that local plaque hemorrhage and increased intraplaque vascular density are independently correlated with future cardiovascular outcomes, and this relationship is independent from other clinical risk factors and

medical drug usage. Similar observations were made by Qiao et al. (2012), who associated intraplaque hemorrhage with previous cerebrovascular events. This evidence suggests plaque neovascularization and its density can provide prognostic information to evaluate atherosclerosis progression and vulnerability (Di Stefano et al., 2009; Sluimer et al., 2009).

To assess plaque neovascularization, contrast-enhanced ultrasound (CEUS) has been used with mixed success. Huang et al. (2006) used CEUS to detect the intraplaque microvasculature because the ultrasound contrast (i.e., microbubble) only stays inside the vasculature because of its size (1–8 μm). Varetto et al. (2015) found a statistically significant correlation between contrast enhancement inside plaque and the extent of plaque neovascularization (i.e., vascular density). However, the resolution provided by CEUS is not sufficient to accurately quantify the microvessel size and density because it is limited by the diffraction limit of ultrasound. This situation has been changed in recent years with the advancement in ultrasound imaging techniques. Ultrasound microvascular imaging (MVI) becomes possible by combining broad-view imaging technique and microbubble contrast enhancement (Couture et al., 2018; O'Reilly & Hynynen, 2013; Viessmann, Eckersley, Christensen-Jeffries, Tang, & Dunsky, 2013).

With the help of the microbubble, MVI can resolve blood vessels beyond the diffraction limit of ultrasound (Couture et al., 2018; O'Reilly & Hynynen, 2013; Viessmann et al., 2013) to map plaque neovascularization. In brief, this is achieved by first capturing images of microbubbles perfused alongside blood streams. Microbubble locations are then identified by either performing a Gaussian fitting (Christensen-Jeffries, Browning, Tang, & Dunsby, 2015), deconvolution operation (Errico et al., 2015), or hysteresis thresholding (Lin et al., 2017) to locate the centroid of the microbubble within blood vessels. The final microvascular image is formed with a high persistence that accumulates the microbubble positions over time (typically in seconds). To reduce false positive registration of microbubbles, spatiotemporal denoising has been proposed (Song et al., 2018). However, a major drawback of MVI is that it is susceptible to tissue motion artifacts, especially in the case of carotid plaque where the plaque moves constantly because of wall distension; even a very slow drift (3 mm/s) could introduce hundreds of micrometer displacement during the persistence phase and significantly degrade the final image quality.

Several attempts have been made to address this issue. One has proposed to suppress artifact motion by rejecting those data frames contaminated by tissue motion (Yu, Lavery, & Kim, 2018). Another approach reduces tissue motion blurring artifact by first estimating the global tissue motion and then compensating for it during the accumulation phase (Hingot et al., 2017). These algorithms work only when the tissue motion is global and rigid. Another algorithm that tracks tissue deformation has been

studied (Harput et al., 2018); it makes use of well-developed image registration method to track tissue deformation and then account for the deformation during the persistence phase. However, this is still limited to global tissue deformation.

In this work, we present a new motion-resistant microvascular imaging (MRMVI) framework that can cope with local tissue motion and deformation to map the microvessel network. In designing this framework, we hypothesize that a micrometer-level imaging resolution can be consistently achieved *in vivo* by integrating contrast-enhanced plane wave ultrasound imaging with a micrometer-level motion compensation scheme. Such motion compensation scheme employs a multi-angle vector Doppler technique (Ketterling et al., 2017; Yiu & Yu, 2016) to estimate interframe local tissue displacement for every pixel and the local tissue displacements are then compensated for on a per-pixel basis during microvascular image formation process. This is similar to the motion artifact suppression used in synthetic transmit aperture imaging (Gammelmark & Jensen, 2014). The performance was first evaluated on a micro-flow channel for calibration. We later demonstrated *in vivo* feasibility on a rat eye as an alternative to plaque neovascularization model.

5.2 Theory

5.2.1 Principle of Ultrasound MRMVI

Our MRMVI framework is founded upon the principle that microbubbles act like strong point scatterers that stay only inside the blood pool/microvasculature. The microvasculature can therefore be traced and mapped by tracking these strong point scatterers inside the imaging view (Errico et al., 2015; O'Reilly & Hynynen, 2013). To achieve this, we have exploited the following principles:

- Strong scattering strength of microbubbles;
- Coherent full-view image acquisition enabled by parallel beamforming of channel-domain data received from unfocused plane wave transmission strategy;
- Deconvolution to locate the microbubbles;
- Pixel-based tissue motion tracking enabled by multi-angle vector Doppler technique; and
- Motion/deformation compensation on a per-pixel basis.

In the following, we present further details on how each principle was incorporated into MRMVI.

5.2.2 Microvascular Imaging Framework

Microbubble Signal Extraction

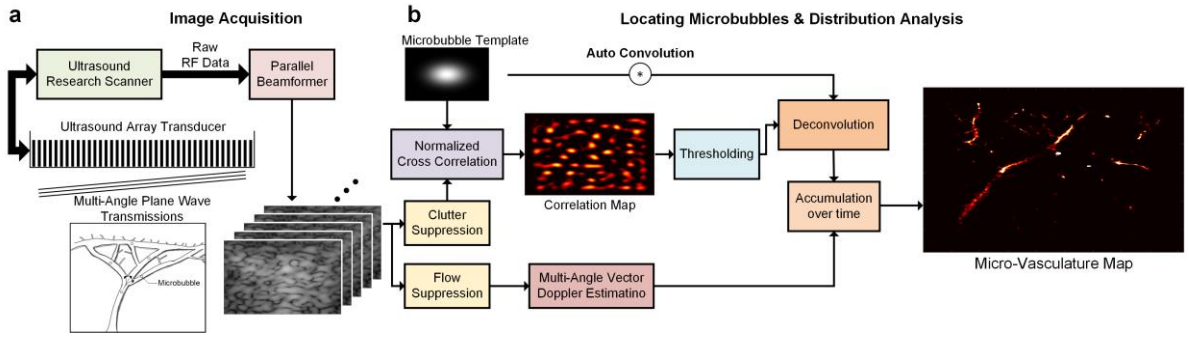

Figure 5.1. Conceptual illustration of MRMVI is shown. (a) Multi-angle plane wave data acquisition at a region of interest with perfusing microbubbles using a research-purpose ultrasound scanner that generate high-frame-rate ultrasound images; (b) Overview of the microbubble bubble signal extraction using normalized cross correlation with a microbubble template, and position estimation procedure using deconvolution process to estimate the microbubble positions before accumulating over time to generate microvasculature image with tissue motion accounted for.

Figure 5.1 depicts the overall MRMVI framework. First, multi-angle plane wave excitations *we*re used to excite the microbubbles within the imaging view. Strong echoes from the moving microbubbles *we*re then received by all array elements and parallel beamforming is employed to generate image frame for each pulse-echo sensing event. These images *we*re then stacked together to form a slow-time dataset (see Figure 5.1(a)). Clutter filtering is subsequently applied along the slow-time axis to suppress the tissue clutter and extract the signal of moving microbubbles (see Figure 5.1(b)). The extracted microbubble signal S at time t after clutter filtering can be expressed as follows.

$$S_t = PSF * (P_{x,y,t} \cdot A_{x,y,t}) + \varepsilon \tag{5.1}$$

where *PSF* is the point spread function of the imaging system, * denotes convolution operation, $P_{x,y,t}$ is sum of Dirac delta functions, representing the positions of moving microbubbles in the imaging view at different time points, $A_{x,y,t}$ is the scattering strength of each microbubble, and ε is the random white noise. This equation holds when the concentration of microbubbles is low enough such that overlapping of microbubbles is insignificant.

Microbubble Position Estimation

Once the microbubble signals were extracted from the surrounding tissues, the microbubble position was derived by previously described method (Errico et al., 2015) as illustrated in Figure 5.1(b). In brief, a coarse search of microbubble position was done by performing normalized cross correlation with the PSF template of the imaging system. This step can be regarded as convolving S_t with *PSF*, normalized by the local signal statistics σ_{local}

$$C_t \approx \frac{PSF * PSF * P_{x,y,t} \cdot A_{x,y,t} + PSF * \varepsilon}{\sigma_{local}} \quad (5.2).$$

It is essentially looking for the similarity between the extracted microbubble speckle pattern and the template. This results in a correlation map with value ranging from 0–1 (see the correlation map in Figure 5.1(b)); a high correlation value suggests that this speckle pattern is more likely coming from a microbubble. The equation can be simplified as

$$C_t \approx PSF * PSF * P_{x,y,t} + \frac{PSF * \varepsilon}{\sigma_{local}} . \quad (5.3)$$

Over this process, the scattering strength *A* in (5.2) is eliminated. A threshold is then applied to suppress false detections coming from noise ε (Errico et al., 2015) as it has low correlation value. The correlation map C_t can subsequently be rewritten as the autoconvolution of *PSF* convolved with microbubble position *P*

$$C_t \approx PSF * PSF * P_{x,y,t} . \quad (5.4)$$

Finally, the estimated microbubble position map $P'_{x,y,t}$ at time *t* is localized using the established Lucy-Richardson deconvolution procedure (van Kempen, van Vliet, Verveer, & van der Voort, 1997; Laasmaa, Venderlin, & Peterson, 2011), defined as

$$P'_{x,y,t} = C_t/(PSF * PSF) \quad (5.5)$$

where the division operator denotes deconvolution procedure. This step essentially uses deconvolution procedure to pinpoint the exact location of microbubbles within the imaging view.

In microvascular imaging, the microbubble positions in (5.5) are accumulated over time period *T* to map the microvasculature

$$MVImage = \sum_{t}^{T} P'_{x,y,t} . \quad (5.6).$$

However, when there is tissue motion, (5.6) becomes

$$MVImage = \sum_{t}^{T} P'(x + d_{x,t}, y + d_{y,t}, t) \quad (5.7).$$

where $d_{x,t}$ and $d_{y,t}$ are the interframe tissue displacement at time *t*, which shifts the microbubble positions and introduce motion artifact in the form of image blurring. To suppress such motion artifact, a local motion vector estimation is required to derive the interframe tissue displacement and pixel-based

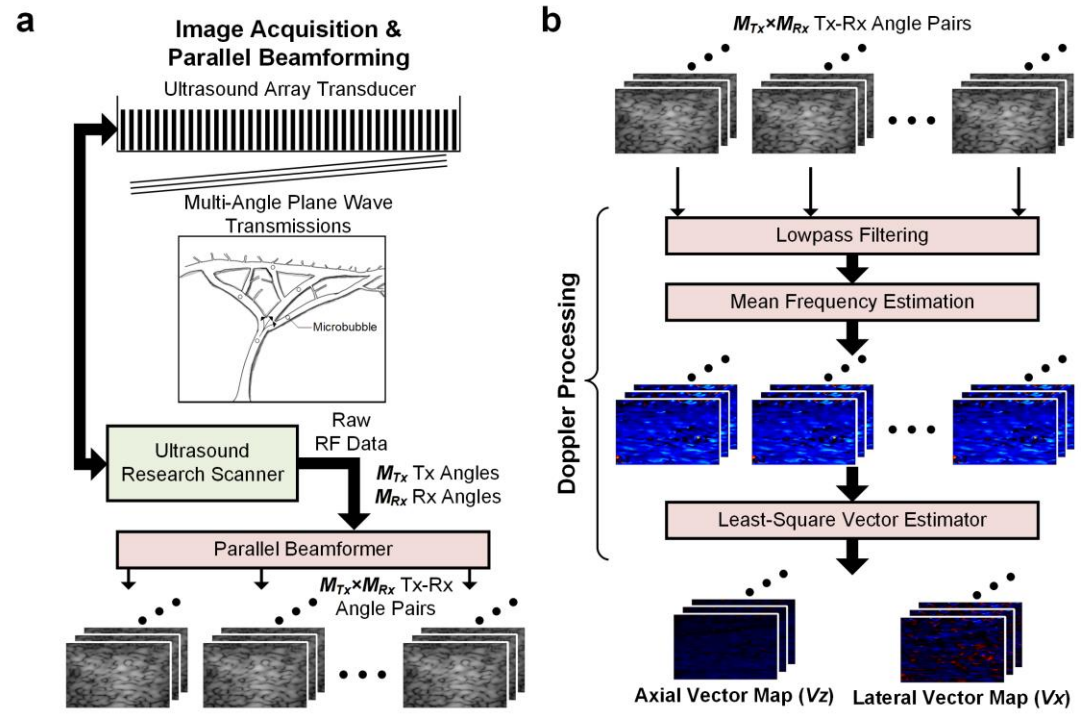

Figure 5.2. This image shows a block diagram illustration of tissue motion estimation for MRMVI. (a) M_{Tx} Tx-angle plane wave data acquisition with M_{Rx} Rx-angle parallel beamforming to generate a set of images with M_{Tx}×M_{Rx} Tx-Rx angle pairs; (b) Per-pixel based Doppler processing including low-pass filtering, mean frequency estimation and least-square vector estimation to deduce the local tissue motion vectors.

motion compensation can then be used to counter shift this displacement, as will be described in the following subsections.

5.2.3 Tissue Motion and Deformation Estimation

To track the 2-D tissue motion displacement at fine resolution, we employed a multi-angle least square vector Doppler framework (Ketterling et al., 2017; Yiu & Yu, 2016) with extended ensemble length (detailed formulation can be found in Sect. 1.5.2.2). Figure 5.2 illustrates the overall estimation process. In brief, for each of the M_{Tx} transmit angles of the transmission sequence, this framework first performs parallel receive beamforming with a set of M_{Rx} receive steering angles (Figure 5.2(a)); this results in $M_{Tx} \times M_{Rx}$ unique transmit-receive (Tx-Rx) angle pairs. For each of the $M_{Tx} \times M_{Rx}$ Tx-Rx pairs, slow-time processing includes clutter filtering and mean frequency estimation are executed (Figure 5.2(b)). The extended ensemble length enables a finer Doppler resolution when deriving the mean frequency estimates and in turn finer velocity resolution. The mean frequency estimates of the $M_{Tx} \times M_{Rx}$ Tx-Rx pairs are subsequently used as inputs for a least-square estimator according to (1.6) and (1.7) to derive the axial and lateral tissue motion vector. This process is repeated for every frames to derive the axial

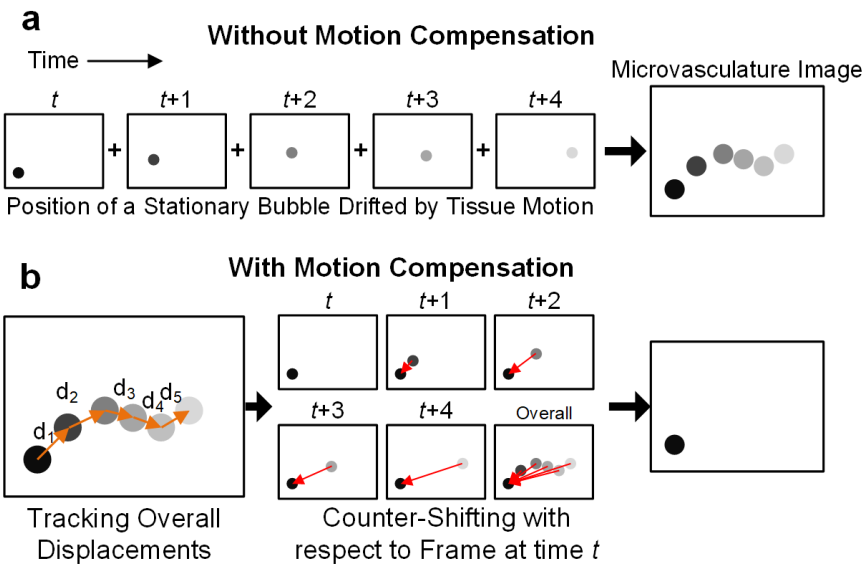

Figure 5.3. The image shows a conceptual illustration of motion compensation scheme in MRMVI. (a) Illustration of stationary microbubbles drifted by tissue motion, and the final microvascular image formed with tissue motion artifact (smearing); (b) Using the derived motion vectors (see Figure 5.2(b)) to counter-shift the tissue motion drift and eventually generate the final microvascular image motion free of motion artifact.

and lateral tissue velocity maps (v_z and v_x) at different time points that are later used for motion compensation.

5.2.4 Microvascular Image Formation

The microvasculature image is formed by accumulating the derived microbubble positions (Section 5.2.2) with the interframe tissue motion taken into account (Section 5.2.3). The importance of this step is shown in Figure 5.3(a) for the case of a stationary microbubble drifted by surrounding tissue motion. The microbubble is drifted away from its original position (black dot) to different locations over time because of the surrounding tissue motion; this results in motion artifact in the final microvascular image. This drifting can be alleviated by tracking the tissue motion as described in Section 5.2.3. Figure 5.3(b) illustrates the overall motion compensation process. The process starts with calculating the interframe displacements (d_1-d_5 in Figure 5.3(b)) from the tissue velocity maps derived in Section 5.2.3 as follows,

$$d_x[x,z,t] = d_x[x,z,t] + v_x[x + d_x[x,z,t], z + d_z[x,z,t], t] \times t_{PRI} \tag{5.6}$$

$$d_z[x,z,t+1] = d_z[x,z,t] + v_z[x + d_x[x,z,t], z + d_z[x,z,t], t] \times t_{PRI} \tag{5.7}$$

with

$$d_x[x,z,0] = 0 \tag{5.8}$$

and $$d_z[x, z, 0] = 0 \quad (5.9)$$

where $d_z(x, z, t)$ and $d_x(x, z, t)$ are respectively the cumulative axial and lateral displacements at time t for pixel initially at (x, z). The microbubble positions are then counter-shifted by the deduced displacements to align with the starting position at time t (see Figure 5.3(b) mid-column), and the motion-resistant microvasculature image is formed accordingly. This procedure can be expressed as

$$MVImage[x, y] = \sum_{t=0}^{Q} P_t[x + d_x[x, z, t], z + d_z[x, z, t]] \quad (5.10)$$

where *MVImage* is the microvasculature image and Q is the number of frames for accumulation. This aligns the microbubble positions and suppresses the motion artifact seen in Figure 5.3(a). In other words, this procedure essentially tracks the overall tissue displacement, extracts the corresponding pixel value from the microbubble position map P_t, and sums it to *MVImage*.

5.3 Implementation of MRMVI

5.3.1 *In Vitro* Imaging Hardware and Data Acquisition

We implemented MRMVI on a programmable research platform that is built upon our group's prior work in ultrasound flow imaging innovations (Yiu et al., 2014; Yiu & Yu, 2013). The platform was equipped with a 128-channel programmable transmit front-end (SonixTouch; Analogic Ultrasound, Peabody, MA, USA). The received echo was digitized by a pre-beamform DAQ tool with 80 MHz sampling rate and 10-bit resolution (Cheung et al., 2012). The acquired raw data were processed with a high-speed processing platform based on graphic processing unit (GPU) technology (Yiu et al., 2011) for beamforming and signal processing. We programmed our research platform to perform high-frame-rate data acquisition as required. Full-view acquisition at 3 kHz was achieved with dual angle plane wave excitations (-5º & 5 º transmission; 15.6 MHz transmit center frequency, 2-cycle pulse) using an L26.13 linear array (0.1 mm pitch; Vermon, Tours, France). Accordingly, raw data frames were acquired at a rate of 6,000 fps, with an effective frame rate of 3,000 fps for each transmit angle. In each acquisition, the raw channel-domain data was stored on the DAQ tool until the internal 16 GB memory buffer was filled (3 s duration at 2.5 cm imaging depth). The data was then streamed offline to the GPU platform for processing.

5.3.2 Plane Wave Image Formation

For each frame of the acquired dataset, parallel beamforming was performed on the GPU computing platform using a codec programmed in Matlab (R2016a; Mathworks Inc., Natick, MA, USA) in which

the GPU-accelerated parallel beamforming library (Yiu et al., 2011) was invoked. The codec first applied a 12.6.18.6 MHz bandpass filter to the received RF data on a per-channel basis to suppress out-of-band white noise. The filter was implemented as a finite-impulse-response (FIR) filter in Matlab, with minimum filter order (30 taps) formulated using the Parks-McClellan equiripple design algorithm (McClellan & Park, 2005). The analytic form of the acquired data was subsequently obtained using a FIR-based Hilbert transformer (50th order), as described earlier (Yiu et al., 2011). With the analytic RF data, image frames were finally parallel beamformed using our GPU-based delay-and-sum algorithm (a constant F-number of 2 was used, with Hanning apodization). Spatial compounding was subsequently carried out to improve the spatial resolution. In this study, the microvascular imaging view was reduced to a confined area (4×2.5 mm^2 ($w \times h$)), centered on the micro-flow channel and optic nerve head of rat eye (to be discussed in Section 5.4) with a 5 μm pixel spacing; this resulted in a image size of 800×500 ($w \times h$). This four-stage process was repeated for the data of different slow-time sampling instants, thereby generating a stack of image frames over slow-time for microbubble position estimation.

5.3.3 Signal Processing for Microvascular Imaging

Microbubble Position Estimation

To extract the speckle signal of moving microbubbles, we used a high-pass filter (134th order) with a cutoff frequency at 75 Hz. The extracted signals were then convolved with a PSF template to extract the microbubble signals. This PSF template was obtained by taking an image (based on the same acquisition parameters and image formation process described in Section 5.3.1 and 5.3.2, respectively) of a 25 μm-diameter tungsten wire (AA44191H4; Thermo Fisher Scientific, Waltham, MA) suspended under water at 12.5 mm depth. The constructed correlation map C highlighted the positions of microbubbles. A threshold of 0.8 was applied to remove the random noises and falsely detected microbubbles. This threshold value was empirically chosen to reduce false detection of microbubbles. The microbubble positions $P_{x,y}$ at different time points were consequently estimated using Lucy-Richardson deconvolution method (Laasmaa et al., 2011; van Kempen et al., 1997) with the auto-convolution of PSF as template according to (5.5).

Multi-Angle Least-Square Tissue Vector Estimation

Aside from the microbubble position derivation, the same dataset was used to derive tissue motion vector using the least-square estimator previously reported (Yiu & Yu, 2016). This multi-angle least-squares estimator has been shown to be consistent in both low-frequency and high-frequency applications (Ketterling et al., 2017; Yiu & Yu, 2016). As discussed in Section 5.2.3, for each of the

transmit angles (-5º & 5º), a set of image frames were first generated using parallel beamforming for a set of receive steering angles (-5º, 0º & 5º). Next, Doppler processing was performed on a per-pixel basis for all images; a low-pass FIR filter (134th order) with a cutoff frequency at 150 Hz was used to suppress moving microbubble signal and retain the near stationary tissue. Mean frequency estimation was subsequently performed with an ensemble vector size of 128 for every pixel. This long ensemble gives better resolution in estimating the mean frequency for flow vector derivation. After this, we measured a total of six mean frequencies, each from a unique Tx-Rx angle pairs. They were subsequently used as inputs for the least-square estimator to derive the motion vector maps v_x and v_z as described in (Yiu & Yu, 2016). A time-series of tissue motion vector maps was finally derived by repeating this estimation process for every pixel at all time points.

Microvasculature Image Formation

The motion compensated microvasculature images were consequently formed from the derived $P_{x,y,t}$, $v_{x,t}$, and $v_{z,t}$ according to (5.6)-(5.10) with Q (the accumulation duration) equaled to 300 frames (for *in vitro* experiment) and 4500 frames (for *in vivo* experiment), which were equivalent to 100 ms and 1500 ms of observation period respectively. Note that a spline interpolation was used for sub-pixel displacement.

5.4 Experimental Methods

5.4.1 Design and Fabrication of Micro-Flow Model and Flow Circuit Setup

To evaluate the performance of MRMVI in suppressing motion artifact, we devised a micro-flow model with known flow channel diameter and flow channel separation. As illustrated in Figure 5.4(a), the micro-flow channel model was consisted of two parallel flow channels that were 50 μm in diameter at fixed separation (300 μm edge to edge, or 350 μm center to center). The diameter of the flow channel allowed us to attest both the axial and lateral resolution of MRMVI, whereas we used the channel separation to evaluate the resolvability of MRMVI framework when there is tissue motion.

To fabricate the microflow model, a lost-core method modified from previously reported protocol (Ho et al., 2017) was employed, and tungsten wires with diameter of 50 μm (AA10405H4; Thermo Fisher Scientific) were used as the cores. To ensure the separation between the tungsten wires, we first drafted a mounting bridge on computer-aided design (CAD) software (SolidWorks; Dassault Systems, Waltham, MA, USA). As shown in Figure 5.4(b), the mounting bridge has pillars at two ends, with slots at the top of each pillar. The dimensions of these slots were 100×100 μm^2 ($w \times h$) and the separations between adjacent slots were 300 μm (measured from edge to edge), as shown in Figure

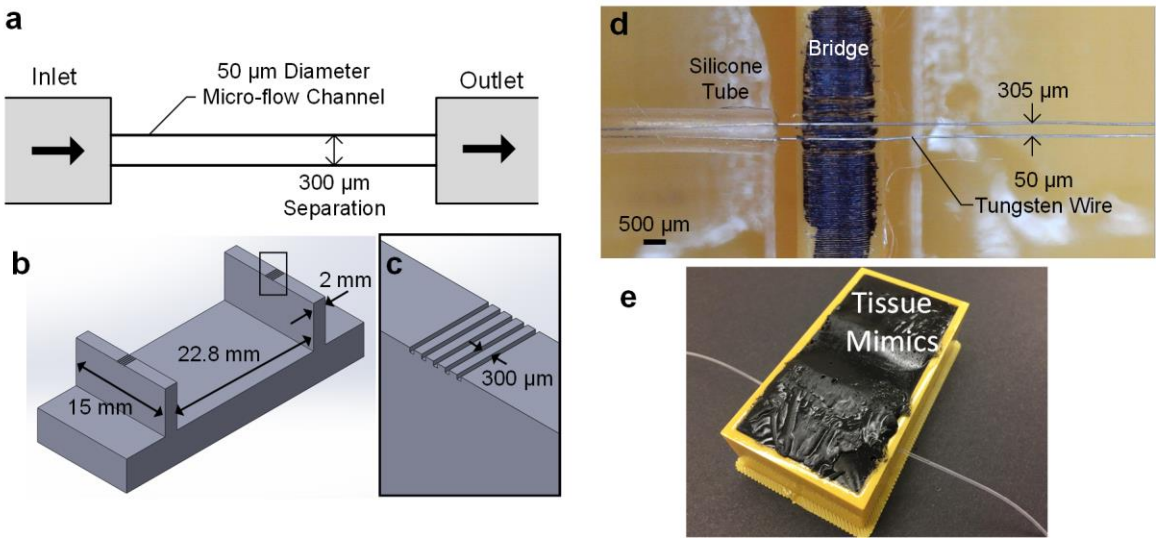

Figure 5.4. The image is an overview of micro-flow phantom. (a) Illustration of the flow channel dimensions; (b) CAD draft of the casting bridge that holds the tungsten wires; (c) enlarged view of the slots to highlight the slot dimension and distance in between; (d) mounting configuration of the tungsten wires captured using a microscope; and (e) the fabricated micro-flow channel phantom after casting.

5.4(c). These slots guided the tungsten wires during casting process to ensure the separations between the tungsten wires. Note that five slots were included in the draft to increase the chance of having two adjacent slots printed successfully.

The bridge was fabricated using a 3-D printer (Model DX; Creatbot 3D Printer, Zhengzhou, China) with a nozzle size of 250 µm and 50 µm layer thickness. Figure 5.4(d) shows the fabricated bridge with tungsten wires mounted on top. The separations were measured to be 305 µm (or 355 µm center-to-center) under a microscope at 32 X magnification (Digital Microscope Pro; Celestron, Torrance, CA, USA). We later moved the bridge mount into a casting case, and casted tissue mimic around by: (a) pouring PVA solution into the phantom case and (b) administering three freeze-thaw-cycles (freeze in 20°C for 24 hours followed by thawing at 4°C for 24 hours). Note that the PVA mixture was consisted of 10% PVA (341584; Sigma-Aldrich, St Louis, MO, USA), 3% graphite (282863; Sigma-Aldrich), 0.3% potassium sorbate (85520; Sigma-Aldrich), and 86.7% distilled water. The acoustic attenuation and speed of this tissue mimic were respectively 0.229 dB/(cm·MHz) and 1535 m/s as reported earlier (Ho et al., 2017). Upon completing the thermal cycling process, the flow channels were instated by simply sliding the tungsten wires out from one end of the phantom

5.4.2 Flow Circuit Setup and Microbubble Perfusion

The fabricated micro-flow channel phantom was connected to syringes on both ends, as shown in Figure 5.5(a). The inlet end was connected to a syringe held above the inlet level that served as a reservoir (see

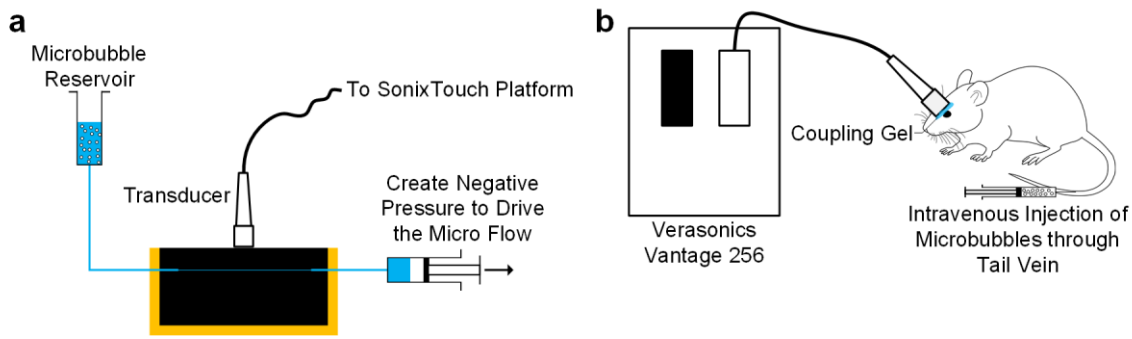

Figure 5.5. The image shows an illustration of (a) flow circuit setup of the micro-flow channel phantom, the outlet syringe was drawn to introduce negative pressure to facilitate microbubble perfusion; and (b) *in vivo* setup for rat experiment; microbubbles were injected intravenous through the tail vein.

left side of Figure 5.5(a)) and the outlet end was connected to another syringe that provided negative pressure to facilitate microbubble perfusion at an averaged flow rate of 50 µl/min (averaged over 10 min). During experiments, we administered a bolus of microbubble contrast agents (USphere Prime; Trust BioSonics, Hsinchu, Taiwan) through the reservoir to map the micro-flow channels. Plane wave data acquisitions of the cross-section of the micro-flow channels were performed as described in Section 5.3.1 and the MRMVI frames were generated based on the signal processing described in Section 5.3.2 and 5.3.3.

5.4.3 Introduction of Tissue Motion

To test the effectiveness of our proposed framework in alleviating the tissue motion artifact in microvasculature image, tissue displacements were introduced to the acquired dataset by shifting the location of beamforming pixels during the image formation process. To be specific, the pixel coordinates that passed to the parallel beamforming module (Yiu et al., 2011) were updated for every image frames as follows:

$$x_n = x_0 + n \times m_x \times t_{PRI} \tag{5.9}$$

$$z_n = z_0 + n \times m_z \times t_{PRI} \tag{5.10}$$

where x_n and z_n were the coordinate maps used to form the n^{th} image frame, and m_z and m_x were the interframe axial and lateral tissue velocities. The tested tissue velocities ranged from 3–15 mm/s, covering typical range of tissue motion observed in arterial distension.

There were three advantages using simulated tissue motion: (a) it removed the stepping noise accompanying stepping motor that would be used as a source of tissue motion otherwise; (b) a much finer displacement (in the order of micrometer) can be achieved; and (c) it eliminated potential

confounding factors that might hinder the comparison between different tissue speeds as we tested the same dataset for all tested velocities.

5.4.4 *In Vivo* Pilot Trial on Rat Eye

As a proof-of-concept, we conducted an *in vivo* experiment on a rat eye model to evaluate the effectiveness of the proposed framework in visualizing the choroid vascular bed near the optic nerve head (an animal model previously reported; Urs et al., 2018). The optic nerve head served as an analog of carotid atherosclerotic plaque as the nerve head has readily observable microvasculature (choroid layer) with comparable size (~4 × 2 mm^2 (w × h)) as carotid plaque. Figure 5.5(b) illustrates the experimental setup for the *in vivo* experiment. During the experiment, a bolus of microbubble contrast agent was injected intravenously through the tail vein of the rat. Plane wave image acquisition was then performed on the left eye of the rat using a Vantage 128 system (Verasonics, Inc., Kirkland, WA, USA) equipped with a L22-14v high frequency transducer (Verasonics). The imaging parameters were the same as the *in vitro* experiments except the sampling rate was set at 62.5 MHz. The L22-14v transducer has the same pitch, and number of elements as the L26.13 transducer used for *in vitro* experiments. The acquired data were then processed to generate the microvasculature images according to the signal processing procedures described in Section 5.3.2 and 5.3.3

5.5 Results (Micro-Flow Channels)

5.5.1 MRMVI Resolves Micro-Flow Channels beyond Diffraction Limit

MRMVI was found to be able to resolve the micro-flow channels smaller than the wavelength of the transmit pulse, as shown in Figure 5.6. Figures 5.6(a) and 5.6(b), respectively, show the B-mode image (acquired using SonixTouch clinical mode) and the resolved microvasculature image for the same cross-sectional view of the micro-flow phantom. One key observation is that the two 50 μm-diameter flow channels were clearly visualized in the microvasculature image (Figure 5.6(b)), although they were inseparable in the B-mode image (Figure 5.6(a)). Figure 5.6(c) shows the enlarged segment marked by the gray box in Figure 5.6(b). It is clear the two flow channels resembled circular shapes in line with the cross-sectional profile of the tungsten wires. The measured separation between the flow channels center were 396 μm, close to the expected value of 355 μm.

Another key observation is that the detected flow channel size is smaller than the both the half of the transmit pulse length ($2\lambda/2$ = 100 μm) and the diffraction limit ($\lambda \cdot F\#$ = 200 μm). The cross-sectional profiles of the detected flow channels were plotted in Figure 5.6(d–g) with their corresponding positions marked in Figure 5.6(c). The measured size at full-width half-maximum (FWHM) of the two flow

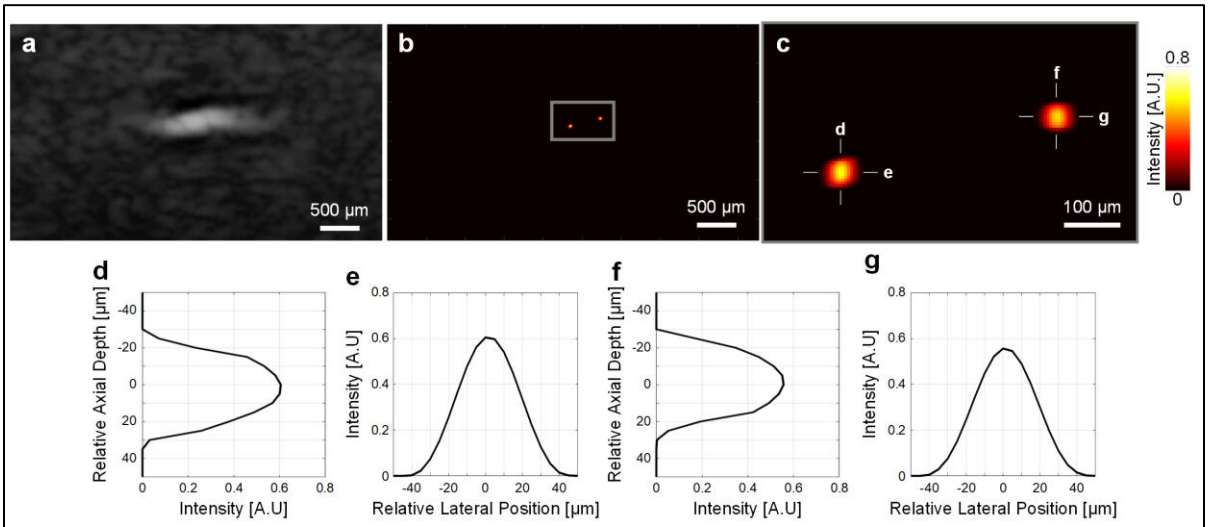

Figure 5.6. (a) B-mode image of the micro-flow phantom obtained from a clinical scanner; (b) MRMVI image for the same imaging view; (c) enlarged view of the grey box area marked in (b); the (d) axial and (e) lateral lumen cross-sectional profile of the left flow channel; and (f) the axial and (g) lateral lumen cross-sectional profile of the right flow channels. Their corresponding positions are marked in (c).

channels were 39 µm in lateral and 42.5 (left) and 40 µm (right) in the axial. The cross-sectional flow profiles were generally parabolic in shape, consistent with the theoretical Poiseuille flow profile (Reynolds number = 5 in this case).

5.5.2 MRMVI Maintains Image Quality in the Presence of Tissue Motion

Our MRMVI demonstrated its efficacy in coping with tissue motion and maintaining its resolution, as shown in Figure 5.7. Figures 5.7(a) and 5.7(b) show the obtained microvasculature images (Q = 300 frames, equivalent to 100 ms) with the presence of axial and lateral tissue motion (3 mm/s), respectively. As can be seen, the detected flow channels were smeared along the direction of applied tissue motion. This significantly reduced the resolution and resolvability of MVI (Figure 5.7(b)). In contrast, the flow channels detected by MRMVI remained similar sizes as compared to Figure 5.6(c), as shown in Figures 5.7(c) and 5.7(d; same imaging view as Figures 5.7(a) and 5.7(b), respectively). This observation was further substantiated by the cross-luminal profiles plotted in Figures 5.7(e–l). The dark lines represents the lumen cross-sectional profile obtained in Figures 5.7(c) and 5.7(d), whereas the gray lines represents those obtained in Figure 5.6. It can be observed that the lumen cross-sectional profile profile closely resembled those obtained without any tissue motion, suggesting that MRMVI can suppress tissue motion artifact and maintain resolution and resolvability.

To further evaluate the performance of MRMVI under different tissue motion velocities, Figure 5.8 plots the axial and lateral channel size acquired at six different tissue velocities, measured at FWHM. The axial channel size reduced slightly from 48.5 ± 3.5 µm (reference, i.e., no tissue motion) to 46.7 ±

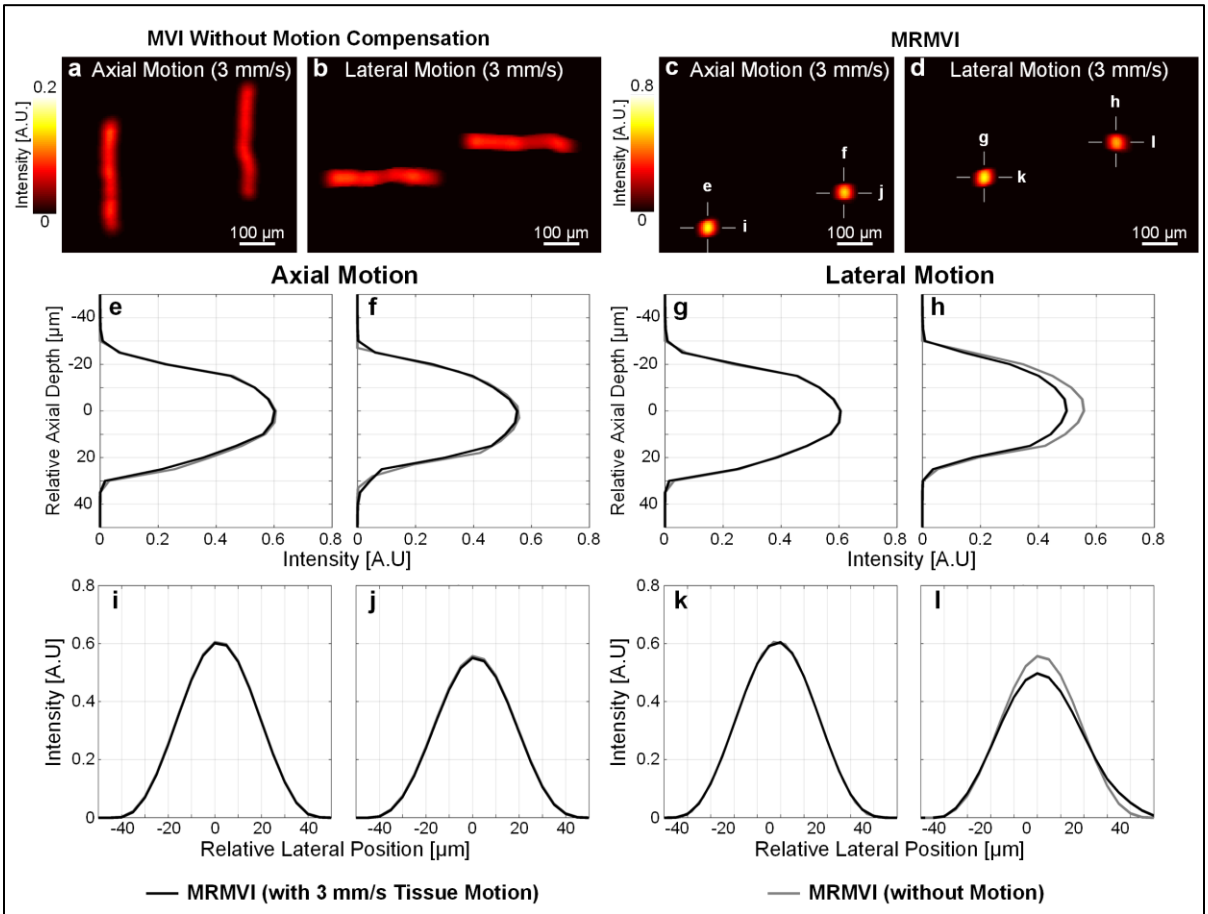

Figure 5.7. First row: microvasculature images obtained using MVI (left) and MRMVI (right) in the presence of 3 mm/s axial (a & c) and lateral (b & d) tissue motion; the axial (second row) and lateral (third row) lumen cross-sectional profile of the left and right flow channels with axial tissue motion (left) and lateral tissue motion (right). The dark and grey lines respectively depict the lumen cross-sectional profiles obtained using MRMVI with tissue motion and those without tissue motion (obtained in Figure 5.6).

3.3 µm (15 mm/s axial motion) as the tissue velocity increased. A similar trend can be observed for the lateral tissue motion (48.5 ± 3.5 µm reduced to 45.9 ± 3.3 µm). This could be attributed to the drop in flow channel intensity depicted in Figures 5.7(h) and 5.7(l). In contrast, the lateral channel size remained similar in size with less than 1 µm difference (see Figure 5.8(b)). This suggests that our MRMVI framework can reliably suppress tissue motion artifacts and maintain the achieved resolution and resolvability over the tested range of tissue velocities.

5.6 Results (*In Vivo* Rat Experiment)

5.6.1 MRMVI Can Consistently Track Tissue Motion *In Vivo*

As a demonstration, Movie 5.1 renders a 1.5-second duration of B-mode image sequence acquired at the optic nerve head of the rat eye. Five dots were overlaid on top and they were displaced based on the

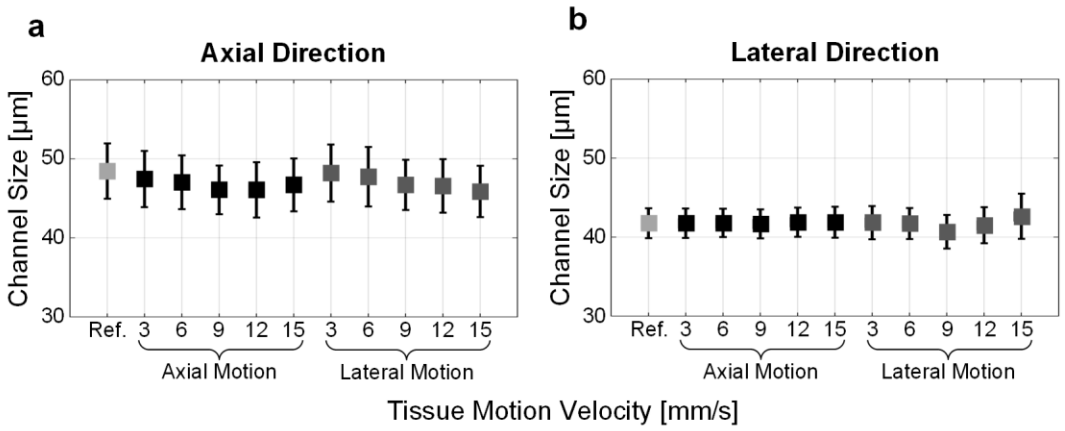

Figure 5.8. Channel size in (a) axial, and (b) lateral direction, measured at FWHM, in the presence of axial (dark square) and lateral (gray square) tissue motion. Channel size measured without tissue motion is plotted (light gray) and marked as reference.

estimated instantaneous tissue velocities at their current positions according to (4)-(7), with $Q = 4500$ (equivalent to 1.5s duration). As can be seen from the cineloop, the dots were generally able to follow the bright speckles underneath throughout the 1.5 s duration. This demonstrates that our MRMVI is able to track tissue displacement consistently. This ability to track tissue displacement consistently over an extended period of time (> 1s) plays a crucial role in suppressing tissue motion artifacts in microvasculature image.

5.6.2 MRMVI Can Visualize the Choroidal Microvasculature of the Rat Eye

Movie 5.2 shows the detected microvasculature map overlaid on top of B-mode images over time with motion compensation. It can be seen that the microvasculature was gradually mapped by the microbubbles and MRMVI. It roughly took 1.2s to map the central retinal artery (CRA) that supplies blood to the choroid (the main vessel at the image center), and an additional 0.3s to map the remaining side branches and small vessels. Even though there was noticeable tissue motion as depicted in the background of Movie 5.2, MRMVI was still able to accumulate the detected microbubble positions at the right positions to form the final microvasculature image.

Figures 5.9(a) and 5.9 (b) show the mean power Doppler map obtained after clutter suppression (averaged across the 1.5s duration) and the MRMVI frame ($Q = 4500$) shown in Movie 5.2. Our MRMVI frame was able to visualize the CRA and the side branches with finer details. Several areas marked in Figure 5.9(a: gray boxes) were selected, enlarged and plotted in the second (power Doppler) and third row (MRMVI) of Figure 5.9. It can be observed that the blurry vessels depicted by the power Doppler (Figures 5.9(c) and 5.9(e)) were highlighted by our MRMVI in greater details (see Figures

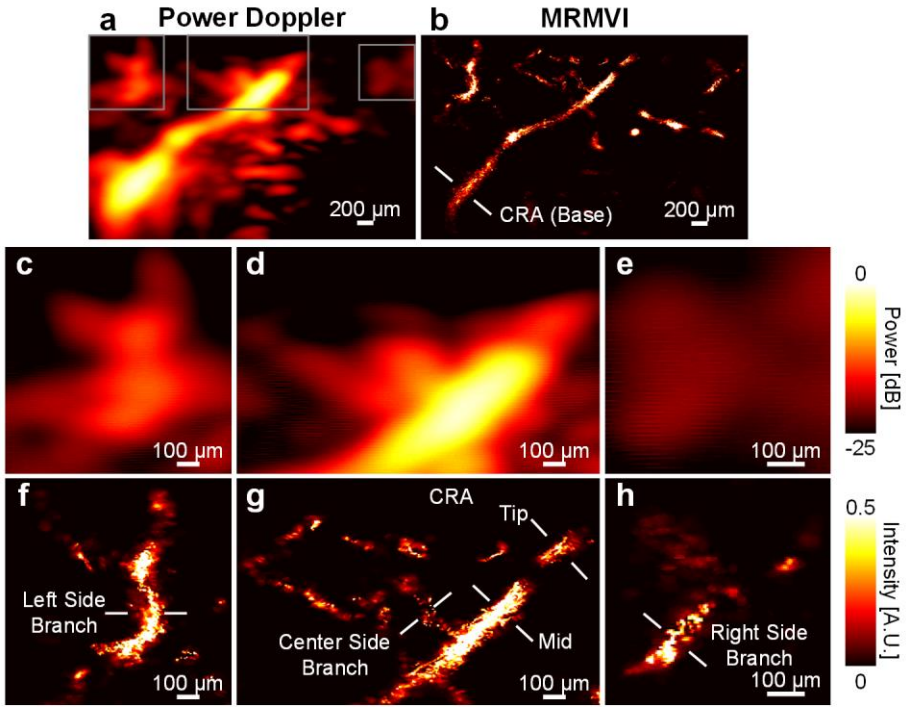

Figure 5.9. First row: microvasculature mapped by (a) power Doppler and (b) MRMVI, depicting the central retinal artery (CRA) at the center and the side branches that supply blood flow to the choroid. Enlarged view of areas marked by the grey box in (a) from power Doppler (second row) and MRMVI (third row) for left side branch (left column), tip of main branch (middle column) and right side branch (right column). See Figure 5.10 for the corresponding cross-luminal profile for the CRA and the three side branches.

5.9(f) and 5.9(h)). To be specific, the Y-shaped side branch in Figure 5.9(c) was better resolved by MRMVI in Figure 5.9(f). Furthermore, MRMVI was able to resolve the branch splits and separations that were missed in power Doppler; the side branch coming off the CRA was clearly visualized by MRMVI, as shown in Figure 5.9(g), as compared to a color patch in Figure 5.9(d). Moreover, the vascular network at the upper left corner of Figure 5.9(g) was rendered as either background noise or blurry color patches in Figure 5.9(d). The upper right corner color patch of Figure 5.9(a; see Figure 5.9(e) for enlarged view) was resolved into another side branch with connecting vasculatures, as shown in Figure 5.9(h). This suggests that our MRMVI framework is able to resolve microvasculature with a better resolution.

5.6.3 MRMVI Can Suppress *In Vivo* Motion Artifact

It was found that MRMVI was able to address the artifacts caused by tissue motion. Figure 5.10 plots several lumen cross-sectional profiles of the CRA and side branches marked in Figure 5.9 with white lines. We found that most of the lumen cross-sectional profiles mapped by MVI have misalignments at the vessel center, giving a false impression that there were two vessels in close proximity. This was

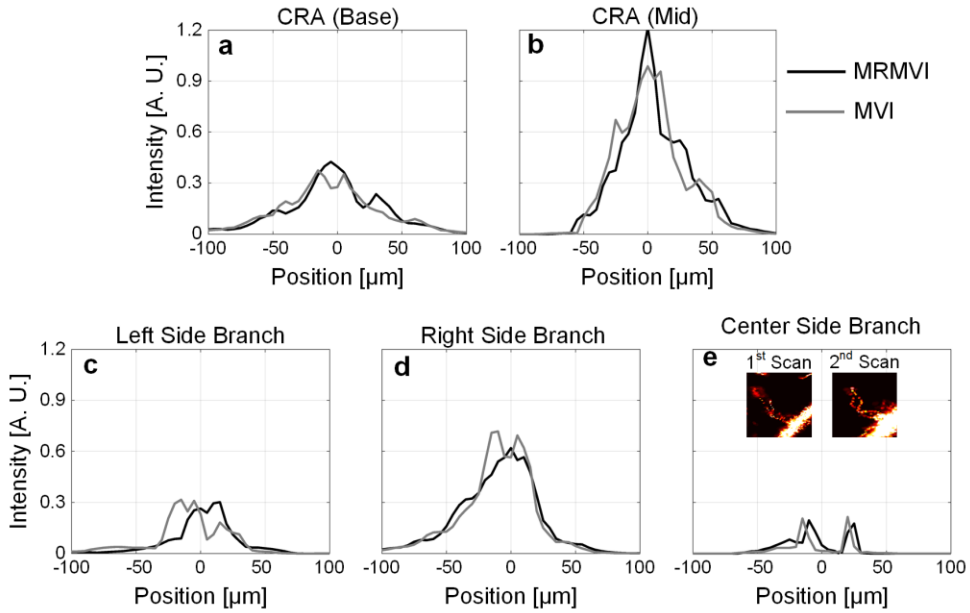

Figure 5.10. Cross section profile comparisons between MRMVI (dark lines) and MVI (grey lines) for the main branch (top row) and the side branches (bottom row) with their corresponding positions marked in Figure 5.9. An image comparison of the center side branch between consecutive scan is shown in (e) as thumbnail to confirm the branching.

caused by the drift of microbubble positions during the accumulation phase due to tissue motion (see Figure 5.3(a)). In contrast, our MRMVI framework was able to remove the drift and realign the vessel centers. For instance, the base (Figure 5.10(a)) and the mid-section (Figure 5.10(b)) of CRA have misalignments at the vessel center region for MVI (gray line). Our MRMVI estimated the interframe drifts and realign the detected microbubble positions, creating smoother vessel profiles. The vessel sizes measured at FWHM were, respectively, 44.4 µm and 23.3 µm for the base and midsection of CRA using MRMVI, as opposed to 55 µm and 47.9 µm using MVI. A similar trend was observed for the left and right side branches as well (see Figures 5.10(c–d)). The splitting of the center side branch (Figure 5.10(e)) were confirmed by a separate image acquisition of the same imaging view shown at the top right corner as thumbnail (a zoom in from Figure 5.9(g) was also shown for comparison).

5.7 Discussion

5.7.1 Significance of This Work

Contrast-enhanced ultrasound microvasculature mapping can provide information such as vascular density and vessel size for diseases diagnosis and treatment evaluation; one potential application is the early detection and prognosis of plaque neovascularization. Mapping microvasculature *in vivo* is not a trivial task, especially in the presence of tissue motion. As demonstrated in Figures 5.7(a–b), tissue

motion as slow as 3 mm/s can already cause significant artifacts in the resultant maps. MRMVI has been specifically designed to address these tissue motion artifacts. Two key features collectively enable MRMVI to suppress motion artifacts. First, MRMVI is equipped with a multi-angle vector Doppler estimator to derive tissue motion consistently (Figure 5.2); this enables us to track the tissue displacement over extended time. The performance of this estimator has been demonstrated in previous works (Ketterling et al., 2017; Yiu & Yu, 2016). Second, it uses a per-pixel based compensation to counter-shift the estimated interframe drifts (Figure 5.3). This is crucial when the tissue motion and deformation are local.

We have demonstrated MRMVI's efficacy in suppressing the tissue motion artifacts under *in vitro* and *in vivo* environments. The theoretical performance of MRMVI was first evaluated on a micro-flow channels setup (Figure 5.4) with simulated tissue motions. The motion artifacts (Figures 5.7(a–b)) were suppressed by MRMVI (Figures 5.7(c–d)) with only slight degradation in mapping quality in terms of micro-flow channel size (Figure 5.8). The practical merit was further established through an *in vivo* experiment where the optic nerve head of a rat eye was imaged (Figure 5.5(b)). The choroid microvasculature of the rat eye serves as a good analog of the plaque neovascularization model as both share similar sizes but choroid has a well defined microvessel network. Our MRMVI was found to be able to track the tissue motion consistently over an extended period (> 1s, Movie 5.1). This attribute enabled MRMVI to extend the persistence duration to map the microvasculature of the choroid (Movie 5.2). The mapped microvasculature by MRMVI provides greater details of the choroid layer compared to power Doppler mapping (Figure 5.9). Moreover, the motion artifacts introduced by the tissue motion were largely suppressed by MRMVI (Figure 5.10). MRMVI represents a new way to visualize and quantify the intraplaque microvasculature in terms of the density of microvessels and vessel diameter, where plaque neovascularization is an important indicators of unstable plaque and a predictor of future cerebrovascular event. This might facilitate clinicians to personalize treatment strategy and perform risk evaluation before carotid surgery.

5.7.2 Other Potential Applications of MRMVI

MRMVI can also be used to improve the image quality of molecular imaging. Ultrasound contrast can be functionalized with ligand molecules that bind to specific target surface markers as reviewed by Unnikrishnan and Klibanov (2012). For example, P-selectin-targeted microbubbles (McEver & Cummings, 1997) can be used to detect inflammatory response and locate early atherosclerosis lesions, as demonstrated by Ramos et al. (1999), serving as an early detection strategy of atherosclerosis (Kaufmann et al., 2010). It should be noted that our MRMVI framework is not limited to high frequency transducer used in this study; it can be applied to low frequency transducer for carotid imaging and

other applications by calibrating the PSF used for microbubble position estimation. Furthermore, the exceptional signal strength given by the microbubbles could allow the mapping of cerebrovascular microvasculature (O'Reilly & Hynynen, 2013) and in turn quantify it in terms of vascular density. This enables the detection of regional cerebral blood flow reduction if there is a drop in regional vascular density, which has found to be an early sign of dementia as reported by other studies (Inui, Ito, Kato, & SEAD-J Study Group, 2017; Johnson et al., 2005; Niwa et al., 2016; Xekardaki et al., 2014).

5.7.3 Limitations and Future Work

The primary focus of this work is to report on a motion resistant framework for microvascular imaging; its performance was only evaluated under *in vitro* scenario and a proof-of-concept *in vivo* experimentation was conducted on the choroid microvasculature. Our initial experimentation has nonetheless demonstrated the potential of MRMVI in visualizing *in vivo* microvasculature under the presence of tissue motion. In the future, an *in vivo* pilot study should be conducted to attest the efficacy of MRMVI in mapping intraplaque microvessels. This can be made possible by implementing the MRMVI framework on the live imaging platform presented in Chapter 2.

Another direction worth pursuing is to employ blind deconvolution to localize microbubbles. One of the limitations of microvascular imaging is that the PSF derived from the metal wire (25 μm in diameter) may be different from that of microbubble (~1 μm in diameter), thus introducing errors in microbubble localization. In this regards, blind deconvolution does not require prior information on the PSF of the imaging system to achieve super resolution imaging (i.e., localization of microbubble in this context) as demonstrated by Sroubek, Cristobal, & Flusser (2007) and Bruce and Butte (2013). This approach may further improve resolution achieved with MRMVI and may extend the applicability of MRMVI to other applications because prior knowledge on the system PSF is no longer required.

Besides blind deconvolution, a natural extension of this work is to pursue 3-D microvascular mapping. Microvessel networks are 3-D in nature. However, with a 1-D array, we are limited to 2-D plane imaging of the vasculature. One potential solution is to use a 2-D array to capture the volumetric information in one transmission. This is important for microbubble localization because it would keep the speckle pattern of microbubbles consistent between transmissions and hence facilitating localization. The imaging framework presented in this chapter can readily be translated to volumetric imaging with small changes. Nonetheless, development of new imaging hardware is required for 3-D imaging.

5.8 Conclusion

The full potential of microvasculature imaging has not been realized because of tissue motion artifacts. In this paper, we have presented a new microvasculature imaging framework called MRMVI that can map microvasculature consistently by first tracking the interframe local tissue displacements and then taking them into account during the image formation process. With this technique, we mapped *in vivo* microvasculature, and plaque neovascularization could be quantified in terms of vascular density and vessel diameter. This framework may facilitate early identification of vulnerable plaque to prevent future stroke events.

Chapter 6
Volumetric Flow Rate Estimator for Global Cerebral Blood Flow Quantification

6.1 Introduction

Cerebral blood flow (CBF) reduction has recently been shown to be a predicting factor of cognitive decline (Chao et al., 2010; Kitagawa, 2010; Xekardaki et al., 2014) and dementia (including Alzheimer's disease; Encinas et al., 2003; Hirao et al., 2005; Schuff et al., 2009; Snyder et al., 2015). Using advanced neuroimaging techniques (Inui et al., 2017; Niwa et al., 2016; Xekardaki et al., 2014), it has been shown that patients with mild cognitive impairment (or MCI, a precursor of dementia) have up to 20% CBF reduction compared to cognitively intact individuals (Johnson et al., 2005). This CBF reduction leads to insufficient supply of oxygen and nutrients to meet the neurometabolic demand, causing hypoxia/ischemia and consequently brain atrophy, and then eventually dementia with chronic exposure (de la Torre, 2000, 2016). This pathological cascade is more prominent for those with atherosclerosis. The vascular hypothesis of Alzheimer's disease (de la Torre, 2018) suggests that atherosclerosis imposes additional burden onto the already declining CBF due to aging (Chen et al., 2011; Leenders et al., 1990). Thus, it is beneficial to routinely assess the impact the co-occurrence of atherosclerosis with CBF reductions to prevent the development of MCI and, in turn, dementia.

Routinely evaluating CBF is not a trivial task as the brain is encapsulated inside the skull. Transcranial Doppler (TCD) has been designed to tackle this task (Naqvi, Yap, Ahmand, & Ghosh, 2013; Willie et al., 2011). TCD quantifies CBF by measuring flow velocities of intracranial arteries such as middle cerebral arteries (MCA, supplied by the internal carotid arteries: Beishon, Haunton, Panerai, & Robinson, 2017; Topcuoglu et al., 2012) and its efficacy in detecting CBF reduction has been demonstrated in longitudinal studies (Chung, Lee, Lin, & Wang, 2017; Ruitenberg et al., 2005). However, the measured velocity is only a surrogate measure of CBF; it is only proportional to CBF when vessel cross-sectional area remains constant (Clark et al., 1996), which may not be a valid assumption in extreme physiology or different patient populations (Ainslie & Hoiland, 2014). Furthermore, TCD lacks spatial resolution as it can only measure flow velocity one vessel at a time (Wintermark et al., 2005). Instead of assessing CBF from intracranial arteries like MCA, extracranial arteries like the internal carotid and vertebral arteries (Oktar et al., 2006; Schebesch, Simka, Woertgen, Brawanski, & Rothoerl, 2004; Yazici, Erdogmus, & Tugay, 2005) can be used as global surrogates of CBF (Thomas, Lewis, Hill, & Ainslie, 2015); color flow imaging (CFI; Acar, Degirmenci, Yucel, Albayrak, & Haktanir, 2005; Oktar et al., 2006) and pulsed Doppler (PD: Yazici et al., 2005) have been

used to measure CBF from these sites. Unlike TCD, CFI and PD measure both time-averaged mean velocities and vessel diameter at the same time to derive CBF (Acar et al., 2005; Mitrasinovic et al., 2010; Oktar et al., 2006). However, such measurement cannot be performed in patients with abnormal arterial geometry (e.g., kinking or tortuosity; Dorfler, Puls, Schlieber, Maurer, & Becker, 2000; Trattnig et al., 1993). Thus, there is a need for innovations to develop new measurement techniques that can routinely and consistently assess extracranial CBF.

To address such need, a new volumetric flow rate measurement framework has been proposed (Kripfgans, Rubin, Hall, Gorden, & Fowlkes, 2006; Rubin, Tuthill, & Fowlkes, 2001). It first measures out-of-plane flow flux (flow rate per unit area) by analyzing the temporal correlation over time. The blood flow rate is then computed by integrating the flow flux over the blood vessel lumen. Initial results have demonstrated the feasibility of such framework under constant flow scenarios. One drawback is that, in theory, a very high-frame-rate (> 1,000 frame per second or fps) is required to estimate the interframe correlation consistently, which is not achievable with conventional beamline-based scanning methods. This may be solved by employing high-frame-rate ultrasound (HiFRUS) imaging principles, which can offer a 10,000 fps rate (Tanter & Fink, 2014), as demonstrated by Zhou et al. (2018), in which they derived the blood flow rate by measuring the spatial speckle decorrelations of ultrasound contrast over time. The benefit of this approach over the advanced 2-D array systems (Holbet, Pihl, Ewertsen, Nielsen, & Jensen, 2016; Jensen et al., 2016b) is that the hardware requirement (in terms of channel count and computation) is much less.

In this work, we present a new ultrasound framework called an instantaneous volumetric flow rate estimator (IVFRE) that can measure instantaneous blood flow rate without the need of ultrasound contrast. This framework leverages on the broad-field insonation imaging paradigm (Tanter & Fink, 2014) to acquire coherent blood flow RF data for the entire imaging view at high sampling rate, as previously demonstrated (Yiu, Chee, Tang, Luo, & Yu, 2019). From these RF data, two crucial pieces of information can be derived: (a) out-of-plane flow flux by analyzing speckle correlation over time and (b) in-plane flow vectors by multi-angle vector Doppler (Yiu & Yu, 2016). The instantaneous blood flow rate can consequently be derived as will be described in Section 6.2. This estimator is implemented on a live HiFRUS scanner (Section 6.3) and its performance evaluation based on *in vitro* and *in vivo* experiments will be presented in Sections 6.4, 6.5, and 6.6, respectively.

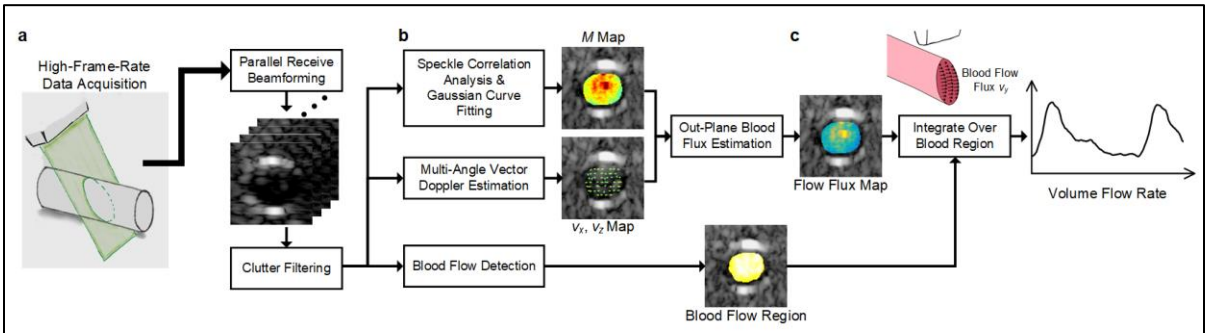

Figure 6.1. Overview of the volumetric flow rate estimation framework is shown: (a) image acquisition using high-frame-rate ultrasound and parallel beamforming; (b) three separate signal processing routines of the framework: (upper row) temporal correlation analysis, (mid-row) flow vector estimation, and (bottom row) blood flow detection; (c) estimation of volumetric flow rate based on the derived flow flux map and detected flow region from (b).

6.2 Theory

6.2.1 Overview of Volumetric Flow Rate Estimation Framework

IVFRE is founded upon two key principles: (a) the flow flux of each pixel can be derived by performing temporal correlation analysis (Rubin et al., 2001) and (b) the volumetric flow rate Q can then be deduced by integrating the flow flux v_y over the cross-sectional area A as

$$Q = \int_A v_y dA \tag{6.1}$$

Figure 6.1 gives an overview of the overall measurement framework. First, unsteered plane wave pulses are transmitted to interrogate the blood flow across the vessel cross section, as shown in Figure 6.1(a). The acquired pulse-echo RF signals are parallel beamformed to generate full-view images. This enables the coherent sampling of blood flow signal of the entire imaging at very high sampling rate as previously reported by Yiu et al. (2016) and Ishii, Yiu, & Yu (2017). Next, the blood signal of each pixel is extracted by applying a high-pass filter to suppress unwanted tissue clutter. Once the blood signal is extracted, multiple signal processing routines are carried simultaneously (see Figure 6.1(b)). As will be described in Section 6.2.3, blood speckle temporal correlation analysis (Figure 6.1(b) top row) is performed to estimate the overall velocity at a particular pixel. Here, time coherency of the blood speckle is exploited for correlation analysis, as opposed to spatial coherency used in previous work (Zhou et al., 2018), which may be hindered by the velocity gradient inside the blood vessel. At the same time, in-plane flow vectors are derived using the multi-angle least-squares estimator (midrow) described in (Yiu et al., 2014; Yiu & Yu, 2016). The out-of-plane flow flux v_y can consequently be deduced by subtracting the in-plane flow vectors from the overall velocity. This process is repeated for

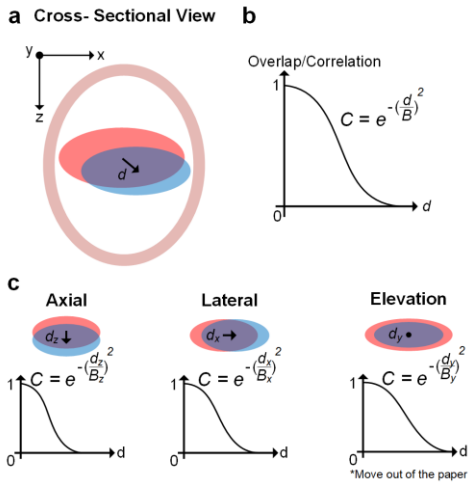

Figure 6.2. A conceptual illustration of the relationship between displacement and correlation is shown. (a) Illustration of a point scatterer (blue ellipsoid) moves away from its original position (red ellipsoid) with displacement *d* in 3-D space (the size of blue ellipsoid is reduced to depict the point scatterer move out of the paper); (b) the change in correlation (represented as overlapping area between the red and blue ellipsoids in (a)) as a function of displacement; (c) Illustration on how the correlation-displacement curve would vary in different direction of movements.

all pixels within the imaging view to generate a flow flux map, as shown in Figure 6.1(c). The cross-sectional flow area *A* is determined separately using Doppler flow detection (Figure 6.1(b) bottom row, to be discussed in Section 6.2.5). Finally, the blood flow rate *Q* is computed by integrating the corresponding v_y within the flow detected area *A*.

6.2.2 Background Principle of Flow Flux Estimation

As illustrated in Figure 6.2(a), the key concept behind the flow flux estimation is that as the blood speckles (highlighted in blue) moves away from their original position (highlighted in red), their correlation (illustrated as purple overlapping area) diminishes gradually. Figure 6.2(b) plots their correlation *C* as a function of displacement *d*; it has been shown that such relationship can be well approximated by a Gaussian function (Wear & Popp, 1987)

$$C[d] = e^{-(\frac{d}{B})^2} \tag{6.2}$$

where *B* is the beam correlation width (BCW: Rubin et al., 2001) that defines the correlation curve. The parameter *B* is related to the point spread function (PSF) and signal-to-noise ratio (SNR) for a particular imaging setup. A higher BCW means the blood speckle has to travel further to reduce the correlation to a certain level. Given that the PSF profile is different on each direction (axial, lateral and elevation), the 1D model in (3.2) in fact should be generalized into a 3-D Gaussian model such that

$$C = e^{-\left(\left(\frac{d_x}{B_x}\right)^2+\left(\frac{d_y}{B_y}\right)^2+\left(\frac{d_z}{B_z}\right)^2\right)} \tag{6.3}$$

where d_x, d_y, and d_z are the respective displacements in each direction, and B_x, B_y, and B_z are the constants that describe the change in correlation for a given displacement in the corresponding direction. With $v = d/t$, C can be expressed as a function of time

$$C[t] = e^{-\left(\frac{vt}{B}\right)^2} = e^{-\left(\left(\frac{v_x t}{B_x}\right)^2+\left(\frac{v_y t}{B_y}\right)^2+\left(\frac{v_z t}{B_z}\right)^2\right)} \tag{6.4}$$

where v is the overall velocity, v_z and v_x are axial and lateral velocity, and v_y is the out-of-plane flow flux, assuming the velocities do not change within the observation period. Taking log on both sides, (6.4) can be simplified as

$$\left(\frac{v}{B}\right)^2 = \left(\frac{v_x}{B_x}\right)^2 + \left(\frac{v_y}{B_y}\right)^2 + \left(\frac{v_z}{B_z}\right)^2 \tag{6.5}.$$

From (6.5), it can be seen that the flow flux v_y can be derived from the measured v/B (by Gaussian fitting the observed correlation-time curve) and in-plane flow vectors v_x & v_z (via multi-angle vector Doppler). Flow rate Q can consequently be deduced according to (6.1). It should be pointed out that B_x, B_y, and B_z are constants that depend on the imaging setup, and they can be determined by performing calibration experiments (to be discussed in Section 6.4.1).

6.2.3 Flow Flux Estimation through Blood Speckle Temporal Correlation Analysis and Gaussian Fitting

To derive the flow flux of each pixel, we need to first estimate the individual correlation-time curve through temporal correlation analysis (Rubin et al., 2011). This can be done by performing cross-correlation on the extracted blood signal s after clutter filtering (see Figure 6.1(a)), along the slow-time axis. To compute the correlation-time curve at time t, an ensemble of N samples is extracted from and correlated to s as

$$C_t[l] = \frac{\sum_{i=1}^{N}(s[t+i]-\mu_t)(s^*[t+i+l]-\mu_{t+l})}{N\sigma_t\sigma_{t+l}} \tag{6.6}$$

with

$$\mu_t = \frac{1}{N}\sum_{n=1}^{N} s[t+n] \tag{6.7}$$

$$\mu_{t+l} = \frac{1}{N}\sum_{n=1}^{N} s[t+n+l] \tag{6.8}$$

$$\sigma_t = \frac{1}{N}\sum_{n=1}^{N}(s[t+n] - \mu_t)^2 \tag{6.9}$$

$$\sigma_{t+l} = \frac{1}{N}\sum_{n=1}^{N}(s[t+n+l] - \mu_{t+l})^2 \tag{6.10}$$

where $C_t(l)$ is the l^{th} lag correlation coefficient at time t, μ_t, μ_{t+l}, σ_t, and σ_{t+l} are the local mean values and standard deviations for the N-sample segment of s at time t and $t+l$, and * denotes complex conjugate; this is repeated for $l = 0$ to $L - 1$ to generate the correlation-time curve C_t. Next, Gaussian fitting is applied to the correlation-time curve:

$$C[t] = e^{-(Mt)^2} = e^{-\left(\frac{vt}{B}\right)^2} \tag{6.11}$$

where M, the fitted parameter, is the decorrelation rate. By observation, the decorrelation rate M *is* equal to v/B and (6.5) becomes

$$M^2 = \left(\frac{v_x}{B_x}\right)^2 + \left(\frac{v_y}{B_y}\right)^2 + \left(\frac{v_z}{B_z}\right)^2 \tag{6.12}.$$

In practice, our blood signal is corrupted by random noise n and the observed signal s becomes $b + n$ where b is the true blood signal. The curve C_t derived in (6.6) is therefore only an estimate ($\hat{C}_t$) of the true correlation-time curve. To obtain a consistent estimate of the correlation-time curve C_t, one simple way is to take average of multiple estimates $\hat{C}_t$, in other words

$$\bar{C}_t[l] = \frac{1}{K}\sum_{k=0}^{K-1}\hat{C}_{t+k}[l] \tag{6.13}$$

where $\bar{C}_t(l)$ is the averaged correlation-time curve. The same Gaussian fitting procedure in (6.11) can then be performed to compute M. These procedures are repeated for all pixels at different time points to generate a time series of flow flux maps after taking into account of in-plane flow vectors (further discussed in Section 6.2.4) in (6.12).

6.2.4 In-Plane Flow Vector Estimation

More crucial data for flow flux estimation are the in-plane flow vectors. These are measured by using the multi-angle vector Doppler technique (Ishii et al., 2017; Yiu & Yu, 2016). In brief, P receive steering angles are used to generate P image frames from the channel RF data acquired from each unsteered plane wave transmission; this is repeated for acquired data. For each set of these images, pixel-based Doppler processing procedures are carried out similar to previous works (Yiu et al., 2014;

Yiu & Yu, 2013). First, clutter filtering is performed to extract the blood flow signal, followed by lag-one auto-correlation to estimate the mean Doppler frequency. After that, the measured vector **u** containing the *P* mean Doppler frequencies is passed to the least-squares estimator to derive the in-plane flow vectors (v_x, v_z) as

$$\begin{bmatrix} v_z \\ v_x \end{bmatrix} = \mathbf{A}^{\dagger}\mathbf{u} \tag{6.14}$$

where $\mathbf{A}^{\dagger}$ is the pseudoinverse of the angle matrix (Yiu & Yu, 2016). This is repeated for all pixels at different time points to generate a time series of flow vectors maps for flow flux estimation.

6.2.5 Flow Area Estimation based on Correlation Coefficient

The last step to derive instantaneous blood flow rate is to estimate the flow area that the flow flux is about to integrate over. This is achieved by detecting the flow using the correlation analysis performed for flow flux estimation. The idea is that the correlation of blood speckle at different lags would be noticeably higher than that of noise (close to zero for white noise). A mean correlation map *D* for flow detection can therefore be computed by taking average correlation across several lag as

$$D[t] = \sum_{l=1}^{l=l_o} \bar{C}_t[l] \tag{6.15}$$

where l_o is the maximum lag for averaging. Note that $\bar{C}_t(0)$ is not used because it is always 1, even for noise region. The flow area can thus be detected by applying a threshold to the mean correlation map *D*, where pixels with high correlation value correspond to flow pixel. The instantaneous volumetric flow is consequently computed by summing the flow flux of those flow pixels, multiplied by the pixel area, according to (6.1).

6.3 Imaging Methods

6.3.1 Imaging Hardware and Data Acquisition

The presented framework was implemented on a 192-channel programmable real-time HiFRUS imaging platform that our group developed earlier (Yiu, Walczak, Lewandowski, & Yu, 2019a) as an additional imaging mode for data acquisition. During operation, the default imaging mode (Yiu, Walczak, et al., 2019) that provides live feedback was first used to navigate to the region of interests. Once the region of interest was located, the operator switched to the data acquisition mode (with live feedback) to collect raw channel RF data. This was achieved by reprogramming the ultrasound module with a modified JavaScript object notation file (JSON) to switch from default imaging sequence to a new sequence designed for volumetric flow rate estimation. With this new sequence, full-view

acquisition at 8 kHz was achieved with unsteered plane wave excitation (0º transmission; 5 MHz center frequency, 5-cycle pulse) using an SL1543 probe (0.298 mm pitch; Esaote, Genova, Italy) connected to the HiFRUS imaging platform. The received echoes were sampled at 25 MHz sampling rate. Accordingly, raw data frames were acquired at a rate of 8,000 fps. In each acquisition, the channel radiofrequency (RF) data were stored on the 32 GB cyclic buffer residing in the personal computer (PC) system memory (6 s duration at 4 cm imaging depth). The data were then streamed offline to another Graphical processing unit (GPU) platform for processing (Yiu et al., 2011).

6.3.2 Plane Wave Image Formation

For each acquired dataset, parallel beamforming was performed to generate the image stack for flow rate estimation. We did this on the GPU computing platform using a codec programmed in Matlab (R2016a; Matworks Inc., Natick, MA, USA) in which the GPU accelerated parallel beamforming library (Yiu et al., 2011) was invoked. The codec first applied a 30th-order equiripple finite impulse response (FIR) bandpass filter (3-7 MHz with 50 dB out-of-band suppression; McClellan & Park, 2005) to the received channel RF data on a per-channel basis to suppress out-of-band white noise as described earlier (Yiu et al., 2011; Yiu, Walczak, et al., 2019). The analytic form of the filtered RF data was subsequently obtained using a FIR-based Hilbert transformer (50th order), as reported earlier (Yiu et al., 2011). With the analytic RF data, image frames (with 0.1 mm pixel spacing) were finally parallel beamformed with a set of $P = 3$ receive steering angles (-10°, 0°, 10°) using our GPU-based delay-and-sum algorithm (with 96 array channels used with Hanning apodization). This three-stage process was repeated for the data of different slow-time sampling instants, thereby generating three stacks of image frames over slow-time for correlation analysis (using 0° image stack) and multi-angle vector Doppler estimation (using all image stacks).

6.3.3 Signal Processing for Instantaneous Flow Rate Estimation

Flow rate estimation was carried out at various slow-time instants on a per pixel basis with procedures similar to those previously reported (Yiu et al., 2014; Yiu & Yu, 2013). First, for each image stack, a Doppler clutter filter was applied to suppress tissue echoes; this filter was implemented as a 134th order FIR high-pass filter (cutoff at 200 Hz with 100 dB suppression). Correlation analysis was performed on the 0° transmission image stack over ensemble vectors of $N = 128$ slow-time samples with a max lag L of 64. We obtained the mean correlation-time curve by averaging $K = 64$ estimates according to (3.13). Gaussian fitting was then performed on the mean correlation-time curve to measure M; we did this using an open source toolkit for GPU-accelerated curve fitting (Przybylski, Thiel, Keller-Finderisen, Stock, & Bates, 2017). We repeated this by sliding the observation window by 32 samples

to generate a time series of decorrelation rate map for full-view flow flux mapping. This is equivalent to 250 blood flow rate estimates per second

As for multi-angle vector Doppler estimation, all $P = 3$ image stacks were used to derive the in-plane flow vectors (Ishii et al., 2017; Yiu & Yu, 2016). First, for each stack, mean Doppler frequency estimation was conducted over ensemble vectors of $N = 128$ slow-time samples. The derived mean Doppler frequencies were stacked to form a $P = 3\times1$ measurand vector $\mathbf{u}$ and then multiplied by $\mathbf{A}^{\dagger}$ to obtain the in-plane flow vectors v_x and v_z according to (6.14). This two-stage procedure was repeated by sliding the observation window by 32 samples to generate a time series of flow vector maps that matched with the decorrelation rate maps M. A time series of flow flux v_y map was consequently computed with M, v_x, v_z as inputs according to (6.12).

At the same time, the mean correlation map D at each time point was derived based on (6.15) with the maximum lag for averaging $l_o = 4$. The flow area was then detected by applying a threshold of 0.3 to the mean correlation map; pixels with mean correlation above the threshold were categorized as flow detected pixels. Note that we chose this threshold given that the mean correlation from non-flow pixel (i.e., noise area) is low. The instantaneous volumetric flow rate was finally computed by integrating the flow flux v_y of the flow detected pixels multiplied by the pixel area according to (6.1).

6.4 Experimental Methods

6.4.1 Calibration of Beam Correlation Width for Flow Flux Estimation

To determine the beam correlation width B_x, B_y, and B_z in (6.12), we acquired several datasets, as described in Section 6.3.1, on a poly-vinyl alcohol (PVA)-based tissue mimicking phantom. The tissue phantom was fabricated based on the protocol reported earlier (Ho et al., 2017). In brief, we poured a PVA mixture into a casting box ($10\times10\times10$ cm^3) and administered three 24-hour thermal cycles to solidify the PVA mixture. The PVA mixture was consisted of 10% PVA (341584; Sigma-Aldrich, St Louis, MO, USA), 3% graphite (282863; Sigma-Aldrich), 0.3% potassium sorbate (85520; Sigma-Aldrich), and 83.7% distilled water. The acoustic speed and attenuation of this tissue mimic were, respectively, 1535 m/s and 0.229/(cm·MHz), as reported earlier.

Using the imaging system described in Section 6.3.1, tissue motion signals were obtained as illustrated in Figure 6.3(a); the transducer was translated using a linear motion stage (XYZ-BSMAE-F40L; InterlLiDriver, Southampton, PA, USA) at a constant speed (6 cm/s) along, for example, x-direction only. This would set v_y and v_z to zeros and reduce (6.12) to

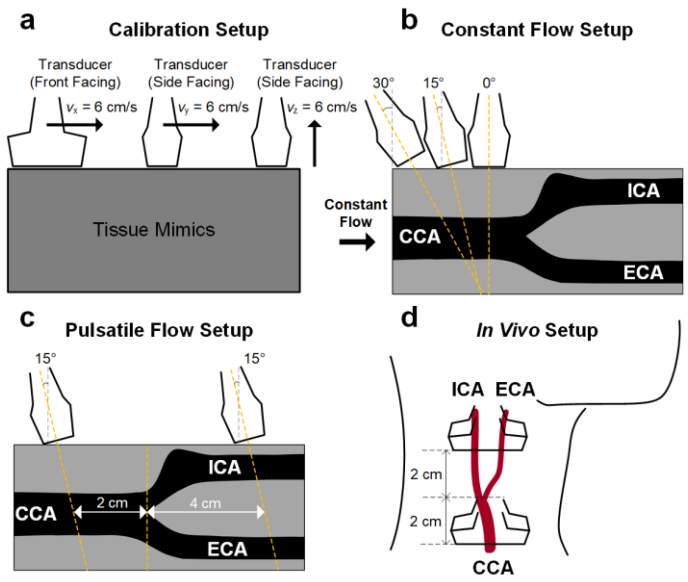

Figure 6.3. An illustration diagram of *in vitro* and *in vivo* imaging setups; (a) Experimental setup for beam correlation width (*B*) calibration; the transducer was mounted on a linear motion stage with different orientations to derive the beam correlation widths. (b) Imaging setup for constant flow calibration; the transducer was tilted with different angles in elevation to cover typical imaging scenarios (imaging planes were indicated as yellow lines). (c) Imaging setup for pulsatile flow; the transducer was placed 2 cm and 4 cm from the bifurcation point (center yellow line) with a 15° tilting in elevation. (d) Sketch diagram illustrating the imaging setup for *in vivo* experiment; the transducer was slightly tilted (~5-10°) from 90° and the acquisition planes were placed 2 cm away from the bifurcation site.

$$M^2 = \left(\frac{v_x}{B_x}\right)^2. \tag{6.16}$$

Given the speed of the motion stage, the constant B_x can be deduced by the measured M obtained as described in Sections 6.3.2 and 6.3.3. This was repeated for y- and z-directions as well to determine B_y and B_z with the transducer configured, as shown in Figure 6.3(a).

6.4.2 *In Vitro* Performance Evaluation using Carotid Bifurcation Phantom

To evaluate the estimation performance of the proposed framework, we conducted flow rate measurements on a 50% eccentric stenosed carotid bifurcation phantom that was developed earlier (Yiu, Chee, et al., 2019). The bifurcation phantom was connected to a flow circuit consisting of a programmable flow pump circulating blood mimicking fluid. The flow pump can deliver constant and carotid flow profile and the blood mimicking fluid was fabricated according to a standardized formula (Ramnarine et al., 1998). The fabrication procedure has been documented in previous work (Ho et al., 2017). We matched its dynamic viscosity (4.1 mPa·s) and density (1037 kg/m3) to that for blood.

Volumetric flow rates were measured at the common carotid artery (CCA) branch (see Figure 6.3(b)) with a diameter of 6 mm under different constant flow conditions (2-12 ml at 2 ml increment) according to the imaging procedures described in Section 6.3.1. This was repeated with different beam-flow angles (0°, 15°, 30° relative to the elevation direction; see Figure 6.3(b)) to investigate the effect of axial flow on flow rate estimation. To further demonstrate that our framework can measure instantaneous flow rate consistently, we separately measured the flow rate waveforms at CCA and internal and external carotid artery (ICA & ECA) branches under pulsatile flow condition (15 ml systolic flow rate, 60 bpm). Note that the transducer was placed at 2 cm and 4 cm away from the bifurcation for CCA and ICA+ECA acquisitions respectively to minimize the effect of disturbed flow on flow rate estimation, as shown in Figure 6.3(c). The flow rates were subsequently derived based on the procedures described in Sections 6.3.2 and 6.3.3. Note that the flow area for ICA and ECA were manually labelled by drawing enclosure maps for each vessel using Matlab built-in tool.

6.4.3 *In Vivo* Pilot Trial on Human Carotid Artery

An *in vivo* pilot study was conducted on five healthy adults (25 ± 5 years of age; one woman) with ethics approval (#22794) from the institutional review board. We asked the volunteers to rest in the supine position for 10 minutes prior to data acquisition. During the experiments, blood velocities in the longitudinal plane were first measured using a clinical ultrasound scanner (iE33; Philips Medical Systems, Andover, USA) with an L9-3 transducer (Philips Medical Systems) placed at the CCA, ICA and ECA, to confirm the forward flow profile, as shown in Figure 6.3(d). Instantaneous blood flow rate was then acquired with the HiFRUS imaging platform at the same arteries in the cross-sectional view, roughly 2 cm from the bifurcation site (Oktar et al., 2006), as shown in Figure 6.3(d), with a slight (~5-10°) probe tilt from 90°. The ICA and ECA cross-sections were acquired in the same scan in the same field of view and they are manually labelled the same way as the *in vitro* case. During the high-frame-rate data acquisition, the participants were asked to hold their breath during acquisition to reduce tissue motion (Au et al., 2018). Blood pressure and cerebral blood flow of the MCA were continuously monitored by finger photoplethysmography (Finapres NOVA; Finapres Medical Systems, Amsterdam, The Netherlands) and a transcranial Doppler device (WAKIe; Atys Medical, Soucieu en Jarrest, France), respectively. The synchronization signals from the ultrasound scanners and the TCD were fed to the data acquisition module (LabChart; ADInstruments, Colorado Springs, CO, USA) to synchronize the acquired instantaneous flow rate to the pressure waveform and MCA blood velocity.

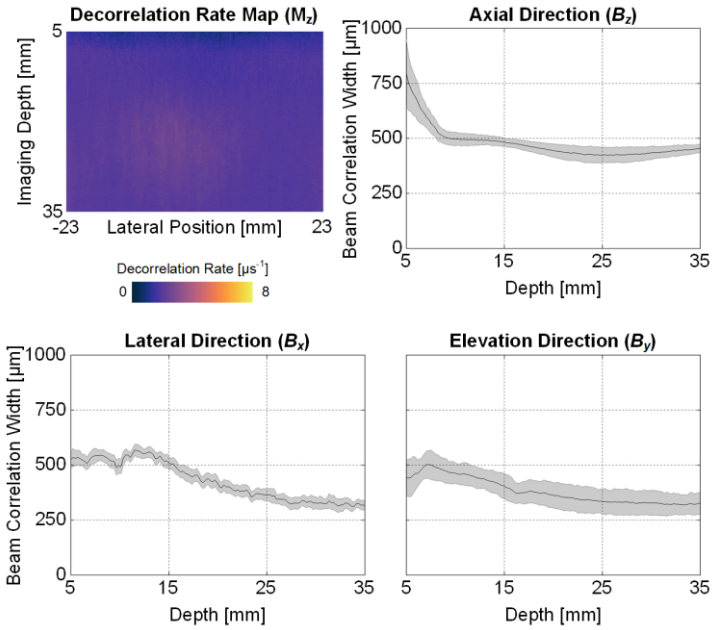

Figure 6.4. (a) The derived decorrelation rate map based on temporal correlation analysis; (b) axial; (c) lateral; and (d) elevation beam correlation width. The grey shaded area shows the variance along the lateral direction (see (a)) with ± 1 standard deviation.

6.5 Results

6.5.1 Consistent Decorrelation Rate Estimation across the Imaging View

The derived decorrelation rate was consistent along the lateral direction, and only dependent on the imaging depth, as shown in Figure 6.4(a). Figure 6.4(a) shows the decorrelation rate map obtained by scanning the tissue phantom while translating the transducer along the axial direction at 6 cm/s speed, as discussed in Section 6.4.1. Using this map, the B_z was deduced for every pixel, according to (6.16), and then averaged across the lateral direction. The derived B_z is plotted in Figure 6.4(b) with two observations. First, the variance along the lateral direction (shaded area, ±1 standard deviation) was small (36 μm). Second, the BCW varied less than 80 μm or 16% in the far field region (10 mm depth onward).

The same procedure was repeated to obtain the B_x and B_y along depth and was plotted in Figures 6.4(c) and 6.4(d). Contrary to the B_z, B_x and B_y had larger changes along depth. Both B_x and B_y gradually decreased from 500–300 μm in the far field region. This could be attributed to the lower SNR at greater depth. The lateral variance was consistent along depth for both B_x and B_y; the variance for B_y was roughly 50 μm, slightly higher than that of B_x (25 μm) and B_z (36 μm)

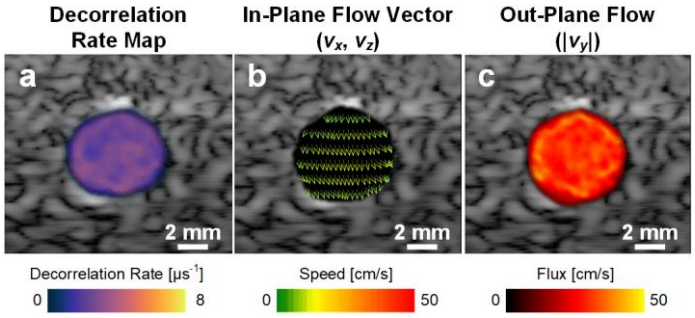

Figure 6.5. Mapping results of different signal processing routes are shown. (a) The derived decorrelation rate map based on temporal correlation analysis; (b) in-plane flow vectors derived using multi-angle least square estimator (Yiu, 2016); and (c) derived out-of-plane flow flux according to (12) with (a) and (b) as inputs.

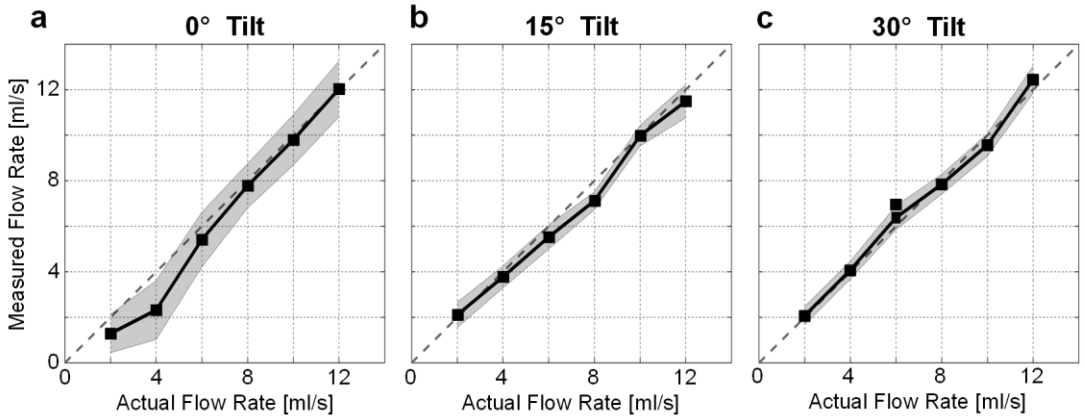

Figure 6.6. Measured flow rate versus actual flow rate obtained with (a) 0° tilting, (b) 15° tilting; and (c) 30° tilting in elevation as shown, along with the theoretical performance (dashed line). The square markers and shaded area represent estimate means and ± 1 standard deviation.

6.5.2 IVFRE Can Consistently Derive Volumetric Flow Rate

Our IFR framework measured the blood flow rate using the decorrelation rate map and in-plane flow vectors. Figures 6.5(a) and 6.5(b) show the corresponding maps obtained, as described in Sections 6.2.3 and 6.2.4 from the CCA branch with 10 ml/s constant flow rate and 15° tilt configuration (see Figure 6.3(b)), overlaid on top of a B-mode image. It can be seen that the estimated decorrelation rate is higher at the vessel center and lower near the wall region in Figure 6.5(a). At the same time, the derived flow vectors in Figure 6.5(b) were moving away from the transducer, consistent with the imaging setup (see Figure 6.3(b)). From these estimates, the out-of-plane flow flux map was deduced according to (6.12) and is shown in Figure 6.5(c). The vessel center has higher flow flux than the area near the wall region, consistent with laminar flow profile (Reynolds number = 537). The volumetric flow rate was found by integrating the flow flux within the flow detected region, as stated in (6.1).

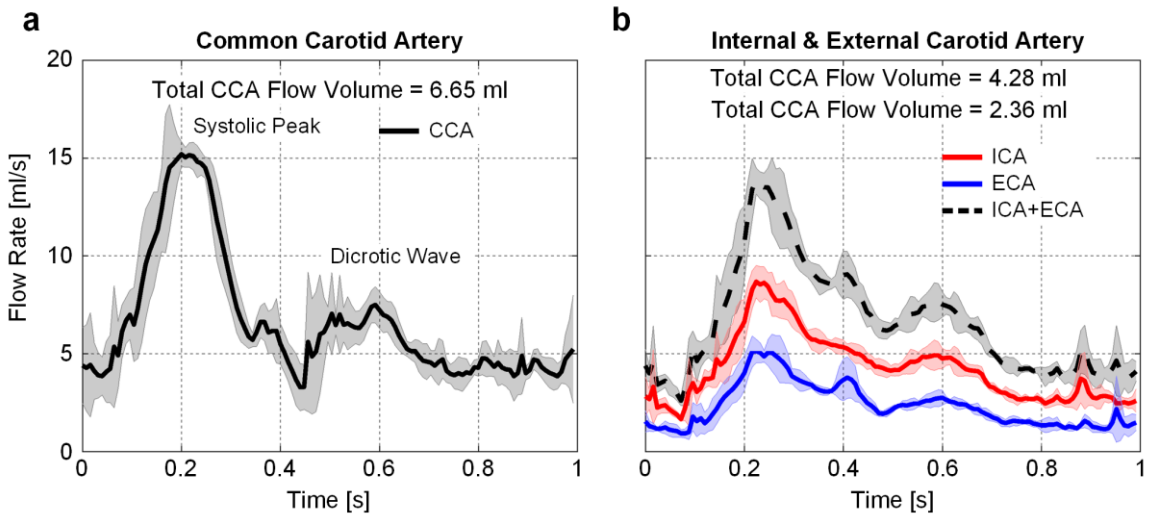

Figure 6.7. Time traces of volumetric flow rate at (a) CCA branch (dark), showing the systolic peak and dicrotic wave; and (b) ICA (red line) and ECA (blue line) branches and the sum of the two (dark dash line). The shaded area shows the estimation variance of ±1 standard deviation across 5 cycles.

Figures 6.6(a)–6.6(c) plot the measured flow rates against the actual ones for 0°, 15°, and 30° tilt configurations, respectively. The square markers and the gray shaded area, respectively, represent the estimate means and ±1 standard deviation (derived from 250 samples, equivalent to 1-second duration). There are three observations. First, IVFRE was in general able to measure flow rate consistently (<1 ml/s difference) over the tested range for all tilt configurations; the average estimation bias was 0.27 ml/s or 5.8%. Second, a significant underestimation (up to -41%) was observed for the 0° tilt at low flow rate (2-4 ml/s). This is probably due to the fact that flow signals were largely suppressed by the clutter filter when flow velocity and, in turn, Doppler shift was low. Third, the estimation variance was low for 15° and 30° tilt (0.5 ml/s) as compared to that of 0° tilt (1.1 ml/s). This was expected because the beam-flow angle for 0° tilt was close to 90°.

6.5.3 IVFRE can Resolve Flow Waveform with High Temporal Resolution

The characteristics of the pulsatile wave form at CCA, ICA, and ECA were clearly captured by our flow rate estimator, as plotted in Figure 6.7, averaged across 5 cycles. The flow profile acquired at CCA (F igure 6.7(a)) resembled a typical carotid flow profile (Holdsworth et al., 1999) with peak systolic flow at t = 0.1s, followed by the dicrotic notch at t = 0.4s. The measured systolic flow rate was close to the expected value at 15 ml/s. The estimation variance, shown as the shaded area in Figure 6.7(a), was on average 1.25 ml/s, and the variance was higher than average during the early systolic phase, early dicrotic, and end diastole.

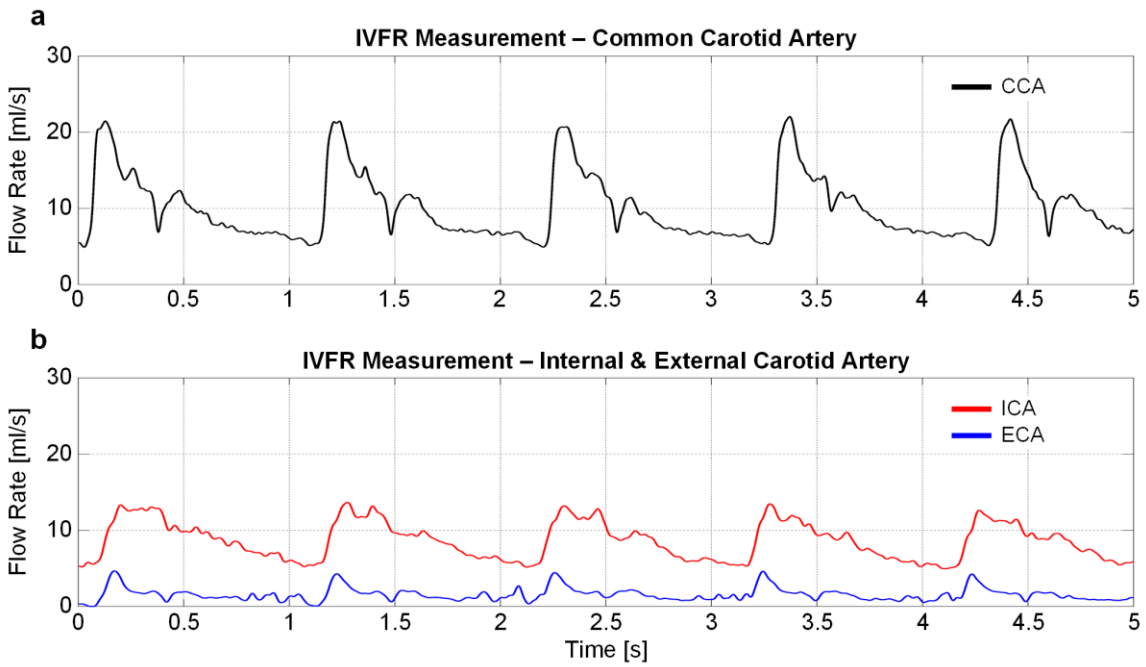

Figure 6.8. The graphs show the IVFRE-derived flow profile for (a) CCA (dark line); and (b) ICA (red line) and ECA (blue line) over 5 seconds. Note that the CCA flow profile and ICA-ECA flow profile were acquired separately.

Compared to the CCA, the ICA and ECA flow profiles have less distinctive systolic peaks and dicrotic waves, as shown in Figure 6.7(b). When combining both flow profiles together (dark dashed line in Figure 6.7(b)), a noticeable difference in the flow waveform can be observed from that of CCA profile. The peak flow rate at systole was reduced, the end systolic phase was dampened, and the dicrotic notch was less apparent. These could be attributed to the compliance of the phantom. During the systolic phase, the vessel phantom passively expanded due to increased pressure, reducing flow entering the ICA and ECA branches. At the final diastolic phase, the intraluminal pressure reduced and the phantom recoiled, passing the retained flow to the ICA and ECA branches, and dampening the end diastole and dicrotic wave. Despite the differences in the flow profiles, the time-averaged flow rate of ICA and ECA branches combined (6.64 ± 0.14 ml/s) matched that of CCA branch (6.65 ± 0.08 ml/s), further demonstrating the consistency of our flow rate estimator in measuring volumetric flow rate.

6.5.4 *In Vivo* Measurements are Consistent with Literature Data

When IVFRE was applied *in vivo*, it captured the volumetric flow profiles of the CCA, ICA, and ECA, which were consistent with those previously reported (Ford, Alpherin, Lee, Holdsworth, & Steinman, 2005; Hoi et al., 2010; Holdsworth et al., 1999). Figures 6.8(a) and 6.8(b) plot representative flow profiles captured from the CCA, ICA, and ECA of one participant over 5 seconds. There are three

Table 6.1

FLOW RATE SUMMARY OF DIFFERENT VESSELS ACQUIRED USING IVFRE

	Mean Volumetric Flow Rate VFR_{avg} (ml/s)				Peak Systolic Flow Rate VFR_{peak} (ml/s)				
Vessel	Mean	σ_{inter}	Min.	Max.	Mean	σ_{inter}	σ_{intra}	Min.	Max.
CCA	7.82	1.35	6.19	9.89	19.2	3.26	0.83	13.84	22.0
ICA	6.16	1.27	5.06	8.59	10.1	3.01	0.69	7.67	14.8
ECA	1.57	0.55	0.56	2.14	5.36	2.34	0.42	2.75	7.84

observations. First, the captured CCA profile (Figure 6.8(a)) contained distinctive features such as systolic peaks and the dicrotic notches, consistent with previously reported profiles (Holdsworth et al., 1999; Hoi et al., 2010). Second, the ECA flow profile (blue line in Figure 6.8(b)) was similar to CCA ones but lower in magnitude. Because of the high downstream resistance (Halpen et al., 1998), the ECA end diastolic flow rate was very low (< 1 ml/s); this resulted in lower mean flow rate. Third, the ICA flow profile (red line in Figure 6.8(b)) had flatter systolic peaks and dampened dicrotic waves in contrast. This is in line with previously reported observations (Ford et al., 2005; Hoi et al., 2010). The high diastolic flow rate observed in ICA (> 5 ml/s) helps to maintain cerebral perfusion and is largely controlled by the downstream cerebrovascular resistance (Panerai, 2008)

The measured mean flow rate and peak systolic flow rate for all three vessels are summarized in Table 6.1. We derived the mean flow rate by averaging the flow rate across 5 cardiac cycles. The mean flow rate of ECA (1.57 ± 0.55 ml/s) was close to reported values, while those of CCA (7.82 ± 1.35 ml/s) and ICA (6.16 ± 1.27) were higher than expected (CCA: 6.48 ± 1.23 ml/s; ICA: 4.08 ± 1.02 ml/s; Hoi et al., 2010). This could be due to the difference in mean group age between our recruited subjects and the groups in the literature because there is a noticeable drop in CBF at older age (Leenders et al., 1990). Meanwhile, the combined mean flow rate of ICA and ECA was 7.73 ±1.54 ml/s, which matched well to the CCA mean flow rate. Together with the low intra-individual estimation variance across three vessels (< 1ml/s) summarized in Table 6.1, these findings demonstrate the estimation consistency of IVFRE *in vivo*.

6.5.5 IVFRE Yields Comparable Variance to TCD

Comparing IVFRE to TCD measurements, we found that IVFRE yielded similar variance trends as TCD. Table 6.2 summarizes the flow velocities obtained from TCD. Relatively large inter-individual variances were noted in the mean flow velocity (FV_{avg}, 7.05 cm/s) and the peak flow velocity (FV_{peak},

Table 6.2

SUMMARY OF CEREBRAL BLOOD FLOW ACQUIRED USING TRANSCRANIAL DOPPLER ULTRASOUND

	Mean Flow Velocity FV_{avg} (cm/s)				Peak Flow Velocity FV_{peak} (cm/s)				
	Mean	σ_{inter}	Min.	Max.	Mean	σ_{inter}	σ_{intra}	Min.	Max.
MCA	45.2	7.05	35.78	51.42	67.4	9.34	2.65	61.1	81.2

9.34 cm/s). In contrast, we observed a small intra-individual variance (2.65 cm/s) in the peak flow velocity. These findings were in line with those observed in IVFRE. In terms of normalized variances (with respect to their corresponding mean values), we observed a discrepancy in the inter-individual variance (ICA: 30%; MCA: 14%); this could be due to side branch arteries between ICA and MCA (e.g., anterior cerebral artery not taken into account by the TCD measurement). However, IVFRE has a similar intra-individual variance to that of TCD (ICA: 7%; MCA: 4%). This may suggest that IVFRE has similar performance in deriving cerebral blood flow as TCD.

6.6 Discussion

6.6.1 IVFRE as a New Tool to Assess Blood Flow

Measuring instantaneous volumetric flow rate noninvasively is not a trivial task. In particular, three technical challenges must be addressed when devising a new flow rate estimation framework: (a) at a given time instant, the cross-sectional flow speed may vary spatially (e.g., deviate from a parabolic flow profile) because of the vessel geometry and flow condition; (b) over a cycle, the cross-sectional area of the artery may vary temporally due to vessel compliance and pulsatile nature of blood flow; and (c) both flow speed and cross-sectional area need to be measured simultaneously to derive instantaneous volumetric flow rate consistently. IVFRE has been specifically designed to overcome these challenges. It is equipped with three key features that have collectively enabled consistent estimation of volumetric flow rate. First, it can image blood vessel at cross-sectional area at very high-frame-rate (Tanter & Fink, 2014), enabling simultaneous sampling of blood flow signal and the blood flow area of multiple vessels at the same time (Figure 6.1(a)). Second, it integrates temporal correlation analysis (Rubin et al., 2001) and multi-angle vector Doppler technique (Ishii et al., 2017; Yiu & Yu, 2016) to derive the cross-sectional flow flux (Figure 6.1(b)). Third, it detects the blood flow area by analyzing the correlation at different lags and integrates the flow flux within the flow detected area to deduce the volumetric flow rate (Figure 6.1(c)). Together, these features contribute to a robust volume flow estimator with low intra-beat variability, which also shows promise in *in vivo* applications.

We have demonstrated IVFRE's efficacy in measuring instantaneous blood flow rate under different flow scenarios. We first evaluated the performance of IVFRE on the CCA branch of a carotid bifurcation phantom (Figure 6.3(b)). We showed that IVFRE was generally able to measure the flow rate consistently over the tested flow range with different transducer orientations (Figure 6.6), suggesting that our IVFRE can cope with different vascular geometries. The temporal resolution of IVFRE was further tested by acquiring the CCA, ICA, and ECA flow profiles from the bifurcation phantom (Figure 6.3(c)), and IVFRE was able to capture the distinctive features such as systolic peaks and dicrotic notches in the flow profile (Figure 6.7) previously reported by Holdsworth et al. (1999) and Ford et al. (2005). Furthermore, the mean flow rate passing through CCA matched well with the sum of that of ICA and ECA, demonstrating the consistency of IVFRE. More important, we established the practical merit of IVFRE with an *in vivo* pilot study (Figure 6.3(d)). We found it to be effective in measuring blood flow rate from CCA, ICA, and ECA (Figure 6.8) with small intra-individual variance (Table 6.1), even with beat-to-beat variability in cardiac output. Comparing it to standardize clinical research tools like TCD (Table 6.2), IVFRE yielded similar intra-individual and inter-individual variance (normalized with respect to mean measurements). This suggests that IVFRE has similar performance in deriving CBF as TCD.

6.6.2 Using IVFRE to Assess Global Cerebral Blood Flow and Cerebral Autoregulation

IVFRE represents an image-based, noninvasive blood flow rate measurement tool with fine temporal resolution without the use of contrast. It can provide a direct measurement of the global CBF by summing the measured blood flow rate at the arteries that supply all the blood to the brain, i.e. two ICAs and two vertebral arteries, instead of using TCD, which is known to have limitations in assessing global CBF due to unknown cerebral arterial diameter changes (e.g., exercise, altitude, chronic disease; Ainslie & Hoiland, 2014). From a dementia prevention standpoint, IVFRE has demonstrated its potential in providing routine measurement of CBF, and it is possible to detect global CBF reduction at early stage. This may help to identify MCI (Balestrini et al., 2013; Johnson et al. 2005; Marshall, 2012) at early stage before the disease deteriorates into dementia (Ruitenberg et al., 2005; Solfrizzi et al., 2004; Toth, Tarantini, Csiszar, & Ungvari, 2017).

IVFRE can also be used to evaluate dynamic cerebral autoregulatory responses. Cerebral autoregulation is a dynamic process (Panerai, 2008) responsible for actively redistributing blood flow to maintain CBF during changes in cerebral perfusion pressure (Panerai, 2008). Dynamic changes in perfusion pressure, such as standing up, which can elicit a rapid drop in blood pressure (Yang et al., 2014) are challenging to study, and IVFRE may provide a sensitive method to simultaneously assess extracranial blood flow redistribution related to the autoregulatory response (demonstrated in Figure

6.8(b)). This is important because autoregulatory impairment is a risk factor for cognitive impairment and dementia (Popa-wagner, Buga, Popescu, & Muresanu, 2015; Toth et al., 2017). IVFRE as an ultrasound-based (i.e., bedside) imaging modality also enables clinicians to monitor the ICA-ECA flow ratio in a single scan throughout the course of chronic disease and treatment (Eckstein et al., 2003).

6.6.3 Limitations and Future Work

In the future, some technical shortcomings can be refined to improve IVFRE. First, the segmentation of vessels can be improved. In cases where there are two or more vessels in the imaging view (e.g., ICA, ECA jugular vein), manual segmentation is required to segment and label these vessels to obtain the correct flow rate for each vessel. This task can be replaced by advanced image segmentation algorithms (Mao, Gill, Downey, & Fenster, 2011; Yang et al., 2013) and potentially deep learning algorithms (Trebeschi et al., 2017; Zhou, Takayama, Wang, Hara, & Fujita, 2017). Doppler power, correlation coefficients, and other parameters can supplement these algorithms to improve the segmentation performance. Furthermore, deep-learning algorithms (Zhang, Ying, Yang, Ahuja, & Chen, 2016) may be employed to label the vessels based on the pulsed wave Doppler waveforms and flow waveforms.

From a signal processing perspective, adaptive clutter-filtering techniques like eigen filtering can improve the framework through enhancing flow detection performance (Mauldin et al., 2011; Yu & Cobbold, 2008a). The advantage is twofold. First, eigen filtering further suppresses clutter at slow flow regions, reducing the effect of clutter on flow flux estimation. Second, eigen filtering would improve the flow detection performance, especially during the diastolic phase when flow is slow. Collectively, these two would further reduce the flow rate estimation variance.

6.7 Conclusion

CBF is undoubtedly an important indicator of cerebrovascular health. In this paper, we presented a new high-frame-rate ultrasound framework called IVFRE to noninvasively measure blood flow rate for the entire image view at fine temporal resolution by estimating the out-of-plane flow flux over time without the use of contrast. With this technique, CBF can be routinely monitored and may facilitate early detection of autoregulatory impairment and cognitive decline. It can also provide prognostic information useful in personalizing treatment strategy.

Chapter 7
Summary and Future Directions

7.1 Summative Recap of Contributions

Stroke and dementia remain the leading causes of mortality and serious long-term disability worldwide (WHO, 2018). Carotid atherosclerosis, a high prevalence disease (25% in general population; Prati et al. 1992), is one of the major causes of both diseases. However, current risk stratification strategies cannot identify individual risk because they still rely on (a) conventional risk factors that have well-documented limitations (Weber et al., 2015) and (b) structural changes of artery in which atherosclerotic plaques with identical degree of stenosis could have substantial differences in their associated risk (Nighoghossian et al., 2005; Rothwell et al., 2000). To better stratify carotid atherosclerotic risk and in turn stroke and dementia risks for each individual, we must go beyond the traditional risk factors and structural changes of the carotid arterial wall.

In this dissertation, we have reported a new noninvasive HiFRUS-based imaging framework and demonstrated how it can be used to consistently visualize and quantify vascular biomarkers; these quantified biomarkers may improve the atherosclerotic risk stratification performance when incorporated. With HiFRUS imaging, a frame rate of 1000+ fps can be achieved to enable advanced signal processing strategies to extract the necessary information in deriving vascular biomarkers, which can predict future cerebrovascular events (plaque neovascularization; Hellings et al., 2010; Michel at al., 2011) and development of mild cognitive impairment and dementia (cerebral blood flow reduction; Snyder et al., 2015; Xekardaki et al., 2014). We hypothesized that these vascular biomarkers directly related to atherosclerotic risk and its treatment can be quantified and visualized through the design of new HiFRUS functional mapping techniques.

From the results provided in Chapter 2, it can be seen that vascular biomarkers (in this case disturbed flow) can be visualized and quantified using HiFRUS imaging techniques like CESI. Furthermore, the live imaging capacity demonstrated in Chapter 2 provides live feedback for navigation, facilitating a human pilot study, as demonstrated in Chapter 6, and potentially routine monitoring of vascular biomarkers. The hypothesis is further substantiated by the results presented in Chapters 4, 5, and 6 where HiFRUS-based imaging algorithms were used to map and quantify disturbed flow, visualize microvasculature, and measure blood volume flow rate. In particular, Chapter 4 showed that HiFRUS-based disturbed flow mapping technique (DUBI) has a better detection performance than the conventional Doppler variance imaging approach (see Section 7.1.3 for further discussion). Furthermore, as discussed in Section 7.1.3, the microvasculature mapped by MRMVI reported in

Chapter 5 has much finer details than the one obtained by power Doppler imaging. Finally, the IVFRE framework presented in Chapter 6 can measure mean blood flow rate consistently and capture the carotid blood flow rate waveform at a much higher resolution in real time, which cannot be done by the conventional scanline-based paradigm (see Section 7.1.4 for further elaboration). The *in vivo* efficacy of the presented framework is further demonstrated on healthy subjects in initial pilot studies as discussed in Chapters 2, 5, and 6. Results showed that the framework can visualize arterial disturbed flow, map microvasculatures, and quantify blood flow rate. In-depth *in vivo* studies on patients with carotid atherosclerosis should be conducted to evaluate its effectiveness on quantifying the vascular biomarkers at different stages of atherosclerosis.

From an engineering standpoint, this dissertation has addressed several existing issues in ultrasound research. First, the new imaging platform reported in Chapter 2 has addressed the current challenges in developing HIFRUS imaging innovations by enabling researchers to implement custom transmit sequences, image formation strategies, and display rendering. These are not possible with current clinical scanners (see Section 7.1.1 for elaboration). Second, the novel flow phantom described in Chapter 3 enables the comprehensive evaluation of novel flow imaging algorithms with flow signal conditions resembling *in vivo* scenarios, which are not readily available with existing setups (see Section 7.1.2 for details). Third, the imaging algorithms presented in Chapter 4, 5, and 6 have demonstrated better performance in visualizing and quantifying vascular biomarkers compared to scanline-based method (further discussed in Sections 7.1.3 & 7.1.4).

From the clinical perspective, the reported overall framework has several implications. First, it represents an all-round solution in assessing carotid atherosclerosis with imaging modules that focus on initiation (DUBI) and progression (MRMVI) of atherosclerosis (see Section 7.1.3 for details), and another module (IVFRE) that focuses on evaluating the impact of atherosclerosis (see Section 7.1.4 for discussion). Second, the imaging algorithms developed in this thesis can also be used to study how these vascular biomarkers change at different stages of atherosclerosis. This could generate new insights into the pathophysiology of atherosclerosis and spark new treatment strategies of atherosclerosis (see 7.1.3 for discussion). Third, the presented framework denotes a complete solution for clinical translation; its compact size allows multisite study to be carried out easily (see Section 7.1.1 for elaboration). We anticipate that this framework will improve the atherosclerotic risk stratification process to more quickly identify at-risk individuals and facilitate the management of atherosclerotic and, in turn, stroke and dementia risks.

7.1.1 Specific Contribution: A Live Imaging System for HiFRUS Imaging

Chapter 2 presented a new open platform for HiFRUS imaging algorithm development and *in vivo* experimentation. This platform addresses the several challenges in developing HiFRUS algorithms with current scanners, forming the cornerstone of this thesis study. First, it enables the implementation of custom transmit sequence specifically designed for HiFRUS imaging application (as described in Section 2.2.1), which cannot be achieved with current clinical scanners. Second, it grants access to the channel-domain RF data acquired from all array elements in parallel (Section 2.2.2), enabling implementation of custom image-formation strategies to generate image frames at high-frame-rate (1,000+ fps). These image frames are subsequently used for advanced signal processing to quantify the vascular biomarkers. Third, the high computation capacity provided by the GPU allows these custom image-formation strategies and advanced signal-processing techniques to execute in real time (Section 2.3). These features collectively allow HiFRUS imaging algorithms to be implemented on the platform to perform live imaging experimentation.

The effectiveness of this platform was tested by implementing CESI framework on the platform (Section 2.3) and conducting *in vivo* experiments (Section 2.4). Results show that this live platform can provide live feedback for navigation (Section 2.5.1), crucial in *in vivo* experimentations as demonstrated in Chapter 6 (see Sections 6.4.3 and 6.5.4). Moreover, the implemented CESI was able to resolve the complex flow dynamics in bifurcations (Section 2.5.2); this shows the potential of HiFRUS imaging algorithms in visualizing and quantifying vascular biomarkers.

This is the first open platform that allows researchers to implement custom transmit sequences, custom image formation strategies, and custom image display simultaneously. Note that the latter two are executed in real time to provide live image feedback. From the ultrasound research standpoint, this platform allows researchers to develop any novel imaging algorithms on this platform, from imaging algorithm innovations like those presented in Chapters 4, 5, and 6, to advanced signal processing techniques (e.g., eigen-filtering; Yu & Cobbold (2008a, antialiasing scheme; Ekroll et al., (2016)), to complex visualization such as vector projectile imaging (Yiu et al., 2014) and particle visualization (Angelelli et al., 2014). On the clinical side, this platform provides a means to demonstrate novel imaging algorithms under *in vivo* settings and eventually conduct clinical trials to evaluate their effectiveness. The compact size of the open platform allows it to be carried to multiple locations for multisite study, facilitating clinical trials.

7.1.2 Specific Contribution: A Calibration Tool for Ultrasound Flow Imaging Experimentation

The design protocol of a new spiral flow phantom is reported in **Chapter 3**. This phantom is specifically designed with two key design aspects to attest the performance of novel flow estimation algorithms. First, the spiral geometry generates an omnidirectional flow profile that allows researchers to evaluate flow estimation performance from all possible flow directions and velocities. Second, the phantom fabrication process is lost-core centric (easy to fabricate); the spiral core is fabricated with PLA that is dissolvable in chlorinated solvent while the tissue-mimicking material is inert to the solvent.

The spiral phantom is used to evaluate the performance of a multi-angle least-squares estimator for vector flow imaging (Yiu et al., 2014; Yiu & Yu, 2016) which is one of the core components of the imaging algorithms presented in Chapters 5 and 6. Results have shown that the calibrated least-squares estimator (Yiu & Yu, 2016) is able to derive flow vectors consistently for all flow directions over the entire imaging view (see Section 3.4.3) and can render the spiral flow pattern inside the spiral phantom consistently using the projectile visualization technique previous reported (Yiu et al., 2014). This demonstrates that the new spiral flow phantom can be used evaluate the estimation performance of novel flow imaging algorithm as well as the effectiveness of new visualization technique. The calibrated multi-angle vector Doppler estimator is applied to other applications to study different complex flow dynamics, such as in utero flow (Ketterling et al., 2017) and urinary flow (Ishii et al., 2017).

This flow phantom addresses several issues with current evaluation methods. First, it provides a known flow profile that encompasses omnidirectional flow not readily available in the straight tube flow model used by Yiu et al. (2014). Second, it offers realistic signal characteristics matched to actual blood flow, including spatial and temporal decorrelation and signal-to-noise ratio, which are quite different from those provided by rotating disk phantom as presented by Walker et al. (2008), Kripfgans, Rubin, Hall, & Fowlkes, (2006), and Yiu & Yu, (2016). Third, it provides a flow velocity distribution that is evenly distributed across the imaging view, as opposed to the linear profile offered by rotating disks (low velocities around the center and high velocities near the edge). These attributes together enable a comprehensive assessment of performance of novel estimation algorithms, such as in terms of flow estimation variance and bias.

7.1.3 Specific Contribution: Visualization and Quantification of Vascular Biomarkers that Play Critical Roles in Atherogenesis and Progression

This dissertation presents two new HiFRUS imaging algorithms that focus on vascular biomarkers at different stages of atherosclerosis. Chapter 4 reported an imaging module called DUBI that focus on quantifying and visualizing disturbed flow, which is an important vascular biomarker in early plaque formation and promoting plaque growth (see Section 1.4.1). The overall framework is complemented by MRMVI (reported in Chapter 5**)** that focus on detecting and visualizing intraplaque microvasculature, a significant biomarker for plaque vulnerability at the mid-late stage of atherosclerosis and predictor of a future stroke event in a later stage of atherosclerosis (see Section 1.4.2).

Results have shown that DUBI is able to consistently visualize the differences in stable and unstable flow in terms of Doppler bandwidth and its spatial distribution at different time points; this is difficult to achieve with conventional Doppler variance imaging (Section 4.3.1.1). Furthermore, DUBI can detect the disturbed flow inside the unstable flow region identified using CEUS with better sensitivity and specificity (0.72 & 0.83 versus 0.68 & 0.66, see Section 4.3.1). Furthermore, because of the high temporal resolution achieved by the HiFRUS technique, DUBI can visualize the formation and dissipation of disturbed flow under pulsatile flow scenarios (Section 4.3.2). This could provide new insights into the effect of vessel geometry on disturbed flow dynamics and how disturbed flow progressively alters the vessel geometry. This demonstrates the effectiveness of DUBI in visualizing and quantifying unstable flow using Doppler bandwidth.

Results have demonstrated that MRMVI can consistently map a 50 μm-diameter vessel, which is smaller than the diffraction limit of ultrasound (Section 5.5), even in the presence of tissue motion. Such high spatial resolution enables MRMVI to map *in vivo* microvasculature of the choroidal layer with fine details, as reported in Section 5.6, which cannot be revealed by power Doppler imaging. The choroidal microvascular layer is similar in size to the intraplaque microvasculature. With MRMVI, intraplaque microvessels may be consistently mapped, even in the presence of arterial wall distension motion.

These two algorithms can provide prognostic information to facilitate atherosclerosis management. For instance, as demonstrated in Section 4.3.2, DUBI can be used to monitor the development of disturbed flow by tracking its intensity and extent, while MRMVI can be used to monitor the growth of intraplaque microvessels and evaluate its associated risk. More important, these two algorithms have demonstrated a new way to quantify vascular biomarkers that cannot be measured consistently before. With HiFRUS imaging, all data are captured; it is up to researchers to come up with innovative imaging

algorithms and signal processing strategies to extract the information needed to quantify the biomarkers.

7.1.4 Specific Contribution: Evaluating Impact of Carotid Atherosclerosis on Cerebral Blood Flow

Chapter 6 reported a new estimation method called IVFRE that offers a tool for measuring CBF to routinely evaluate the impact of carotid atherosclerosis on cognitive health. Carotid atherosclerosis has been suggested as one of the underlying causes of dementia in recent years by vascular hypothesis of Alzheimer's disease (de la Torre, 2018), which posits that atherosclerosis puts extra burden onto the already declining CBF (discussed in Section 1.4.3). Current strategies in evaluating CBF rely on heavy imaging modalities like PET/CT and MRI, which either uses ionizing radiation or has a long wait time (Ariste & Fortin, 2007; Emery et al., 2009), which makes them not suitable for routine monitoring. In contrast, IVFRE uses ultrasound which is a bed side imaging modality to derive CBF in real time, ideal for routine monitoring.

Results have demonstrated that IVFRE can derive the blood flow rate consistently over the range of tested flow rate (2–12 ml/s) with bias less than 6%, without the use of contrast (see Section 6.5.2). In particular, IVFRE can derive the blood flow rate consistently at different transducer orientations, as discussed in Section 6.5.2. This allows IVFRE to remain effective under different *in vivo* imaging scenarios. This is further demonstrated when conducting a pilot *in vivo* trial, as presented in Section 6.5.4; IVFRE is able to capture the blood flow rate waveform at high temporal resolution, which is not possible with a scanline-based paradigm (see Section 6.5.3). Moreover, IVFRE can measure the blood flow rate of different individuals, and the average flow rate is comparable to those reported in literature (see Section 6.5.4). Lastly, the intra-individual variation of IVFRE is comparable to that of TCD (7% vs 4%), which is common tool in assessing CBF. These results suggest that IVFRE is effective in evaluating the blood flow rate under an *in vivo* situation and provides comparable results to current clinically used tools.

IVFRE depicts an alternative way to monitor the actual CBF on a regular basis from TCD, which measures CBF velocity as a surrogate. More important, IVFRE can simultaneously capture the flow rate waveform of multiple vessels with fine temporal resolution within the same imaging view as demonstrated in Section 6.5.3. This may be used to evaluate the flow distribution between ICA and ECA at different phases of cardiac cycle, enabling one to assess one's cerebral autoregulatory response which has been shown to be a risk factor for cognitive impairment and dementia (Popa-wagner et al., 2015; Toth et al., 2017). Lastly, IVFRE can be used to assess global cerebral blood flow by measuring

the blood flow rate at the internal carotid and vertebral arteries. This could provide information to facilitate atherosclerosis management and treatment evaluation.

7.2 Future Directions

7.2.1 Toward Real-Time 3-D High-Volume-Rate Imaging

One natural extension of this thesis study is to move toward real-time 3-D ultrasound imaging. Complex flow patterns are 3-D in nature; current imaging strategies are limited to a 2-D slice of the 3-D flow pattern, which sometimes does not depict the overall flow scenario. One possible approach is to acquire the 3-D flow pattern retrospectively using gating, as demonstrated by Ho et al. (2017), but unfortunately it requires the flow pattern to be stable and repeatable, which is not possible for unstable flow where the flow pattern changes every cardiac cycle. An alternative is to use 2-D array to acquire volumetric information in real time. Nonetheless, there are several obstacles to be addressed: (a) the high channel count associated with 2-D array; (b) the massive amount of data generated from the high channel count; (c) the intense amount of computation required to generate volumetric image in real-time; and (d) the need of an intuitive visualization of the acquired data.

To address the first obstacle, researchers have proposed to use a row-column addressed 2-D array (Christiansen et al., 2015; Sauvage et al., 2018; Seo & Yen, 2009) that has the same total number of array element (1,000+) but fewer active ones per transmission (64–256), so that it can be used on current scanners. One drawback is that it takes multiple transmissions to acquire the same volumetric information (Holbek et al., 2016; Sauvage et al., 2018) as opposed to one transmission in a fully populated 2-D array. The 2-D spiral array is also proposed to perform volumetric imaging (Ramalli, Boni, Sovoia, & Tortoli, 2015); it has the same number (256) of elements as a typical array, but the element placements are optimized for volumetric imaging with focused transmission. The suitability of using spiral array for broad-view transmission remains to be studied.

As for the data issue, this live imaging platform can be extended to tackle the second issue by connecting multiple platforms together to acquire the channel-domain RF data from a fully populated array (1,000+ channels), as demonstrated by Provost et al. (2014) using a different system. The advantage of this approach is that the data transfer load is shared by the connected systems, lowering the hardware demand on a single system, at the expense of a larger overall size of the integrated system. With the flexibility of the presented system, custom transmit sequences, image formation strategies, and visualization techniques may be implemented with real-time performance.

GPU's processing power can be harnessed to address the third hurdle. The real-time implementation strategies discussed in this dissertation serve as guidelines on how imaging algorithms and advanced signal processing techniques can be implemented on GPU to achieve real-time performance. Other GPU implementations also serve as examples (Chee et al., 2017; Rosenzweig, Palmeri, & Nightingale, 2011; Yiu & Yu, 2015).

The critical challenge with volumetric imaging is how the 3-D volume information can be rendered in an intuitive way. The complexity of this multidimensional information makes it difficult to visualize and comprehend, especially in the case of HiFRUS functional imaging. For instance, Provost et al. (2014) and Provost, Papadacci, Gennisson, Tanter, & Pernot (2015) have presented new ways to visualize color Doppler volumetric images acquired using the HiFRUS technique with mixed success. This topic deserves more in-depth studies of different possibilities in visualizing the multidimensional information.

Besides the imaging system, experimental tools are crucial in developing novel imaging algorithms. The spiral flow phantom devised in this dissertation can be extended to facilitate the development of 3-D flow imaging algorithms. Instead of a spiral geometry, a toroidal one can be adopted to produce omnidirectional flow in all three dimensions. This provides a platform for researchers to perform a comprehensive evaluation on their novel algorithms, similar to the spiral phantom in the case of 2-D imaging. The same platform can also be used to facilitate the development of innovative 3-D visualization schemes.

7.2.2 Other Vascular Biomarkers Related to Atherosclerosis

Other vascular biomarkers are related to atherogenesis and plaque progression. For instance, wall shear stress (WSS) may play a significant role in the endothelial dysfunction and formation of plaque streak (Chiu & Chien, 2011). As discussed in Section 1.4.1, the endothelium's function is to maintain the mean WSS within a certain level (15-20 dyn/cm^2: Giddens et al., 1993; Girerd et al., 1996; Malek et al., 1999). If there is a sustained alteration in mean WSS, the endothelium will respond to this stimulation and attempt to restore the wall shear stress by undergoing various morphological changes including formation of fatty streaks (i.e., atherosclerotic lesions; Bonetti, Lerman, & Lerman, 2003; Gimbrone et al., 2000). Therefore, atherosclerotic lesions can be identified at early stage by detecting sustained WSS alteration.

Ricci, Swillens, Ramalli, Segers, & Tortoli (2017) demonstrated that wall shear rate (WSR; WSS divided by blood viscosity) can be estimated for a spatial location *in vivo* using a vector Doppler approach. Inspired by this, Ho (2018) developed a new imaging framework that can map WSR for the

entire imaging view using the HiFRUS framework and demonstrated its effectiveness in *in vitro* scenarios. The full potential of this WSR estimation framework can potentially be realized by implementing the framework onto the live imaging platform we reported above, and its *in vivo* efficacy may then be evaluated with pilot trials.

Another vascular biomarker related to atherosclerosis is *pulse wave velocity* (PWV), which refers to how quickly the blood pressure wave travels inside the artery. This pressure wave is created when the heart contracts to transport blood, and it travels along the arterial trees, causing the vessel wall to expand. The propagation speed of this pressure wave is determined by the stiffness of the artery; the stiffer the artery, the faster the pressure wave. PWV has been strongly associated with atherosclerosis (Boesen et al., 2015; van Popele et al., 2001; Wada et al., 1994). In clinical settings, PWV is typically measured using carotid-femoral pulse velocity (Asmar et al., 1995), which measures the global arterial stiffness (including aorta and large conduit arteries) instead of the local carotid.

As demonstrated in Chee et al. (2016), local stiffness of the carotid artery can be assessed by using HiFRUS to track the propagation of a pressure wave within the imaging view for *in vitro* models. This allows a more localized stiffness estimation. Apostolakis et al. (2016) have further demonstrated that local vascular disease can be detected by performing piecewise pulse wave imaging of the artery *in vivo*. This may facilitate the detection of local atherosclerotic lesions before significant plaque progression.

7.2.3 Regional Cerebral Blood Flow Mapping

Routine monitoring of global CBF could provide a mean to detect early signs of CBF reduction related to cognitive impairment and dementia, with the limitation that it does not pinpoint the affected region. It has been shown that patients with MCI and dementia have lower regional CBF (Johnson et al., 2005; Niwa et al., 2016; Park et al., 2012). The microvascular imaging technique (MRMVI reported in Chapter 6) can fill this niche by mapping the local cerebral microvasculature and in turn the regional cerebral vascular density. Errico et al. (2015) have demonstrated initial success in mapping cerebral microvasculature by using similar technique. Regions with lower CBF is believed to have lower vascular density; by using MRMVI to map the local vascular density, regional reduction in CBF can therefore be detected. This information coupled with global CBF reduction may be used to identify patients at risk of developing MCI and dementia. In-depth studies should be conducted to (a) investigate the feasibility of using MRMVI to map human cerebral microvasculature; (b) confirm the correlation between vascular density and regional CBF; and (c) determine the predictive power of vascular density in MCI and dementia.

7.2.4 Colocalization of Vascular Biomarkers to Achieve Multiparametric Assessment

Although it seems that each of the reported imaging modules has its own imaging strategy, they share the same transmission scheme. It is therefore possible to integrate these modules into one by implementing the common transmission scheme. The same dataset can then be used by each imaging module to extract the relevant information to derive the target vascular biomarkers. For example, the DUBI algorithm (presented in Chapter 4) can be applied to the dataset acquired by the CESI framework (described in Chapter 2) to extract the Doppler bandwidth and detect and quantify any disturbed flow in the same imaging view. This allows multiple vascular biomarkers to be extracted at the same time with high coherency between the derived biomarkers. This could enable multiparametric assessment for atherosclerotic risk assessment and improve stratification accuracy. With the HiFRUS imaging technique, we can derive various vascular biomarkers related to different diseases. It is up to researchers to design novel imaging schemes and signal processing strategies to extract the necessary information to visualize and quantify the target biomarkers.

References

2016 BRFSS survey data and documentation. Centers for Disease Control and Prevention website. https://www.cdc.gov/brfss/annual_data/annual_2016.html. Accessed May 21, 2019.

Aboyans, V., Criqui, M. H., Denenberg, J. O., Knoke, J. D., Ridker, P. M., & Fronek, A. (2006). Risk factors for progression of peripheral arterial disease in large and small vessels. *Circulation*, *113*(22), 2623-2629.

Acar, M., Degirmenci, B., Yucel, A., Albayrak, R., & Haktanir, A. (2005). An evaluation of internal carotid artery and cerebral blood flow volume using color duplex sonography in patients with vertebral artery hypoplasia. *Eur J Radiol*, *53*(3), 450-453.

Agency for Healthcare Research and Quality. Total expenditures in millions by condition, United States, 1996–2015: Medical Expenditure Panel Survey. https://meps.ahrq.gov/mepstrends/hc_cond/. Accessed May 21, 2019.

Ainslie, P. N., & Hoiland, R. L. (2014). Transcranial Doppler ultrasound valid, invalid, or both?. *J Appl Physiol*, *117*(10), 1081-1083.

Alonso, A., Artemis, D., & Hennerici, M. G. (2014). Molecular imaging of carotid plaque vulnerability. *Cerebrovasc Dis*, *39*(1), 5-12.

Ammirati, E., Moroni, F., Norata, G. D., Magnoni, M., & Camici, P. G. (2015). Markers of inflammation associated with plaque progression and instability in patients with carotid atherosclerosis. *Mediators Inflamm*, 2015, Art. no. 718329.

Anand, S., Shantha Selva Kumari, R., Thivya, T., & Jeeva, S. (2013). Sharpening enhancement of ultrasound images using contourlet transform. *Optik*, 124(21), 4789-4792.

Anderson, C. M., Saloner, D., Lee, R. E., Griswold, V. J., Shapeero, L. G., Rapp, J. H., Nagarkar, S., … Gooding, G. A. W. (1992). Assessment of carotid artery stenosis by MR angiography comparison with x-ray angiography and color-coded Doppler ultrasound. *AJNR Am J Neuroradiol*, *13*(3), 989-1003.

Andreucci, M., Faga, T., Serra, R., De Sarro, G., & Michael, A. (2017). Update on the renal toxicity of iodinated contrast drugs used in clinical medicine. *Drug Healthc Patient Saf*, *9*, 25-37.

Angelelli, P. Snare, S. R., Nyrnes, S. A., Bruckner, S., Hauser, H. & Lovstakken, L. (2014). Live ultrasound-based particle visualization of blood flow in the heart. In *Proc. 30th Spring Conf Comput Graph*, 13-20.

Antigam, L., & Steinman, D. A. (2009). Rethinking turbulence in blood. *Biorheology*, *46*(2), 77-81.

Apostolakis, I. Z., Nandlall, S. D., & Konofagou, E. E. (2016). Piecewise pulse wave imaging (pPWI) for detection and monitoring of local vascular disease in murine aortas and carotids *in vivo*. *IEEE Trans Med Imag*, *35*(1), 13-28.

Ariste, R., & Fortin, G. (2007). Could MRI and CT scanners be operated more intensively in Canada?. *Health Policy*, *3*(1), e113-e120.

Asgfaq, M., Brunke, S. S., Dahl, J. J., Ermet, H., Hansen, C., & Insana, M. F. (2006). An ultrasound research interface for a clinical system. *IEEE Trans Ultrason Ferroelectr Freq Control*, *53*(10), 1772-1782.

Asmar, R., Benetos, A., Topouchian, J., Laurent, P., Pannier, B., Brisac, A. E., … Levy, B. L. (1995). Assessment of arterial distensibility by automatic pulse wave velocity measurement. *Hypertension*, *26*(3), 485-490.

Assmann, G., Cullen, P., & Schulte, H. (2002). Simple scoring scheme for calculating risk of acute coronary events based on the 10-year follow-up of the prospective cardiovascular Munster (PROCAM) study. *Circulation*, *105*(3), 310-315.

Au, J. S., Hughson, R. L., & Yu, A. C. H. (2018). Riding the plane wave: Considerations for *in vivo* study designs employing high-frame-rate ultrasound. *Appl Sci*, *8*(2), Art. no. 286.

Avdal, J., L. Lovstakken, & Torp, H. (2015). Effects of reverberations and clutter filtering in pulsed Doppler using sparse sequences. *IEEE Trans Ultrason Ferroelectr Freq Control*, *62*(5), 828-838.

Babadi, B., & Brown, E. N. (2014). A Review of Multitaper Spectral Analysis, *IEEE Trans Biomed Eng*, 61(5), 1555-1564.

Baber, U., Mehran, R., Sartori, S., Schoos, M. M., Sillesen, H., Muntendam, P., … Fuster, V. (2015). Prevalence, impact, and predictive value of detecting subclinical coronary and carotid atherosclerosis in asymptomatic adults: the bioimage study. *J Am Coll Cardiol*, *65*(11), 1065-1074.

Balestrini, S., Perozzi, C., Altamura, C., Vernieri, F., Luzzi, S., Bartolini, M., … Silvestrini, M. (2013). Severe carotid stenosis and impaired hemodynamics can influence cognitive deterioration. *Neurology*, *80*(23), 2145-2150.

Bascom, P. A. J., Cobbold, R. S. C., Routh, H. F., & Johnston, K. W. (1993). On the Doppler signal from a steady flow asymmetrical stenosis model: effects of turbulence. *Ultrasound Med Biol*, *19*(3), 197-210.

Barber, K. M., Pinero, A., & Truskey, G. (1998). Effects of recirculating flow on U-937 cell adhesion to human umbilical vein endothelial cells. *Am J Physiol Heart Circ Physiol*, *275*(2), H591-H599.

Barnett, H. J. M., Meldrum, H. E., & Eliasziw, M. for the North American Symptomatic Carotid Endarterectomy Trial (NASCET) Collaborators (2002). The appropriate use of carotid endarterectomy. *CMAJ*, *166*(9), 1169-1179.

Bassiouny H. S., Song, R. H., Hong, X. F., Singh, A., Kocharyan, H., & Glagov, S. (1998). Flow regulation of 72-kD collagenase IV (MMP-2) after experimental arterial injury. *Circulation*, *98*(2), 157-163.

Beishon, L., Haunton, V. J., Panerai, R. B., & Robinson, T. G. (2017). Cerebral hemodynamics in mild cognitive impairment: A systematic review. *J Alzheimers Dis*, *59*(1), 369-385.

Belcaro, G., Nicolaides, A. N., Ramaswami, G., Cesarone, M. R., De Sanctis, M., Incandela, L., … Martines, G. (2001). Carotid and femoral ultrasound morphology screening and cardiovascular events in low risk subjects: a 10-year foloow-up study (the CAFES-CAVE study). *Atherosclerosis*, **156**, 379-387.

Benjamin, E. J., Muntner, P., Alonso, A., Bittencourt, M. S., Callaway, C. W, Carson, A. P., … Virani, S. S., on behalf of the American Heart Association Council on Epidemiology and prevention statistics committee and Stroke Statistics subcommittee (2019). Heart disease and stroke statistics – 2019 update: A report from the American Heart Association. *Circulation*, *139*, e56-e528.

Bercoff, J., Montaldo, G., Loupas, T., Savery, D., Mezierem, F., Fink, M., & Tanter, M. (2011). Ultrafast compound Doppler imaging: providing full blood flow characterization. *IEEE Trans Ultrason, Ferroelectr, Freq. Control*, *58*(1), 134-147.

Bjaerum. S., Torp, H., & Kristoffersen, K. (2002). Clutter filter design for ultrasound color flow imaging. *IEEE Trans Ultrason Ferroelectr Freq Control*, *49*(2), 204-216.

Bluestein, D., Niu, L., Schoephoerster, R. T., & Dewanjee, M. K. (1997). Fluid mechanics of arterial stenosis: relationship to the development of mural thrombus. *Ann Biomed Eng*, *25*, 344-356.

Bobryshev, Y., Cherian, S. M., Inder, S. J., & Lord, R. S. A. (1999). Neovascular expression of VE-cadherin in human atherosclerotic arteries and its relation to intimal inflammation. *Cardiovasc Res*, *43*(4), 1003-1017

Bonetti, P. O., Lerman, L. O., & Lerman A. (2003). Endothelial dysfunction: a marker of atherosclerotic risk. *Arterioscler Thromb Vasc Biol*, *23*(2), 168-175.

Boni, E., Bassi, L., Dallai, A., Guidi, F., Meacci, V., Ramalli, A., … Tortoli, P. (2016). ULA-OP 256: A 256-channel open scanner for development and real-tim implementation of new ultrasound methods. *IEEE Trans Ultrason Ferroelectr Freq Control*, *63*(10), 1488-1495.

Boni, E., Yu, A. C. H., Freear, S., Jensen, J. A., & Tortoli, P. (2018). Ultrasound open platforms for next-generation imaging technique development. *IEEE Trans Ultrason Ferroelectr Freq Control*, *65*(7), 1078-1092.

Browne, J. E. (2014). A review of Doppler ultrasound quality assurance protocols and test devices. *Phys Med*, *30*(7), 742-751.

Bruce, M. A., & Butte, M. J. (2013). Real-time GPU-based 3D deconvolution. *Opt Express*, 21(4), 4766-4773.

Burg, J. P. (1972). The relationship between maximum entropy spectra and maximum likelihood spectra. *Geophyscis*, *37*(2), 375-376.

Capineri, L., Scabia, M., & Masotti, L. (2002). A Doppler system for dynamic vector velocity maps. *Ultrasound Med Biol*, *28*(2), 237-248.

Centers for Disease Control and Prevention (CDC) (2009) Prevalence and most common causes of disability among adults: United States, 2005. *MMWR. Morb Mortal Wkly Rep*, *58*(16), 421–426

Chang, L. J., & Tarbell, J. M. (1988). A numerical study of flow in curved tubes simulating coronary arteries. *J Biomech*, *21*(11), 927-937.

Chao, L. L., Buckley, S. T., Kornak, J., Schuff, N., Madison, C., Yaffe, K., … Weiner, M. W. (2010). ASL perfusion MRI predicts cognitive decline and conversion from MCI to dementia. *Alzheimer Dis Assoc Disord*, *24*(1), 19-27.

Chee, A. J. Y., Ho, C. K., Yiu, B. Y. S., & Yu, A. C. H. (2016). Walled carotid bifurcation phantoms for imaging investigations of vessel wall motion and blood flow dynamics. *IEEE Trans Ultrason Ferrorlectr Freq Control*, *63*(11), 1852-1864.

Chee, A. J. Y., Yiu, B. Y. S., & Yu, A. C. H. (2017). A GPU-parallelized Eigen-based clutter filter framework for ultrasound color flow imaging. *IEEE Trans Ultrason. Ferroelectr Freq Control*, *64*(1), 150-163.

Chee, A. J. Y., & Yu, A. C. H. (2018). Receiver operating characteristic analysis of eigen-based clutter filters for ultrasound color flow imaging. *IEEE Trans Ultrason Ferroelectr Freq Control*, *65*(3), 390-399.

Chen, J. J., Rosas, H. D., & Salat, D. H. (2011). Age-associated reductions in cerebral blood flow are independent from regional atrophy. *NeuroImage*, *55*(2), 468-478.

Chen, J., Tung, C. H., Mahmood, U., Ntziachristos, V., Gyurko, R., Fishman, M. C., … Weissleder, R. (2002). *In vivo* imaging of proteolytic activity in atherosclerosis. *Circulation*, *105*(23), 2766-2771.

Cheung, C. C. P., Yu, A. C. H., Salimi, N, Yiu, B. Y. S., Tsang, I. K. H., Kerby, B., … Dickie, K. (2012). Multi-channel pre-beamformed data acquisition system for research on advanced ultrasound imaging methods. 59(2), 243-253.

Chung, C. P., Lee, H. Y., Lin, P. C., & Wang, P. N. (2017). Cerebral artery pulsatility is associated with cognitive impairment and predicts dementia in individuals with subjective memory decline or mild cognitive impairment. *J Alzheimers Dis*, *60*(2), 625-632.

Chien, S. (1972). Present state of blood rheology. In: Hemodilution, theoretical basis and clinical application, edited by Messmer, K. and Schmid-Schonbein, H. B.: Karger.

Chien, S. (2003). Moelcular and mechanical bases of focal lipid accumulation in arterial wall. *Prog Biophys Mol Biol*, *83*(2), 131-151.

Chiu, J. J., Wang, D. L., Chien, S., Skalak, R., & Usami, S. (1998). Effects of disturbed flow on endothelial cells. *J Biomech Eng*, *120*(2), 2-8.

Chiu, J. J., & Chien, S. (2011). Effects of disturbed flow on vascular endothelium: pathophysiological basis and clinical perspectives. *Physiol Rev*, *91*(1), 327-387.

Christiansen, T. L., Rasmussen, M. F., Bagge, J. P., Moesner, L. N., Jensen, J. A., & Thomsen, E. V. (2015). 3-D imaging using row-column-addressed arrays with integrated aprodization – part II: transducer fabrication and experimental results. *IEEE Trans Ultrason Ferroelectr Freq Control*, *62*(5), 959-971.

Christensen-Jeffries, K., Browning, R. J., Tang, M. X., Dunsby, C., & Eckersley, R. J. (2015). *In vivo* acoustic super-resolution and super-resolved velocity mapping using microbubbles. *IEEE Trans Med Imag, 34*(2), 433-440.

Cikes, M., Tong, L., Sutherland, G. R., & D'hooge, J. (2014). Ultrafast cardiac ultrasound imaging. *JACC-Cardiovasc Imag, 7*(8), 812-823.

Clark, J. M., Skolnick, B. E., Gelfand, R., Farber, R. E., Stierheim, M., Stevens, W. C., … Lambertsen, C. J. (1996). Relationship of 133Xe cerebral blood flow to middle cerebral arterial flow velocity in mean at rest. *J Cereb Blood Flow Metab, 16*(6), 1255-1262.

Clevert, D. A., Sommer, W. H., Zengel, P., Helck, A., & Reiser, M. (2011). Imaging of carotid arterial diseases with contrast-enhanced ultrasound (CEUS). *Eur J Radiol, 80*(1), 68-76.

Cloutier, G., Allard, L., & Durand, L. G. (1996). Characterization of blood flow turbulence with pulsed-wave and power Doppler ultrasound imaging. *J Biomech Eng, 118*(8), 318-325.

Cloutier, G., Chen, D., & Durand, L. G. (2001). Performance of time-frequency representation techniques to measure blood flow turbulence with pulsed-wave Doppler ultrasound. *Ultrasound Med Biol, 27*(4), 535-550.

Clowes, A. W., Kirkman, T. R., & Clowes, M. M. (1986). Mechanisms of arterial graft failure. II. Chronic endothelial and smooth muscle cell proliferation in healing polytetrafluoroethylene prostheses. *J. Vasc Surg, 3*(6), 877-884.

Cocker, M. S., Mc Ardle, B., Spense, J. D., Lum, C., Hammond, R. R., Ongaro, D. C., … Beanlands, R. S. B. (2012). Imaging atherosclerosis with hybrid [^{18}F]fluorodeoxyglucose positron emission tomography/computed tomography imaging: what Leonardo da Vinci could not see. *J Nucl Cardiol, 19*(6), 1211-1225.

Cohklin, B. S., Zhong, D. S., Zhao, W., Lin, P. H., & Chen, C. (2002). Shear stress regulates occluding and VEGF expression in porcine arterial endothelial cells. *J Surg Res, 102*(1), 13-21.

Couture, O., Hingot, V., Heiles, B., Muleki-Seya, P., & Tanter, M. (2018). Ultrasound localization microscopy and super-resolution: a state of the art. *IEEE Trans Ultrason Ferroelectr Freq Control, 65*(8), 1304-1320.

D'Agostino, R. N. Sr., Vasan, R. S., Pencina, M. J., Wolf, P. A., Cobain, M., Massaro, J. M., & Kannel, W. B. (2008). General cardiovascular risk profile for use in primary care: the Framingham heart study. *Circulation, 117*(6), 743-753.

Davies, M. J., & Woolf, N. (1993). Atherosclerosis: what is it and why does it occur?. *Br Heart J*, *69*(1 Suppl), S3-S11.

Davies, P. F. (1995). Flow-mediated endothelial mechanotransduction. *Physiol Rev*, *75*(3), 519-560.

de Hoon, M. J. L., van der Hagen, T. H. J. J., Schoonewelle, H., & van Dam, H. (1996). Why yule-walker should not be used for autoregressive modelling. *Am Nucl Energy*, *23*(15), 1219-1228.

de la Torre, J. (2000). Critically attained threshold of cerebral hypoperfusion: the CATCH hypothesis of Alzheimer's pathogenesis. *Neurobiol Aging*, *21*(2), 331-342.

de la Torre, J. (2016). Alzheimer's turning point: a vascular approach to clinical prevention. Springer, Geneva, Switzerland, 185-197.

de la Torre, J. (2018). The vascular hypothesis of Alzheimer's disease: a key to preclinical prediction of dementia using neuroimaging. *J Alzheimers Dis*, *63*(1), 35-52.

DePaola, N., Davies, P. F., Pritchard, Jr, W. F., Florez, L., Harbeck, N., & Polacek, D. C. (1999). Spatial and temporal regulation of gap junction connexin43 in vascular endothelial cells exposed to controlled disturbed flows *in vitro*. *Proc Natl Acad Sci USA*, *96*(6), 3154-3159.

Dorfler, P., Puls, I., Schlieber, M., Maurer, M., & Becker, G. (2000). Measurement of cerebral blood flow volume by extracranial sonography. *J Cereb Blood Flow Metab*, *20*(2), 269-271.

Dyverfeldt, P., Kvitting, J. P. E., Sigfridsson, A., Engvall, J., Bolger, A. F., & Ebbers, T. (2008). Assessment of fluctuating velocities in disturbed cardiovascular blood flow: *in vivo* feasibility of generalized phase-contrast MRI. *J Magn Reson Imaging*, *28*(3), 655-663.

Eckstein, H. H., Eichbaum, M., Klemm, K., Doerfler, A., Ringleb, P., Bruckner, T., & Allenberg, J. R. (2003). Improvement of carotid blood flow after carotid endarterectomy – evaluation using intraoperative ultrasound flow measurement. *Eur J Vasc Endovasc Surg*, *25*(2), 168-174.

Ekroll, I., Swillens, A., Seger, P., Dahl, T., Torp, H., & Lovstakken, L. (2013). Simultaneous quantification of flow and tissue velocities based on multi-angle plane wave imaging. *IEEE Trans Ultrason Ferroelectr Freq Control*, *60*(4), 727-738.

Ekroll, I., Avdal, J., Swillens, A., Torp, H., & Lovstakken, L. (2016). An extended least squares method for aliasing-resistant vector velocity estimation. *IEEE Trans Ultrason Ferroelectr Freq Control*, *63*(11), 1745-1757.

Eid, M., De Cecco, C. M., Schoepf, U. J., Mangold, S., Tesche, C., Varga-Szemes, A., … Caruso, D. (2016). The role of MRI and CT in the diagnosis of atherosclerosis in an aging population. *Curr Radiol Rep, 4*(12).

Emery, D., Forster, A. J., Shojania, K. G., Magnan, S., Tubman, M., & Feasby, T. (2009). Management of MRI wait lists in Canada. *Health Policy, 4*(3), 76-86.

Encinas, M., de Juan, R., Marcos, A., Gil, R., Barabash, A., Fernandez, C., … Cabranes, J. A. (2003). Regional cerebral blood flow assessed with 99mTc-ECD SPET as a marker of progression of mild cognitive impairment to Alzheimer's disease. *Eur J Nucl Med Mol Imaging, 30*(11), 1473-1480.

Errico, C., Pierre, J., Pezet, S., Desailly, Y., Lenkei, Z., Couture, O., & Tanter, M. (2015). Ultrafast ultrasound localization microscopy for deep super-resolution vascular imaging. *Nature, 527*, 499-507.

Etesami, M., Hoi, Y., Steinman, D. A., Gujar, S. K., Nidecker, A. E., Astor, B. C., … Wasserman, B. A. (2013). Comparison of carotid plaque ulcer detection using contrast-enhanced and time-of-flight MRA techniques. *AJNR Am J Neuroradiol, 34*(1), 177-184.

Evans, D. H. (2010). Color flow and motion imaging. *Proc. Inst Mech Eng H J Eng Med, 224*(2), 241-253.

Evans, D. H., Jensen, J. A., & Nielsen, M. B. (2011). Ultrasound color Doppler imaging. *Interface Focus, 1*(4), 490-502.

van Exel, E., Gussekloo, J., Houx, P., de Craen, A. J. M., Macfarlane, P. W., Bootsma-van der Wiel, A., … Westendorp, R. G. J. (2002). Atherosclerosis and cognitive impairment are linked in the elderly. The Leiden 85-plus study. *Atherosclerosis, 165*(2), 353-359.

Falk, E. (2006). Pathogenesis of Atherosclerosis. *J Am Coll Cardiol, 47*(8), C7-C12.

Falke, P., Matzsch, T., Sternby, N. H., Bergqvist, D., & Stavenow, L. (1995). Intraplaque haemorrhage at carotid artery surgery – a predictor of cardiovascular mortality. *J Intern Med, 238*(2), 131-135.

Faurie, J., Baudet, M., Assi, K. C., Auger, D., Gilbert, G., Tournoux, F., & Garcia, D. (2017). Intracardiac vortex dynamics by high-frame-rate Doppler vortography-*In vivo* comparison with vector flow mapping and 4-D flow MRI. *IEEE Trans Ultrason Ferroelectr Freq Control, 64*(2), 424-432.

Fluss, R., Faraggi, D., & Reiser, B. (2005). Estimation of the Yoden index and its associated cutoff point. *Biom J, 47*(4), 458-472.

Flynn, J., Daigle, R., Pflugrath, L., Linkhart, K., & Kaczkowski, P. (2011). Estimation and display for vector Doppler imaging using plane wave transmissions. *In: Proc IEEE Int Ultrasonics Symp, 2011*, 413-418.

Ford, M. D., Alperin, N., Lee, S. H., Holdsworth, D. W., & Steinman, D. A. (2005). Characterization of volumetric flow rate waveforms in the normal internal carotid and vertebral arteries. *Physiol Meas, 26*(4), 477-488.

Fosse, E., Johnsen, S. H., Stensland-Bugge, E., Joakimsen, O., Mathiesen, E. B., Arnesen, E., & Njolstad, I. (2006). Repeated visual and computer-assisted carotid plaque characterization in a longitudinal population-based ultrasound study: the Tromso study. *Ultrasound Biol Med, 32*(1), 3-11.

Fung, Y. C. (1997). Biomechanics: circulation. New York: Springer.

Gabriel, S. A. Ding, Y., & Feng, Y. (2017). Quantifying the influence of oscillatory flow disturbances on blood flow. *J Theor Biol, 430*, 195-206.

Gambillara, V., Chambaz, C., Montorzi, G., Roy, S., Stergiopulos, N., & Silacci, P. (2006). Plaque-prone hemodynamics impair endothelial function in pig carotid arteries. *Am J Physiol Heart Circ, 290*(6), H2320-H2328.

Gammelmark, K. L., & Jensen, J. A. (2014). 2-D tissue motion compensation of synthetic transmit aperture imaging. *IEEE Trans Ultrason Ferroelectr Freq Control, 61*(4), 594-610.

Garbini, J. L., Forster, F. K., & Jorgensen, J. E. (1982a). Measurement of fluid turbulence based on pulsed ultrasound techniques. Part 1. Analysis. *J Fluid Mech, 118*, 445-470.

Garbini, J. L., Forster, F. K., & Jorgensen, J. E. (1982a). Measurement of fluid turbulence based on pulsed ultrasound techniques. Part 2. Experimental investigation. *118*, 471-505.

Garcia, D., Le Tarnec, L., Muth, S., Montagon, E., Poree, J., & Cloutier, G. (2013). Stolt's f-k migration for plane wave ultrasound imaging. *IEEE Trans Ultrason Ferroelectr Freq Control, 60*(9), 1853-1867.

Gasecki, A. P., Eliasziw, M., Furguson, G. G., Hachinski, V., & Barnet, H. J. M. (1995). Long-term prognosis and effect of endarterectomy in patients with symptomatic server carotid stenosis and contralateral carotid stenosis or occlusion: result from NASCET. *J Neurosurg, 83*(5), 778-782.

Gbinigie, I. I., Reckless, I. P., & Buchan, A. M. (2016). Stroke: management and prevention. *Medicine*, *44*(9), 521-529.

Geng, Y. J., & Libby, P. (2002). Progression of atheroma: a struggle between death and procreation. *Arterioscler Thromb Vasc Biol*, *22*(9), 1370-1380.

Gibbons, G. H., & Dzau, V. J. (1994). The emerging concept of vascular remodeling. *N Engl J Med*, *330*, 1431-1438.

Giddens, D. P., Zarins, C. K., & Glagov, S. (1993). The role of fluid mechanics in the localization and detection of atherosclerosis. *J Biomech Eng*, *115*(4B), 588-594.

Gimbrone, M. A. Jr, Topper, J. N., Nagel, T., Anderson, K. R., & Garcia-Cardena, G. (2000). Endothelial dysfunction, hemodynamic forces, and atherogenesis. *Ann N Y Acad Sci*, *902*(1), 230-240.

Girerd, X., London, G., Boutouyrie, P., Mourad, J. J., Safar, M., & Laurent, S. (1996). Remodeling of the radial artery in response to a chronic increase in shear stress. *Hypertension*, *27*(3), 799-803.

Goddi, A., Bortolotto, C., Fiorina, I., Raciti, M. V., Fanizza, M., Turpini, E., … Calliada, F. (2017). High-frame rate vector flow imaging of the carotid bifurcation. *Insights Imag*, *8*(3), 319-328.

Goddi, A., Bortolotto, C., Raciti, M. V., Fiorina, I., Aiani, L., Magistretti, G., … Calliada, F. (2018). High-frame rate vector flow imaging of the carotid bifurcation in healthy adults: Comparison with color Doppler imaging. *J Ultrasound Med*, *37*(9), 2263-2275.

Godin, D., Ivan, E., Johnson, C., Magid, R., & Galis, Z. S. (2000). Remodeling of carotid artery is associated with increased expression of matrix metalloproteinases in mouse blood flow cessation model. *Circulation*, *102*(23), 2861-2866.

Gogia, S., Kaiser, Y., & Tawakol, A. (2016). Imaging high-risk atherosclerotic plaques with PET. *Curr Treat Options Cardio Med*, *18*, 76.

Grant, E. G. Benson, C. B, Monenta, G. K., Alexandrov, A. V., Baker, J. D., Bluth, E. I., … Zierler R. E. (2003). Carotid artery stenosis: gray-scale and Doppler US diagnosis-society of radiologists in ultrasound consensus conference. *Radiology*, *229*(2), 340-346.

Guo, Z., Durand, L. G., Allard, L., Gloutier, G., Lee, H. C., & Langlois, Y. E. (1993). Cardiac Doppler blood-flow signal analysis part 2 time/frequency representation based on autoregressive modelling. *Med Biol Eng Comput*, *31*(3), 236-248.

Ha, H., Hwang, D., Kim, G. B., Kweon, J., Lee, S. J., Baek, J., … Yang, D. H. (2016). Estimation of turbulent kinetic energy using 4D phase-contrast MRI: Effect of scan parameters and target vessel size. *Magn Reson Imaging*, *34*(6), 715-723.

Hallam, M. J. Reid, J. M., & Cooperberg, P. L. (1989). Color-flow Doppler and conventional duplex scanning of the carotid bifurcation: prospective, double-blind, correlative study. *AJR Am J Roentgenol*, *152*(5), 1101-1105.

Harput, S., Christensen-Jeffries, K., Brown, J., Li, Y., Williams, K. J., Davies, A. H., Eckersley, R. J., … Tang, M. X. (2018). Two-stage motion correction for super-resolution ultrasound imaging in human lower limb. *IEEE Trans Ultrason Ferroelectr Freq Control*, *65*(5), 803-814.

Hathout, G. M., Fink, J. R., El-Sadern, S. M., & Grant, E. G. (2005). Sonographic NASCET index: a new Doppler parameter for assessment of internal carotid artery stenosis. *AJNR Am J Neuroradiol*, *26*(1), 68-75.

Hansen K. L., Udesen, J., Oddershede, N., Henze, L., Thomsen, C., Jensen, J. A., & Nielsen, M. B. (2009). *In vivo* comparison of three ultrasound vector velocity techniques to MR phase contrast angiography. *Utrasonics*, *49*(8), 659-667.

Hansen, K. L., Moller-Sorensen, H., Pedersen, M. M., Hansen, P. M., Kjaergaard, J., Lund, J. T., … Nielsen, M. B. (2015). First report on intraoperative vector flow imaging of the heart among patients with healthy and diseased aortic valves. *Ultrasonics*, *56*, 243-250.

Hansen, K. L., Moller-Sorensen, H., Kjaergaard, J., Jensen, M. B., Jensen, J. A., & Nielsen, M. B. (2017). Aortic valve stenosis increases helical flow and flow complexity: A study of intra-operative cardiac vector flow imaging. *Ultrasound Med Biol*, *43*(8), 2611-2618.

Harry, B. L. Sanders, J. M., Feaver, R. E., Lansey, M., Deem, T. L., Zarbock, A., … Ley K. (2008). Endothelial cell PECAM-1 promotes atherosclerotic lesions in areas of disturbed flow in ApoE-deficient mice. *Arteroscler Thromb Vasc Biol*, *28*(11), 2003-2008

Hasegawa, H., & Kanai, H. (2008). Simultaneous imaging of artery-wall strain and blood flow by high-frame-rate acquisition of RF signals. *IEEE Trans Ultrason Ferroeclectr Control*, *55*(12), 2626-2639.

Hebert, L. E., Weuve, J., Scherr, P. A., & Evans, D. A.(2013). Alzheimer disease in the United States (2010-2050) estimated using the 2010 census. *Neurology*, *80*(19), 1778-1783.

Hellings, W. E., Peeters, W., Moll, F. L., Piers, S. R. D., van Setten, J., Van der Spek, P. J., ... Pasterkamp, G. (2010). Composition of carotid atherosclerotic plaque is associated with cardiovascular outcome: a prognostic study. *Circulation*, 121(17), 1941-1950.

Hessel, S. J., Adams, D. F., & Abrams, H. L. (1981). Complications of angiography. *Radiology, 138*(2), 273-281.

Hirao, K., Ohnishi, T., Hirata, Y., Yamashita, F., Mori, T., Moriguchi, Y., … Asada, T. (2005). The prediction of rapid conversion to Alzheimer's disease in mild cognitive impairment using regional cerebral blood flow SPECT. *NeuroImage, 28*(4), 1014-1021.

Ho, C. K., Chee, A. J. Y., Yiu, B. Y. S., Tsang, A. C. O., Chow, K. W., & Yu, A. C. H. (2017). Wall-less flow phantoms with tortuous vascular geometries: design principles and a patient-specific model fabrication example. *IEEE Trans Ultrason Ferroelectr Freq Control*, *64*(1), 150-163.

Ho, C. K. (2018). Time-resolved wall shear rate mapping using high-frame-rate ultrasound. *UWSpace*. *http://hdl.handle.net/10012/13415*

Ho, S. S. Y. (2016). Current status of carotid ultrasound in atherosclerosis. *Quant Imaging Med Surg*, *6*(3), 285-296.

Hofman, A., Ott, A., Breteler, M. M., Bots, M. L., Slooter, A. J. C., van Harskamp, F., … Grobbee, D. E. (1997). Atherosclerosis, apolipoprotein E, and prevalence of dementia and Alzheimer's disease in the Rotterdam Study. *LANCET*, *349*(9046), 151-154.

Hoi, Y., Wasserman, B. A., Xie, Y. J., Najjar, S. S., Ferruci, L., Lakatta, E. G., … Steinman, D. A. (2010). Characterization of volumetric flow rate waveforms at the carotid bifurcations of older adults. *Physiol Meas*, *31*(3), 291-302.

Hoit, B. D., Jones, M., Eidbo, E. E., Elias, W., & Sahn, D. J. (1989). Sources of variability for Doppler color flow mapping of regurgitant jets in an animal model of mitral regurgitation. *J Am Coll Cardiol*, *13*(7), 1631-1636.

Holbet, S., Pihl, M. J., Ewertsen, C., Nielsen, M. B., & Jensen, J. A. (2015). *In vivo* 3-D vector velocity estimation with continuous data. *In: Proc IEEE Int Ultrasonics Symp*, *2015*, 1-4.

Holbet, S., Christiansen, T. L., Stuart, M. B., Beers, C., Thomsen, E. V., & Jensen, J. A. (2016). 3-D vector flow estimation with row-column-addressed arrays. *IEEE Trans Ultrason Ferroelectr Freq Control*, *63*(11), 1799-1814.

Holdsworth, D. W., Norley, C. J., Frayne, R., Steinman, D. A., & Rutt, B. K. (1999). Characterization of common carotid artery blood-flow waveforms in normal human subject. *Physiol Meas, 20*(3), 219-240.

Hoskins, P. R. (2008). Simulation and validation of arterial ultrasound imaging and blood flow. *Ultrasound Med Biol, 34*(5), 693-717.

Hoskins, P. R. (2010). Haemodynamics and blood flow measured using ultrasound imaging. *Proc Inst Mech Eng H J Eng Med*, *224*(2), 255-271.

Howard, V. J., Howard, G., Harpold G. J., Nunn, C. L., Myers, L. G., McKinney, W. M., … Toole, J. F. (1989). Correlation of carotid bruits and carotid atherosclerosis detected by B-mode real-time ultrasonography. *Stroke*, *20*(10), 1331-1335.

Huang, R., Abdelmoneim, S. S., Ball, C. A., Nhola, L. F., Farrell, A. M., Feinstein, S., … Mulvagh, S. L. (2016). Detection of carotid atherosclerotic plaque neovascularization using contrast enhanced ultrasound: a systematic review and meta-analysis of diagnostic accuracy studies. *J Am Soc Echocardiogr, 29*(6), 491-502.

Huo, Y., Wischgoll, T., & Kassab, G. (2007). Flow patterns in three-dimensional porcine epicardial coronary arterial tree. *Am J Physiol Heart Circ Physiol*, *293*(5), H2959-H2970.

Hur, B. Y., Lee, J. Y., Chu, A. J., Kim, S. H., Han, J. K., & Choi, B. I. (2014). UltraFast Doppler ultrasonography for hepatic vessels of liver recipients: Preliminary experiences. *Ultrasonography*, *34*(1), 58-65.

Hurd, M. D., Martorell, P., Delavande, A., Mullen, K. J., & Langa, K. M. (2013). Monetary costs of dementia in the United States. *N. Engl J Med, 368*, 1326-1334.

Hussain, A. K. M. F., & Ramjee, Y. (1976). Effects of axisymmetric contraction shape on incompressible turbulent flow. *J Fluid Eng-T AMSE, 98*(1), 58-68.

Hutter, R., Speidl, W. S., Valdiviezo, C., Sauter, B., Corti, R., Fuster, V., & Badimon, J. J. (2013). Macrophages transit potent proangiogenic effects of oxLDL *in vitro* and *in vivo* involving HIF-1α activation: a novel aspect of angiogenesis in atherosclerosis. *J Cardiovasc Trans Res*, *6*(4), 558-569.

Idzenga, T., Gaburov, E. Vermin, W., Mensen, J., & De Korte, C. L. (2014). Fast 2-D ultrasound strain imaging: The benefits of using a GPU. *IEEE Tras Ultrason Ferroelectr Freq Control*, *61*(1), 207-213.

Inui, Y., Ito, K., Kato, T., & SEAD-J Study Group (2017). Longer-term investigation of the value of ^{18}F-FDG-PET and magnetic resonance imaging for predicting the conversion of mild cognitive impairment to Alzheimer's disease: a multicenter study. *J Alzheimers Dis*, *60*(3), 877-887.

Ishii, T., Yiu, B. Y. S., & Yu, A. C. H. (2017). Vector flow visualization of urinary flow dynamics in a bladder outlet obstruction model. *Ultrasound Med Biol*, *43*(11), 2601-2610.

Iwamoto, T., Shinozaki, K., Kiuchi, A., Umahara, T., & Takasaki, M. (2003). Evaluation of B-mode ultrasonographic images of carotid lesions by computer analysis as compared with visual assessment. *J Stroke Cerebrovasc Dis*, *12*(2), 59-65.

Jahromi, A. S., Cina, C. S., Liu, Y., & Clase, C. M. (2005). Sensitivity and specificity of color duplex ultrasound measurement in the estimation of internal carotid artery stenosis: a systematic review and meta-analysis. *J Vasc Surg*, *41*(6), 962-972.

Jensen J., Stuart, M. B., & Jensen, J. A. (2016). Optimized plane wave imaging for fast and high-quality ultrasound imaging. *IEEE Trans Ultrason Ferroelectr Freq Control*, *63*(11), 1922-1934.

Jensen, J., Hoyos, C. A. V., Stuart, M. B., Ewertson, C., Nielson, M. B., & Jensen, J. A. (2017). Fast plane wave 2-D vector flow imaging using transverse oscillation and directional beamforming. *IEEE Trans Ultrason Ferroelectr Freq Control*, *64*(7), 1050-1062.

Jensen, J. A., Nikolov, S. I., Gammelmark, K. L., & Pedersen, M. H. (2006). Synthetic aperture ultrasound imaging, *Ultrasonics*, *44*(Supplement), e5-e15.

Jensen, J. A. (2007). Medical ultrasound imaging. *Prog Biophys Mol Biol*, **93**, 153-165.

Jensen, J. A., Holten-Lund, H., Nilsson, R. T., Hansen, M., Larsen, U. D., Domsten, R. P., … Rasmussen, M. F. (2013). SARUS: A synthetic aperture real-time ultrasound system. *IEEE Trans Ultrason Ferroelectr Freq Control*, *60*(9), 1838-1852.

Jensen, J. A., Nikolov, S. I., Yu, A. C. H., & Garcia, D. (2016a). Ultrasound vector flow imaging – Part I: Sequential systems. *IEEE Trans Ultrason Ferroelectr Freq Control*, *63*(11), 1704-1721.

Jensen, J. A., Nikolov, S. I., Yu, A. C. H., & Garcia, D. (2016b). Ultrasound vector flow imaging – Part II: Parallel systems. *IEEE Trans Ultrason Ferroelectr Freq Control*, *63*(11), 1722-1732.

Johnson, N. A., Jahng, G. H., Weiner, M. W., Miller, B. L., Chui, H. C., Jagust, W. J., … Schuff, N. (2005). Pattern of cerebral hypoperfusion in Alzheimer disease and mild cognitive impairment measured with arterial spin-labeling MR imaging: initial experience. *Radiology*, *234*(3), 851-859.

Johri, A. M., Herr, J. E., Li, T. Y., & Nambi, V. (2017). Novel ultrasound methods to investigate carotid artery plaque vulnerability. *J Am Soc Echocardiogr, 30*(2), 139-148.

Joseph, P., & Tawakol, A. (2016). Imaging atherosclerosis with positron emission tomography. *Eur Heart J, 37*(39), 2974-2980.

Kajishima, T., Taira, K. (2017). Reynolds-averaged Navier-Stokes equations. In: Computational Fluid Dynamics. Cham: Springer, 237-258.

Kasai, C., Namekawa, K., Koyano, A., & Omoto, R. (1985). Real-time tow-dimensional blood flow imaging using an autocorrelation technique. *IEEE Trans Son Ultrason, 32*(3), 458-464.

Kaufmann, B. A., Carr, C. L., Belcik, T., Xie, A., Yue, Q., Chadderdon, S., … Lindner, J. R. (2010). Molecular imaging of the initial inflammatory response in atherosclerosis: Implications for early detection of disease. *Arterioscler Thromb Vasc Biol, 30*(1), 54-59.

Kefayati, S., & Poepping, T. L. (2013). Transitional flow analysis in the carotid artery bifurcation by proper orthogonal decomposition and particle image velocimetry. *Med Eng Phys, 35*(7), 898-909.

Kefayati, S., Holdsworth, D. W., & Poepping, T. L. (2014). Turbulence intensity measurements using particle image velocimetry in diseased carotid artery models: Effect of stenosis severity, plaque eccentricity and ulceration. *J Biomech*, 2014, *47*(1), 253-263.

Ketterling, J. A. Aristizabal, O., Yiu, B. Y. S., Turnbull, D. H., Phoon, C. K. L., Yu, A. C. H., & Silverman, R. H. (2017). High-speed, high-frequency ultrasound, *in utero* vector-flow imaging of mouse embryos. *Sci Rep, 7*(1), Art. no. 16658.

Khanichehm, E., Mitterhuber, M., Xu, L., Haeuselmann, S. P., Kuster, G. M., & Kaufmann, B. A. (2013). Noninvasive ultrasound molecular imaging of the effect of statins on endothelial inflammatory phenotype in early atherosclerosis. *PLoS ONE, 8*(3), e58761.

Khatri, J. J., Johnson, C., Magid, R., Lessner, S. M., Laude, K. M., Dikalov, S. I., …, Galis, Z. S. (2004). Vascular oxidant stress enhanced progression and angiogenesis of experimental atheroma. *Circulation, 109*(4), 520-525.

Khoshniat, M., Thorne, M. L., Poepping, Hirji, S., Holdsworth, D. W., & Steinman, D. A. (2005). Real-time numerical simulation of Doppler ultrasound in the presence of nonaxial flow. *Ultrasound Med Biol, 31*(4), 519-528.

Kim, S. Y., Kim, K. W., Choi, S. H., Kwon, J. H., Song, G. W., Kwon, H. J., … Lee, S. G. (2017). Feasibility of ultrafast Doppler in post-operative evaluation of hepatic artery in recipients following liver transplantation. *Ultrasound Med Biol*, **43**, 2611-2618.

King, D. M., Ring, M., Moran, C. M., & Browne, J. E. (2010). Development of a range of anatomically realistic renal artery flow phantoms. *Ultrasound Med Biol*, *36*(7), 1135-1144.

Kistler, J. P., & Furie, K. L. (2000). Carotid endarterectomy revisited. *N. Engl J Med*, *342*(23), 1743-1745.

Kitagawa, K., (2010). Cerebral blood flow measurement by PET in hypertensive subjects as a marker of cognitive decline. *J Alzheimers Dis*, *20*(3), 855-859.

Kleindorfer, D., Khoury, J., Moomaw, C. J., Alwell, K., Woo, D., Flaherty, M. L., Khatri, P., … Kissela, B. M. (2010). Stroke incidence is decreasing in whites, but not in blacks: a population-based estimate of temporal trends in stroke incidence from the greater Cincinnati/Northern Kentucky stroke study. *Stroke*, *41*(7), 1326-1331.

Klibanov, A. L., & Hossack, J. A. (2015). Ultrasound in radiology: from anatomic, functional, molecular imaging to drug delivery and image-guided therapy. *Invest Radiol*, *50*(9), 657-670.

Klingebiel, R., Kentenich, M., Bauknecht, H. C., Masuhr, F., Siebert, E., Busch, M., & Bohner G. (2008). Comparative evaluation of 64-slice CT angiography and digital subtraction angiography in assessing the cervicocranial vasculature. *Vasc Health Risk Manag*, *4*(4), 901-907.

Knopp, M. V., von Tengg-Kobligh, H., Floemer, F., & Schoenberg, S. O. (1999). Contrast agents for MRA: future directions. *J Magn Reson Imaging*, *10*(3), 314-316.

Kohler, T. R., & Jawien, A. (1992). Flow affects development of intimal hyperplasia after arterial injury in rats. *Arterioscler Thromb*, *12*(8), 963-971.

Kohler, T. R., & Kirkman, T. R. (1999). Dialysis access failure: a sheep model of rapid stenosis. *J Vasc Surg*, *30*(4), 744-751.

Kohler, T. R., Toleikis, P. M., Gravett, D. M., & Avelar, R. L. (2007). Inhibition of neointimal hyperplasia in a sheep model of dialysis access failure with the bioabsorbable vascular wrap paclitaxel-eluting mesh. *J Vasc Surg*, *45*(5), 1029-1037.

Koktzoglou, I., Walker, M. T., Meyer, J. R., Murphy, I. G., & Edelman, R. R. (2016). Nonenhanced hybridized arterial spin labeled magnetic resonance angiography of the extracranial carotid arteries using a fast low angle shot readout at 3 Tesla. *J Cardiovasc Magn Reson*, *18*(18).

Kono, Y., Pinnell, S. P., Sirlin, C. B., Sparks, S. R., Geoogy, B., Wong, W., & Mattrey, R. F. (2004). Carotid arteries: contrast-enhanced US angiography - preliminary clinical experience. *Radiology*, *230*(2), 561-568.

Korshunov, V. A., & Berk, B. C. (2003). Flow-induced vascular remodeling in the mouse: a model for carotid intima-media thickening. *Arterioscler Thromb Vasc Biol*, *23*(12), 2185-2191.

Korshunov, V. A., Mohan, A. M., Georger, M. A., & Berk, B. C. (2006). Axl, a receptor tyrosine kinase, mediates flow-induced vascular remodeling. *Circ Res*, *98*(11), 1446-1452.

Kragel, A. H., Reddy, S. G., Wittes, J. T., & Roberts, W. C. (1989). Morphometric analysis of the composition of atherosclerotic plaques in the four major epicardial coronary arteries in acute myocardial infarction and in sudden coronary depth. *Circulation*, *80*(6), 1747-1756.

Kraiss, L. W., Geary, R. L., Mattsson, E. J. R., Vergel, S., Au, Y. P. T., & Clowes, A. W. (1996), Acute reductions in blood flow and shear stress induce platelet-derived growth factor-A expression in baboon prosthetic grafts, *Circ Res*,*79*(1), 45-53.

Krams, R., Bambi, G., Guidi, F., Helderman, F., van der Steen, A. F. W., & Tortoli, P. (2005). Effect of vessel curvature on Doppler derived Velocity profiles and fluid flow. *Ultrasound Med Biol*, *31*(5), 663-671.

Kripfgans, O. D., Rubin, J. M., Hall, A. L., & Fowlkes, J. B. (2006). Vector Doppler imaging of a spinning disc ultrasound Doppler phantom. *Ultrasound Med Biol*, *32*(7), 1037-1046.

Kripfgans, O. D., Rubin, J. M., Hall, A. L., Gorden, M. B., & Fowlkes, J. B. (2006). Measurement of volumetric flow. *J Ultrasound Med*, *25*(10), 1305-1311.

Kumar, A., & Lindner, V. (1997), Remodeling with neointima formation in the mouse carotid artery after cessation of blood flow. *Arterioscler Throm Vasc Biol*, *17*(10), 2238-2244.

Laasmaa, M., Venderlin, M., & Peterson, P. (2011). Application of regularized Richardson-Lucy algorithm for deconvolution of confocal microscopy images. *J Microsc*, *243*(Pt 2), 124-140.

Lai, X., Torp, H., & Kristoffersen, K. (1997). An extended autocorrelation method for estimation of blood velocity. *IEEE Trans Ultrason Ferroelectr Freq Control*, *44*(6), 1332-1342.

Lai, S. S. M., Yiu, B. Y. S., Poon, A. K. K., & Yu, A. C. H. (2013). Design of anthropomorphic flow phantoms based on rapid prototyping of compliant vessel geometries. *Ultrasound Med Biol*, *39*(9), 1654-1664.

Langheinrich, A. C., Kampschulte, M., Buch, T., Bohle, R. M., Vasa vasorum and atherosclerosis - Quid novi?. *Thromb Haemost*, *97*(6), 873-879.

Langille, B. L., & O'Donnell, F. (1986). Reductions in arterial diameter produced by chronic decreases in blood flow are endothelium-dependent. *Science*, *231*(4736), 405-407.

Laub, G. A., & Kaiser, W. A. (1988). MR angiography with gradient motion refocusing. *J Comput Assist Tomogr*, *12*(3), 377-382.

Lassen, N. A. (1985). Normal average value of cerebral blood flow in younger adults is 50 ml/100 g/min. *J Cereb Blood Flow Metab*, *5*(3), 347-349.

Latchaw, R. E., & Albers, S. L. (2017). Imaging the cervical vasculature. *Prog Cardiovasc Dis*, *59*(6), 555-584.

Lee, S., Antiga, L., Spence, J. D., & Steinman, D. A. (2008). Geometry of the carotid bifurcation predicts its exposure to disturbed flow. *Stroke*, *39*(8), 2341-2347.

Leenders, K. L., Perani, D., Lammertsma, A. A., Heather, J. D., Buckingham, P., Healy, M. J. R., … Jones, T. (1990). Cerebral blood flow, blood volume and oxygen utilization. *Brain*, *113*(Pt 1), 27-47.

Li, Y. S., Haga, J. H., & Chien, S. (2005). Molecular basis of the effects of shear stress on vascular endothelial cells. *J Biomech*, *38*(10), 1949-1971.

Lin, F., Shelton, S. E., Espindola, D., Rojas, J. D., Pinton, G., and Dayton, P. A. (2017). 3-D ultrasound localization microscopy for identifying microvascular morphology features of tumor angiogenesis at a resolution beyond diffraction limit of conventional ultrasound. *Theranostics*, *7*(1), 196-204.

Link, J., Brossmann, J., Grabener, M., Muller-Huelsbeck, S., Steffens, J. C., Brinkmann, G., & Heller, M. (1996). Spiral CT angiography and selective digital subtraction angiography of internal carotid artery stenosis. *AJNR Am J Neuroradiol*, *17*(1), 89-94.

Liu, H., & Zhang, J. (2012). Cerebral hypoperfusion and cognitive impairment: the pathogenic role of vascular oxidative stress. *Int J Neurosci*, *122*(9), 494-499.

Liu, Y., Hua, Y., Feng, W., & Ovbiagele, B. (2016). Multimodality ultrasound imaging in stroke: current concepts and future focus. *Expert Rev Cardiovasc Ther*, *14*(12), 1325-1333.

Lovett, J. K., Gallagher, P. J., Hands, L. J., Walton, J., & Rothwell, P. M. (2004). Histological correlates of carotid plaque surface morphology on lumen contrast imaging. *Circulation*, *110*(15), 2190-2197.

Lovstakken, L., Bjaerum, S., Martens, D., & Torp, H. (2006). Blood flow imaging – A new real-time 2-D flow imaging technique. *IEEE Trans Ultrason Ferroelectr Freq Control*, *53*(2), 289-299.

Malek, A. M., Alper,S. I., & Izumo, S. (1999). Hemodynamic shear stress and its role in atherosclerosis. *JAMA*, *282*(21), 2035-2042.

Manninen A. L., Isokangas, J. M., Karttunen, A., Siniluoto, T., & Nieminen, M. T. (2012). A comparison of radiation exposure between diagnostic CTA and DSA examinations of cerebral and cervicocerebral vessels. *AJNR Am J Neuroradiol*, *33*(11), 2038-2042.

Mao, F., Gill, J., Downey, D., & Fenster, A. (2011). Segmentation of carotid artery in ultrasound images: Method development and evaluation technique. *Med Phys*, *27*(8), 1961-1970.

Marckmann, P., Slov, L., Rossen, K., Dupont, A., Damholt, M. B., Heaf, J. G., Thomsen, H. S. (2006). Nephrogenic systemic fibrosis: suspected causative role of cadodiamide used for contrast-enhanced magnetic resonance imaging. *J Am Soc Nephrol*, *17*(9), 2359-2362.

Marshall, R. S. (2012). Effects of altered cerebral hemodynamics on cognitive function. *J Alzheimers Dis*, *32*(3), 633-642.

Marulanda-Londono, E., & Chaturvedi, S. (2016). Stroke due to large vessel atherosclerosis: five new things. *Neurol Clin Pract*, *6*(3), 252-258.

Mauldin, F. W. Jr, Lin, D., & Hossack, J. A. (2011). The singular value filter: a general filter design strategy for PCA-based signal separation in medical ultrasound imaging. *IEEE Trans Med Imag*, *30*(11), 1951-1964.

McCarthy, M. J., Loftus, I. M., Thompson, M. M., Jones, L., Londo, N. J. M., Bell, P. R. F., … Brindle, N. P. J. (1999). Angiogenesis and the atherosclerotic carotid plaque: an association between symptomatology and plaque morphology. *J Vasc Surg*, *30*(2), 261-268.

McClellan, J. H., & Parks, T. W. (2005). A personal history of the Parks-McClellan algorithm. *IEEE Signal Process Mag*, *22*(2), 82-86.

McDicken, W. N., & Hoskin, P. R. (2014). Physics: principles, practice and artifacts. In: Poznia M. A., Allan, P. L., eds. Clinical Doppler ultrasound. Churchill, Livingstone: Elsevier; p.1-25.

McEver, R. P., & Cummings, R. D. (1997). Role of PSGL-1 binding to selectins in leukocyte recruitment. *J Clin Invest*, *100*(11 Suppl), 485-492.

Melkumyants, A. M., Balashov, S. A., & Khayutin, V. M. (1989). Endothelium dependent control of arterial diameter by blood viscosity. *Cardiovasc Res*, *23*(9), 741-747.

Meschia, J. F., Bushnell, C., Boden-Albala, B., Braun, L. T., Bravata, D. M., Elkind, M. S. V., … Wilson, J. A. on behalf of the American Heart Association Stroke Council, Council on Cardiovascular and Strole Nursing, Council on Clinical Cardiology, Council on Functional Genomics and Translational Biology, and Council on Hypertension (2014). Guidelines for the primary prevention of stroke: a statement for healthcare prefessionals from the American Heart Association/American Stroke Association. *Stroke*, *45*(12), 3754-3832.

Meyerson S. K., Skelly, C. L., Curi, M. A., Shakur, U. M., Vosicky, J. E., & Schwartz, L. B. (2001). The effects of extremely low shear stress on cellular proliferation and neointimal thickening in the failing bypass graft. *J Vasc Surg*, *34*(1), 90-97.

Michel, J. B., Virmani, R., Arbustini, E., & Pasterkamp, G. (2011). Intraplaque haemorrhages as the trigger of plaque vulnerability. *Eur Heart J*, *32*(16), 1977-1985.

Middleton, W. D., Foley, W. D., & Lawson, T. L. (1988). Color-flow Doppler imaging of carotid artery abnormalities. *AJR Am J Roentgenol*, *150*(2), 419-425.

Mitrasinovic, A., Radak, S., Kolar, J., Aleksic, N., Otasevic, P., Popovic, M., & Radak, D. (2010). Color Doppler sonographic evaluation of flow volume of the internal carotid and vertebral arteries after carotid endarterectomy. *J Clin Ultrasound*, *38*(5), 238-243,

Mo, L. Y. L., & Cobbold, R. S. C. (1986). "Speckle" in continuous wave Doppler ultrasound spectra: a simulation study. *IEEE Trans Ultrason Ferroelectr Freq Control*, *33*(6), 747-753.

Mohamied, Y., Rowland, E. M., Bailey, E. L., Sherwin, S. J. Schwartz, M. A. & Weinberg, P. D. (2015). Change of direction in the biomechanics of atherosclerosis. *Ann Biomed Eng*, *43*(1), 16-25.

Montaldo, G., Tanter, M., Bercoff, J., Benech, N., & Fink, M. (2009). Coherent plane-wave compounding for very high-frame-rate ultrasonography and transient elastography. *IEEE Trans Ferroelectr Freq Control*, *56*(3), 489-506.

Moreno, P. R., Purushothaman, K. R., Fuster, V., Echeverri, D., Truszczynska, H., Sharma, S. K., … O'Conner, W. N. (2004). Plaque neovascularization is increased in ruptured atherosclerotic lesions of human aorta. *Circulation*, *110*(14), 2032-2038.

Moreno, P. R., Purushothaman, K. R., Sirol, M., Levy, A. P., & Fuster, V. (2006). Neovascularization in human atherosclerosis. *Circulation, 113*(18), 2245-2252.

Mortimer, R., Nachiappan, S., & Howlett, D. C. (2018). Carotid artery stenosis screening: where are we now?. *Br J Radiol*, 91(1090).

Mozaffarian, D., Benjamin, E. J., Go, A. S., Amett, D. J., Blaha, M. J., Cushman, M., … Turner, M. B. (2016). Heart Disease and Stroke Statistics – 2016 Update A Report From the American Heart Association. *Circulation*, *133*(4), e38-e360.

Mynard, J. P., Wasserman, B. A., & Steinman, D. A. (2013). Errors in the estimation of wall shear stress by maximum Doppler velocity. *Atherosclerosis*, *227*(2), 259-266.

Napoli, C., Lerman, L. O., de Nigris, F., Gossl, M., Balestrieri, M. L., & Lerman, A. (2006). Rethinking primary prevention of atherosclerosis-related diseases. *Circulation, 114*(23), 2517-2527.

Naqvi, J. Yap, K. H., Ahmand, G., & Ghosh, J. (2013). Transcranial Doppler ultrasound: a review of the physical principle and major applications in critical care. *Int J Vasc Med, 2013*, Art. no. 629378

Nerem, R. M., Alexander, R. W., Chappell, D. C., Medford, R. M., Varner, S. E., & Taylor, W. R. (1998). The study of the influence of flow on vascular endothelial biology. *Am J Med Sci*, *316*(3), 169-175.

Nicolaides, A. N., Kakkos, S. K., Kyriacou, E., Griffin, M., Sabetai, M., Thomas, D. J., … Abbott, A. L. for the Asymptomatic Carotid Stenosis and Risk of Stroke (ACSRS) Study Group. Asymptomatic internal carotid artery stenosis and cerebrovascular risk stratification. *J Vasc Surg*, *52*(6), 1486-1496.

Nighoghossian, N., Derex, L., & Douek, P. (2005). The vulnerable carotid artery plaque: current imaging methods and new perspectives. *Stroke*, *36*(12), 2764-2772.

Nikolov, S., Gammelmark, K., & Jensen, J. A. (1999). Recursive ultrasound imaging. *In: Proc. IEEE Int Ultrasonics Symp, 1999, 2*, 1621-1625.

Niwa, F., Kondo, M., Sakurada, K., Nakagawa, M., Imanishi, J., & Mizuno, T. (2016). Regional cerebral blood flow in [123]I-IMP single-photon emission computed tomography and the Wechsler memory scale-revised in nondemented elderly subjects with subjective cognitive impairment. *Intern Med*, *55*(24), 3571-3578.

North American Symptomatic Carotid Endarterectomy Trial (NASCET) (1991). North American symptomatic carotid endarterectomy trial: methods, patient characteristics, and progress. *Stroke*, *22*(6), 711-720.

O'Brien, K. D., McDonald, T. O., Chait, A., Allen, M. D., & Alpers, C. E. (1996), Neovascular Expression of E-Selectin, Intercellular Adhesion Molecule-1, and Vascular Cell Adhesion Molecule-1 in Human Atherosclerosis and Their Relation to Intimal Leukocyte Content, *Circulation*, *93*(4), 672-682.

Oktar, S. O., Yucel, C., Karaosmanoglu, D., Akkan, K., Ozdemir, H., Tokgoz, N., & Tali, T. (2006). Blood-flow volume quantification in internal carotid and vertebral arteries: comparison of 3 different ultrasound techniques with phase-contrast MR imaging. *AJNR Am J Neuroradiol*, *27*(2), 363-369.

O'Reilly, M. A., & Hynynen, K. (2013). A super-resolution ultrasound method for brain vascular mapping. *Med Phys*, *40*(11), Art. no. 110701.

Osmanski, B. F., Pernot, M., Montaldo, G., Bel. A., Messas, E., & Tanter, M. (2012). Ultrafast Doppler imaging of blood flow dynamics in the myocardium. *IEEE Trans Med Imag*, *31*(8), 1661-1668.

Palombo, C., & Kozakova, M. (2016). Arterial stiffness, atherosclerosis and cardiovascular risk: Pathophysiologic mechanisms and emerging clinical indications. *Vascul Pharmacol*, 77, 1-7.

Panerai, R. B. (2008). Cerebral autoregulation: from models to clinical applications. *Cardiovasc Eng*, *8*(1), 42-59.

Papageorgiou, N., Briasoulis, A., Androulakis, E., & Tousoulis, D. (2017). Imaging subclinical atherosclerosis: where do we stand?. *Curr Cardiol Rev*, *13*(1), 47-55.

Park, K. W., Yoon, H. J., Kang, D. Y., Kim, B. C., Kim, S. Y., & Kim, J. W. (2012). Regional cerebral blood flow differences in patients with mild cognitive impairment between those who did and did not develop Alzheimer's disease. *Psychiatry Res Neuroimaging*, *203*(2-3), 201-206.

Park, M. Y., Jung, S. E., Choi, J. I., & Byun, J. Y. (2016) Optimization of beam-flow angles for Doppler ultrasound flow velocity measurements using slanted gel pads. *SpringerPlus*, *5*, 328.

Partovi, S., Loebe, M., Aschwanden, M., Baldi, T., Jager, K. A., Feinstein, S. B., & Staub, D. (2012). Contrast-enhanced ultrasound for assessing carotid atherosclerotic plaque lesions. *Neuroradiology*, *198*(1), W13-W19.

Pastorelli, A., Torricelli, G., Scabia, M., Biagi, E., & Masotti, L. (2008). A real-time 2-D vector Doppler system for clinical experimentation. *IEEE Trans Med Imag, 27*(10), 1515-1524.

Pedersen, M. M., Pihl, M. J., Haugaard, P., Hansen, J. M., Hansen, K. L., Nielsen, M. B., & Jensen, J. A. (2012). Comparison of real-time *in vivo* spectral and vector velocity estimation. *Ultrasound Med Biol, 38*(1), 145-151.

Petrusca, L., Varray, F., Souchon, R., Bernard, A., Chapelon, J. Y., Liebgott, H., N'Djin, W. A., & Viallon, M. (2017). A new high channels density ultrasound platform for advanced 4D cardiac imaging. *In: Proc IEEE Int Ultrasonics Symp, 2017*, 1-4

Phelps, J. E., & DePaola, N. (2000). Spatial variations in endothelial barrier function in disturbed flows *in vitro*. *Am J Physiol Heart Circ Physiol, 278*(2), H469-H476.

Phelps, M. E. (2000). Positron emission tomography provides molecular imaging of biological processes. *Proc Natl Acad Sci U S A, 97*(16), 9226-9233.

Pianco, E. & Paterni, M. (2015). Ultrasound tissue characterization of vulnerable atherosclerotic plaque. *Int J Mol Sci, 16*(5), 10121-10133.

Piscaglia, F., Nolsoc, C., Dietrich, C. F., Cosgrove, D. O., Gilja, O. H., Bachmann Nielsen M. T., … Weskott, H. P. (2012). The EFSUMB Guidelines and recommendations on the clinical practice of contrast enhanced ultrasound (CEUS): update 2011 on non-hepatic applications. *Ultraschall in Med, 33*(1), 33-59.

Poepping, T. L., Nikolov, H. N., Rankin, R. N., Lee, M., & Holdsworth, D. W. (2002). An *in vitro* system for Doppler ultrasound flow studies in the stenosed carotid artery bifurcation. *Ultrasound Med Biol, 28*(4), 495-506.

Poepping, T. L., Rankin, R. N., & Holdsworth, D. W. (2010). Flow patterns in carotid bifurcation models using plused Doppler ultrasound: effect of concentric vs eccentric stenosis on turbulence and recirculation. *Ultrasound Med Biol, 36*(7), 1125-1134.

Pohl, U., de Wit, C., & Gloe, T. (2000). Large arterioles in the control of blood flow: role of endothelium-dependent dilation. *Acta Physiol Scand, 168*(4), 505-510.

Popa-Wagner, A., Buga, A. M., Popescu, B., & Muresanu, D. (2015). Vascular cognitive impairment, dementia, aging and energy demand. A vicious cycle. *J Neural Transm, 122* Suppl 1. S47-S54.

Poree, J., Posada, D., Hodzic, A., Tournoux, F., Cloutier, G., & Garcia, D. (2016). High-frame-rate echocardiography using coherent compounding with Doppler-based motion-compensation. *IEEE Trans Med Imag*, *35*(7), 1647-1657.

Posada, D., Poree, J., Pellissier A., Chayer, B., Tournoux, F., Cloutier, G. & Garcia, D. (2016). Staggered multiple-PRF ultrafast color Doppler. *IEEE Trans Med Imag*, *35*(6), 1510-1521.

Prati, P., Vanuzzo, D., Casaroli, M., Di Chiara, A., De Biasi, F., Feruglio, G. A., & Touboul, P. J. (1992). Prevalence and determinants of carotid atherosclerosis in a general population. *Stroke*, *23*(12), 1705-1711.

Provost, J., Papadacci, C., Arango, J. E., Imbault, M., Fink, M., Gennisson, J. L., … Pernot, M. (2014). 3D ultrafast ultrasound imaging *in vivo*. *Phys Med Biol*, *59*(19), L1-L13.

Provost, J., Papadacci, C., Gennisson, J. L., Tanter, M., & Pernot, M. (2015). 3-D ultrafast Doppler imaging applied to the noninvasive mapping of blood vessels *in vivo*. *IEEE Trans Ultrason Ferroelectr Freq Control*, *62*(8), 1467-1472.

Przybylski, A., Thiel, B., Keller-Finderisen, J., Stock, B., & Bates, M. (2017). Gpufit: An open-source toolkit for GPU-accelerated curve fitting. *Sci Rep*, **7**, Art. no. 15722.

Qiao, Y., Etesami, M., Astor, B. C., Zeiler, S. R., Trout, H. H., III, & Wasserman, B. A. Carotid plaque neovascularization and hemorrhage detected by MR imaging are associated with recent cerebrovascular ischemic events. *AJNR Am J Neuroradiol*, *33*(4), 755-760.

Rafailidis, V., Charitanti, A., Tegos, T., Destanis, E., & Chryssogonidis, I. (2017). Contrast-enhanced ultrasound of the carotid system: a review of the current literature. *J Ultrasound*, *20*(2), 97-109.

Rafailidis, V., Chryssogonidis, I., Tegos, T., Kouskouras, K., Charitanti-Kouridou, A. (2017). Imaging of the ulcerated carotid atherosclerotic plaque: a review of the literature. *Insights Imaging*, *8*(2), 213-225.

Ramalli, A., Boni, E., Savoia, A. S., & Tortoli, P. (2015). Density-tapered spiral arrays for ultrasound 3-D imaging. *IEEE Trans Ultrason Ferroelectr Freq Control*, *62*(8), 1580-1588

Ramnarine, K. V., Nassiri, R. J., Hoskins, P. R., & Lubbers, P. R. (1998). Validation of a new blood-mimicking fluid for use in Doppler flow test objects. *Ultrasound Med Biol*, *24*(3), 451-459.

Ramos, C. L., Huo, Y., Jung, U., Ghosh, S., Manka, D. R., Sarembock, I. J., & Ley, K. (1999). Direct demonstration of P-selectin and VCAM-1-dependent mononcular cell rolling in early atheorscelerotic lesions of apolipolprotein E-deficient mice. *Circ Res*, *84*(11), 1237-1244.

Ricci, S., Swillens, A., Ramalli, A., Segers, P., & Tortoli, P. (2017). Wall shear rate measurement: validation of a new method through multiphysics simulations. *IEEE Trans Ultrason Ferroelectr Freq Control*, *64*(1), 66-77.

Ricci, S., Ramalli, A., Bassi, L., Boni, E., & Tortoli, P. (2018). Real-time blood velocity vector measurement over a 2-D region. *IEEE Trans Ultrason Ferroelectr Freq Control*, *65*(2), 201-209.

Rosenzweig, S., Palmeri, M., & Nightingale, K. (2011). GPU-based real-time small displacement estimation with ultrasound. *IEEE Trans Ultrason Ferroelectr Freq Control*, *58*(2), 399-405.

Ross, R. (1986). The pathogenesis of atherosclerosis – an update. *N. Engl J Med*, *314*(8), 488-500.

Rothwell, P. N., Gibson, R., & Warlow, C. P. (2000). Interrelation between plaque surface morphology and degree of stenosis on carotid angiograms and the risk of ischemic stroke in patients with symptomatic carotid stenosis. *Stroke*, *31*(3), 615-621.

Roux, E., Ramalli, A., Liebgott, H. Cachard, C., Robini, M. C., & Tortoli, P. (2017). Wideband 2-D array design optimization with fabrication constraints for 3-D US imaging. *IEEE Trans Ultrason Ferroelectr Freq Control*, *64*(1), 108-125.

Rubin, J. M., Tuthill, T. A., & Fowlkes, J. B. (2001). Volume flow measurement using Doppler and grey-scale decorrelation. *Ultrasound Med Biol*, *27*(1), 101-109.

Rubens, D. J., Bhatt, S.,Nedelka, S., & Cullinan, J. (2006). Doppler artifacts and pitfalls. *Radiol Clin North Am*, *44*(6), 805-835.

Ruitenberg, A., den Heijer, T., Bakker, S. L. M., van Swieten, J. C., Koudstaal, P. J., Hofman, A., & Breteler, M. M. B. (2005). Cerebral hypoperfusion and clinical onset of dementia: the Rotterdam study. *Ann Neurol*, *57*(6), 789-794.

Saba, L., Caddeo, G., Sanfilippo, R., Montisci, R., & Mallarini, G. (2007a). Efficacy and sensitivity of axial scans and different reconstruction methods in the study of the ulcerated carotid plaque using multidetector-row CT angiography: comparison with surgical result. *AJNR Am J Neuroradiol*, *28*(4), 716-723.

Saba, L., Caddeo, G., Sanfilippo, R., Montisci, R., & Mallarini, G. (2007b). CT and ultrasound in the study of ulcerated carotid plaque compared with surgical results: potentialities and advantages of multidetector row CT angiography. *AJNR Am J Neuroradiol*, *28*(6), 1061-1066.

Saba, L., Sanfilippo, R., Sannia, S., Anzidei, M., Montisci, R., Mallarini, G., & Suri, J. S. (2012). Association between carotid artery plaque volume, composition, and ulceration: a retrospective assessment with MDCT. *AJR Am J Neuroradiol, 199*(1), 151-156.

Sabbah, H. N., Blick, E. F. & Stein, P. D. (1977). High-frequency pressure fluctuations: Their significance in the documentation of turbulent blood flow. *Cathet Cardiovasc Diagn, 3*(4), 375-384.

Sahn, D. J. (1988). Instrumentation and physical factors related to visualization of stenotic and regurgitant jets by Doppler color flow mapping. *J Am Coll Cardiol, 12*(5), 1354-1365.

Sauvage, J., Flesch, M., Ferin, G., Nguyen-Dinh, A., Poree, A., Tanter, M., … Deffieux, T. (2018). A large aperture row column addressed probe for *in vivo* 4D ultrafast Doppler ultrasound imaging. *Phys Med Biol, 63,* Art. no. 215012.

Schebesch, K. M., Simka, S., Woertgen, C., Brawanski, A., & Rothoerl, R. D. (2004). Normal values of volume flow in the internal carotid artery measured by a new angle-independent Doppler technique for evaluating cerebral perfusion. *Acta Neurochir (Wien), 146*(9), 983-986.

Schuff, N., Matsumoto, S., Kmiecik, J., Studholme, C., Du, A., Ezekiel, F., … Weiner, M. W. (2009). Cerebral blood flow in ischemic vascular dementia and Alzheimer's disease, measured by arterial spin labeling magnetic resonance imaging. *Alzheimers Dement, 5*(4), 454-462.

Seo, C. H., & Yen, J. T. (2009). A 256 x 256 2-D array transducer with row-column addressing for 3-D rectilinear imaging. *IEEE Trans Ultrason Ferroelectr Freq Control, 56*(4), 837-847.

Sho, E., Singh, T. M., Xu, G., Zarins, C. K., & Masuda, H. (2001). Blood flow decreases induces apoptosis of endothelial cells in previously dilated arteries resulting from chronic high blood flow. *Arterioscler Thromb Vasc Biol, 21*(7), 1139-1145.

Sirlin, C. B., Lee, Y. Z., Girard, M. S., Peterson, T. M., Steinbach, G. C., Baker, K. G., Mattrey, R. F. (2001). Contrast-enhanced B-mode US angiography in the assessment of experimental *in vivo* and *in vitro* atherosclerotic disease. *Acad Radiol, 8*(2), 162-172.

Skagen, K., Skjelland, M., Zamani, M., & Russell, D. (2016). Unstable carotid artery plaque: new insights and controversies in diagnostics and treatment. *Croat Med J, 57*(4), 311-320.

Skilbeck, C., Westwood, S. M., Walker, P. G., David, T., & Nash, G. B. (2001). Dependence of adhesive behavior of neutrophils on local fluid dynamics in a region with recirculating flow. *Biorheology, 38*(2-3), 213-227.

Snyder, H. M., Corriveau, R., Craft, S., Faber, J. E., Greenberg, S. M., Knopman, D., … Carrillo, M. C. (2015). Vascular contributions to cognitive impairment and dementia including Alzheimer's disease. *Alzheimers Dement, 11*(6), 710-717.

So, H. K. H., Chen, J., Yiu, B. Y. S., & Yu, A. C. H. (2011). Medical ultrasound imaging: To GPU or not to GPU?. *IEEE Micro, 31*(5), 54-65.

Solfrizzi, V., Panza, F., Colacicco, A. M., D'Introno, A., Capurso, C., Torres, F., … Capurso, A. (2004). Vascular risk factors, incidence of MCI, and rates of progression to dementia. *Neurology, 63*(10), 1882-1891.

Song, P., Manduca, A., Trzasko, J. D., & Chen, S. (2017). Ultrasound small vessel imaging with block-wise adaptive local clutter filtering. *IEEE Trans Med Imag, 36*(1), 251-262.

Song, P., Trzasko, J. D., Manduca, A., Huang, R., Kadirvel, R., Kallmes, D. F., & Chen, S. (2018). Improved super-resolution ultrasound microvessel imaging with spatiotemporal nonlocal means filtering and bipartite graph-based microbubble tracking. *IEEE Trans Ultrason Ferroelectr Freq Control, 65*(2), 149-167.

Sroubek, F., Cristobal, G., & Flusser, J. (2007). A unified approach to superresolution and multichannel blind deconvolution. *IEEE Trans Image Process*, 16(9), 2322-2332.

Steel, R., & Fish, P. J. (2002). Velocity bais and fluctuation in the standard dual beam Doppler reconstruction algorithm. *IEEE Trans Ultrason Ferroelectr Freq Control, 49*(10), 1375-1383.

Di Stenfano, R., Felice, F., & Balbarini, A. (2009). Angiogenesis as risk factor for plaque vulnerability. *Cur Pharm Des, 15*(10), 1095-1106.

Stein, J. H., Korcarz, C. E., Hurst, T., Lonn, E., Kendall, C. B., Mohler, E. R., … Post, W. S. (2008). Use of carotid ultrasound to identify subclinical vascular disease and evaluate cardiovascular disease risk: a consensus statement from the American Society of Echocardiography carotid intima-media thickness task force endorsed by the Society for Vascular Medicine. *J Am Soc Echocardiogr, 21*(2), 93-111.

Steinberg, D. (2002). Atherogenesis in perspective: hypercholesterolemia and inflammation as partners in crime. *Nat Med, 8*(11), 1211-1217.

Steinberg, D., & Witztum, J. L. (2002). Is the oxidative modification hypothesis relevant to human atherosclerosis?. *Circulation, 105*(17), 2107-2111.

Steinke, W., Kloetzsch, C., & Hennerici, M. (1990). Carotid artery disease assessed by color Doppler flow imaging: correlation with standard Doppler sonography and angiography. *AJR Am J Roentgenol, 154*(5), 1061-1068.

Steinman, A. H., Lui, E. Y. L., Johnston, K. W., & Cobbold, R. S. C. (2004). Sample volume shape for pulsed-flow velocity estimation using a linear array. *Ultrasound Med Biol, 30*(10), 1409-1418.

Sullivan, C. J., & Hoying, J. B. (2002). Flow-dependent remodeling in the carotid artery of fibroblast growth factor-2 knockout mice. *Arterioscler Thromb Vasc Biol*, *22*(7), 1100-1105.

Swillens, A., Segar, P., Torp, H., & Lovstakken, L. (2010). Two-dimensional blood velocity estimation with ultrasound: Speckle tracking versus crossed-beam vector Doppler based on flow simulations in a carotid bifurcation model. *IEEE Trans Ultrason Ferroelectr Freq Control*, *57*(2), 327-339.

Tamura, T., Cobbold, R. S. C., & Johnston, K. W. (1991). Quantitative study of steady flow using color Doppler ultrasound. *Ultrasound Med Biol*, *17*(6), 595-605.

Tanaka, T., Asami, R., Kawabata, K., Itatani, E. K., Uejima, T., Nishiyama, T., & Okada, T. (2015). Intracardiac VFM technique using diagnostic ultrasound system, *Hitachi Rev*, *64*, 488-492.

Tanter, M., & Fink, M. (2014). Ultrafast imaging in biomedical ultrasound. *IEEE Trans Ultrason, Ferroelectr, Freq. Control*, *61*(1), 102-119.

Tarkin, J. M., Joshi, F. R., & Rudd, J. H. F. (2014). PET imaging of inflammation in atherosclerosis. *Nat Rev Cardiol*, *11*(8), 443-457.

Tawakol, A., Singh, P., Mojena, M., Pimentel-Santillana, M., Emami, H., MacNabb, M., … Bosca, L. (2015). HIF-1α and PFKFB3 mediate a tight relationship between proinflammatory activation and anerobic metabolism in atherosclerotic macrophages. *Arterioscler Thromb Vasc Biol*, *35*(6), 1463-1471.

Tay, P. C., Garson, C. D., Acton, S. T., & Hossack, J. A. (2010). Ultrasound despeckling for contrast enhancement. *IEEE Trans. Image Process*, 19(7), 1847-1860.

ten Kate, G. L., Sijbrands, E. J., Staub, D., ten Cate, F. J., Feinstein, S. B., & Schonkel, A. F. L. (2010). Noninvasive imaging of the vulnerable atherosclerotic plaque. *Curr Probl Cardiol*, *35*(11), 556-591.

ten Kate, G. L., van Dijk, A. C., van den Oord, S, C. H., Hussain, B., Verhagen, H. J. M., Sijbrands, E. J. G., … Schinkel, A. F. L. (2013a). Usefulness of contrast-enhanced ultrasound for detection

of carotid plaque ulceration in patients with symptomatic carotid atherosclerosis. *Am J Cardiol*, *112*(2), 292-298.

ten Kate, G. L., van den Oord, S. C. H., Sijbrands, E. J. G., van der Lugt, A., de Jong, N., Bosch, J. G., … Schinkel, A. F. L. (2013b). Current status and future developments of contrast-enhanced ultrasound of carotid atherosclerosis. *J Vasc Surg*, *57*(2), 539-546.

Thomas, K. N., Lewis, N. C. S., Hill, B. G., & Ainslie, P. N. (2015). Technical recommendations for the use of carotid duplex ultrasound for the assessment of extracranial blood flow. *Am J Physiol Regul Integr Comp Physiol*, *309*(7), R707-R720.

Thomson, D. J. (1982). Spectrum estimation and harmonic analysis. *Proc. IEEE*, 70(9), 1055-1096.

Thorne, M. L., Rankin, R. N., Steinman, D. A., & Holdsworth, D. W. *In vivo* Doppler ultrasound quantification of turbulence intensity using a high-pass frequency filter method. *Ultrasound Med Biol*, *36*(5), 761-771.

Tibaut, M., Caprnda, M., Kubatka, P., Sinkovic, A., Valentova, V., Filipova, S., … Petrovic, D. (2019). Markers of atherosclerosis: part 2 – genetic and imaging markers. *Heart Lung Circ*, *28*(5), 678-689.

Tiran, E., Deffieux, T., Correia, M., Maresca, D., Osmanski, B. F., Sieu, L. A., … Tanter, M. (2015). Multiplane wave imaging increases signal-to-noise ratio in ultrafast ultrasound imaging, *Phys Med Biol*, *60*(21), 8549-8566.

Topcuoglu, M. A. (2012). Transcranial Doppler ultrasound in neurovascular diseases: diagnostic and therapeutic aspects. *J Neurochem*, *123* Suppl. 2, 39-51.

Tortoli, P., & Jensen, J. A. (2006) Introduction to the special issue on novel equipment for ultrasound research. *IEEE Trans Ultrason Ferroelectr Freq Control*, *53*(10), 1705-1706.

Toth, P., Tarantini, S., Csiszar, A., & Ungvari, Z. (2017). Functional vascular contributions to cognitive impairment and dementia: Mechanisms and consequences of cerebral autoregulatory dysfunction, endothelial impairment, and neurovascular upcoupling in aging. *Am J Heart Circ Physiol*, *312*(1), H1-H20.

Trattnig, S., Matula, C., Karnel, K., Daha, K., Tschabitscher, M., Schwaighofer, B. (1993). Difficulties in examination of the origin of the vertebral artery by duplex and color-coded Doppler sonography: anatomical considerations. *Neuroradiology*, *35*(4), 296-299.

Trebeschi, S., van Griethuysen, J. J. M., Lambregts, D. M. J., Lahave, M. J., Parmer, C., Bakers, F. C. H., … Aerts, H. J. W. K. (2017). Deep learning for fully-automated localization and segmentation of rectal cancer on multiparametric MR. *Sci Rep*, **7**, Art. no. 5301.

Tremblay-Darveau, C., Sheeran, P. S., Vu, C. K., Williams, R., Zhang, Z., Bruce, M., & Burns, P. N. (2018). The role of microbubble echo phase lag in multipulse contrast-enhanced ultrasound imaging. *IEEE Trans Ultrason Ferroelectr Freq Control*, *65*(8), 1389-1401.

Ubeyli, E. D., & Guler, I. (2004). Spectral analysis if internal carotid arterial Doppler signal using FFT, AR, MA, and ARMA methods. *Comput Biol Med*, *34*(4), 293-306.

Urs, R., Ketterling, J. A., Yu, A. C. H., Lloyd, H. O., Yiu, B. Y. S., & Silverman, R. H. (2018). Ultrasound imaging and measurement of choroidal blood flow. *Transl Vis Sci Tech*, *7*(5), Art. no. 5.

van Cauwenberge, J., Lovstakken, L., Fadnes, S., Rodriguez-Morales, A., Vierendeels, J., Segers, P., & Swillens, A. (2016). Assessing the performance of ultrafast vector flow imaging in the neonatal heart via multiphysics modeling and *in-vitro* experiments. *IEEE Trans Ultrason Ferroelectr Freq Control*, *63*(11), 1722-1785.

van Kempen, G. M. P., van Vliet, L. J., Verveer, P. J., & van der Voort, H. T. M. (1997). A quantitative comparison of image restoration methods for confocal microscopy. *J Microsc*, *185*(3), 354-365.

van Lammeren, G. W., Pasterkamp, G., de Vries, J. P. P. M., Bosch, L., de Haan, J. J., de Kleijn, D. P. V., …Vink, A. (2012). Platelets enter atherosclerotic plaque via intraplaque microvascular leakage and intraplaque hemorrhage: a histopathological study in carotid plaques. *Atherosclerosis*, *222*(2), 355-359.

Van Popele, N. M., Grobbee, D. E., Bots, M. L., Asmar, R., Topouchian, J., Reneman, R. S., … Witteman, C. M. (2001). Association between arterial stiffness and atherosclerosis: The Rotterdam study. *Stroke*, *32*(2), 454-460.

Varetto, G., Gibello, L., Castagno, C., Quaglino, S., Ripepi, M., Benintende, E., … Rispoli, P. (2015). Use of contrast-enhanced ultrasound in carotid atherosclerotic disease: limits and perspectives. *Biomed Res Int*, *2015*, 293163.

Versteeg, H. K., & Malalasekera, W. (2007). *An Introduction to Computation Fluid Dynamics: The Finite Volume Method*. Harlow, U.K.: Pearson Ed. Limited, 2007.

Viessmann, O., Eckersley, R. J., Christensen-Jeffries, K., Tang, M. X., & Dunsby, C. (2013). Acoustic super-resolution ultrasound and microbubbles. *Phys Med Biol*, *58*(18), 6447-6458.

Virmani, R., Kolodgie, F. D., Burke, A. P., Finn, A. V., Gold, H. K., Tulenko, T. N., … Narula, J. (2005). Atherosclerotic plaque progression and vulnerability to rupture: angiogenesis as a source of intraplaque hemorrhage. *Arterioscler Thromb Vasc Biol*, *25*(10), 2054-2061.

von Reutern, G. M., Goertler, M. W., Bornstein, N. M., Del Sette, M., Evans, D. H., Goertler, M. W., … Yasaka, M., on behalf of the Neurosonology Research Group of the World Federation of Neurology. (2012). Grading carotid stenosis using ultrasonic methods. *Stroke*, *43*(3), 916-921.

Vos, K. (2013). A fast implementation of Burg's method. www.opus-codec.org/decs/vos_fastburg.pdf, August 2013.

Wada, T., Kodaira, K., Fujishiro, K., Maie, K., Tsukyiyama, E., Fukumoto, T., … Yamazaki, S. (1994). Correlation of ultrasound-measured common carotid artery stiffness with pathological findings. *Atheroscler Thromb Vasc Biol*, *14*(3), 479-482.

Walczak, M., Lewandowski, M., & Zolek, N. (2013). Optimization of real-time ultrasound PCIe data streaming and OpenCL processing for SAFT imaging. *In: Proc IEEE Int Ultrasonics Symp*, *2013*, 2064-2067.

Walker, A., Henriksen, E., Ringqvist, I., & Ask, P. (2009). A rotating cylinder phantom for flow and tissue color Doppler testing. *Ultrasound Med Biol*, *35*(11), 1892-1898.

Walpola, P. L., Gotlieb, A. I., Cybulsky, M. I., & Langille, B. L. (1995). Expression of ICAM-1 and VCAM-1 and monocyte adherence in arteries exposed to altered shear stress. *Arterioscler Thromb Vasc Biol*, *15*(1), 2-10.

Wang, L., Luo J. Y., Li, B., Tian, X. Y., Chen, L. J., Huang, Y., … Huang,Y. (2016). Integrin-YAP/TAZ-JNK cascade mediates atheroprotective effect of unidirectional shear flow. *Nature*, **540**, 579-592.

Wang, S., Herbst, E. B., Pye, S. D., Moran, C. M., & Hossack, J. A. (2017). Pipe phantoms with applications in molecular imaging and system characterization. *IEEE Trans Ultrason Ferroelectr Freq Control*, *64*(1), 39-52.

Watts, D. M., Sutcliffe, C. J., Morgen, R. N., Meagher, S., Wardlaw, J., Connel, M., … Black, R. A. (2007). Anatomical flow phantoms of the nonplanar carotid bifurcation, part I: Computer-aided design and fabrication. *Ultrasound Med Biol*, *33*(2), 296-302.

Weber, L. A., Cheezum, M. K., Reese, J. M., Lane, A. B., Haley, R. D., Lutz, M. W., & Willines, T. C. (2015). Cardiovascular Imaging for the primary prevention of atherosclerotic cardiovascular disease events, *Curr Cardiovasc Imaging Rep*, *8*(9), Art. no. 36.

Wells, P. N. T. (2006). Ultrasound imaging. *Phys Med Biol*, *51*(13), R83-R98.

Wendell, C. R., Waldstein, S. R., Ferrucci, L., O'Brien, R. J., Strait, J. B., & Zonderman, A. B. (2012). Carotid atherosclerosis and prospective risk of dementia. *Stroke*, *43*(12), 3319-3324.

Willie, C. K., Colino, F. L., Bailey, D. M., Tzeng, Y. C., Jones, L. W., Haykowsky, M. J., … Ainslie, P. N. (2011). Utility of transcranial Doppler ultrasound for the integrative assessment of cerebrovascular function. *J Neurosci*, *196*(2), 221-237.

Wilson, T., Zagzebski, J., Varghese, T., Chen, Q. & Rao, M. (2006). The ultrasonix 500RP: A commercial ultrasound research interface. *IEEE Trans Ultrason Ferroelectr Freq Control*, *53*(10), 1772-1782.

Wintermark, M., Sesay, M., Barbier, E., Borbely, K., Dillon, W. P., Eastwood, J. D., … Yonas, H. (2005). Comparative overview of brain perfusion imaging techniques. *Stroke*, *36*(9), e83-e99.

Wissler, R. W. (1995). An overview of the quantitative influence of several risk factors on progression of atherosclerosis in young people in the Unite States: pathobiological determinants of atherosclerosis in youth (PDAY) research group. *Am J Med Sci*, **310**, S29-S36.

Wolters, F. J., Zonneveld, H. I., Hofman, A., van der Lugt, A., Koudstaal, P. J., Vernooij, M. W., Ikram, M. A., on behalf of the heart-brain collaborative research group (2017). Cerebral perfusion and the risk of dementia: A population-based study. *Circulation*, *136*(8), 719-728.

Wong, E. Y., Nikolov, H. N., Thorne, M. K., Poepping T. L., Rankin, R. N., & Holdsworth, D. W. (2009). Clinical Doppler ultrasound for the assessment of plaque ulceration in the stenosed carotid bifurcation by detection of distal turbulence intensity: a matched model study. *Eur Radiol*, *19*(11), 2739-2749.

Wootton, D. M., & Ku, D. N. (1999). Fluid mechanics of vascular systems, diseases, and thrombosis, *Annu Rev Biomed Eng*, *1*, 299-329.

World Health Organization (WHO) (2018). Global Health Estimates 2016: Deaths by Cause, Age, Sex, by Country and by Region, 2000-2016

World Health Organization (WHO) (2019) Dementia fact sheet. https://www.who.int/news-room/fact-sheets/detail/dementia. Accessed May 21, 2019.

Xekardaki, A., Rodriguez, C., Montandon, M. L., Toma, S., Tombeur, E., Herrmann, F. R., … Haller, S. (2014). Arterial spin labeling may contribute to the prediction of cognitive deterioration in healthy elderly individuals. *Radiology*, *274*(2), 490-499.

Yang, C., Gao, Y., Greaves, D. K., Villar, R., Beltrame, T., Fraser, D. S. & Hughson, R. L. (2014). Prior head-down tilt does not impair the cerebrovascular response to head-up tilt. *J Appl Physiol*, *118*(11), 1356-1363.

Yang, X., Jin, J., Xu. M., Wu, H., He, W., & Yuchi, M. (2013). Ultrasound common carotid artery artery segmention based on active shape model. *Comput Math Method M*, *2013*, Art. no. 345968.

Yazici, B., Erdogmus, B., & Tugay, A. (2005). Cerebral blood flow measurements of the extracranial carotid and vertebral arteries with Doppler ultrasonography in healthy adults. *Diagn Interv Radiol*, *11*(4), 195-198.

Yiu, B. Y. S., Tsang, I. K. H., & Yu, A. C. H. (2011). GPU-based beamformer: Fast realization of plane wave compounding and synthetic aperture imaging. *IEEE Trans Ultrason Ferroelectr Freq Control*, *58*(8), 1698-1705

Yiu, B. Y. S., Yu, A. C. H. (2013). High-Frame-Rate Ultrasound Color-Encoded Speckle Imaging of Complex Flow Dynamics. *Ultrasound Med Biol*, *39*(6), 1015-1025.

Yiu, B. Y. S., Lai, S. S. M., & Yu, A. C. H. (2014). Vector Projectile Imaging: Time-Resolved Dynamic Visualization of Complex Flow Patterns. *Ultrasound Med Biol*, *40*(9), 2295-2309.

Yiu, B. Y. S., & Yu, A. C. H. (2015). GPU-based minimum variance beamformer for synthetic aperture imaging of the eye. *Ultrasound Med Biol*, *41*(3), 871-883.

Yiu, B. Y. S., & Yu, A. C. H. (2016). Least-squares multi-angle Doppler estimators for plane-wave vector flow imaging. *IEEE Trans. Ultrason Ferroelectr Freq Control*, *63*(11), 1733-1744.

Yiu, B. Y. S., & Yu, A. C. H. (2017). Spiral flow phantom for ultrasound flow imaging experimentation. *IEEE Trans Ultrason Ferroelectr Freq Control*, *64*(12), 1840-1848. © 2017 IEEE. Reprinted, with permission, from Yiu, B. Y. S., & Yu, A. C. H. Spiral flow phantom for ultrasound flow imaging experimentation, IEEE Transactions on Ultrasonics, Ferroelectrics, and Frequency Control, December 2017.

Yiu, B. Y. S., Walczak, M., Lewandowski, M., & Yu, A. C. H. (2019). Live ultrasound color encoded speckle imaging platform for real-time complex flow visualization *in vivo*. *IEEE Trans Ultrason Ferroelectr Freq Control*, *66*(4), 656-669. © 2019 IEEE. Reprinted, with permission, from Yiu, B. Y. S., Walczak, M., Lewandowski, M., & Yu, A. C. H. Live ultrasound color encoded speckle

imaging platform for real-time complex flow visualization *in vivo*, IEEE Transactions on Ultrasonics, Ferroelectrics, and Frequency Control, April 2019.

Yiu, B. Y. S., Chee, A. J. Y., Tang, G., Luo, W., & Yu, A. C. H. (2019). High-frame-rate Doppler ultrasound bandwidth imaging for flow instability mapping. *Med Phys*, *46*(4), 1620-1633.

Yu, A. C. H., Steinman, A. H., & Cobbold, R. S. C. (2006). Transit-time broadening in pulsed Doppler ultrasound: a generalized amplitude modulation model. *IEEE Trans Ultrason Ferroelectr Freq Control*, *53*(3), 530-541.

Yu, A. C. H., & Cobbold, R. S. C. (2008a). Single-ensemble-based eigen-processing methods for color flow imaging-part I. the Hankel-SVD filter. *IEEE Trans Ultrason Ferroelectr Freq Control*, *55*(3), 559-572.

Yu, A. C. H., & Cobbold, R. S. C. (2008b). Single-ensemble-based eigen-processing methods for color flow imaging-part II. the Matrix Pencil estimator. *IEEE Trans Ferroelectr Freq Control*, *55*(3), 573-587.

Yu, A. C. H., & Lovstakken, L. (2010). Eigen-based clutter filter design for ultrasound color flow imaging: A review. *IEEE Trans Ultrason Ferroelectr Freq Control*, *57*(5), 1096-1111.

Yu, J., Lavery, L., & Kim, K. Super-resolution ultrasound imaging method for microvasculature *in vivo* with a high temporal accuracy. *Sci Rep*, *8*, Art. no. 13918.

Yuan, J., Usman, A., Das, T., Patterson, A. J., Gillard, J. H., & Graves, M. J. (2017). Imaging carotid atherosclerosis plaque ulceration: comparison of advanced imaging modalities and recent developments. *AJNR Am J Neuroradiol*, *38*(4), 664-671.

Yucel, E. K., Anderson, C. M., Edelman, R. R., Grist, T. M., Baum, R. A., Manning, W. J., Pearce, W. (1999). AHA scientific statement. Magnetic resonance angiography: update on applications for extracranial arteries. *Circulation*, *100*(22), 2284-2301.

Zhang, F., Lanning, C., Mazzaro, L., Barker, A. J., Gates, P. E., Strain, W. D., … Shandas, R. (2011). *In vitro* and preliminary *in vivo* validation of echo particle image velocimetry in carotid vascular imaging. *Ultrasound Med Biol*, *37*(3), 450-464.

Zhang, Y., Ying, M. T. C., Yang, L., Ahuja, A. T., & Chen, D. Z. (2016). Coarse-to-fine stacked fully convolutional nets for lymph node segmentation in ultrasound images. *In 2016 IEEE International Conference on Bioinformatics and Biomedicine (BIBM), 2016*, 443-448.

Zhou, X., Kenwright, D. A., Wang, S., Hossack, J. A., & Hoskins, P. R. (2017). Fabrication of two flow phantoms flor Doppler ultrasound imaging. *IEEE Trans Ultrason Ferroelectr Freq Control*, *64*(1), 53-65.

Zhou, X., Takayama, R., Wang, S., Hara, T., & Fujita, H. (2017). Deep learning of the sectional appearances of 3D CT images for anatomical structure segmentation based on an FCN voting method. *Med Phys*, *44*(10), 5221-5233.

Zhou, X., Leow, C. H., Rowland, E., Riemer, K., Rubin, J. M., Weinberg, P. D., & Tang, M. X. (2018). 3-D velocity and volume flow measurement *in vivo* using speckle decorrelation and 2-D high-frame-rate contrast-enhanced ultrasound. *IEEE Trans Ultrason Ferroelectr Freq Control*, *65*(12), 2233-2244.

Appendix

This appendix lists the video files referenced in this dissertation.

Movie 1.1.mp4: CESI cineloop acquired from a healthy volunteer at the carotid bifurcation. Flow enters from the common carotid branch (left) and moves to the internal carotid branch (right); a flow recirculation can be observed at the bulb region at end systole. A spectrogram acquired at inlet (indicated by the red box) was also shown to depict the cardiac phase. This demonstrates that HiFRUS algorithms (CESI) can be used to capture and display the flow dynamics of complex flow pattern. See Section 1.5.2 for detailed interpretation.

Movie 1.2.mp4: VPI cineloop acquired from a healthy volunteer at the carotid bifurcation. The cineloop depicts flow entering from the common carotid artery (right) splitting into the external (top) and the internal (bottom) branches at the bifurcation site. A recirculation zone can be observed at the carotid bulb (distal wall of internal branch) at end systole. This shows that HiFRUS imaging algorithm can derive angle-independent flow vectors consistently and render them intuitively. See Section 1.5.2 for detailed interpretation.

Movie 2.1.mp4: Video clip showing a sonographer using the CESI platform to acquire flow information from a common carotid artery. Bottom panel shows the platform's output image during the acquisition. This shows that the live imaging capacity of the CESI platform. See Section 2.5.1 for detailed interpretation.

Movie 2.2.mp4: CESI cineloop captured from a brachial bifurcation using the live CESI platform. The rendered flow speckle depicts the flow direction (from right to left) and the acceleration and deceleration of flow throughout the cardiac cycle. It also highlights the spatiotemporal dynamics of the retrograde flow at end systole. The retrograde flow was confirmed by the spectrogram acquired from the inlet of ulnar artery. See Section 2.5.2 for detailed interpretation.

Movie 2.3.mp4: CESI cineloop acquired from the brachial vein showing the flow dynamics during a clench maneuver. Flow acceleration can be observed at first, and flow gradually slowed down and stopped as the venous blood pool depletes. This suggests that the live imaging platform can also be used to capture changes in flow dynamics due to external manipulation. See Section 1.5.2 for detailed interpretation. See Section 2.5.3 for detailed interpretation.

Movie 3.1.mp4: Visualization of flow vectors using vector flow imaging (left panel) and VPI (right panel), captured from the spiral flow phantom. It can be seen that omnidirectional flow is present inside

the devised phantom. Furthermore, VPI can more intuitively render the spiraling flow path toward the outlet at the center. See Section 3.4.4 for detailed interpretation.

Movie 4.1.mp4: Cineloops of the nozzle flow rendered with DUBI (top row), color Doppler (middle row), and Doppler variance imaging (bottom row) for different flow conditions (Re = 375, 750, and 1125). DUBI is more effective in depicting the differences in flow instability as the Reynolds number increased, compared to the two other methods. See Section 4.3.1 for detailed interpretation.

Movie 4.2.mp4: Rendering of CEUS, highlighting the flow trajectory of microbubbles to identify unstable flow regions for different flow conditions. At Re = 375, laminar flow was observed as the microbubble trajectories did not cross. At Re = 750, unstable flow started to emerge, as depicted by the crossing of microbubble trajectories; this crossing point marks the transition from stable to unstable flow, indicated by the white dotted line. The unstable flow region moved toward the inlet at Re = 1125. See Section 4.3.1 for detailed interpretation.

Movie 4.3.mp4: DUBI rendering of flow stability in carotid bifurcation phantoms (healthy model, with 50% stenosis, and 75% stenosis). Unstable flow due to pathological condition can be highlighted by DUBI as the Doppler bandwidth increased in the presence of stenosis. See Section 4.3.2 for detailed interpretation.

Movie 5.1.mp4: This video demonstrates the ability of the motion compensation algorithm in MRMVI. The background B-mode image was acquired from a rat choroid with physiological motion observed over the course of the acquisition. Random positions were seeded (colored dots) on the imaging view and their positions were updated by the algorithm to compensate the background motion. The dots were able to closely trace the physiological motion. See Section 5.6.1 for detailed interpretation.

Movie 5.2.mp4: Time lapse of microvascular imaging acquired from a rat choroid. The microvasculature inside the choroid was gradually mapped by MRMVI in 1.5 seconds. See Section 5.6.2 for detailed interpretation.